Dynamics and Control of Membrane Mirrors for Adaptive Optic Applications

by

Jamil M. Renno

Dissertation submitted to the Faculty of the
Virginia Polytechnic Institute and State University
in partial fulfillment of the requirements for the degree of

Doctor of Philosophy

in

Mechanical Engineering

Dr. Daniel J. Inman, Chair
Dr. Martin E. Johnson
Dr. Mehdi Ahmadian
Dr. Andrew J. Kurdila
Dr. Ali H. Nayfeh

September 2, 2008
Blacksburg, Virginia

Keywords: structural dynamics, structural control, piezoelectricity, adaptive optics

Copyright by Jamil M. Renno, 2008

Dynamics and Control of Membrane Mirrors for Adaptive Optic Applications

Jamil M. Renno

Virginia Polytechnic Institute and State University, 2008

Advisor: Daniel J. Inman, Ph.D.

ABSTRACT

Current and future space exploration operations rely heavily on space-borne telescopes, of which mirrors are an integral component. However, traditional solid mirrors are heavy and require a big storage space. Deploying membrane mirrors can alleviate many of these obstacles. Membrane mirrors are light and can be compactly stowed resulting in cheap launching costs. It was also demonstrated that membrane mirror would provide quality optical imaging capabilities.

However, membrane mirrors exhibit undesirable vibrations that can be caused by thermal gradients or internally-induced excitations. The undesirable vibration degrades the performance of these mirrors. Hence, it is proposed to augment membrane mirrors with smart actuators around their outer rim. Smart actuators can be used to suppress the undesirable vibration. More importantly, such a system provide the capability to form appropriate surfaces to correct for aberrations in an incoming wavefront.

In this spirit, this work aims at modeling and control a membrane mirror augmented with smart actuators. The approach here to consider a membrane strip augmented with smart actuators as a prelude for studying circular membranes. We consider strips of membrane material, and treat two such structures: a membrane strip augmented with a single piezoceramic bimorph acting in bending, and a membrane strip augmented with multiple macro-fiber composite bimorphs. The later structure is studied under two actuation configurations. In the first configuration, both actuators act in bending. In the

other configuration, one actuator acts in bending and the second acts in tension. The developed models of both structures were validated experimentally. Then, control laws were derived for both structures. An optimal proportional-integral controller is used for the membrane strip augmented with a single piezoceramic bimorph. For the membrane strip augmented with two macro-fiber composite bimorphs, a sliding mode controller with a switching command is used. Simulation results are presented to demonstrate the efficacy of the proposed control laws.

Then, a circular membrane augmented with macro-fiber composite bimorph actuators is considered. We derive the governing equation of the structure for the general configuration, where actuators are producing bending moments and radial loading. Then, we seek a reduced order model of the structure. We work on obtaining a Galerkin expansion of the model where the test functions used are the mode shapes of the structure as obtained from a finite element analysis conducted in a commercial software package. Then the control problem is considered. The objective is to correct for optical aberrations, so the Zernike polynomial basis functions are used. A transformation from the optical modes to the mechanical modes is presented and an augmented adaptive controller is used to correct for image aberrations. The results presented show the efficacy of the controller.

بسم الله الرحمن الرحيم

In the Name of Allah, the Most Gracious, the Ever Merciful

إلى المدينة التي لم أزرها، حيفا...
سأحن إليك دوماً، ما حلقت الطيور فوق جبل الكرمل الخلاب، ما تكسرت الأمواج على شواطئك، و ما طلعت الشمس على خليجك الرائع...

To the city that I have never been to, Haifa...
I will always miss you, as long as birds fly over the majestic Mount Karmel, as long as waves splash at your shores, and as long as the sun rises over your magnificent bay...

﴿قل إن صلاتي و نسكي و محياي و مماتي لله رب العالمين
لا شريك له و بذلك أمرت و أنا أول المسلمين﴾
(الأنعام ١٦٢-١٦٣)

Say: Truly, my prayer and my service of sacrifice, my life and my death, are (all) for Allah, the Cherisher of the Worlds, No partner hath He: this am I commanded, and I am the first of those who bow to His will.
(The Holly Quran, 6: 162-163)

﴿و قل ربي زدني علما﴾
(طه ١١٢)

Say: My Lord! Increase my knowledge. (The Holly Quran, 20:112)

Acknowledgments

I truly believe that we are shaped, to a large extent, by the people we meet and deal with throughout our life. This chapter is meant to be about *Acknowledgments*, however, in the following, I will not only thank the people who have directly helped in this dissertation. I will talk about how people shaped my life, and how they changed who I am, at different levels, and to different degrees.

I have always been a religious person: nothing can be accomplished without the aid of Allah the Almighty; my humble efforts come next. I believe that praise and thanks should first be offered to Allah the Almighty. Prophet Mohamad (Peace and Blessing be upon Him) said: "He who does not thank the people, does not thank Allah the Almighty." In this spirit, I will thank as many people as my memory enables me, and for those I mistakenly forget, please forgive my shortcoming.

My Family

My parents deserve many thanks. Mr. Mohamad Renno always encouraged me to be more educated. When I was young, he insisted that I attend a private school. Not only he provided the finances, often depriving himself of many things for my sake. He provided much of the inspiration for what I have done in my life. Clarence B. Kelland once said: "My father did not tell me how to live; he lived, and let me watch him do it." My father's silence is more eloquent than words. I really cannot thank this man enough; I can only try to raise my kids the way he raised me. Mrs. Inaam Renno is so loving and caring. This woman is the embodiment of the word "mother." She cared for her family, made sure we had what we needed. She listened to us, and she was so patient; it is not

even real! I will never forget her teaching me the world's capitals at the age of two. I will never forget that she used to listen and read the science fiction stories I used to write. Mom and dad: you are amazing...

To my mother and father, I apologize for there is no way to say thank you. However, I can promise, and so far I have kept my promises, that I will absolutely do everything possible to raise my kids with the same ethics, standards and dedication your raised me with.

My brother Wessam, and my sisters Salam and Samah were very loving and caring. I was always thinking of them while working on this document. I often thought of my late grandfather Jamil Ahmed Renno who believed me since I was a kid; please allow me to say this one more time: the tall boy holding your name did not and will never disappoint you.

I would also like to thank my father and mother in law: Chakib Chreidi and Hasna Hleihel. They stood by my side in my darkest moments, and helped me as much as they could. I am fortunate to have them as my parents in law. I would also like to thank my brother in law Ibrahim Chreidi for his friendship and readiness to help.

Dissertation Committee and Funding Agency

I would like to thank my committee members: Dr. Mehdi Ahmadian, Dr. Andrew Kurdila, Dr. Martin Johnson and Dr. Ali H. Nayfeh. They were very helpful and always provided positive input to further improve this work. Dr. Eric Ruggiero of GE Global Research served as an external reviewer on my committee. We always had fruitful discussions and he was of great help in many things. I am also grateful for the funding of this work which was administered by the Center for Intelligent Material Systems and Structures at Virginia Polytechnic Institute and State University, on behalf of the Air Force Office of Scientific Research under grant FA9550-06-1-0143. I would also like to thank Mr. Daniel Marker of the Air Force Research Laboratory for motivating parts of this research.

My advisor

I cannot emphasize how much I was lucky to work with Dr. Daniel J. Inman. Dr. Inman is an accomplished and extraordinary academician. He is a leader in his field, and the author of bestselling graduate and undergraduate books in vibration and dynamics. But that is not who Dan Inman is; I think this is only a small part of who this individual is. Dr. Inman is the *advisor*. Yes, I think Dr. Inman is the *advisor*; this is how you define an advisor. He does not only monitor the academic and research progress of his students. Rather, he tries to make sure they succeed in their careers, and he actually helps to the best of his ability and beyond. He honestly point to his students their strengths and things they need to work on; he never mentions weaknesses! He advises on the writing style, problem approach, research methodology, career search, job interviews, all the way to how to carry yourself and answer questions in the professional world. He is an amazing person all around. Dan Inman is a demonstration of how you can be a great academic with an extremely busy schedule, while remaining a successful father and husband, and an amazing boss who can touch the lives of all his subordinates. Truly, a one of a kind family man, with unsurpassed social and personal skills. Being around him is so much fun, and watching him carry himself in any situation is just mesmerizing. Dr. Inman is student oriented, often chatting with us, and asking about our families and whenever he receives awards, Dr. Inman always acknowledged his students first. I am deeply affected by Dr. Inman, and I really wish I could become an advisor like him one day.

Professors at Virginia Tech

At Virginia Tech, I was extremely fortunate to study with some amazing scientists and educators. I want to specifically thank Dr. Konda Reddy who taught me the basics of nonlinear control, Dr. Naira Hovakimyan who taught me the theory of adaptive control, and Dr. Scott Hendricks who taught me dynamics in a way I would never forget. I regret missing the opportunity to take a class with Dr. Saad Ragab, and although he did not

serve on my committee, I often discussed my work with him and he was always willing to help. However, there are two faculty that affected me in a much deeper way, and these are Dr. Ali H. Nayfeh and Dr. Liviu Librescu.

Dr. Ali H. Nayfeh

I had the honor to study "Perturbation Techniques" and "Nonlinear Dynamics" with Dr. Ali H. Nayfeh. Dr. Nayfeh's presence in the class is very strong. The man's understanding of his field, and amazingly other fields, is absolutely, categorically solid. A thorough comprehension of the physics, math and engineering concepts behind everything he talks about, is just stunning to witness in one man. He used to smoothly flow between concepts, and takes you from math to physics to engineering, often switching domains with great agility, one cannot even describe. Despite this, he never conveyed to me or to the class his superiority. Dr. Nayfeh is an exceptional person who has touched my life. I have also known Dr. Nayfeh outside the classroom. He was always kind, humble and helpful.

Late Dr. Liviu Librescu

I was fortunate to get my knowledge on "Plates and Shells" and "Composite Structures" from late Dr. Liviu Librescu. Dr. Librescu was unique in his teaching. He was extremely dedicated to his profession. The zeal and enthusiasm he shows when teaching are tremendous, and they effected me a great deal. It is near impossible to attend his class and not get interested in what he is explaining. His energy transfers through the classroom, demanding the concentration of everyone while he shows the intricate details of the theory. His formality might wrongly project that he is unapproachable. The opposite is correct; Dr. Librescu was extremely friendly. Knowing Dr. Librescu made me fully realize the importance of passions and love for one's work.

Virginia Tech and Blacksburg Community

I have had the pleasure of knowing many people in Virginia Tech, starting with the colleagues at the Center for Intelligent Material Systems and Structures (CIMSS), where the environment was so friendly and everyone was willing to help with everything. Pablo Tarazaga was a great help in the lab. I also appreciate the friendship of Thomas Micheal Seigler, Justin Farmer, Steve Anton, Tim Allison and Vishnu Baba Sundaresan, and Daniel Piers. David Neal and Austin Creasy always brought joy to the lab, and David Hopkinson coached me on running and swimming and advised me on hiking and camping. Andy Sarles shared his secret recipes with me and always gave me new ways to cook: I still remember that pasta recipe Andy. Alper Erturk was a great colleague on all levels, very knowledgeable in his field and always willing to discuss problems and offer help. Onur Belgin, Armaghan Salehian, Mana Afshari, Mohamad Amin Karami, and Woon Kim were amazing friends and colleagues. The administrative assistant of CIMSS, Beth Howell, facilitated everything for me, and took care of all our needs. She also coached me on running among many other things. I want to say thank you for everyone at CIMSS. This place is great because everyone of you.

During my stay in Blacksburg, I also had many roommates. I would like to thank Sherif Agha, Adam Daken, Ahmed and Amjad Eltayeb, Nurullah Ketene and Mohammed Elyyan. My roommate for the longest time was Mohammed Elyyan, who became a dear friend, in fact a brother. I enjoyed his friendship so much, and I would never forget the times we spent together, the food we used to cook and our shopping endeavors.

The Muslim community in Blacksburg was also amazing. Mazen Arafeh was always an older brother for me. He helped me in everything from the moment I arrived to Blacksburg. Qasem Abdelal, Eihab Abdel-Rahman, Haider Arafat, Mohammed Daqaq, Osama Marzouk, Shaadi Elswaifi, Ahmed Ghoniem, Rami Musa, Mohamad Abou Saker, Emad Saif, Hussam Almulhim, Helmi Temimi, Mahboub Baccouch, Ahmed Sidky, Mohammad Al-Smadi, Shouib Qudah, Ahmed Athamneh, Amr and Tamer Desouky, Numan Al-Rayyan, Shereef Sadek, Amjad Zibdeh, Abdulmuhsen Alqahtani (Abou Yazid), Ahmed Kamal Ali, Abdulilah Dawoud, Mohamed Naguieb, Abdelmounaam Rezgui, Mohammad

Shehada, Amine Chigani, Morsi Mahmoud, AbdulShakur Abdullah, Abdel-Halim Salem Said, Abdel-Salam Gomaa, Firas Almatar (Abou Yousef), Dr. Hanif Sherali, Dr. Slimane Adjerid, Dr. Hesham Rakha, and Olivia Monem; all contributed to an intellectual atmosphere that encouraged me to move forward. Imran Akhtar remains a special person also. His dedication to his work, while raising a family is a valuable source of learning. Amr Eid Helal is a special brother who is always willing to listen and help. I also learned many things from Khaled Adjerid, and I always enjoyed his company. Amjad Mustafa was also a dear friend whom I enjoyed spending time with. Everyone of you made Blacksburg feel more than home. Thank you very much, just for being there, and I want to wish everyone of you a joyful and successful life.

Finally, my dearest friend through these years is Bashar Hammad. I was very fortunate to meet Bashar, on my first day in Blacksburg. Bashar always cared, and asked for nothing in return. He was always by my side, and he was always willing to help even when he himself needed help. Bashar's friendship is something I am very proud of.

And, the sweet comes at the end. Hiba Chreidi: my lovely wife. This lady stood by my side to the extreme. In my darkest moments ever, Hiba did not leave me. Hiba stayed with me and chose me over everything else; her love and trust are unwaivering. She always brings a smile to my face, even when she is thousands of miles away; I just cannot recall my life before knowing her. May our life together be filled with joy and happiness forever. I love you Hiba...

JAMIL M. RENNO

Virginia Polytechnic Institute and State University
September 2008

Contents

List of Tables

List of Figures

Nomenclature

γ	air damping coefficient, N.s/m^2
γ_{ij}	shear strain
v	Poisson's ratio
ρ	mass density, kg/m^3
σ	stress, N/m^2
$\boldsymbol{C}$	damping matrix
$\boldsymbol{K}$	stiffness matrix
$\boldsymbol{M}$	mass matrix
A	area, m^2
a	bimorph constant, m^3
c	Kelvin-Voigt damping coefficient, N.s/m^2
d_{31}	piezoelectric coupling coefficient in the {31} mode, m/V
E	Young's modulus of elasticity, N/m^2
e_i	normal strain in the i-th direction
f	applied force per unit length, N/m
N	number of temporal coordinates
R	raduis, m
t	time, s
U	displacement, m
V	voltage applied to actuator, V
y	ordinate, m
z	coordinate along the thickness direction, m

Subscripts

a	property of actuator
exp	value obtained experimentally
FEM	value obtained through the finite element method
i	index of variable or property
j	index of variable or property
k	property of, or input to the k-th bimorph ($k = 1,2$)
m	membrane property
p	piezoelectric actuator property

Superscripts

A	axial property
B	bending property
T	transpose of a matrix or vector

Acronyms

FEA	Finite Element Analysis
FEM	Finite Element Method
GA	Genetic Algorithm
LQR	Linear Quadratic Regulator
MEMS	Micro Electro Mechanical Systems
MFC	Macro Fiber Composite
MIMO	Multi-Input, Multi-Ouput
NASA	National Aeronautics and Space Administration
PI	Proportional-Integral
PVDF	Polyvinylidene Fluoride
PZT	Lead Zirconate Titanate
RBF	Radial Basis Function
SISO	Single-Input, Single-Output
SMA	Shape Memory Alloy

Chapter 1

Introduction

Man has tried to explore space since the dawn of humanity. Space exploration was limited to observation through earth based telescopes until 1957. On October 4, 1957, the former Soviet Union launched **Sputnik 1**, the first man-made object to orbit the planet. This achievement, regarded a milestone, started a new era in space exploration, leading the way to the first moon landing by American **Apollo 11** on July 20, 1969.

Following these events, space observation could actually move from monitoring space from the earth to monitoring space from space itself. Indeed, the idea of space-based telescopes predates the first human endeavors in space. In 1946, Dr. Spitzer was the first to propose launching a space-based telescope. He argued that a space-based telescope will avoid the atmosphere and bad weather. Moreover, such telescope could observe infrared and ultraviolet light that are usually absorbed by the atmosphere (Spitzer, 1946). This actually led to the launch of the Hubble telescope, Fig. 1.1, in 1990[1].

One of the problems that hinder the advancement of space telescopes is their weight. For instance, the Hubble telescope, has a mass of 11,110 kg (Endelman, 1990). Reducing the weight of space telescopes would immediately reduce launching and operating costs. In this spirit, the James Webb Space Telescope, Fig. 1.2, has 18 hexagonal Beryllium mirrors, each 51 inches wide. The complete arrangement will be half the weight of Hubble's main mirror, and 2.5 times bigger[1].

[1]Copyright statement: "NASA still images, audio files and video generally are not copyrighted. You may use NASA imagery, video and audio material for educational or informational purposes, including photo collections, textbooks, public exhibits and Internet Web pages. This general permission extends to personal Web pages.", provided at http://www.nasa.gov/multimedia/guidelines/index.html, accessed on September 19, 2008.

Figure 1.1: The Hubble space telescope.
Image courtesy of NASA.

This concept applies well to any other equipment that will function in space. For instance, lightweight structural elements (that can be inflated if needed) are proposed to solve a multitude of spacecraft problems. Spacecrafts equipped with light structural elements are inexpensive to launch. However they suffer from nutational instabilities. The scientific community saw a significant example in 1958 of such instabilities, when the Explorer satellite was launched. The vibration of the antennae resulted in energy transfer between the rigid and flexible motion of the satellite. This incident clearly brought attention to the need to model and study lightweight flexible structures.

Moreover, during the 1950's, the space community started to investigate a new concept. This would be of "gossamer" based spacecraft. Gossamer structures are ultra-lightweight structures, relying mainly on membrane-like structures. These structures could be flat plates or inflated curved panels, but they cannot resist compressive loads. The U.S. Air Force Research Laboratory (AFRL) began a program of research on membrane technologies in 1995. Various government organizations, including the U.S. Air Force, the U.S. Department of Defense, and NASA agencies like the Jet Propulsion Laboratory have a mounting interest in this area, (Jenkins, 2001). Consequently, two major problems can be identified:

a) **Modeling of Gossamer Structures** Most gossamer structures are made of polymers

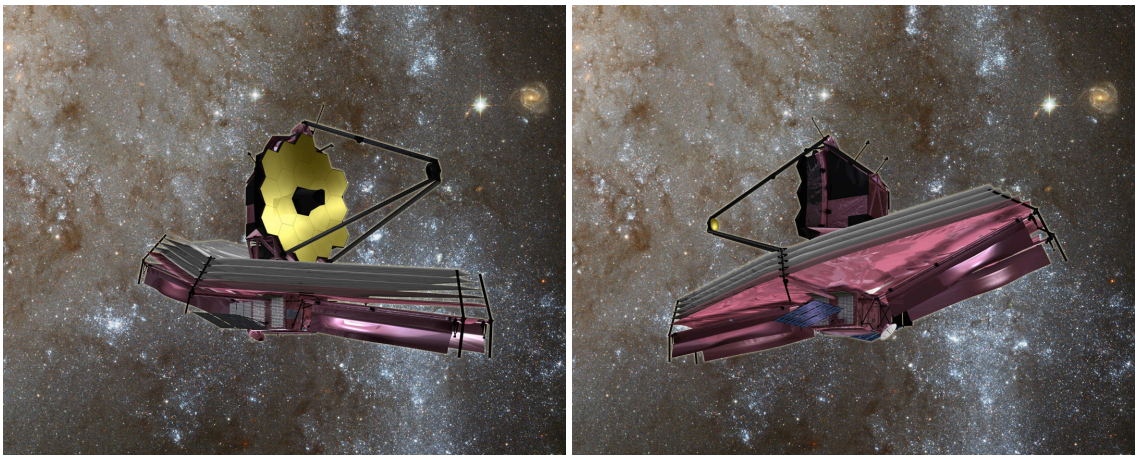

(a) Front view of the telescope. (b) Back view of the telescope.

Figure 1.2: Artistic illustration of the James Webb Space Telescope.
Images courtesy of NASA.

which are viscoelastic materials. Hence, when modeling gossamer structures, one has to address material nonlinearities. Moreover, these structures are geometrically complicated (for instance membranes augmented with smart actuators, etc ...), which poses numerous modeling challenges. And as one speaks of modeling, one has to mention that some of the structures under study are too large (or too expensive) to be tested before launching, and hence accurate modeling is extremely important in this case.

b) **Control** As these structures are highly flexible, the control question arises. These structures require vibration suppression and shape control. In other words, it is desired to maintain these structures at their equilibrium configuration despite the presence of various disturbances (large thermal gradients, internally induced excitations, etc...). Vibration suppression after performing pre-determined maneuvers is also required. Moreover, in some applications, the goal is to change the configuration of these structures in a favorable way to accomplish certain tasks.

The problems mentioned above are the main two problems to be considered. A host of other problems require treatment, depending on the application. For instance, wrinkle prediction and characterization is categorically crucial for adaptive optic applications,

but less important for solar sail applications. As this dissertation treats a wide spectrum of subjects, and before moving further, some definitions are in order,

- **Adaptive Optics** Tyson (2000) defined adaptive optics as "*a scientific and engineering discipline whereby the performance of an optical signal is improved by using information about the environment in which it passes*".
- **Shape Control** *The problem of regulating a structure to a non-equilibrium configuration. Many approaches are available to handle shape control. In-plane actuation, pressure supported canopies, and boundary angulation are usually used. In this work, in-plane actuation will be treated.*
- **Zernike Polynomials** *This is a set of orthogonal polynomials that can be used to describe typically encountered optical aberrations of a circular mirror. A linear combination of Zernike polynomials can be used to describe the aberration in an incoming wavefront over the surface of a circular mirror.*

In the following, a literature review of the research relevant to the work to be presented in this dissertation will be presented. Section 1.1 reviews the research done in the area of gossamer structures. Previous literature conducted in the area of membrane mirrors is surveyed in Section 1.2. Recently published research in the area of adaptive optics is compiled in Section 1.3. Section 1.4 reviews the research done in the area of predicting membrane wrinkles. An overview of control theory for space structure is provided in Section 1.5. More specifically, the relevant research published in the area of structural shape control is surveyed in Section 1.6. The objective of this dissertation, our treatment approach and the document's layout are given in Section 1.7.

1.1 Gossamer Structures

Research in the field of ultra large ultra-lightweight satellite structures, also known as gossamer structures, has been ongoing since the 1960's. This field of research encompasses many areas and there is a wealth of publications treating its various facets. A brief review of the relevant published research is presented herein.

Hedgepeth (1981) discussed the design requirements of large structures which must be deployed, erected, assembled, or fabricated in space. He specifically mentioned that "the primary requirements will arise from the demands for high dimensional accuracy of the structure..." Cassapakis and Thomas (1995) presented an overview of the development of inflatable structures through the 1990's. They covered the research milestones accomplished and analyzed the lessons learned at the Department of Energy and NASA space programs. Later in the 1990's, a new concept of a filled aperture optical space telescope was presented (Bekey, 1999). Moreover, Bekey's design concept allows for folding the membrane into small packages so that the entire telescope can be launched by a small booster. Jenkins et al. (1999) addressed the problem of modeling and controlling a class of nonlinear, highly compliant structures. Specifically, planar and inflatable membranes were considered. The aim was to introduce intelligent control strategies capable of extracting performance information from precision large membranes and subsequently use this information to achieve maximum surface precision. Slade and Tinker (1999) investigated the dynamic and static deflection behavior of an inflatable cylindrical strut constructed of Kapton. A series of tests and analytical modeling efforts for determining the inflatable cylinder's response at various pressures and loading conditions were documented. Chmielewski et al. (2000) also introduced the "Gossamer Spacecraft Initiative" as a new NASA program to begin the development of large, ultra-lightweight structures. These would include, among other things, optical apertures, infrared and sub-millimeter telescopes.

Garner and Leipold (2000) summarized the developments in solar sails research. They presented a detailed overview of solar sails, and pointed areas were more research effort is required. Darooka and Jensen (2001) discussed inflatable rigidizable structures that would offer unique advantages for achieving reduced overall mass and packaging volume. A two volume series edited by Jenkins (2001, 2006) provides the most comprehensive coverage of gossamer technology, including topics ranging from the mechanics of membranes to inflatable space habitats. Quadrelli and Sirlin (2001) initiated the derivation of the incremental equations of motion of membrane to be used in simulations of gossamer spacecraft and precision inflatable structures. They also presented

a discussion on control problems of membrane structures used in space. Whites and Knowles (2001) numerically solved for the electromagnetic force and torque on selected fibrous sail samples. Fibrous sails are comprised of a conducting carbon fiber network as opposed to polymer sails that typically use thin Kapton or Mylar films. Fibrous sails withstand higher temperatures, and are immune to ultra violet degradation when compared to polymer sails. Cadogan et al. (2002) conducted various tests on shape memory composite materials to meet the requirements of gossamer space structures. The testing encompassed degradation from folding and packaging, storage life and aging characteristics, vacuum stability, outgassing characteristics, and ability to return to shape when heated after packing. Davis and Agnes (2002) examined the environmental disturbances that act upon space structures. The optimization of inflatable space structures requires the knowledge of these external loads. The concern was that these disturbances will hinder the performance of inflatable space structures, where the primary design concern is dimensional accuracy. Dixit et al. (2002) discussed the development of large aperture Fresnel lenses for use in space telescopes. A monolithic Fresnel lens is fabricated. It is verified that such lens can be used in color-corrected diffractive telescopes.

Early (2002) proposed using a Fresnel zone lens made with solar sail materials as the primary optic for large aperture space telescopes. The fabrication technique of a 1 m size and larger Fresnel phase plate optic was also presented. Park et al. (2002) presented an experimental investigation of the vibration testing of inflated, thin-film torus using smart materials. The difficulties in ground testing, due largely to the high damped nature of inflated structures, were explored. PVDF and MFC patches were used as actuators and sensors throughout the testing process. Tzou et al. (2002) studied the control of toroidal shells using piezoelectric patches. They concentrated on studying the actuator location effect on micro-control actions imposed upon the structure. Mathematical models were developed for the combined structure and the effect of actuator location was demonstrated through various meridional/ circumferential positions. Holland et al. (2003) parametrically studied the effect of boom axial loading on the global dynamics of a 2 m solar sail scale model. The experimental model was used for building expertise in finite element analysis and experimental execution. Lyshevski (2003) proposed

designing cognitive high-performance systems for networked large-scale MEMS to control smart variable-geometry flexible control surfaces. The reported results are directly applicable to deformable membrane mirrors. Papa et al. (2003b) summarized original structural dynamics experimental activities with gossamer structures conducted at three NASA centers. The authors alluded to the absence of standardized test methods for gossamer structures model validation. Moreover, many factors caused such testing to be exceptionally difficult: facility size limitations, gravity and air effects, nonlinearities, to name a few. Redding et al. (2003) documented key technologies developed to support the James Webb Space Telescope, Terrestrial Planet Finder, and Actuated Hybrid Mirror Telescope missions. The main focus was on wavefront and figure errors corrections. Ruggiero et al. (2003b) reviewed research conducted in the area of inflatable toroids, with emphasis on experimental modal analysis and the benefits of employing active materials for vibration control.

Ruggiero et al. (2003a) introduced a new multiple-input, multiple-output testing technique for ultra-large structures. This methodology was used to test an inflated torus with bonded membrane mirror to extract modal parameters, such as the damped natural frequencies, modal damping, and mode shapes. The methodology is very suitable for large space structures, as multiple actuators/ sensors would be used in testing these structures. Belvin (2004) defined various classes of large space systems in order to describe the goals and system challenges in structures and material technologies. His work posed future technology challenges to develop a list of technology investments that can have significant impacts on the development of large space systems. Gaspar et al. (2004) focused on the development of modal test techniques for validation of a solar sail gossamer space structure design. In particular, the validation and comparison of the capabilities of various excitation techniques for modal testing of solar sail components were considered. The excitation methods were tested in-air and in-vacuum. Piezoelectric patches on different locations were used to perform the modal tests. More importantly, the capabilities of these methods were assessed as for on-orbit flight testing. Glaese and Bales (2004) considered dynamic tailoring for gossamer structures. A torus with stiffening dimples and an attached central membrane was used for demonstration. The torus

was excited using three reaction mass actuators while the velocity of the central membrane was measured. Lightweight tuned mass dampers were attached to the torus in an attempt to reduce the vibration in a narrow-band region. Piezoelectric polymer patches were attached to the membrane and passive shunting was implemented to illustrate broadband vibration attenuation of the membrane. Jha and Inman (2004) considered the vibration suppression of an inflated space structure using piezoelectric actuators and sensors. In particular, MFC patches were used as actuators and PVDF were used as sensors. A sliding mode controller and observer were developed. The closed loop system was simulated numerically, and the robustness of the system against disturbances and parameter uncertainty was studied. Johnston et al. (2004) documented an attempt to study the gravity-induced deformations of lightly preloaded membranes. Two sub-scale gossamer structures were considered: a single quadrant from a 2 m, 4 quadrant square solar sail and a 1.7 m membrane layer from a multi-layer sunshield. Photogrammetry measurements and nonlinear finite element analysis were used to predict the behavior of the test article under a range of pre-loads and in several orientations with respect to gravity. Ruggiero et al. (2004a) presented a review of the developing research approaches aiming at the shape control of membrane mirrors.

Ruggiero et al. (2004b) investigated the feasibility of using a MIMO modal testing technique on an inflated torus. In particular, they focused on using MFC patches as actuators and sensors. The advantage of MFCs is evident, they can conform to the curved surface of the torus under testing. Despite the presence of multiple actuators, the MIMO technique presented enables the differentiation between modes at nearly identical resonant frequencies. The methodology and post-processing techniques were successfully implemented to an inflated Kapton torus. Tzou et al. (2004) followed up their work (Tzou et al., 2002) by further studying the spatial location effect of actuator placement and evaluate the control authority imposed upon toroidal shells. Ruggiero (2005) developed a basis for conversing between the optical and mechanical realms. The analysis presented demonstrated that structural characteristics of a circular lens could be used favorably as an adaptive optic deformable mirror for eliminating almost 100% of a 5^{th} order image aberration. Greschik (2006) presented a review of the dimensional issues such

as scaling gossamer structures. His work offers insights into engineering bottlenecks and helps identify desirable structural and design qualities to mitigate them. Lee and Lee (2006) investigated the applicability of assumed-strain solid-shell finite elements for analysis of gossamer space and near-space structures. Quadruple precision is explored to further extend the capability of the nine-node assumed strain solid shell elements to analyses of extremely thin structures. Ruggiero and Inman (2006b) addressed the issues of wrinkle elimination and membrane shape control in gossamer structures; they also provided a summary of recent breakthroughs in gossamer technology and pointed out important gaps in the field. Nakaya et al. (2007) discussed the dynamics of a large membrane for achieving spinning solar sail-craft. The concept was demonstrated via two experiments: an ice rink and a balloon experiment. In both experiments, a 10 m and 20 m diameter membrane was deployed successfully.

1.2 Membrane Mirrors

In the spirit of reducing the weight of spacecraft, membranes provide a solution to problem in a natural way. Membranes can be used as mirrors (or lenses) instead of plate elements. However, the low areal density of membranes is accompanied with undesirable wrinkles and vibration issues. To accomplish meaningful goals in this area, the development of strict membrane tolerance, vibration suppression and shape control has to be studied to achieve a functional membrane mirror. In the following, recently published research in the area of membrane mirrors is cited.

Greeschik et al. (1998) studied the pressurization of initially flat and curved axis-symmetric membranes to approximate and exact parabolic shapes, respectively. They also studied the impact of uniform radial edge support displacement on the accuracy of the mirror. Moreover, they discussed the design of initially non-flat membranes to assume a parabolic shape with proper pressurization. Vdovin et al. (1999) developed a membrane micromachined deformable mirror with a 50 mm diameter. The mirror featured a maximum surface deflection of 18 μm and a response time better than 2 ms. Wilkes et al. (1999) presented two methods to achieve optically desirable deterministic

shapes. The first method involved pre-straining the membrane to reduce the spherical aberrations in such a mirror. The second method involved the use of a plunger to translate the central region of the membrane along the optical axis. Dayton et al. (2000) presented laboratory and field experimental results of a membrane mirror as an adaptive optic device. The device can be operated at high temporal bandwidths from a low cost personal computer based control system. Jenkins and Faisal (2001) investigated the effects of thermal loads on the precision of membrane mirror surfaces. They studied their model under different temperature profiles, varying both in temperature and spatial extent. Williams et al. (2001) investigated the use of membrane theory for modeling inflatable space structures. The main concern was whether classical membrane theory can account for the effects of active, surface-mounted piezopolymer patches. The Rayleigh-Ritz method was employed to approximate the natural frequencies and mode shapes of such layered systems.

Choi et al. (2002) investigated the use of networked actuators to control a membrane mirror. In their work, they adopted the concept of power allocation and distribution circuit to network a rectenna/actuator patch array (a rectenna is a **rec**tifying ant**enna**). This concept adds a significant amount of rigidity to the membrane's stiffness and is also relatively heavy; hence, a dipole rectenna array was used as it is flexible and light. The networked actuators were tested to correlate the network coupling effect, power allocation and distribution, and response time. In order to simplify ground testing of large deployable membrane structures, Kukathasan and Pelligrino (2002) included air effects in the finite element models of these structures. Accounting for air effects eliminates the need to carry out extensive tests in vacuum chambers. Rogers and Agnes (2002) modeled an active optical membrane as a laminate of inflatable structural material and piezopolymer sheets. Every electrode was etched individually to allow selective actuation. Witherspoon and Tung (2002) proposed using a MEMS-based flexible sensor and actuator system for membrane mirrors deployed in space. The MEMS sensors would be packaged onto the front side of a polyimide substrate and the MEMS actuators on the backside of the substrate using flexible electro active polymer based material.

Adetona et al. (2003) constructed and tested a haxapod made from inflatable/rigidizable material. The laboratory configuration employed a tensioned membrane mirror that was tested as well. The testing identified more than 300 modes with 21 modes showing damping values less than 1%. Bales et al. (2003) reported on the investigation of challenges faced when performing dynamic characterization of the thin membrane surfaces. Flint et al. (2003) presented the results of a series of measurements to determine the dynamics of doubly curved, very thin film shells. In particular, in-air, in-vacuum, and in-Nitrogen tests were conducted for a 0.5 m and 1.0 m diameter, 51 μm thick shells. Gullapalli et al. (2003) discussed the actuation and control of membrane mirrors. They focused on a set of candidate components: MEMS based large stroke (> 100 microns) ultra lightweight (0.01 g) discrete inch worm actuator technology, and a distributed actuator technology, in the context of a novel lightweight active flexure-hinged substrate concept that uses the nano-laminate face sheet. Lin and Hsu (2003) investigated experimentally and analytically the attenuation effect of a variable optical attenuator with a tunable non-smooth mirror. The working principle of a variable optical attenuator is based on the non-uniform shape deformation of a membrane mirror by thermally driven bimorph actuators. Rogers and Agnes (2003) followed up on their previous work (Rogers and Agnes, 2002), and presented an analytical solution of the simplified axisymmetric system. They used the method of integral multiple scales, and presented results for both static and dynamic formulations of the optical membrane. Solter et al. (2003) presented the development of an actuator concept to perform vibration control from the boundary of a thin-hexapod-film membrane. The actuator was designed to actuate the membrane out-of-plane motion and in-plane tension by varying the boundary conditions.

Gunderson et al. (2004) investigated the concept of an initially parabolic membrane that is flattened due to intrinsic stresses and is re-inflated to a condition of zero apex displacement. The pressure required for re-inflation was determined based on geometrically linear, axis-symmetric assumptions, and geometrically nonlinear finite element analysis of a circular membrane mirror. Lopez et al. (2004) presented interim results from a study of the behavior of unidirectionally tensioned-rectangular flat, and single-

curved membranes. Young and Pai (2004) used the nonlinear membrane theory to derive a model for a pre-tensioned rectangular Kapton membrane. The membrane was excited at four corners by a frame using an electromechanical shaker. Chodimella et al. (2005) performed boundary control on a 0.25 m pressure-augmented-circular membrane mirror to correct certain types of figure errors. Hamelinck et al. (2005) presented a large-circular adaptive deformable mirror with high actuator density. The deformable mirror consisted of a thin continuous membrane which acts as the correcting element. The out-of-plane displacement is imposed through a grid of low voltage electromagnetic push-pull actuators. Hishinuma and Yang (2005) augmented a large-stroke piezoelectric unimorph actuation array to a circular-continuous membrane mirror (50 mm $\times$ 50 mm). The piezoelectric unimorph actuator was optimized and showed a deflection of 5.7 μm at 20 V. The assembled membrane mirror showed an operating frequency bandwidth of 30 kHz. Moore et al. (2005) presented their effort in fabricating and testing a 1 m class lenticular (circular) membrane mirror using active boundary control and stress-coating applications to form a usable aperture for visible imaging applications. Patrick et al. (2005) developed a circular membrane mirror that accounts for spherical and boundary aberrations by coating the membrane with varied thickness stress coating. As the mechanical properties of the membrane are altered, pressurization can be used to shape it in a way matching the design prescription.

In 2006, Patrick et al. presented the final testing data of this membrane mirror. The membrane mirror's diameter was 0.7 m diameter mirror, made of a thin-film polymer material, and their testing involved the use of a canopy augmented with a reflectively-coated membrane and pressurization was used to establish a desired focal length. Ruggiero and Inman (2006c) modeled a tensioned rectangular membrane augmented with a piezoceramic bimorph attached in a bimorph configuration near its boundary. A finite element model was developed, and structural control based on the LQR technique was then used to demonstrate effective vibration control. da Costa Rodrigues (2006) studied local actuation of thin membranes for adaptive optics. Piezoceramics were used and numerical results were presented based on the finite elements method. Shepherd et al. (2006a) provided design criteria for establishing achievable surface deflection perfor-

mance inside a “clear aperture” region for a preselected number of desired Zernike polynomials, and a number of retained quasi-statically-actuated vibration mode shapes. This approach is contrasted with a direct projection method is applied example performed on a commercial finite element model of a piezoelectric-actuated deformable membrane mirror. Wang et al. (2006) developed a deformable mirror actuated by liquid drops. The drop array is confined within hydrophilic areas, covering an electrode array and supporting a membrane mirror.

1.3 Adaptive Optics

The field of adaptive optics typically considers performance enhancement of optical systems by reducing the effect of changing wavefront distortions. However, developing an adaptive optic system calls for more than what is indicated in the formal definition. It requires the coordination of modeling, control and understanding of wavelength behavior to achieve a system that can truly improve the quality of an image, adapt to different mediums, and correct for optical aberrations.

Figure 1.3 illustrates the power of adaptive optics through a collection of images of Io, one of Jupiter's moons[2]. Surface details captured with Keck adaptive optics in the K-band, Fig. 1.3a, show a comparable level of detail to visible light picture taken with the NASA Galileo orbiter, Fig. 1.3b. The L-band image, Fig. 1.3c, is dominated by active volcanic hot spot emissions, located near the center of the disk. An image of Io, Fig. 1.3d, shows what the Keck telescope would see without adaptive optics; note that no hot spots are detected in this image.

Grosso and Yellin (1977) described a membrane mirror assembly which can be deflected by an electrostatic actuator that consists of conducting pads. The procedure for fabricating such membrane mirrors is explained. The parametric equations governing the vibration of the membrane mirror are developed as well. Takami and Iye (1994)

[2]Copyright statement: “Permission is granted to use these images for personal, educational, or nonprofit/non-commercial purposes only. Any other use of these images is prohibited.", provided at http://cfao.ucolick.org/pgallery/, accessed on September 19, 2008.

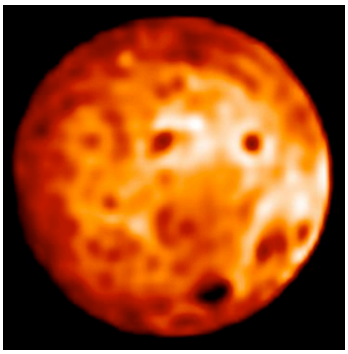

(a) Image taken with Keck adaptive optics, K-band, 2.2 micron.

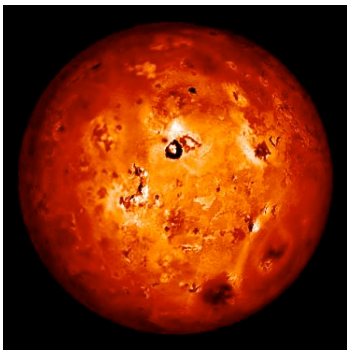

(b) Image based on visible light taken with Galileo spacecraft orbiter.

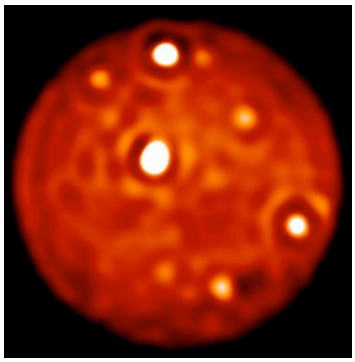

(c) Image taken with Keck adaptive optics, L-band, 3.5 micron.

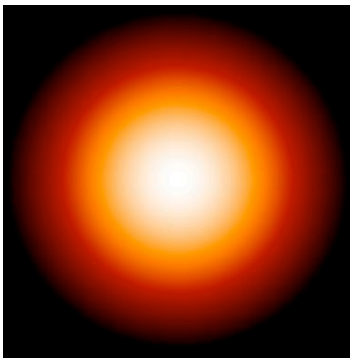

(d) Image without Keck adaptive optics.

Figure 1.3: Images of Io with different imaging techniques.
Images courtesy of Center for Adaptive Optics.

presented the prototype of a membrane deformable mirror for the Cassegrian adaptive optic of SUBARU (Japanese 8 m telescope at Mauna Kea). Electrostatic force was used to produce the deformation of the mirror. Marker and Jenkins (1997) proposed achieving shape modification through enforcing boundary displacements, thereby achieving a desired parabolic profile. They performed shape control of an inflated thin circular disk by using nonlinear finite element analysis. Iroshnikov et al. (1999) investigated the influence of the input field spatial stationary modulation on the pattern formation in a nonlinear optical system. They showed that variation of the input field modulation amplitude changes the spatial dynamics of the system. Marker et al. (1999) examined 75 μm and 125 μm-thick polyimide films under various strain conditions to show how

strain and the optimal optical surface are related. Perreault et al. (1999) presented the design and manufacturing of a micromachined deformable mirror for optical wavefront correction. The mirror employed a flexible Silicon membrane supported by mechanical attachments to an array of electrostatic parallel plate actuators. This mirror showed significant reduction in quasi-static wavefront phase error. Polejaev et al. (1999) presented experimental results of dynamic image aberration correction based on gradient descent algorithm. The setup consisted of a deformable mirror augmented with 37 piezoelectric actuators to distort an input laser beam and a 37 element micromachined deformable membrane mirror to correct the resulting wavefront distortion. Vorontsov (1999) analyzed an opto-electronic feedback system consisting of electrically addressed high-resolution phase spatial light modulators and large-scale arrays of opto-electronic feedback circuits.

Paterson et al. (2000) numerically modeled a membrane mirror. The model was used to optimize the parameters of an adaptive optic system that uses 37 actuators and operates at frame rates up to 800 Hz using a single processor. The system was also tested for Kolmogorov turbulence rejection using a wavefront generator. Gorinevsky and Hyde (2002) discussed how control of a membrane reflector shape can be achieved using embedded actuators distributed over the membrane surface. Perreault et al. (2002) developed a micromachined deformable mirror, that employs a flexible Silicon membrane supported by mechanical attachments to an array of electrostatic actuators. Cheung et al. (2003) used feedback interferometers for aberration correction. The operation of a feedback interferometer which uses a membrane mirror as the phase modulator is demonstrated. deBlonk (2003) presented a framework for quantifying the effects of modeling assumptions upon the optical-level behavior of membrane mirrors. He ordered the models developed in the literature according to the number of model assumptions used. Dimakov et al. (2003) investigated ways to develop lightweight mirrors with imperfect optical quality yet suitable for being used in telescopes with primary mirror's aberration correction. The performance of a deformable membrane mirror with 37 electrodes was studied by Fernández and Artal (2003). The purpose of the study was to characterize the mirror's efficacy as an adaptive optics device. A control procedure was

devised, based on knowledge of the membrane's response under the action of each isolated electrode. Papa et al. (2003a) documented the idea of using hundreds/thousands of projected dots of lights as targets for photogrammety and videogrammetry of space structures. Photogrammetry calculates the three-dimensional coordinates of each target on the structure, and videogrammetry tracks the coordinates versus time. Sobers et al. (2003) explored the feasibility of using embedded piezoelectric materials to control polymer optical surfaces. They constructed membrane-based mirrors to develop and validate their control techniques. They also showed that surface control on the order of tens of wavelength is possible using such systems.

Gavrin et al. (2004) initiated the development of castable electroactive materials that are independent of aqueous systems. Non-aqueous materials allow an increase in voltage limits and the can be used in environments where water would evaporate at high rates. Meyer et al. (2004) designed an experiment to quantify the effects of gravity and boundary support conditions on a scale model of an orbiting, singly-curved parabolic, thin-film reflector to be deployed in space. A fabric-backed Mylar was tested, and it was found that for the same boundary conditions, surface rippling under zero-g conditions was less pronounced than at one-g conditions. Pollard et al. (2004) investigated the nonlinear dynamic behavior of membrane mirrors to visible-optical quality under realistic support and loading scenarios. Celina et al. (2005) considered various piezoelectric polymers based on PVDF for large aperture space-based telescopes. They investigated the degradation of PVDF and its copolymers under various stress environments detrimental to reliable operation in space. Ficocelli and Ben Amara (2005) presented a solution to control system design issues for adaptive optic systems to be used in retinal imaging. The control problem for an adaptive optic system was generalized to that of shape control for a flexible membrane. Marker et al. (2005) presented the development of an adaptive optic with a large correction range. This device is expected to overcome some of the issues facing conventional deformable mirrors, as well as the newly proposed MEMS-based deformable mirrors and liquid crystal based adaptive optics. Li et al. (2006) introduced the construction process and characteristics of a deformable mirror eigenmode. The eigenmode of a 37-element micromachined membrane de-

formable mirror is analyzed as well. Ruggiero and Inman (2006a) utilized a small air gap on the backside of a membrane mirror to demonstrate passive vibration attenuation. The experiments showed a 30 dB reduction in vibration levels with the presence of a 1 mm air cavity.

1.4 Membrane Wrinkle Prediction

Besides being lightweight, the foldability of membranes makes them more attractive for space applications. A membrane can be folded prior to launching, then unfolded and installed (or inflated) in space. This offers a tremendous reduction in storage space. However, as membranes are prominently made of polymers, folding creates wrinkles especially in the neighborhood of the creases. The phenomenon of wrinkling, and the posterior nonlinearities associated with unfolding a membrane received much attention from the scientific community.

Accorsi et al. (1999) studied how to include structural damping and wrinkling into finite element models for parachute dynamics. The opening of a parachute is an unstable processes by nature, and hence including structural damping and wrinkling in the numerical models improves their stability. Murphey and Mikulas (1999) focused on achieving a fundamental understanding of polymer material load-deformation behavior. Most polymers are linear and obey Hooke's law, but after folding and unfolding polymer membranes, permanent wrinkles are created in the local vicinity of creases. Hence, Murphey and Mikulas (1999) investigated the nonlinear effects of these wrinkles on the in-plane stiffness of thin membranes. Tests were conducted, and it was concluded that extensional and shear moduli were found to be reduced and negative Poisson's ratio were observed. Adler and Mikulas (2001) described and demonstrated an approach coined as Iterative Membrane Properties method which was developed earlier (Adler, 2000). This method determines when and how wrinkles affect the stiffness and dynamic behavior of quadrilateral membrane shapes. The method is also capable of aiding the design of inflatable membrane structures by predicting the inflated shape and identifying the wrinkled and unwrinkled portions of the structures.

Reynolds et al. (2001) investigated the dynamic amplitude of wrinkles in thin, tensioned polymer membranes. It was shown that these wrinkles decay in a nonlinear fashion from the time that the in-plane, tensile loads were applied. Murphey (2001) presented a continuum constitutive model for the elastic effects of material wrinkles in thin polymer membranes. The model considered the two-dimensional stress and strain states but neglects the out-of-lane bending. The continuum model is derived after a traditional mechanics analysis of an idealized physical model of random material wrinkles. The model is compared with bi-axial tensile test data for wrinkled Kapton membranes. Blandino et al. (2001) presented results from an experimental study performed to characterize the wrinkling behavior of a thin-film membrane under mechanical and thermal loading. The test article was a square membrane subject to corner loads, and an 80 nm $\times$ 80 nm square section of a corner was investigated. The isothermal loads ranged from 2.45 N to 9.81 N and the mechanical load was 4.9 N. Yang et al. (2001) presented a Bar-Networking Approach for wrinkling analysis of space membrane structures. The membrane was modeled as a network of bars with a special nonlinear constitutive relation characterizing wrinkling behaviors.

Ding et al. (2002) proposed a two-variable-parameter to model membranes. This model describes the basic three states: taut, wrinkle and slack of wrinkled membrane in a systematic format. The two-variable-parameter does not relay on stress iterations, and thus avoids the convergent and pivoting problem in traditional numerical analysis. This way, the original membrane wrinkling problem is converted to a nonlinear complimentary problem and a parametric finite element discretization was developed for wrinkled membranes. Wong and Pelligrino (2002) focused on the amplitude and wavelength of membrane wrinkles which is important for high accuracy applications. A nonlinear finite element simulation technique to predict the wrinkle details. A rectangular membrane was simulated, and it was found that the wrinkled patterns varied abruptly when the load magnitude is changed gradually. Blandino et al. (2002) presented numerical and experimental data for a 0.5 m square, tensioned membrane. The membrane was subject to symmetric and asymmetric mechanical loads. The wrinkle predicted through the numerical model were predicted with the experimental data.

Johnston (2002) considered a structure consisting of multiple layers of pre-tensioned, thin-film membranes supported by deployable booms. A FEA of a sub-scale sun-shield subjected to ground testing was presented. The analysis utilized a nonlinear material model to account for the wrinkling of membranes. Results were presented from a nonlinear static pre-loading analysis to illustrate baseline sun-shield structural characteristics. Tessler et al. (2003) employed a geometrically nonlinear, updated Lagrangian shell formulation using ABAQUS® finite element code to simulate the formation of wrinkled deformation in thin-film membranes. Two modeling strategies were introduced to facilitate convergent solutions of wrinkled equilibrium states. Kukathasan and Pelligrino (2003) investigated the vibration behavior of lightweight membrane structures. A finite element simulation of a square membrane is set up, which uses thin-shell elements. The static wrinkling process is included in the model which was used to obtain the natural modes and frequencies. Leifer et al. (2003) proposed using shear compliant borders along the two opposite edges of rectangular membranes as a means to maintain a membrane wrinkle free. They presented a finite element model to predict the effectiveness of various shear compliant support geometries, and the numerical results were compared with experimental data. Su et al. (2003) developed a buckling solution and a nonlinear post buckling solution for wrinkling analysis of a tensioned Kapton square membrane. Wong and Pelligrino (2003) investigated an idealized solar sail consisting of a uniform, elastic, isotropic square membrane that is pre-stressed by two pairs of equal and opposite forces applied at the corners and the effort was to identify the resulting wrinkling regimes. Sutjahjo et al. (2004) used a nonlinear dynamic finite element solver to analyze wrinkles in a tensioned Kapton square membrane. The solver accounted for large deformation and finite strain. Recently, Wang et al. (2007) used SMA actuators near the boundary to apply tension loads and remove the effects of wrinkles. They used a GA to search for the optimal tension combination on a high dimensional nonlinear surface. An adaptive GA was also utilized to expedite the convergence of the search process.

1.5 Space Control Theory

After a basic understanding of the dynamics of a structure, the performance demands often lead mechanical engineers to the control problem. In this section, a survey of efforts to control space structures is presented. This section serves as a prelude for Section 1.6, where the treatment of shape control will be surveyed in more detail.

Balas (1982) presented a mathematical framework for the discussion of LSS control theory. He also presented a thorough review of LSS control strategies and related topics and tried to emphasize areas of control science which seem destined to play a role in understanding and solving LSS control problems. Salama and Jenkins (2001) discussed control issues relating to gossamer structures. Modeling techniques, actuators, sensors and their interaction with the structure were also treated. Active and passive control strategies were surveyed as well. Baruh (2001) applied multi-variable modal control techniques to control the elastic motion of lightweight multi-body structures. Segmented piezoelectric film actuators were used to control the elastic motion. It was shown that the use of piezoelectric film actuators avoids exciting any rigid body motion, which opens the way for applying decentralized control laws. This immediately translates into controllers that are simple to design and implement. Sung (2002) designed an estimator-based sliding mode controller for a linear stochastic system with a known disturbance to be utilized for the reduction of residual vibration of a flexible spacecraft. The spacecraft is expected to undergo natural deflection during operation. The tracking problem is converted into a regulation problem, and a large slewing maneuver strategy is devised with a tracking mode for nominal trajectory.

Hoagg et al. (2003) treated the control of flexible membranes. In particular, their work treated adaptive disturbance rejection of external disturbances with unknown spectral content. Acoustic excitation and optical sensing were used in the experimental configuration. Scott et al. (2003) looked at the vibration control of a two-dimensional smart structure. Two pairs of piezoelectric bimorphs were used as actuators allowing a controllable ratio of bending and torsion motion. The control law followed a multivariable generalized minimum variance control system. Carreras and Marker (2004) utilized an

inner control ring to control the vibration of a circular membrane. A computer model was presented to serve as a prelude for the design of the inner control ring. The purpose was to develop an autonomous optical figure acquisition and control model for membrane mirror design. Bhoir and Singh (2005) designed a nonlinear controller for the flutter of aeroelastic systems with unsteady aerodynamics. The control law was based on the state-dependent Riccati equation method (Mracek and Cloutier, 1998). An observer was constructed to estimate the unavailable state variables, and the zero state is shown to be locally asymptotically stable.

Ozlu et al. (2006) used arrays of electromagnetically driven micro-membrane actuators to design a smart rigid body motion generator. A large number of micro-sized membrane actuators are used to simultaneously generate the displacement of a large rigid optical mirror; an attempt to bridge the gap between the micro and macro worlds. Korde et al. (2006) used a small number of electrostatic actuators located very closely to two opposite boundaries of a rectangular membrane. A Green's function was used to model the solution and the role of tension within the membrane was examined analytically and experimentally. Sakamoto and Park (2006) observed the degradation of membrane mirror reflectors caused by the attitude-control torque in spacecraft. They proposed an active boundary-control strategy to improve the membrane surface accuracy. The control strategy combined two control techniques: a substructure-based localized controller for the cable network around the membrane, and a reduced-order-model controller to counteract the very-low-frequency-vibrations of the membrane.

1.6 Shape Control

Shape control arises in many applications were it is desired to deform a structure to a certain configuration, and hence the name *s*hape control. In the area of membrane mirrors, maintaining a certain desirable shape might help in removing some optical aberrations. The problem of shape control attracted many researchers. Some of the works published in this area are surveyed in the following.

Varadarajan et al. (1998) discussed the shape control problem of a laminated composite plate integrated with piezoelectric actuators. The efficacy of piezoelectric actuators is assessed in the presence of quasi-statically varying unknown loads. The control effort was devised into finding the initial voltage input that minimized the mean-squared error between the desired and achieved shape, and then adaptively minimize the shape distortion induced by the unknown loads. Kalanovic et al. (1999) presented a spatial discretized a doubly-curved membrane into an array of spring-mass-damper systems. A recursive algorithm is developed and used to simulate the prediction of the surface profile of the membrane. Each spring-mass-damper system is connected to a feedback error learning controller to estimate the system's state, and hence control the membrane structure. Main et al. (1999) reported on the progress in developing large-scale deployable optics with integrated shape control. A control paradigm was introduced for the adaptive structure, where electron beam excitation would be used to control the shape of the membrane mirror, and hence correct for image aberrations.

Forster and Livne (2000) described the synthesis of strain actuated devices. A host structure and an actuator are simultaneously designed. The combined structure is modeled as bending/extension frame elements using the FEM. Maji and Starnes (2000) assessed the out-of-plane displacements of a membrane structure using the Shadow Moiré method. The experimentally measured shape of the structure confirmed the extent of deviation from the ideal optical surface and active control of the shape of the membrane was tested using PVDF actuators.

Yang and Ngoi (2000) addressed the shape control of beams by piezoelectric actuators analytically. Different boundary conditions were considered and several case studies were presented to show how analytical solutions can achieve shape control of the structure. Gorinevsky et al. (2001) proposed using large distributed actuator arrays to efficiently control the shape of gossamer structures. This can be achieved by using an algorithm that uses local errors and actuation for collocated and neighboring positions in each of the distributed actuators. Miyazaki-Kawasaki and Furuya (2001) suggesting augmented membrane mirrors with piezoelectric bimorphs near the creases. The control problem of a one-dimensional membrane model is studied. The effect of the size

of the piezoelectric bimorph is also studied, and the controllability of distribution with piezoelectric films is obtained. Chee et al. (2002) used the slope of deflection as the fine-tuning criterion on top of the common-based displacement shape control. The control algorithm is based on an iterative approach that provides a means of targeting the desired shape of a structure with higher-order criterion such as slope.

Hu and Vukovich (2003) developed a robust control algorithm for shape control of flexible space structures. The system relies on piezoceramic actuators and strain sensors. The designed controller is tested against disturbance rejection and parameter perturbation numerically and experimentally. Nader et al. (2003) considered the vibration of plates augmented with piezoelectric actuators. A spatial shape function of the piezoelastic actuators is sought such that flexural vibration induced by external forces can be completely nullified. An analytic solution is obtained for a Kirchhoff, clamped, circular plate with spatial constant force loading. Sun and Tong (2003) investigated the constrained shape control of structures using piezoelectric actuators. The focus of their work was to optimize the voltage distribution.

Andoh et al. (2004) considered the shape control problem. They first optimized the actuator locations and expanded the reference shape input as a set of eigenfunctions. Ash et al. (2004) discussed how shape control can be achieved by manipulating the intrinsic stresses in the coating of a membrane mirror. FEA was used to demonstrate results, and the author predict zero deformation in the 1-g environment. Peng et al. (2004) investigated applying a GA and neural networks to actively control the wrinkles of inflatable membranes. The membrane under study is rectangular (500 mm$\times$500 mm) pulled by two pairs of forces applied at the four corners along the diagonals. The GA is used to find the optimal force that minimizes the membrane's deflection, and the neural network model is used to map the boundary stretching tensions and space environment to membrane flatness.

Ruggiero et al. (2004c) used the FEM to model a thin cantilevered Euler-Bernoulli beam augmented with a piezoceramic bimorph. Then, they considered the shape control problem. The desired shape was the first mode shape of the beam. Then, an LQR controller was designed to achieve the desired static shape. Sun and Tong (2005) con-

sidered the shape control problem of a local part of a structure rather than the entire structure. They also considered optimizing the energy used to perform shape control. Hence, this control problem has two constraints: the shape control task is constrained spatially, and the energy has to be minimized. Peng et al. (2005) presented a control strategy based on the idea of adjusting the SMA wire temperature as fast as possible. This strategy does not require a hysteresis model or thermal model. The proposed control strategy is used for active shape control of inflatable space structures.

Shepherd et al. (2006b) presented the construction and testing of a five inches deformable mirror actuated in-plane using PZT elements. They compared the experimental data with the finite element model obtained using a commercial software. A control algorithm was implemented based on the finite element model to achieve quasi-static shaping of the mirror surface. Peng et al. (2006) continued the work they published previously (Peng et al., 2004), by implementing their strategy experimentally. They used genetic algorithm to search for the optimal tension which minimizes membrane mirror wrinkles. The algorithm was tested on a 200×300mm rectangular Kapton membrane.

1.7 Dissertation Objective

To this end, the objective of this dissertation is to model a circular membrane mirror augmented with piezoelectric actuators. These actuators can either act in bending or in tension. The ultimate goal is to correct for optical aberrations over the membrane mirror toward the improvement of the imaging quality via changing the shape of the membrane. The idea proposed is simple: augment the membrane mirror with an appropriate number of piezoelectric actuators around its outer rim, Fig. 1.4. The actuators could be in the unimorph or bimorph configurations. Moreover, the bimorph actuator can act either in bending or in tension depending on the polarity of the voltage supplied. This technique is usually referred to as in-plane actuation. Another approach to create a deformable mirror is boundary angulation. The surface of the membrane can be changed appropriately through moving (tilting, plunging, etc...) the boundaries of the circular membrane. In the past, it was shown that this method cannot achieve con-

jugate surfaces for optical control applications (Malin et al., 1983; Nichols et al., 1993). However, Lindler and Flint (2004) recently showed, through numerical simulations and experiments, some promising results using the boundary angulation technique.

In this work, in-plane actuation is the technique of choice. Boundary angulation might be necessary to remove wrinkles commonly experienced in membranes. Moreover, the author believes that eventually, a hybrid technique combining in-plane actuation and boundary angulation is to be used to establish complete control of the optical quality of images reflected by the membrane mirror. Among in-plane actuators available, one can choose between various piezo materials. A discussion of the decision made regarding this issue is included in Subsection 2.2.1. In the following subsection, we lay out the approach to be followed in this dissertation.

1.7.1 Treatment Approach

The problem posed above will be tackled as follows. First, we consider the modeling and control of a membrane strip augmented with bimorph actuators. The membrane strip dissection of the problem, Fig. 1.4, merely enables one to study the one dimensional element of the full scale membrane. First, the dissertation presents a thorough modeling and experimental verification of various configurations of the membrane strip shown in Fig. 1.4. Then, the control problem is treated. Various control strategies are used and simulation results are presented to demonstrate the efficacy of the control laws derived. Finally, we consider the circular membrane augmented with smart actuators.

The analytical approach adopted here is of variational nature. For the membrane strip case, the FEM is used. The development of custom tailored finite element models can reveal interesting features of the structure under study. The augmented actuators change the dynamics of the combined structure, however the FEM can easily handle the introduced non-uniformity and non-homogeneity.

In the case of the circular membrane, a reduced order Galerkin expansion is the approach of choice. The test functions used in this expansion are the mode shapes obtained through an FEA analysis performed using a commercial package. This approach

leads to models that capture the physics of the system with a small number of degrees of freedom. Such results is very favorable, as it facilitates the design of control laws. Moreover, the developed control laws would not be computationally expensive, leading the way to experimental implementation.

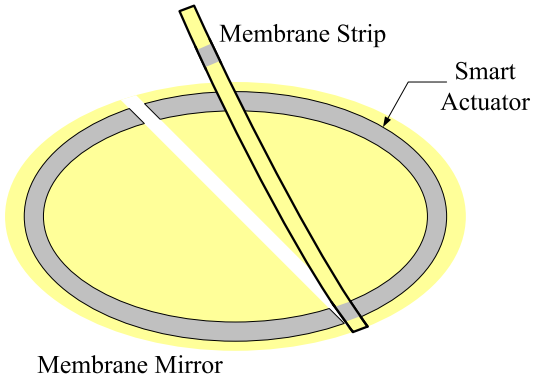

Figure 1.4: Reducing the problem of the membrane mirror.

After obtaining the model using the reduced order Galerkin expansion, we choose to apply augmented adaptive control to the model obtained. We first obtained a linear model for the system, for which we design an LQR controller. The linear system theory is well developed and serves our intermediate goal in designing a controller that "works". This controller is then used as a baseline controller, which we augment to an adaptive controller that acts against uncertainties and possible nonlinearities in the system.

1.8 Dissertation Layout

To this end, this dissertation is organized as follows. Chapter 1 lays out the background of the problem at hand. A literature review was presented along with the dissertation objective and approach. Chapter 2 presents the modeling of three configurations of a membrane strip augmented with bimorph actuators. It also offers experimental validation for all the models developed. The control problem is treated in Chapter 3. Control objectives are defined and proper control laws are derived. The effectiveness of the control laws developed is verified through numerical simulations. The modeling of the circular membrane outfitted with smart actuators is developed in Chapter 4. Finally,

the control of a circular membrane augmented with piezoelectric bimorph actuators is treated in Chapter 5. The major contributions for this work are highlighted in Chapter 6.

CHAPTER 2

MEMBRANE STRIP ACTUATED WITH BIMORPHS – MODELING

In this chapter, a membrane strip actuated using piezoelectric bimorphs is modeled. As laid out in Chapter 1, the modeling of a membrane strip augmented with smart bimorphs will serve as a prelude for the modeling of a circular membrane augmented with smart bimorphs.

The current chapter is arranged as follows. Section 2.1 presents a general model for a membrane strip augmented with two smart bimorphs. The case of a membrane strip augmented with one piezoceramic bimorph is treated in Section 2.2. This exercise will serve as a benchmark for the upcoming developments. The piezoceramic bimorph will be acting in bending only. An experimental validation of the model is presented in Section 2.2 as well. Then, the general case is studied in Section 2.3 and Section 2.4, where a membrane strip is augmented with two MFC bimorphs and two actuation configurations are considered. Section 2.3 presents a model for the membrane strip where both bimorphs act in bending, whereas Section 2.4 presents a model for the membrane strip with one bimorph acting in bending and the other bimorph acts in tension. The models of Section 2.3 and Section 2.4 are both verified experimentally in Section 2.5. Finally, Section 2.6 summarizes this chapter.

The membrane strip will be modeled as a pinned-pinned Euler-Bernoulli beam under tension (Inman, 2007). The structure is modeled as a beam because of the added stiffness of the bimorph actuators. Moreover, the model developed has to account for the mass added by the bimorph actuator(s). On another note, the bimorph(s) are placed

near the boundaries (not at the boundaries). As the membrane strip cannot resist a bending moment at its boundaries, the boundary condition is assumed to be pinned-pinned.

2.1 Modeling

Figure 2.1 shows a schematic of a membrane strip augmented with two bimorph actuators near its boundaries. One of the boundaries cannot translate (left boundary in Fig. 2.1), whereas the position of the right boundary can be adjusted to place the structure under various tensile loads.

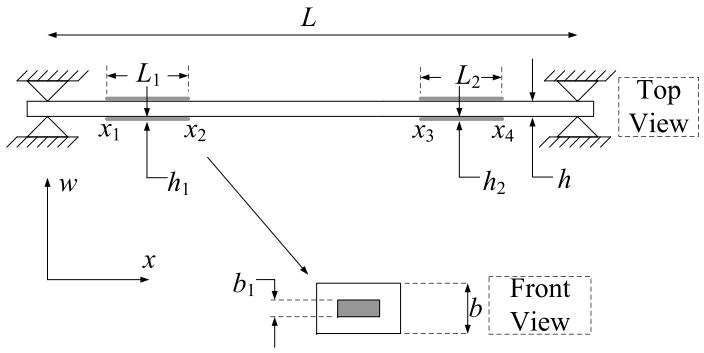

Figure 2.1: Schematic of the membrane strip with two bimorph actuators.

To obtain the governing equation of the transverse vibration of this structure, we start by considering an infinitesimal element of the structure. Figure 2.2 shows the free body diagram of an infinitesimal element of the structure. The infinitesimal element shown in Fig. 2.2 is chosen within the span of the bimorph. The rest of the structure is a special case of this span (i.e. membrane strip only without the bimorph layers).

Banks et al. (1994) used a unit pulse function to present the local changes in linear density and flexural rigidity imposed by the presence of the bimorph patches. Although in Fig. 2.1, it is shown that for every bimorph, the individual patches have the same thickness, the bimorph of Fig. 2.2 is assumed to be asymmetric, i.e., the two smart patches (upper and lower) have different thickness. The purpose of this assumption is to illustrate theoretically the importance of symmetry. Moreover, the use of the same

patches to construct bimorphs is a standard practice, and hence symmetry is the natural, and more practical way of constructing bimorph actuators.

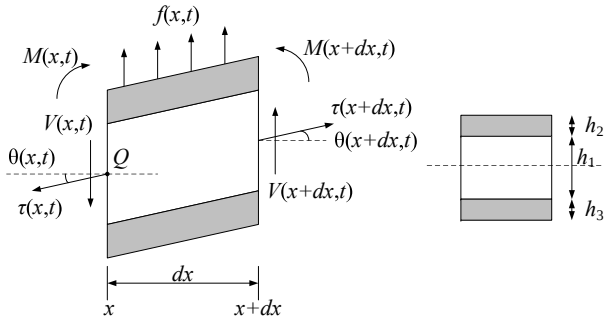

Figure 2.2: Element of strip with two added layers.

Hence, to obtain the governing equation, we start with applying Newton's second law to the infinitesimal element of Fig. 2.2. Now, sum the forces acting on the element along the vertical direction

$$\begin{aligned} V(x+\mathrm{d}x,t)-V(x,t) &+ \tau(x+\mathrm{d}x,t)\sin[\theta(x+\mathrm{d}x,t)] \\ &- \tau(x,t)\sin[\theta(x,t)]+f(x,t)\mathrm{d}x=\rho(x)\mathrm{d}x\frac{\partial^2 w(x,t)}{\partial t^2}\,, \end{aligned} \tag{2.1}$$

where $\rho(x)$ is the linear density, $V(x)$ is the shear force, $\tau(x)$ is the tensile load and $\theta(x,t)$ is the slope of the deflection (assuming small deflection and linear beam theory). The shear force can be expanded about the spatial variable using Taylor Series, and hence the shear terms in Eq. (2.1) simplify as follows

$$V(x+\mathrm{d}x,t)-V(x,t)\approx V(x,t)+\frac{\partial V(x,t)}{\partial x}\mathrm{d}x-V(x,t)=\frac{\partial V(x,t)}{\partial x}\mathrm{d}x\,.$$

Also, assuming small deflections, the slope of deflection can be expanded using Taylor series as well

$$\begin{aligned} \sin[\theta(x,t)] &\approx \theta(x,t)\approx\frac{\partial w(x,t)}{\partial x}\,, \\ \sin[\theta(x+\mathrm{d}x,t)] &\approx \theta(x,t)+\frac{\partial\theta(x,t)}{\partial x}\approx\frac{\partial w(x,t)}{\partial x}+\frac{\partial^2 w(x,t)}{\partial x^2}\mathrm{d}x\,. \end{aligned}$$

Additionally, the tension can be expanded

$$\tau(x+\mathrm{d}x,t)=\tau(x,t)+\frac{\partial\tau(x,t)}{\partial x}\mathrm{d}x\,. \tag{2.2}$$

Hence, the tension terms in Eq. (2.1) will become (retaining only first order terms):

$$\begin{aligned}
&\tau(x+\mathrm{d}x,t)\sin[\theta(x+\mathrm{d}x,t)]-\tau(x,t)\sin[\theta(x,t)]\,,\\
&\approx \tau(x,t)\frac{\partial^2 w(x,t)}{\partial x^2}\mathrm{d}x+\frac{\partial \tau(x,t)}{\partial x}\frac{\partial w(x,t)}{\partial x}\mathrm{d}x\,,\\
&=\frac{\partial}{\partial x}\Big(\tau(x,t)\frac{\partial w(x,t)}{\partial x}\Big)\mathrm{d}x\,.
\end{aligned}$$

Next, add the moments about point Q in Fig. 2.2. Notice that the tension will have no effect on the moment summation, since the line of action of the tension force passes through Q. The membrane and the actuator are slender, and hence the mass moment of inertia will be neglected,

$$\Big[M(x,t)+\frac{\partial M(x,t)}{\partial x}\mathrm{d}x\Big]-M(x,t)+\Big[V(x,t)+\frac{\partial V(x,t)}{\partial x}\mathrm{d}x\Big]\mathrm{d}x+(f(x,t)\mathrm{d}x)\frac{\mathrm{d}x}{2}=0\,,$$

which yields

$$V(x,t)=-\frac{\partial M(x,t)}{\partial x}\,.$$

The tension contributes to the stress in the infinitesimal element, and hence the bending moment will change. The tension will not be the same in the bimorph layers and the membrane. The assumption here is that the bimorph layers are perfectly bonded (infinite shear stiffness assumption) to the membrane, and hence all three layers will undergo the same strain. Hence, from elementary mechanics of materials, the stress in every layer is given by (see Fig. 2.2),

$$\begin{aligned}
\sigma_1 &= \frac{\tau E_1}{A_1E_1+A_2E_2+A_3E_3}\,,\\
\sigma_2 &= \frac{\tau E_2}{A_1E_1+A_2E_2+A_3E_3}\,,\\
\sigma_3 &= \frac{\tau E_3}{A_1E_1+A_2E_2+A_3E_3}\,,
\end{aligned}$$

where $A_i=b_ih_i$ is the area for $i=1,2,3$. Now perform the integration along the vertical axis to determine the added bending moment resulting from the tension

$$M_{Added}(x,t)=b_1\int_{-h_3-h_2/2}^{-h_2/2}\sigma_1 z\,dz+b_2\int_{-h_2/2}^{h_2/2}\sigma_2 z\,dz+b_3\int_{h_2/2}^{h_1+h_2/2}\sigma_3 z\mathrm{d}z\,.$$

The second term in the above equation vanishes since it is the integral of an odd function ($f(-z)=-f(z)$) over an interval symmetric about the origin. Hence, if there were

no layers attached to the beam, the tension will not affect the bending moment. Carrying out the first and third integrations in the equation above leads to the following result

$$M_{Added}(x,t)=\frac{1}{2}b_3\sigma_3\Big(\frac{h_2^2}{4}-(h_3+\frac{h_2}{2})^2\Big)+\frac{1}{2}b_3\sigma_3\Big((h_3+\frac{h_2}{2})^2-\frac{h_2^2}{4}\Big)\,,$$

Since the two layers of a bimorph are identical, the added bending moment, M_{Added}, vanishes as well and hence the tension would not effect the bending moment in the structure. An interesting case where the tension would effect the bending moment is when using a unimorph for the purpose of sensing for example. In the case of a unimorph, the geometric symmetry would not exist, and there would be a constant bending moment present in the structure at the location of the added layer. In such a case, the bending and tension will be coupled, resulting in the coupling of the transverse and longitudinal motions.

Consequently, the only contribution of the tensile load is to add a traveling wave effect to the dynamics of the structure. Substituting all the findings in Eq. (2.1) (and adding proportional air damping), one obtains the governing equation of transverse vibrations of the system shown in Fig. 2.1,

$$\rho(x)\frac{\partial^2 w(x,t)}{\partial t^2}+\frac{\partial^2 M_x(x,t)}{\partial x^2}-\frac{\partial}{\partial x}\Big(\tau(x,t)\frac{\partial w(x,t)}{\partial x}\Big)+\gamma\frac{\partial w(x,t)}{\partial t}=f(x,t)\,. \qquad (2.3)$$

The added bimorphs will increase the flexural stiffness of the structure, albeit locally, justifying the beam assumption. Being under tension adds a traveling wave term usually appearing in the governing equation of a string (Ruggiero, 2005). Assuming perfect bonding (infinite shear stiffness) between the bimorph and the membrane, the bimorphs and the membrane will undergo the same strain. Consequently, Eq. (2.3) is justified as long as the structure undergoes small transverse deflections.

As the governing equation of the structure is obtained, Eq. (2.3), some treatment of the coefficients in this partial differential equation should be presented. The linear density and flexural rigidity of Eq. (2.3) are discontinuous. As mentioned earlier, Banks et al. (1994) used a unit pulse function to present the local changes in linear density and flexural rigidity imposed by the presence of the bimoprh. This approach will be adopted

here, and hence, to capture the effect of the actuator mass, the linear density of the structure is given by

$$\rho(x) = \rho_m hb + \sum_{k=1}^{2} 2\rho_k h_k b_k \chi_k(x)\,,$$

where $k = 1,2$ reflects the general presence of two bimorphs. As for $\chi_k(x)$, it presents a family of functions characterizing the discontinuity of the physical properties in the structure, defined as

$$\chi_k(x) = \begin{cases} 1 & \text{if} \quad x_{2k-1} \le x \le x_{2k} \\ 0 & \text{otherwise} \end{cases} \qquad \text{where} \quad k = 1,2\,.$$

The internal bending moment is given by

$$M_x(x,t) = EI(x)\frac{\partial^2 w(x,t)}{\partial x^2} + cI(x)\frac{\partial^3 w(x,t)}{\partial t \partial x^2}\,,$$

where $EI(x)$ is the flexural stiffness of the structure. To capture the effect of the bimorph stiffness, the flexural rigidity is given by,

$$EI(x) = \frac{1}{12} bh^3 E + \sum_{k=1}^{2} \frac{2}{3} a_k b_k E_k \chi_k(x)\,.$$

The proper Kelvin-Voigt damping coefficient multiplied by the respective area moment of inertia is

$$cI(x) = \frac{1}{2} bh^3 c_m + \sum_{k=1}^{2} \frac{2}{3} c_k a_k b_k \chi_k(x)\,.$$

The bimorph constant (Banks et al., 1994), a_k, is given by

$$a_k = \left(\frac{1}{2}h + h_k\right)^3 - \left(\frac{1}{2}h_k\right)^3\,.$$

Finding an exact solution for the governing equation, Eq. (2.3), is a formidable task. Approximate methods of analysis provide a convenient, alternative for finding an analytical solution. In the following, we adopt a variational method approach to solve Eq. (2.3).

2.1.1 Weak Formulation

In the subsequent subsections, the subscripts t and x will denote partial differentiation with respect to the temporal and spatial variables, respectively. Let us start this

process by rewriting the governing equation in a more compact form utilizing the subscript notation for the partial derivatives,

$$\rho(x)w_{tt}(x,t)+[EI(x)w_{xx}(x,t)+cI(x)w_{xxt}(x,t)]_{xx}-[\tau(x,t)w_x(x,t)]_x+\gamma w_t(x,t)=f(x,t)\,.$$

The configuration of the structure can be described by two states, the transverse deflection and its velocity. Therefore, instead of using one second order temporal differential equation to describe the system, one can opt for two first order temporal differential equations, and hence Eq. (2.4) becomes

$$\begin{aligned} &w_t(x,t)=v(x,t)\,,\\ &\rho(x)v_t(x,t)=f(x,t)+[\tau(x,t)w_x(x,t)]_x\,,\\ &-[EI(x)w_{xx}(x,t)+cI(x)v_{xx}(x,t)]_{xx}-\gamma v(x,t)\,. \end{aligned} \tag{2.4}$$

Notice that $EI(x)$ and $cI(x)$ have to be differentiated twice, which gives rise to

$$\chi_{kxx}(x)=[H(x-x_{2k})-H(x-x_{2k-1})]_{xx}=[\delta(x-x_{2k})-\delta(x-x_{2k-1})]_x\,, \tag{2.5}$$

where $H(x)$ is the Heaviside function and $\delta(x)$ is the Dirac delta function. The strong form of Eq. (2.4) can lead to computational difficulties for estimation and control applications. Banks et al. (1996b) showed that the retention of the irregular terms of Eq. (2.5) is of great importance when using models with experimental data from actual structures.

To formulate the weak form of Eq. (2.4), multiply each equation with test functions, $\phi(x)$ and $\psi(x)$, respectively,

$$\begin{aligned} &w_t(x,t)\phi(x)=v(x,t)\phi(x)\,,\\ &\rho(x)v_t(x,t)\psi(x)=\Big(f(x,t)+[\tau(x,t)w_x(x,t)]_x\,,\\ &-[EI(x)w_{xx}(x,t)+cI(x)v_{xx}(x,t)]_{xx}-\gamma v(x,t)\Big)\psi(x)\,. \end{aligned}$$

Integrate both equations spatially over the domain of application (the length of the strip),

$$\int_0^L \frac{\partial w(x,t)}{\partial t}\phi(x)\mathrm{d}x=\int_0^L v(x,t)\phi(x)\mathrm{d}x\,,$$

$$\int_0^L \rho(x)\frac{\partial v(x,t)}{\partial t}\psi(x)\mathrm{d}x = \int_0^L \Big(f(x,t)+[\tau(x,t)w_x(x,t)]_x$$
$$-[EI(x)w_{xx}(x,t)+cI(x)v_{xx}(x,t)]_{xx}-\gamma v(x,t)\Big)\psi(x)\mathrm{d}x\,,$$

The differentiation and integration are linear operations and hence can be interchanged, yielding

$$\frac{\partial}{\partial t}\int_0^L w(x,t)\phi(x)\mathrm{d}x = \int_0^L v(x,t)\phi(x)\mathrm{d}x$$
$$\frac{\partial}{\partial t}\int_0^L \rho(x)v(x,t)\psi(x)\mathrm{d}x = \int_0^L \Big(f(x,t)+[\tau(x,t)w_x(x,t)]_x$$
$$-[EI(x)w_{xx}(x,t)+cI(x)v_{xx}(x,t)]_{xx}-\gamma v(x,t)\Big)\psi(x)\mathrm{d}x\,. \tag{2.6}$$

To enforce the boundary conditions of the system, Eq. (2.6) is integrated by parts, were necessary, yielding

$$\frac{\partial}{\partial t}\int_0^L \rho(x)v(x,t)\psi(x)\mathrm{d}x = \int_0^L f(x,t)\psi(x)\mathrm{d}x - \int_0^L \tau(x,t)w_x(x,t)\psi_x(x)\mathrm{d}x$$
$$+[\tau(x,t)w_x(x,t)\psi(x)]_0^L - \int_0^L [EI(x)w_{xx}(x,t)+cI(x)v_{xx}(x,t)]\psi_{xx}(x)\mathrm{d}x$$
$$-\Big[\psi(x)[EI(x)w_{xx}(x,t)+cI(x)v_{xx}(x,t)]_x\Big]_0^L + \Big[\psi_x(x)[EI(x)w_{xx}(x,t)+cI(x)v_{xx}(x,t)]\Big]_0^L$$
$$-\gamma\int_0^L v(x,t)\psi(x)\mathrm{d}x\,. \tag{2.7}$$

Since the membrane strip is pinned-pinned at its boundaries,

$$w(0,t)=w(L,t)=0\,,$$
$$v(0,t)=v(L,t)=0\,,$$
$$EI(0)w_{xx}(0,t)+cI(0)v_{xx}(0,t)=0\,,$$
$$EI(L)w_{xx}(L,t)+cI(L)v_{xx}(L,t)=0\,.$$

These boundary conditions force one of the boundary terms of Eq. (2.7) to vanish. The remaining boundary terms will vanish if the following is enforced,

$$\psi(0)=\psi(L)=0\,.$$

Consequently, the state equations become,

$$\frac{\partial}{\partial t}\int_0^L w(x,t)\phi(x)\mathrm{d}x=\int_0^L v(x,t)\phi(x)\mathrm{d}x\,, \tag{2.8}$$

$$\frac{\partial}{\partial t}\int_0^L \rho(x)v(x,t)\psi(x)\mathrm{d}x=\int_0^L f(x,t)\psi(x)\mathrm{d}x-\int_0^L \tau(x,t)w_x(x,t)\psi_x(x)\mathrm{d}x$$
$$-\int_0^L [EI(x)w_{xx}(x,t)+cI(x)v_{xx}(x,t)]\psi_{xx}(x)\mathrm{d}x-\gamma\int_0^L v(x,t)\psi(x)\mathrm{d}x\,. \tag{2.9}$$

Now approximate the transverse deformation of the structure as the summation of the product of temporal and spatial functions

$$w(x,t)=\sum_{i=1}^{N}\bar{w}_i(t)\phi_i(x)\,, \tag{2.10}$$

$$v(x,t)=\sum_{i=1}^{N}\bar{v}_i(t)\psi_i(x)\,. \tag{2.11}$$

Notice that the test functions, $\phi(x)$ and $\psi(x)$, are dummy functions yet to be determined. Since $\phi(x)$ and $\psi(x)\in H^2(0,L)$ which is the same Hilbert space, we can let $\phi(x)=\psi(x)$. Consequently they can be taken from the same functional space. Substituting the approximation Eq. (2.10) and Eq. (2.11) in Eq. (2.8) and Eq. (2.9) yields

$$\frac{\partial}{\partial t}\sum_{i=1}^{N}\bar{w}_i(t)\int_0^L \phi_i(x)\phi_j(x)\mathrm{d}x=\sum_{i=1}^{N}\bar{v}_i(t)\int_0^L \phi_i(x)\phi_j(x)\mathrm{d}x\,,$$

$$\frac{\partial}{\partial t}\sum_{i=1}^{N}\bar{v}_i(t)\int_0^L \phi_i(x)\phi_j(x)\mathrm{d}x=\int_0^L f(x,t)\psi(x)\mathrm{d}x-\sum_{i=1}^{N}\bar{w}_i(t)\int_0^L \tau(x,t)\phi_i'(x)\phi_j'(x)\mathrm{d}x$$
$$-\sum_{i=1}^{N}\bar{w}_i(t)\int_0^L EI(x)\phi_i''(x)\phi_j''(x)\mathrm{d}x-\sum_{i=1}^{N}\bar{v}_i(t)\int_0^L cI(x)\phi_i''(x)\phi_j''(x)\mathrm{d}x$$

$$-\gamma \sum_{i=1}^{N} \bar{v}_i(t) \int_0^L \phi_i(x)\phi_j(x)\mathrm{d}x \,. \tag{2.12}$$

The structure of Eq. (2.12) depends on the nature of actuation used. To this end, cast Eq. (2.12) in matrix form,

$$\begin{bmatrix} \mathbf{M}_1 & 0_{N\times N} \\ 0_{N\times N} & \mathbf{M}_2 \end{bmatrix} \begin{Bmatrix} \bar{\mathbf{w}} \\ \bar{\mathbf{v}} \end{Bmatrix}_t = \begin{bmatrix} 0_{N\times N} & \mathbf{M}_1 \\ -\mathbf{K}(t) & -\mathbf{C} \end{bmatrix} \begin{Bmatrix} \bar{\mathbf{w}} \\ \bar{\mathbf{v}} \end{Bmatrix} + \mathbf{F}(t)\,. \tag{2.13}$$

The sub-matrices are defined as

$$\begin{aligned}
\mathbf{M}_1 &= \left[\int_0^L \phi_i(x)\phi_j(x)\mathrm{d}x\right]_{i,j=1,\cdots,N}, \\
\mathbf{F}(t) &= \left[\int_0^L f(x,t)\phi_j(x)\mathrm{d}x\right]_{j=1,\cdots,N}, \\
\mathbf{M}_2 &= \left[\int_0^L \rho(x)\phi_i(x)\phi_j(x)\mathrm{d}x\right]_{i,j=1,\cdots,N}, \\
\mathbf{C} &= \left[\int_0^L \left(cI(x)\phi_i''(x)\phi_j''(x)+\gamma\phi_i(x)\phi_j(x)\right)\mathrm{d}x\right]_{i,j=1,\cdots,N}, \\
\mathbf{K}(t) &= \left[\int_0^L \left(EI(x)\phi_i''(x)\phi_j''(x)+\tau(x,t)\phi_i'(x)\phi_j'(x)\right)\mathrm{d}x\right]_{i,j=1,\cdots,N}.
\end{aligned} \tag{2.14}$$

Notice that the stiffness matrix $\mathbf{K}(t)$ can be time dependent as the tension might be time varying. This idea will be explored more in the following subsections.

As the system is presented in its weak form now, one has to make a choice regarding the nature of the test functions ϕ_i. This choice will have an influence over the nature of the matrices of Eq. (2.14) and over the approximations of Eq. (2.10) and Eq. (2.11). The upcoming subsection will treat this point, as the finite element method will be adopted.

2.1.2 Finite Element Formulation

A brief discussion regarding the finite element method is in order. The FEM is known for its computational efficiency. This is due to the symmetrical, banded nature of the developed system matrices $\mathbf{M}_1$, $\mathbf{M}_2$, $\mathbf{K}$, and $\mathbf{C}$ of Eq. (2.13). Additionally, the FEM is an approximate approach for developing a control law for distributed systems (Strang and Fix, 1973). When used, the FEM yields a finite-dimensional representation of a system with an infinite number of degrees of freedom. Although many commercial packages are available, careful design of a tailored finite element solver can reveal information about the system, such as where sensors should be placed on the structure. In this spirit, a custom finite element code is devised for this work.

For this research, the test functions used are cubic B-splines. Cubic B-splines are a set of linearly independent functions that form a basis for the finite element approximation. The following presents a cubic B-spline extending over five elements (Prenter, 1975),

$$L_i^{-3}g(x)=\begin{cases}(x-x_{i-2})^3 & \text{if} \quad x_{i-2}\le x\le x_{i-1}\\ L_i^3+3L_i^2(x-x_{i-1})+3L_i(x-x_{i-1})^2-3(x-x_{i-1})^3 & \text{if} \quad x_{i-1}\le x\le x_i\\ L_i^3+3L_i^2(x_{i+1}-x)+3L_i(x_{i+1}-x)^2-3(x_{i+1}-x)^3 & \text{if} \quad x_i\le x\le x_{i+1}\\ (x_{i+2}-x)^3 & \text{if} \quad x_{i+1}\le x\le x_{i+2}\\ 0 & \text{otherwise}\end{cases},$$

where x_i and x_{i+1} are the nodes of the $i-$th element of length L_i. Cubic B-splines exhibit high connectivity among the discretized structure as every B-spline extends over the range of five elements. Figure 2.3 displays a set of cubic B-splines for a structure discretized into five elements. deBoor et al. (1992) discussed cubic B-splines extensively. Hollig (2001) also presented several types of B-splines basis for approximation and boundary value problems and discussed the implementation of spline-based finite element schemes.

For all the structures considered henceforth, Cubic B-splines with pinned-pinned boundary conditions will be used as test functions to span the space of the FEM approx-

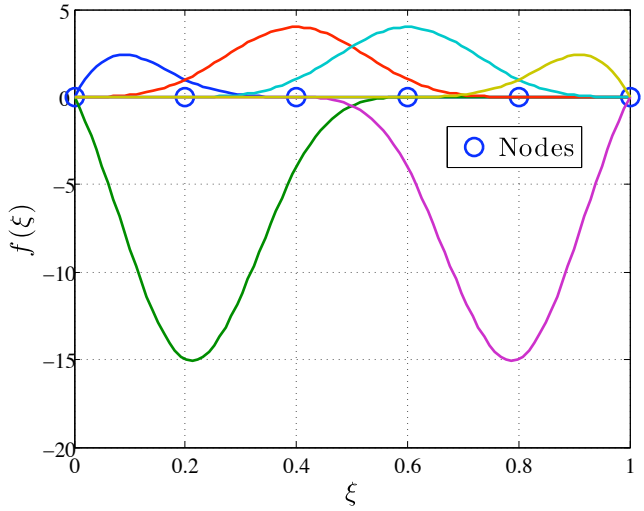

Figure 2.3: Cubic B-splines extending over five elements with pinned-pinned boundary conditions.

imation.

2.2 Membrane Strip Actuated using Single Piezoelectric Bimorph

To verify the model developed in Section 2.1, a membrane strip with a piezoelectric bimorph attached near its end is considered. The bimorph will cause a change in the linear density and flexural stiffness of the structure as mentioned earlier. Including these local changes of the physical characteristics will improve the mathematical model of the structure. Figure 2.4 shows a schematic of the structure at hand.

According to the developments of Section 2.1, the forcing vector, $\mathbf{F}(t)$ in Eq. (2.14) is developed as follows. Following the developments of Banks et al. (1996a), the moment induced by the piezoelectric bimorph is

$$(M_x)_p = -2\kappa_1^B V_1(t)\chi_1(x)\,,$$

where $V_1(t)$ is the voltage applied into both patches, and κ_1^B is the piezoelectric bimorph bending constant, (Banks et al., 1996a), given as,

$$\kappa_1^B = -\frac{1}{2}E_1 b_1(h+h_1)d_{31}^1 \quad \textit{the superscript of } d_{31} \textit{ is to indicate the bimorph number.}\,.$$

In the above, d_{31}^1 is the piezoceramic strain constant. Although the structure of Fig. 2.4 has only one bimorph, the indices (and superscripts) are kept in the above equation to remain consistent with the notation of Section 2.1. However, the forcing function in Eq. (2.3) is a transverse force, and the bimorph is inducing a moment, hence

$$f(x,t) = -\frac{\partial^2 (M_x)_p}{\partial x^2} = 2\kappa_1^B V_1(t)\chi_1''(x)\,.$$

Performing operations similar of those carried out in Subsection 2.1.1, one obtains

$$\mathbf{F}(t) = \begin{bmatrix} 0_{N\times 1} \\ \mathbf{B}_1 \end{bmatrix} V_1(t)\,,$$

where

$$\mathbf{B}_1 = \left[2\kappa_1^B \int_0^L \chi_1(x)\varphi_j''\mathrm{d}x \right]_{j=1,\cdots,N}\,.$$

Now, Eq. (2.13) can be written in the following form,

$$\begin{Bmatrix} \bar{\mathbf{w}} \\ \bar{\mathbf{v}} \end{Bmatrix}_t = \begin{bmatrix} 0_{N\times N} & \mathbf{I}_{N\times N} \\ -\mathbf{M}_2^{-1}K & -\mathbf{M}_2^{-1}\mathbf{C} \end{bmatrix} \begin{Bmatrix} \bar{\mathbf{w}} \\ \bar{\mathbf{v}} \end{Bmatrix} + \begin{bmatrix} 0_{N\times 1} \\ \mathbf{M}_2^{-1}\mathbf{B}_1 \end{bmatrix} V_1(t)\,. \tag{2.15}$$

The system presented in Eq. (2.15) is linear. It can be presented in the standard state space formulation as,

$$\dot{\mathbf{x}}(t) = \mathbf{A}\mathbf{x}(t) + \mathbf{B}V_1(t)\,. \tag{2.16}$$

where $\mathbf{A}$ is the system matrix, $\mathbf{B}$ is the control input matrix given by

$$\begin{aligned} \mathbf{A} &= \begin{bmatrix} 0_{N\times N} & \mathbf{I}_{N\times N} \\ \mathbf{M}_2^{-1}\mathbf{A}_1 & \mathbf{M}_2^{-1}\mathbf{A}_2 \end{bmatrix}, \\ \mathbf{B} &= \begin{bmatrix} 0_{N\times 1} \\ \mathbf{M}_2^{-1}\mathbf{B}_1 \end{bmatrix}, \end{aligned} \tag{2.17}$$

and $\mathbf{x}(t) = \{\ \bar{\mathbf{w}}(t)\quad \bar{\mathbf{v}}(t)\ \}^T$ is the state vector.

2.2.1 Actuator Comparison

Before delving into the case study presented, a comparison among various actuators is conducted briefly. Figure 2.5, Fig. 2.6 and Fig. 2.7 present the frequency response of

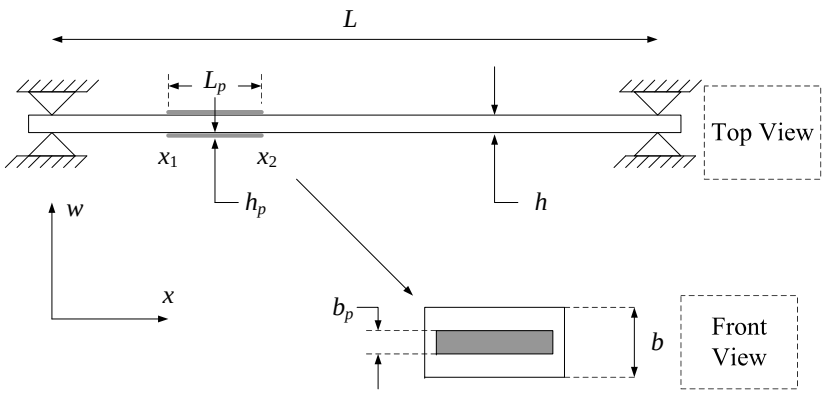

Figure 2.4: Schematic of the membrane strip with piezoelectric bimorph.

the membrane strip to be studied in Subsection 2.2.2 augmented with various actuators. It is obvious that the PVDF has low actuation authority. However, the actuation authority of MFC is comparable to that of the piezoceramic despite the fact that MFC is lighter than monolithic piezoceramics and has a lower modulus of elasticity. This will be demonstrated in Section 2.3 and Section 2.4 later.

2.2.2 Case Study and Experimental Results

To validate the proposed model, a membrane strip made of Kapton is considered. Kapton is a polyimide that has been a commonly used membrane material for recent space applications (Jenkins, 2001, 2006). The piezoelectric bimorph is made of PSI-5H4E wafers manufactured by Piezo Systems, Inc®. The wafers are glued at one end of the strip, specifically at $x_1 = 2.5$ cm, Fig. 2.4. Copper tape is used as a conductive layer on the glued side of the piezoceramic wafer to attach one lead wire. The second lead wire is attached to the opposite side of the piezoceramic wafer using SuperSafe® Superior # 30 Soft Solder Flux Liquid. The electromechanical coupling coefficient of the piezocerarmic wafer used is $d_{31} = -420$ pm/V. Table 2.1 shows the relevant physical properties of the test article. Table 2.1 shows that the mass the membrane strip is 0.3 g and its flexural stiffness is 7.56×10^{-6}Nm^2. On the other hand, the mass of the piezoceramic bimorph is 2.4 g and its flexural stiffness is 0.013 Nm^2. The piezoelectric bimorph is 8 times heavier than the membrane strip, and its flexural stiffness is about 1700 times

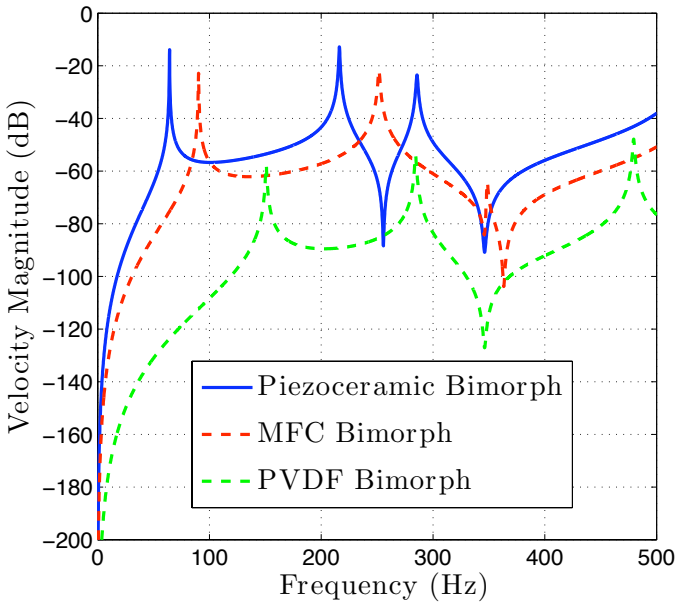

Figure 2.5: Frequency Response with $\tau = 7.5$N

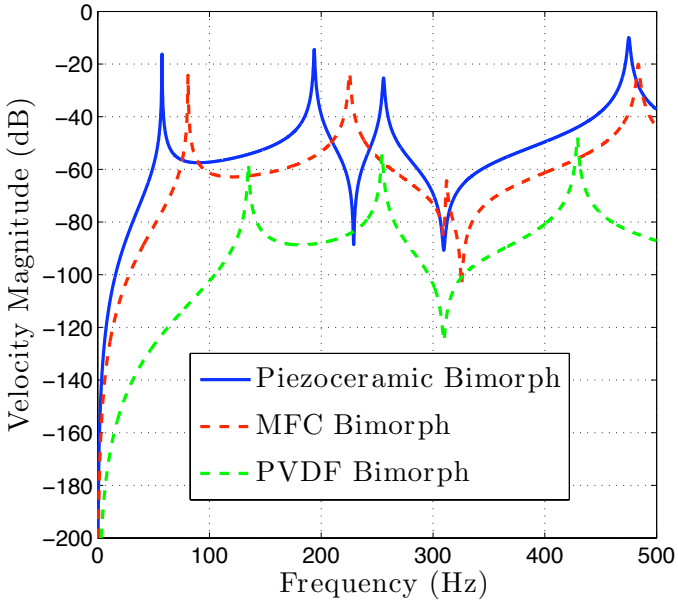

Figure 2.6: Frequency Response with $\tau = 10$N

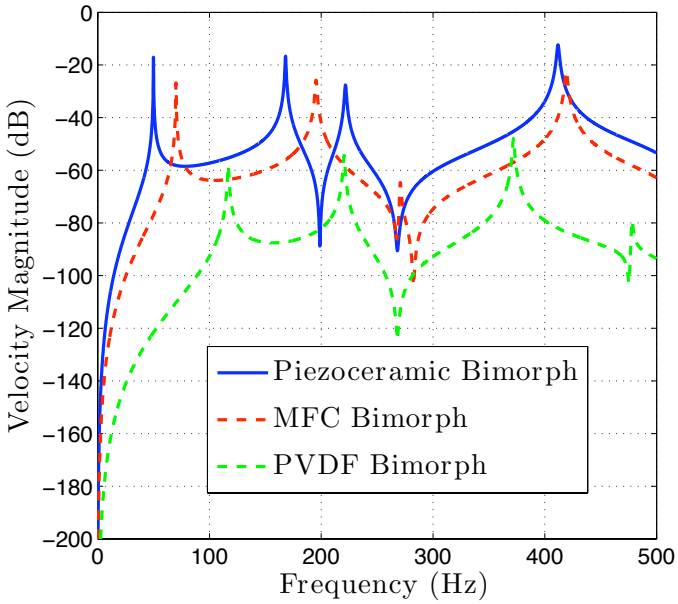

Figure 2.7: Frequency Response with $\tau = 12.5$N

higher than that of the membrane strip. It is expected that this added mass and flexural stiffness will significantly change the behavior of the membrane strip.

Table 2.1: Properties of Kapton strip and piezoceramic patch.

Physical Property	**Kapton Strip**	**Piezoceramic Wafer**
Density [kg/m^3]	1420	7800
Young's Modulus [GPa]	3	62.5
Air Damping Coefficient	0.06	0.06
Kelvin-Voigt Coefficient	5.2495×10^5	2.5536×10^3
Width [cm]	1.9	1.9
Thickness [mm]	51×10^{-3}	0.225
Length [cm]	21.4	3.6

A schematic of the experimental setup built is shown in Fig. 2.8. The Kapton strip is held between two grippers. Each gripper consists of two aluminum rods pushed through two opposite grooves. At each gripper, the rods serve as contact points and hence form the pinned-pinned boundary conditions sought. The left gripper is held fixed, whereas the right gripper's position is adjustable through a lead screw, thus allowing it to travel in the *x-direction*. This produces uniform tensile load in the structure. A MLP-75 load cell, manufactured by Transducer Techniques® is used to measure the tension in the strip.

A TMO-2 signal conditioning module, also manufactured by Transducer Techniques®, is connected to the load cell. A digital voltmeter can be connected to the signal conditioning module to read the voltage response of the load cell.

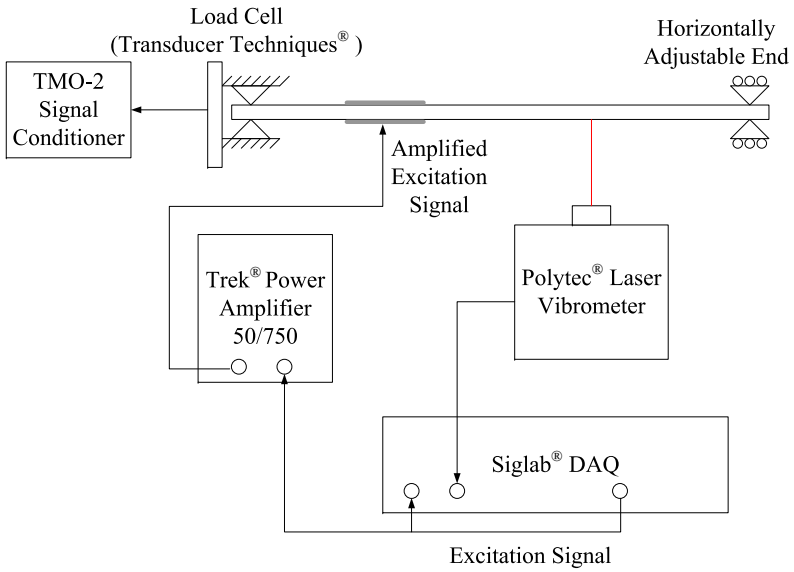

Figure 2.8: Schematic of experimental setup using laser vibrometer.

Keeping in mind that one of the goals of this work is the development of sound and accurate models of the membrane strip augmented with a smart bimorph. The model presented accounts for dynamics of the actuator, and placing a probe in contact with the structure might defeat the purpose of this work. In this spirit, a non-contact vibration measurement device is used. A Polytec® Laser Vibrometer is utilized to measure the velocity of specified points on the centerline of the Kapton strip. The small square dots on the Kapton strip, Fig. 2.9, are highly reflective tape used just to reflect the laser shined by the laser vibrometer.

A burst chirp signal is used to excite the structure. The chirp signal has a peak amplitude of 1 volt and the frequency range is 0.01Hz-500Hz. The excitation signal is amplified by a factor of 30 through a Trek® amplifier. Siglab of Spectral Dynamics® is used to construct the frequency response of the structure. The structure is excited ten times, and the frequency response is measured after every excitation. The ten measurements are averaged, and the obtained average is compared against the theoretical frequency response.

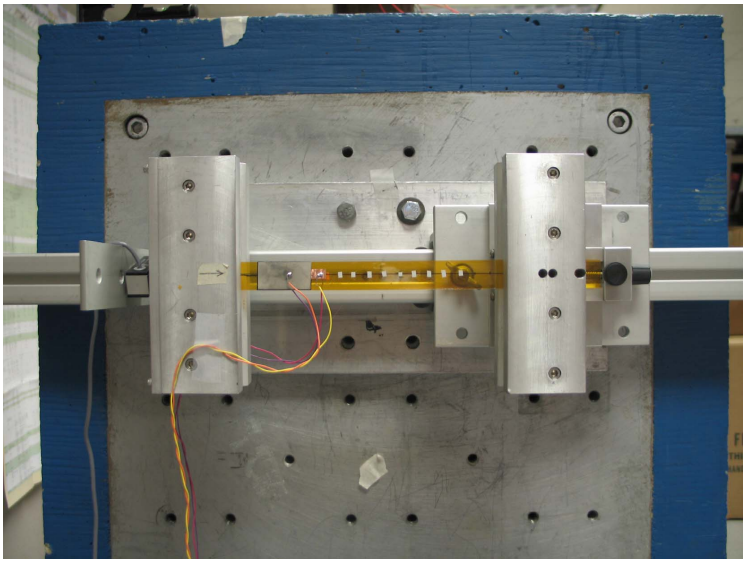

Figure 2.9: Picture of the experimental setup.

Fig. 2.10 shows the frequency response obtained via the finite element model developed in Section 2.1 and the average of the frequency responses obtained via the experimental setup. The coherence of the ten measurements is shown in Fig. 2.11. The tension in the structure was 13.5 N and measurements were taken at 9.1 cm from the left boundary. Fig. 2.12 shows the frequency response of the structure with a tensile load at 13.5 N measured at various points of the structure (from the left boundary).

It is interesting here to note that the FEM model overestimates the first and second frequencies, however it underestimates the third frequency, Fig. 2.10. The finite element method overestimates the natural frequencies by its nature, and hence the behavior of the model for the first two frequencies (of bending) is expected. However, the underestimation of the third frequency is unexplained. Moreover, the damping of the second mode is badly estimated, although the damping of the first and third mode is captured to a large extent. This might be due to the power-cable effect. The cables (wires) connecting to the piezoceramic bimorph, Fig. 2.9, might be causing this discrepancy in the results. It has been observed that signal and power cables (wires) cause nonlinear effects and significant increases in the damping ratio particularly at higher modes (Gooding et al., 2007).

From Fig. 2.10, the natural frequencies of bending were determined to be at 68.5

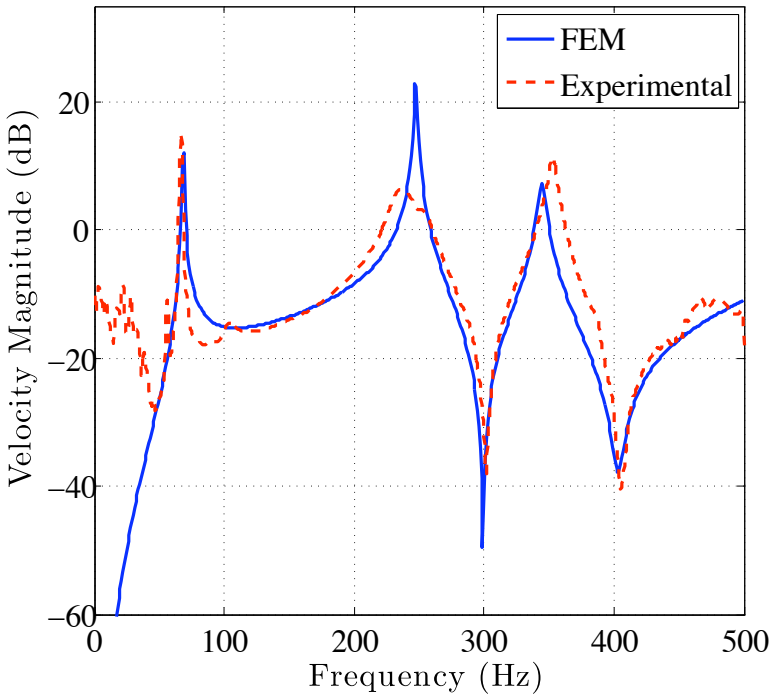

Figure 2.10: Finite element model vs. experimental frequency response (tension is 13.5 N, measurement point at 9.1 cm from the left boundary).

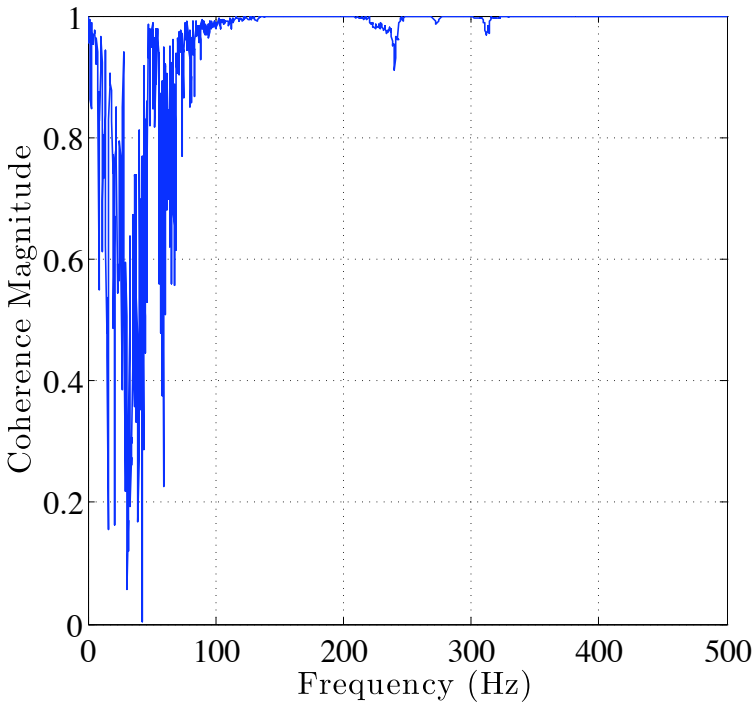

Figure 2.11: Coherence of the experimental frequency response (tension is 13.5 N, measurement point at 9.1 cm from the left boundary).

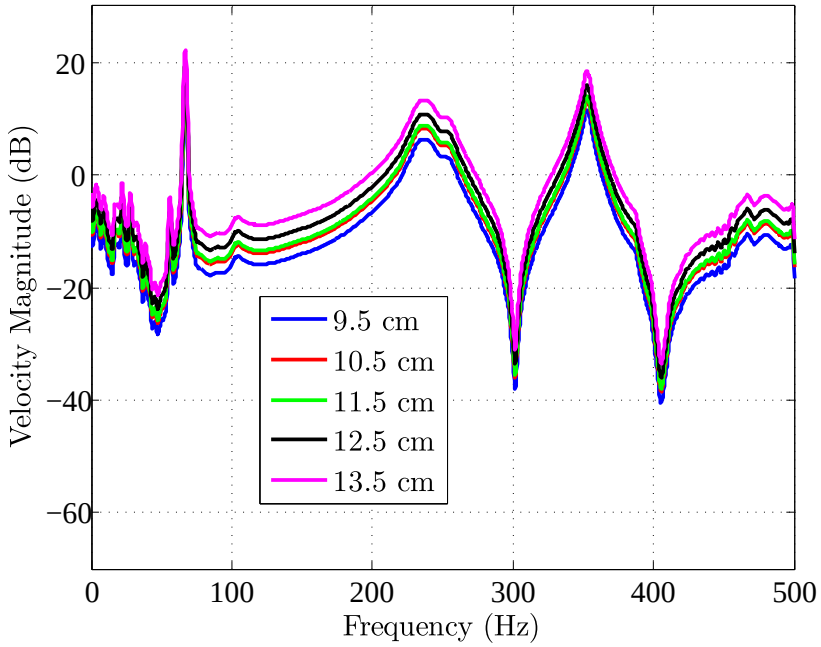

Figure 2.12: Frequency response at different measurement points (13.5 N tension).

Hz, 240 Hz, and 353 Hz. The percentage errors between the FEM results and the experimental results are 2.23%, 1.667%, and 3.11%. Fig. 2.10 requires further analysis. The experimental results show a peak at 54.9 Hz which is not predicted by the FEM model. To uncover the nature of this peak an alternative measurement device was deployed. A Polytec® Scanning Vibrometer is used in the experimental setup in place of the Polytec® Laser Vibrometer. The schematic of the alternative experimental setup is shown in Fig. 2.13.

The structure under study is discretized into a grid of points. The laser shines on the points specified by grid in turn, and the structure is excited three times at each measurement point, Fig. 2.14. Since Kapton has poor reflectivity, the structure is sprayed with a thin layer of white paint.

The peak at 54.9 Hz turns out to be the first torsional natural frequency. This result is in line with the experimental work reported by Ruggiero (2005) who also found a torsional mode in the bandwidth of interest. The first torsional mode shape is shown in Fig. 2.15. Figure 2.16 shows the first three bending mode shapes determined mathematically through the FEM model and experimentally via laser scanning vibrometery.

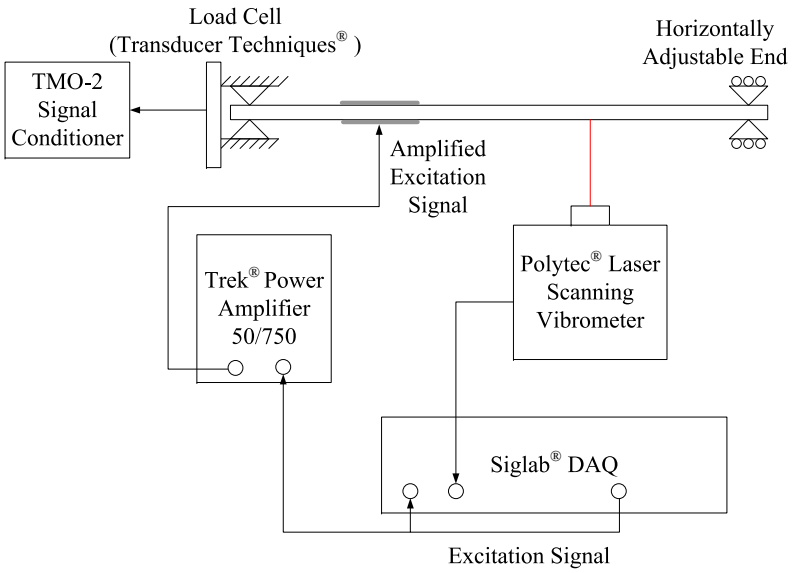

Figure 2.13: Schematic of experimental setup using scanning vibrometer.

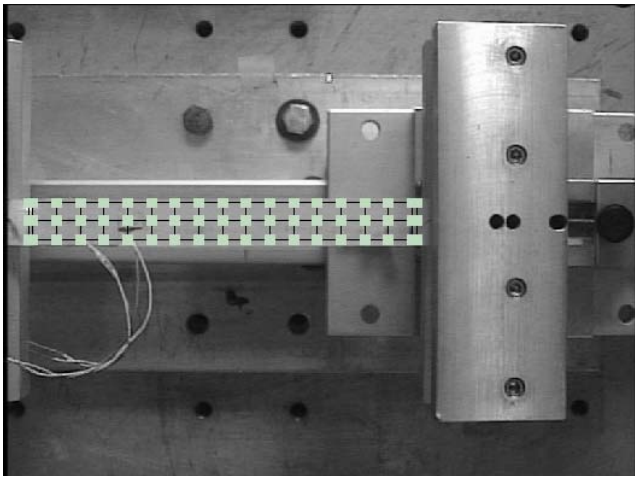

Figure 2.14: Grid of measurement points.

Moreover, while conducting the experiments, it was noticed that the frequency response shifts to higher values as the tension increases. Figure 2.18 shows the first natural frequency vs. tension with tension values ranging from 3.75 N to 12.5 N. This is expected since increasing the tension induces a stiffening effect within the structure. As the structure stiffens, the natural frequencies increase. Figure 2.18 shows this trend furnished with the model prediction and experimentally obtained data. This phenomenon can be traced back to the model presented in Section 2.1. Examining Eq. (2.14) shows that stiffness of the system is a function of the flexural stiffness and the tension. For higher tension values, the stiffness will increase and hence the natural frequencies will increase,

$$K = \left[\int_0^L EI(x)\phi_i''(x)\phi_j''(x)\mathrm{d}x\right]_{i,j=1,\cdots,N} + \left[\int_0^L \tau\phi_i'(x)\phi_j'(x)\mathrm{d}x\right]_{i,j=1,\cdots,N} . \tag{2.18}$$

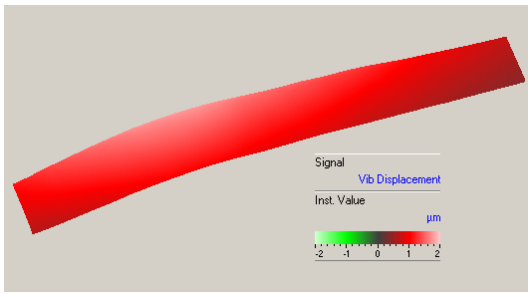

Figure 2.15: Torsional mode at 54.9 Hz.

Figure 2.17 shows the percentage error of the first three natural frequencies. The errors are presented for six tension values. The following equation was used to calculate the percentage errors

$$\text{Error } \% = \frac{|f_{exp} - f_{FEM}|}{f_{exp}} \times 100 . \tag{2.19}$$

Figure 2.19 shows the frequency response of the FEM model without accounting for the piezoelectric bimorph. This frequency response is plotted against the experimental frequency response. Accounting for the piezoelectric bimorph turns out to be crucial,

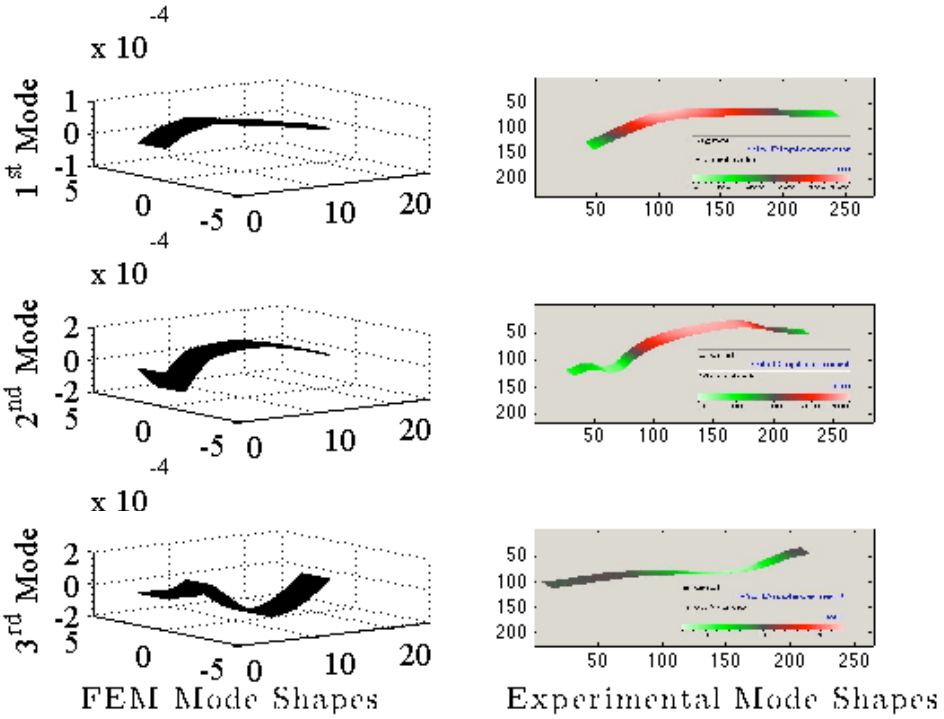

Figure 2.16: Bending mode shapes.

as the first frequency is not captured if the effect of the piezoelectric bimorph was not included in the model.

Vacuum Testing

The same specimen was tested in near vacuum conditions. A Tenney® Environmental Chamber is used to achieve these conditions. The pressure was set to 10 Torr and the temperature was set to 24°C. It takes 40 minutes for the chamber to reach near vacuum conditions. The laser shines on the the structure through a glass window.

Aside from the absence of the air damping, the vacuum environment gives rise to the outgassing phenomenon, (DuPont, 2002). According to the previous reference, Kapton mainly releases carbon monoxide, CO, and carbon dioxide, CO_2, when outgassing. Outgassing has two effects on the structure: the mass of Kapton decreases, and the tension increases. The tension was set to 15.5 N, and when steady vacuum conditions were reached, the tension reading was 16.25 N. That indicates an increase of 4.83%.

Figure 2.18 and Eq. (2.18) suggest that increasing the tension will shift the natural fre-

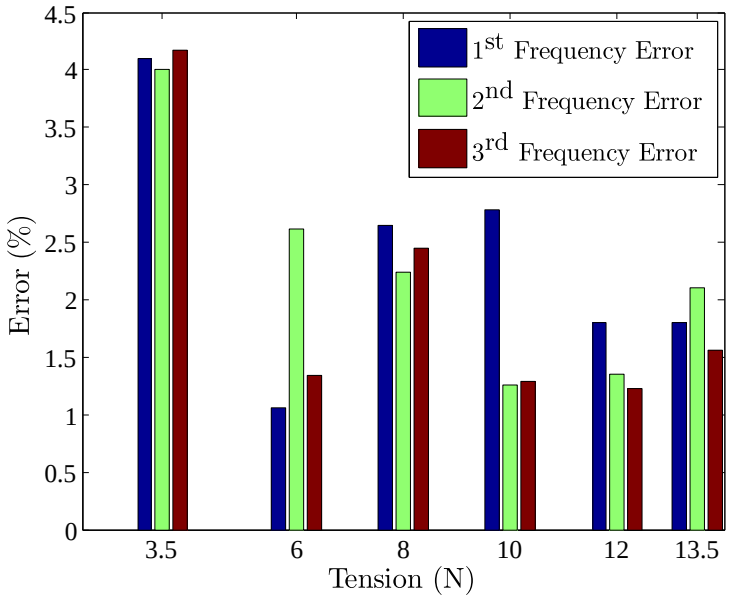

Figure 2.17: Error of the first three resonance frequencies at various tensile loads (measured at 9.1 cm).

quencies to higher values. Moreover, the decrease of mass of the Kapton strip suggests an increase in the natural frequencies as well. On the other hand, the dimensions of strip and the material's properties change due to outgassing. The shift of the frequency due to outgassing cannot be predicted. Fig. 2.20 shows the experimental frequency response for vacuum and ambient environments (measurement taken at 13.1 cm from left boundary), with peaks having lower values at vacuum conditions.

2.3 Configuration I: Bending-Bending

So far, we have considered a membrane strip augmented with a single piezoceramic bimorph. Now, we augment a membrane strip with two MFC bimorphs and we treat two configurations: I and II. For Configuration I, both bimorphs act in bending. In this case, the forcing function on the right side of Eq. (2.3) will be

$$f(x,t) = -\sum_{k=1}^{2} \frac{\partial^2 [M_x(x,t)]_k}{\partial x^2}, \tag{2.20}$$

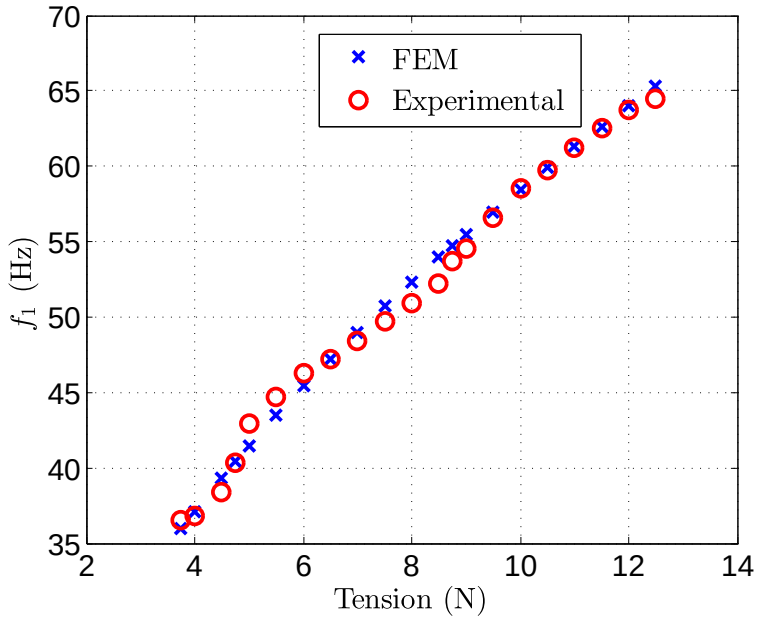

Figure 2.18: First natural frequency vs. tension.

where $[M_x(x,t)]_k$ is the bending moment exerted by the k-th bimorph Banks et al. (1996a), defined as

$$[M_x(x,t)]_k = -2\kappa_k^B \chi_k(x) V_k(t) \quad k = 1,2\,. \tag{2.21}$$

Here κ_k^B is the bending constant of the k-th bimorph Banks et al. (1996a). Substituting Eq. (2.21) in Eq. (2.12), and following the developments of Banks et al. (1996b) yields

$$\mathbf{F}(t) = \sum_{k=1}^{2} 2\kappa_k^B V_k(t) \int_0^L \chi_k(x)\phi_j''(x)\mathrm{d}x = \sum_{k=1}^{2} \begin{bmatrix} 0_{N\times 1} \\ \mathbf{B}_k \end{bmatrix} V_k(t)\,. \tag{2.22}$$

Here $\mathbf{B}_k$ is the $(N \times 1)$ input vector corresponding to the k-th bimorph, defined as

$$\mathbf{B}_k = \left[2\kappa_k^{\mathbf{B}} \int_0^L \chi_k(x)\phi_j''(x)\mathrm{d}x \right]_{k=1,2 \text{ and } j=1,\cdots,N}\,. \tag{2.23}$$

Regarding the tension, there is no actuation in the axial direction, and hence the tension is not time varying. Moreover, it was shown that the tension is constant along the structure in Section 2.1. Consequently the stiffness matrix is constant. Based on these developments, Eq. (2.13) reduces to

$$\left\{ \begin{array}{c} \bar{\mathbf{w}} \\ \bar{\mathbf{v}} \end{array} \right\}_t = \left[\begin{array}{cc} 0_{N\times N} & \mathbf{I}_{N\times N} \\ -\mathbf{M}_2^{-1}\mathbf{K} & -\mathbf{M}_2^{-1}\mathbf{C} \end{array} \right] \left\{ \begin{array}{c} \bar{\mathbf{w}} \\ \bar{\mathbf{v}} \end{array} \right\}$$

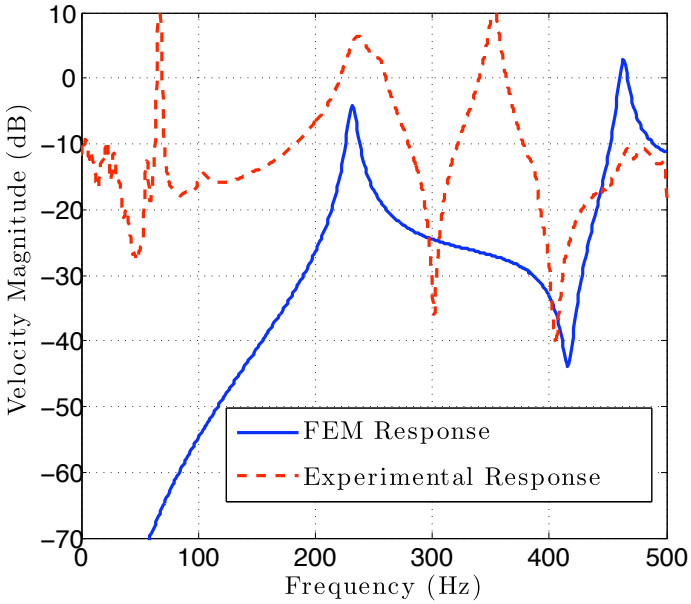

Figure 2.19: Finite element vs. experimental frequency response without accounting for the piezoceramic bimorph.

$$+ \begin{bmatrix} 0_{N\times 1} & 0_{N\times 1} \\ \mathbf{M}_2^{-1}\mathbf{B}_1 & \mathbf{M}_2^{-1}\mathbf{B}_2 \end{bmatrix} \begin{Bmatrix} V_1(t) \\ V_2(t) \end{Bmatrix} . \tag{2.24}$$

Equation (2.24) presents a MIMO linear system. Linear control techniques can be used to perform shape control of this structure.

2.4 Configuration II: Bending-Tension

Configuration II uses an alternative approach. One of the bimorphs is actuated in bending (BMFC), whereas the other bimorph is actuated axially (AMFC). Hence, the tension within the structure is not constant anymore. The tension varies temporally as the applied voltage varies. Moreover, the tension changes at the location of the AMFC bimorph. The tension is defined as

$$\tau(x,t) = \bar{\tau} + 2\kappa_2^A S_{3,4}(x)\chi_2(x)V_2(t)\,. \tag{2.25}$$

The second term in Eq. (2.25) stands for the axial load exerted by applying voltage to the AMFC bimorph, and κ_2^A is the axial constant of the AMFC bimorph (Banks et al., 1996a),

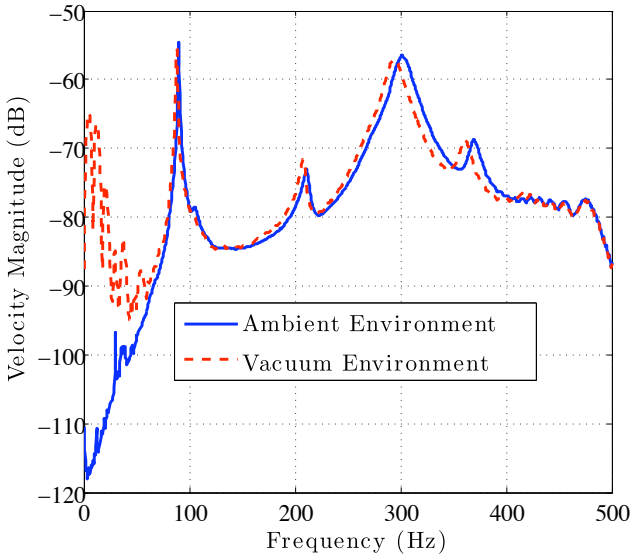

Figure 2.20: Frequency response measured in ambient and vacuum environments.

given as

$$\kappa_2^A = -E_2 b_2 d_{31}^2 \quad \textit{the superscript of } d_{31} \textit{ is to indicate the bimorph number.}$$

The function $S_{3,4}(x)$ characterizes the actuation of AMFC, and is given by

$$S_{3,4}(x) = \begin{cases} 1 & \text{if} \quad x < (x_3 + x_4)/2 \\ 0 & \text{if} \quad x = (x_3 + x_4)/2 \\ -1 & \text{if} \quad x > (x_3 + x_4)/2 \end{cases} . \tag{2.26}$$

Understanding the nature of $\chi_2(x)$ and $S_{3,4}(x)$ turns out to be crucial to understand the behavior of the structure when using Configuration II. The function $\chi_2(x)$ points to structural attributes. It implies the presence of the bimorph regardless of its actuation nature (bending/tension). On the other hand, $S_{3,4}(x)$ is related to the actuation attributes. It simply says that for a positive voltage, opposite but equal strains are generated about the midpoint of the bimorph.

For Configuration II, the stiffness matrix $K(t)$ of Eq. (2.14) becomes

$$\mathbf{K}(t) = \left[\int_0^L \left(EI(x)\phi_i''(x)\phi_j''(x) + \left[\bar{\tau} + 2\kappa_2^A S_{3,4}(x)\chi_2(x)V_2(t) \right] \phi_i'(x)\phi_j'(x) \right) \mathrm{d}x \right]_{i,j=1,\cdots,N} . \tag{2.27}$$

For the scope of this work, $V_2(t)$ is assumed to be constant so that the stiffness matrix defined in Eq. (2.27) would be constant, and the system would linear. Modeling the BMFC is treated as in Renno et al. (2006), and hence the equations of motion for Configuration II become

$$\begin{Bmatrix} \bar{\mathbf{w}} \\ \bar{\mathbf{v}} \end{Bmatrix}_t = \begin{bmatrix} 0_{N\times N} & \mathbf{I}_{N\times N} \\ -\mathbf{M}_2^{-1}\mathbf{K} & -\mathbf{M}_2^{-1}\mathbf{C} \end{bmatrix} \begin{Bmatrix} \bar{\mathbf{w}} \\ \bar{\mathbf{v}} \end{Bmatrix} + \begin{bmatrix} 0_{N\times 1} \\ \mathbf{M}_2^{-1}\mathbf{B}_1 \end{bmatrix} V_1(t)\,. \tag{2.28}$$

The input vector $\mathbf{B}_1$ is given in Eq. (2.23). The case of constant $V_2(t)$ will cause the system to be governed by Eq. (2.28), and this will be referred to as the *quasilinear* state of the system.

2.5 Experimental Validation of Configuration I and Configuration II

An experiment is used to verify the model presented in Section 2.3 and Section 2.4. A membrane strip made of Kapton, a polyimide that has been a commonly used membrane material for recent space applications (Jenkins, 2001), is considered. The MFC patches (M-2814-P1) are made by Smart Materials Corporation®. Figure 2.21 shows a schematic of the experimental setup. The Kapton strip is held between two grippers. The left gripper remains fixed, while the right gripper's position is adjustable through the lead screw, displayed in the photo of Fig. 2.21, to produce a tensile load in the structure. A MLP-75 load cell, by Transducer Techniques®, is used to measure the tension in the structure. While exciting the structure, the right gripper can be fixed to its position via a setscrew. In other words, the right gripper is only used to tension the structure, and the structure is under pinned-pinned boundary conditions when excited. A Polytec® laser vibrometer (OFV 303) is used to measure the velocity of a single point on the centerline of the Kapton strip. The laser vibrometer shines a laser on the structure. The reflection of the laser beam is used to measure the velocity of the structure at that point. Kapton has poor reflective properties, so small pieces of highly reflective tape are therefore placed along the centerline of the test article.

The structure is excited through Siglab of Spectral Dynamics®. Siglab is also used to construct the frequency response of the structure. For all the tests presented thereafter, the excitation signal is a burst chirp signal that is generated every other second. The chirp signal sweeps the frequencies between 0.01 Hz and 300 Hz in one second as well. The frequency resolution is 0.3125 Hz. After every excitation, the frequency response is constructed. The structure is excited ten times, and the measurements collected are averaged. The average measurement is compared with the FEM prediction. A dual channel Trek® amplifier (Model 50/750) is used to amplify the signal. The excitation signal is amplified by a factor of 20.

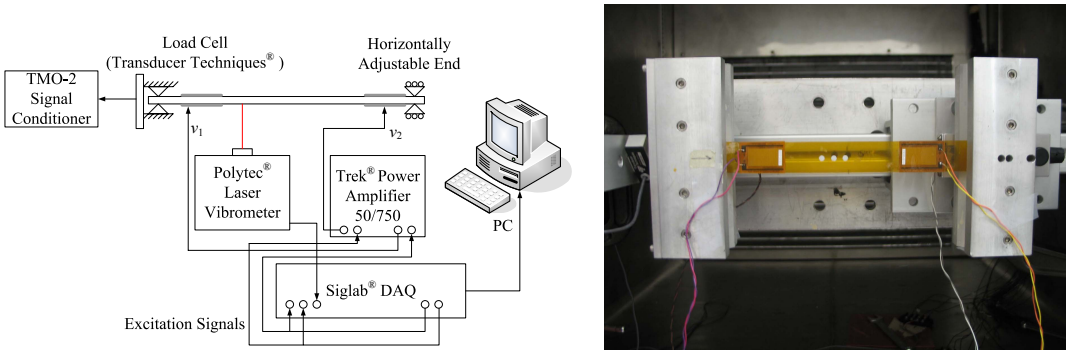

(a) Schematic of experimental setup.

(b) Photo of the test article.

Figure 2.21: Experimental setup.

The frequency values predicted by the FEM model are compared to the experimental values. The percentage errors are calculated using Eq. (2.19) and are also listed below for all the tests conducted.

2.5.1 Treating the Bonding Issue – Vacuum Bagging

The derivation of Eq. (2.3) assumes perfect bonding (infinite shear stiffness) between the membrane strip and the MFC patches. The assumption of perfect bonding implies that both the membrane strip and the MFC patches experience the same strain. To achieve near perfect bonding between the membrane strip and the MFC patches, vacuum bagging is used. Vacuum bagging is a technique widely used when manufacturing composite materials.

To implement this technique, an aluminum plate is used as a working surface. A rectangle is constructed on the surface using sticky sealant (GS#27) of General Sealants® around the section where the MFC will be bonded to the membrane strip. Cyanoacrylate Adhesive of Handibond® is applied to the membrane strip and the MFC patch. A vacuum bag (GS#A-800-3G) of General Sealants® is placed atop the sticky sealant. The tube of a vacuum pump is augmented with a syringe which is inserted in the sealant. A vacuum pump evacuates the sealed chamber. The vacuum bagging setup used is shown in Fig. 2.22.

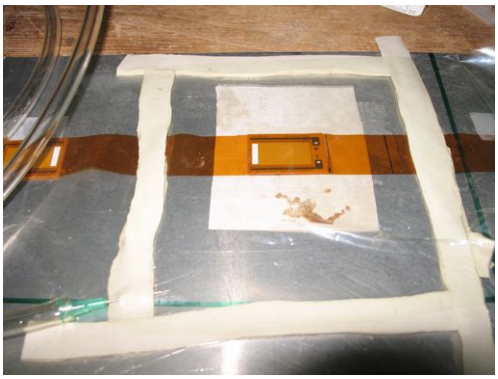

Figure 2.22: Vacuum bagging setup.

This technique eliminates the need to place weights atop the MFC until the adhesive cures. By removing the air from inside the bag, the atmospheric pressure acts against the bag, pressing the MFC against the membrane strip. This pressure is applied evenly and perpendicular to all the surfaces inside the bag.

2.5.2 Experimental Validation of Configuration I

For Configuration I, both bimorphs are excited in bending. The burst chirp signal had a peak amplitude of 0.5 v. The actuators where excited one at a time. Table 2.2 shows the physical properties of the structure that was tested in this configuration. The first bimorph is placed at $x_1 = 3.2$ cm whereas the second bimorph is placed at $x_3 = 14$ cm. The tension in the structure was set to 8 N.

Figure 2.23 displays the frequency response obtained via the experimental setup and that predicted by the FEM model. Table 2.3 lists the results for the natural frequencies. The error did not exceed 2%. Recall that the experimental frequency response viewed in Fig. 2.23 is the average of ten measurements. Figure 2.24 shows the coherence of the measurements.

The first frequency, f_1 is excited with both inputs. On the other hand, f_2 was only excited with the first input V_1 and f_3 was only excited with the second input V_2.

Table 2.2: Properties of Kapton strip and MFC patch – Configuration I.

Property	Kapton Strip	MFC Patch
Density [kg/m^3]	1420	994
Young's Modulus [GPa]	3	34.5
Width [cm]	2.5	2.5
Thickness [mm]	51×10^{-3}	0.3
Length [cm]	18	3.8

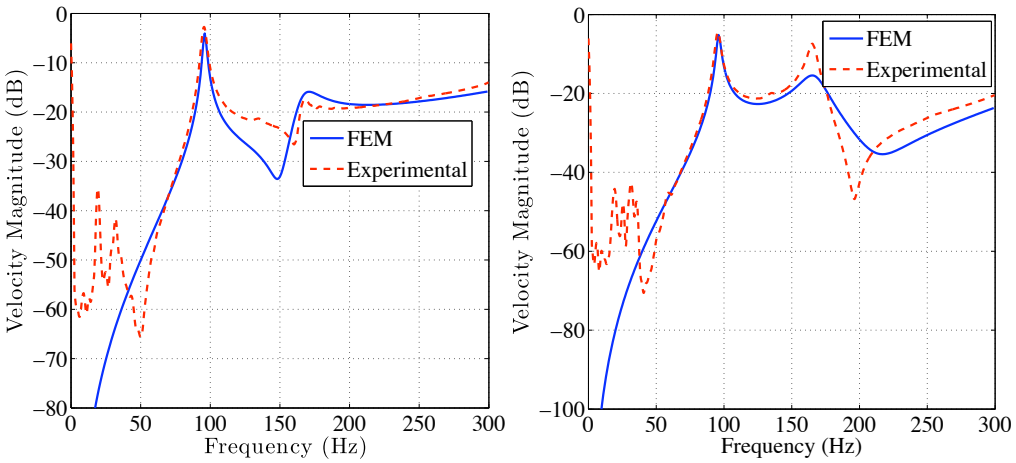

(a) Frequency response – V_1 as input.

(b) Frequency response – V_2 as input.

Figure 2.23: FEM vs. experimental frequency response.

2.5.3 Experimental Validation of Configuration II

As discussed in Section 2.1, the voltage supplied to the AMFC is kept constant during each test to obtain a linear model. The BMFC was placed at $x_1 = 2.5$ cm and the AMFC

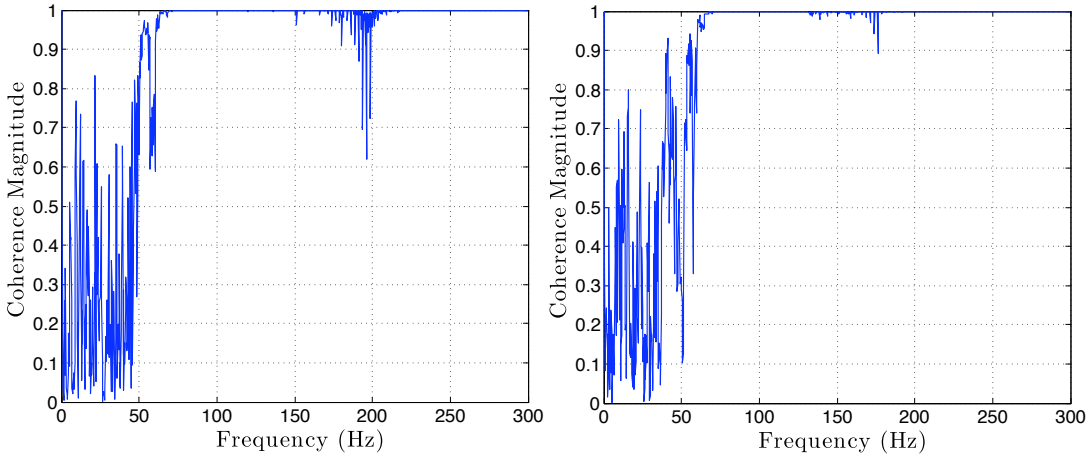

(a) Coherence of results–V_1 as input.

(b) Coherence of results–V_2 as input.

Figure 2.24: Coherence of experimental results.

Table 2.3: Frequencies of the structure tested for Configuration I

Frequency	**FEM Model [Hz]**	**Experimental [Hz]**	**Error [%]**
f_1	96.05	95.6	0.47
f_2	165.25	163.35	1.16
f_3	170.65	168.5	1.28

was placed at $x_3 = 15.2$ cm, Fig. 2.1. The physical properties of the test article tested for this configuration are given in Table Table 2.4. Figure 2.25 shows the experimental and theoretical frequency response of the structure with 0, 75v and 150v applied to the AMFC. The FEM model presented predicts the first two frequencies within 3% error for the three cases tested. Additionally, the first natural frequency consistently shifted to lower values as the voltage supplied to the TBM increased.

For more validation, the following was conducted: three values of nominal tension, $\bar{\tau}$, are applied to the structure: 8 N, 10 N, and 12 N, Eq. (2.25). For each nominal tension value, three voltage values are supplied to the AMFC: 0 v , 75 v and 150 v. For each combination of nominal tension, $\bar{\tau}$, and voltage input to AMFC, V_2, the structure is excited through the BMFC and the frequency response is obtained as explained previously. The peak amplitude of the chirp signal used for this configuration is 0.1 v. In total, nine combinations are tested.

Figure 2.26 shows the frequency response measured at three locations along the cen-

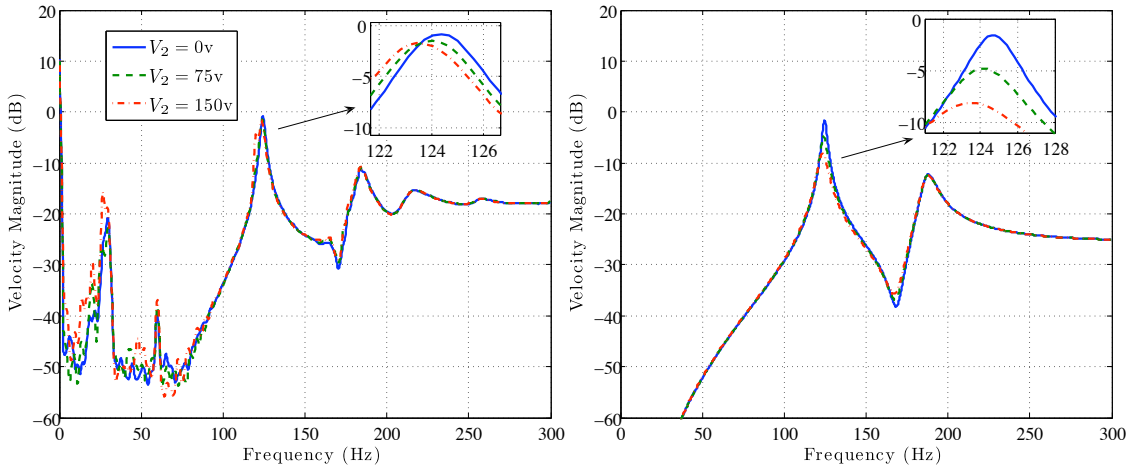

(a) Experimental frequency response.

(b) FEM frequency response.

Figure 2.25: Frequency response of the membrane mirror strip.

terline of the test article: 8.5 cm, 9.5 cm and 10.4 cm (all measured from the left boundary, Fig. 2.21b). The coherence of each measurement set is displayed as well. Figure 2.27, Fig. 2.28 and Fig. 2.29 show the frequency response of the structure for the nine combinations mentioned above. The coherence corresponding to each measurement set is shown as well.

Table 2.5, Table 2.6, and Table 2.7 list the FEM model predictions and the experimentally obtained values of the frequencies. The percentage error is calculated using Eq. (2.19). The percentage error did not exceed 2% for all the values obtained.

Examining the results reveals the following. When no voltage is supplied to the AMFC, i.e. $V_2 = 0$, the frequency response shifts to higher values as the nominal tension increases. This can be predicted if one examines Eq. (2.27). Simply, increasing the tension increases the stiffness which in turn causes an increase of the frequency values.

Now consider the results obtained of the cases where a non-zero voltage is applied to the AMFC, i.e. $V_2 = 75$ v and $V_2 = 150$ v. The frequency response for these two cases shifted to lower values as the value of V_2 increased. The increase in V_2 causes a decrease in tension, Eq. (2.25), at the location of the AMFC. Figure 2.30 shows the characteristic function that describes the behavior of the AMFC bimorph. With positive values of V_2, the AMFC equally expands in both directions with its midpoint being stationary.

This behavior relieves some of the axial load placed on the membrane strip through the nominal tension, at the location of the AMFC. As such, this creates a softening behavior, which yields to lower frequency values as V_2 increases.

Moreover, the effect of the AMFC is dependent upon its size and location. This can be clearly observed if one expands Eq. (2.25),

$$K(t) = \left[\int_0^L EI(x)\phi_i''(x)\phi_j''(x)\mathrm{d}x\right]_{i,j=1,\cdots,N} + \bar{\tau}\left[\int_0^L \phi_i''(x)\phi_j''(x)\mathrm{d}x\right]_{i,j=1,\cdots,N} + 2\kappa_2^A V_2\left[\int_0^L S_{3,4}(x)\chi_2(x)\phi_i''(x)\phi_j''(x)\mathrm{d}x\right]_{i,j=1,\cdots,N}. \tag{2.29}$$

where the last term of Eq. (2.29) can be further expanded as,

$$\int_0^L S_{3,4}(x)\chi_2(x)\phi_i''(x)\phi_j''(x)\mathrm{d}x = \int_{x_3}^{(\frac{x_3+x_4}{2})^-} \phi_i''(x)\phi_j''(x)\mathrm{d}x - \int_{(\frac{x_3+x_4}{2})^+}^{x_4} \phi_i''(x)\phi_j''(x)\mathrm{d}x\,.$$

For example, if the AMFC bimorph is moved to the left, its influence grows. Figure 2.31 displays the frequency response of the FEM model if the AMFC bimorph is moved 3 cm to the left, i.e. $x_3 = 12.2$ cm. The nominal tension $\bar{\tau}$ is set to 8 N, and three voltage values for V_2 are tested. The shift in the natural frequency is more visible in this case.

Table 2.4: Properties of Kapton strip and MFC patch – Configuration II.

Property	**Kapton Strip**	**MFC Patch**
Density [kg/m^3]	1420	994
Young's Modulus [GPa]	3	34.5
Width [cm]	2.5	2.5
Thickness [mm]	51×10^{-3}	0.3
Length [cm]	22	3.8

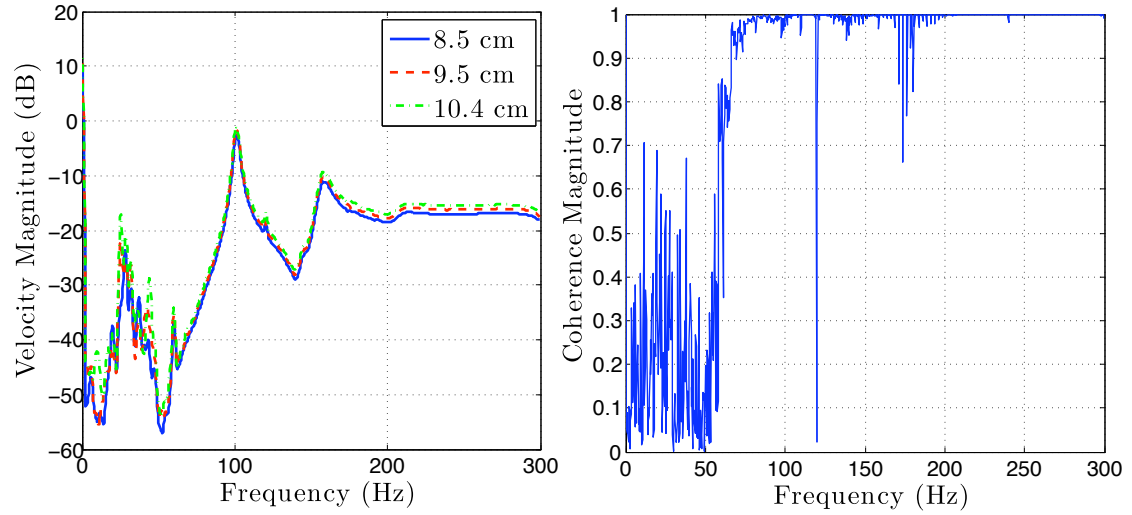

(a) Frequency response.

(b) Coherence for measurements at 8.5 cm.

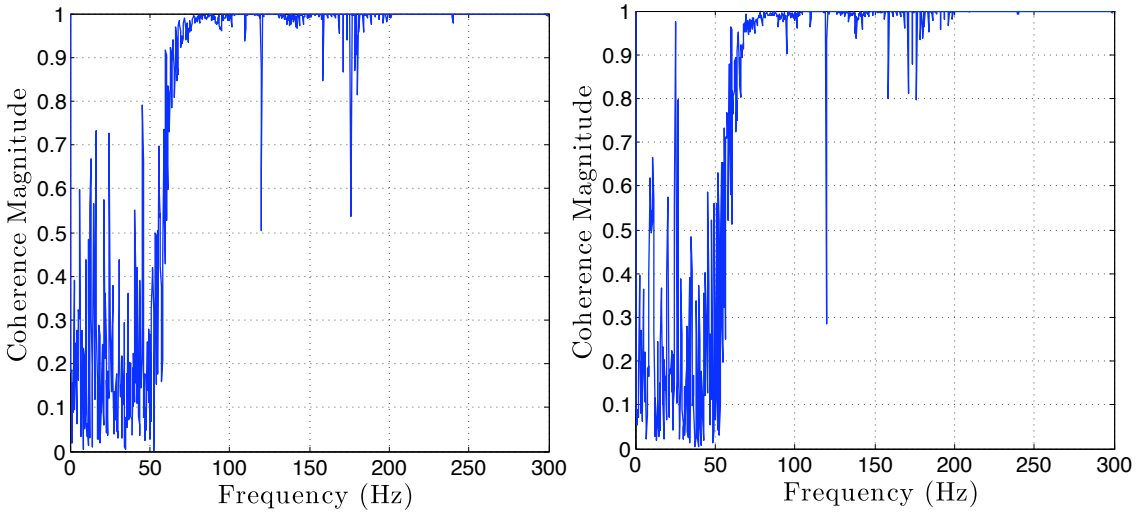

(c) Coherence for measurements at 9.5 cm.

(d) Coherence for measurements at 10.4 cm.

Figure 2.26: Experimental frequency response obtained at various measurement points.

Table 2.5: Frequency values – FEM vs. experimental results: nominal tension $\bar{\tau} = 8$ N.

TMFC Voltage[v]	Frequency[Hz]	FEM Result	Experimental Result	Error [%]
0	f_1	95.85	97.25	1.44
	f_2	153.82	154.95	0.73
75	f_1	94.55	96.36	1.88
	f_2	153.42	154.23	0.53
150	f_1	93.95	95.25	0.73
	f_2	153.40	153.15	0.16

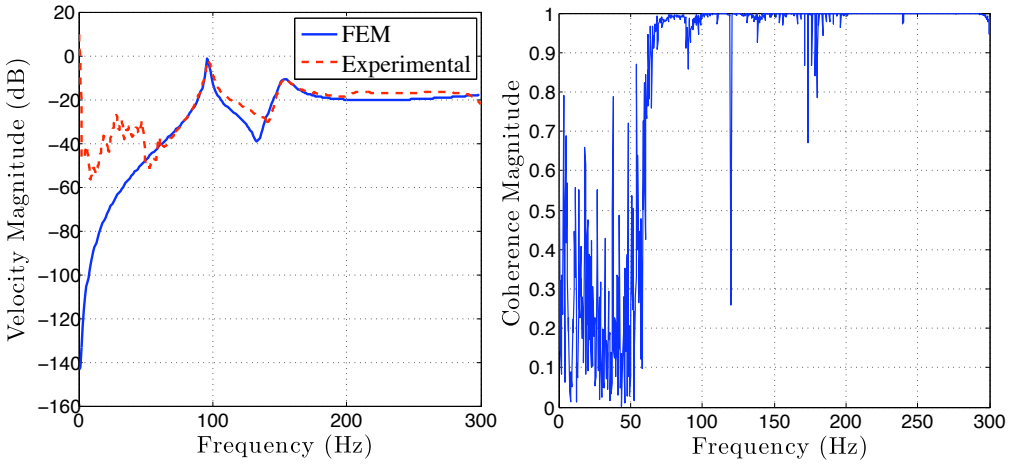

(a) Frequency response – $V_2 = 0$ v. (b) Coherence – $V_2 = 0$ v.

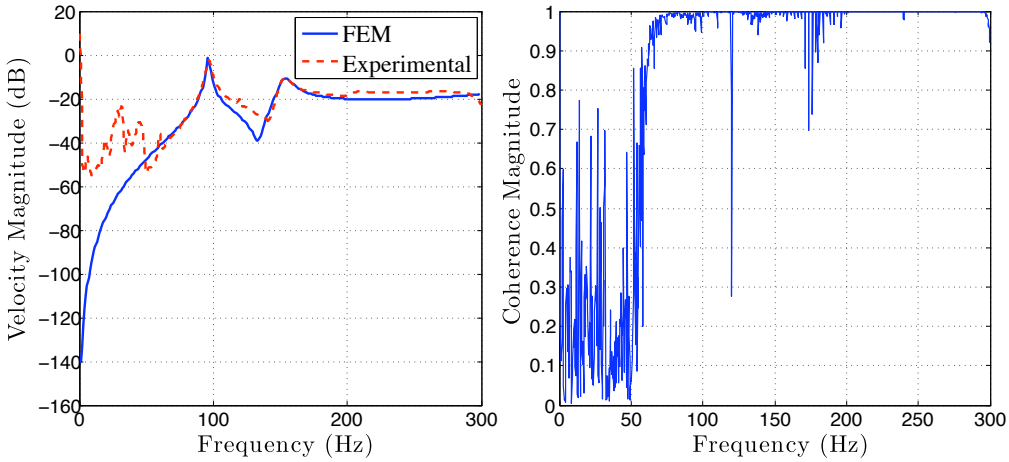

(c) Frequency response – $V_2 = 75$ v. (d) Coherence – $V_2 = 75$ v.

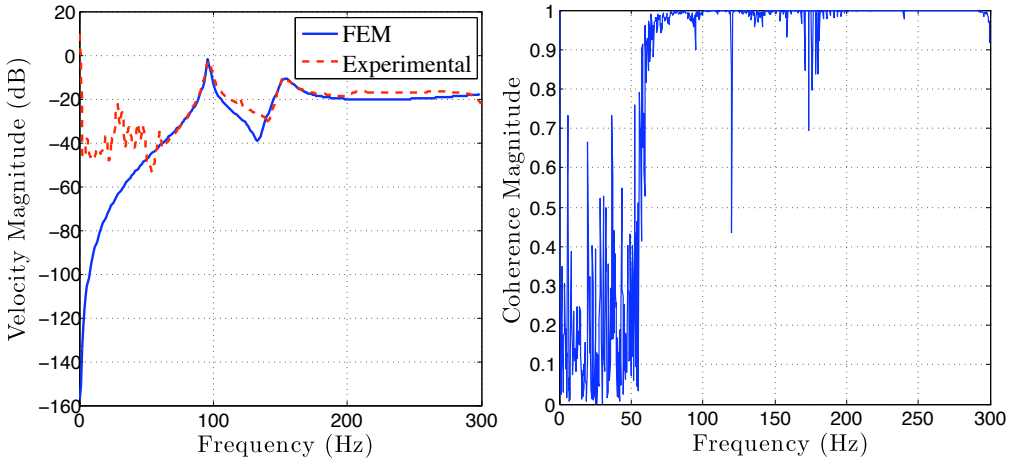

(e) Frequency response – $V_2 = 150$ v. (f) Coherence – $V_2 = 150$ v.

Figure 2.27: FEM vs. experimental frequency response – nominal tension $\bar{\tau} = 8$ N.

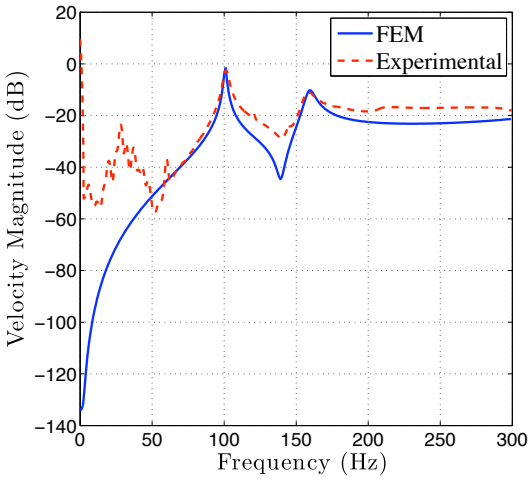

(a) Frequency response – $V_2 = 0$ v.

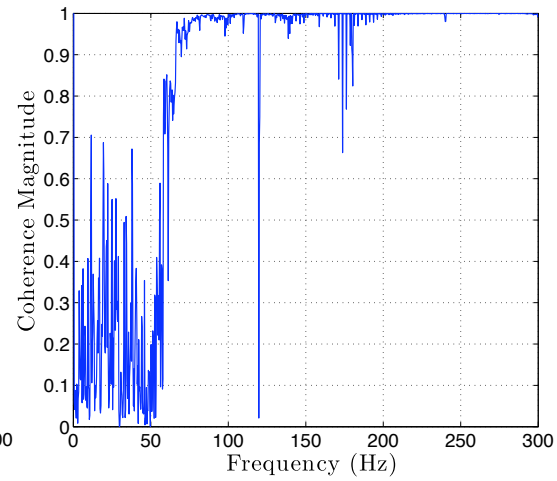

(b) Coherence – $V_2 = 0$ v.

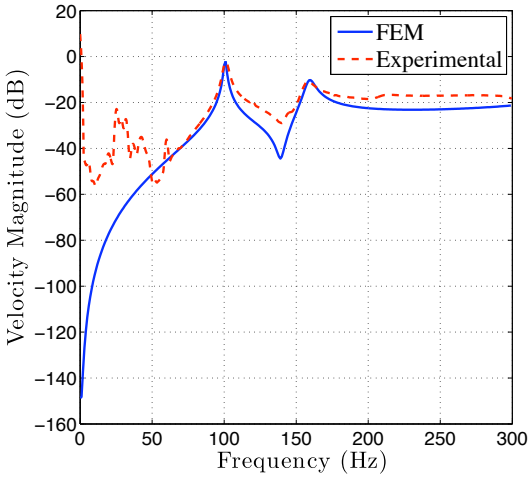

(c) Frequency response – $V_2 = 75$ v.

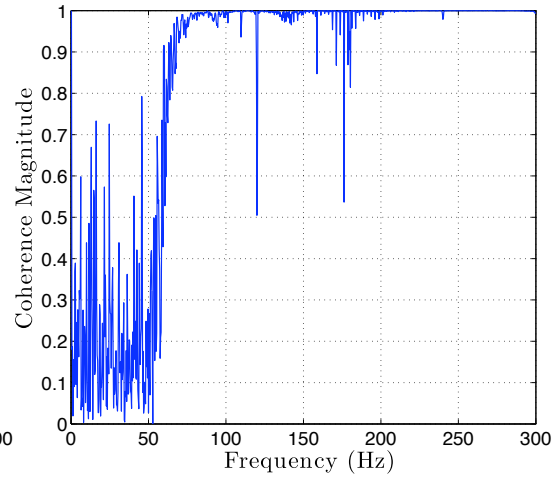

(d) Coherence – $V_2 = 75$ v.

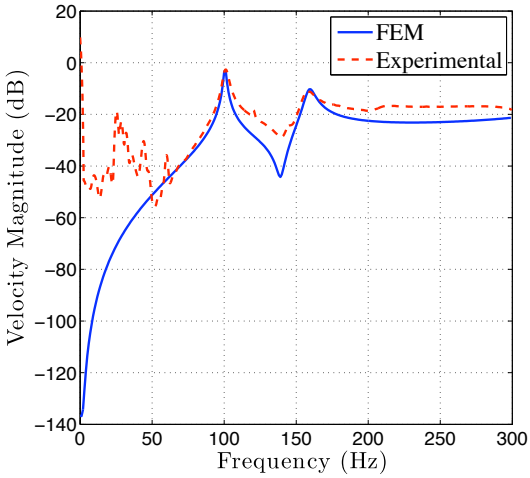

(e) Frequency response – $V_2 = 150$ v.

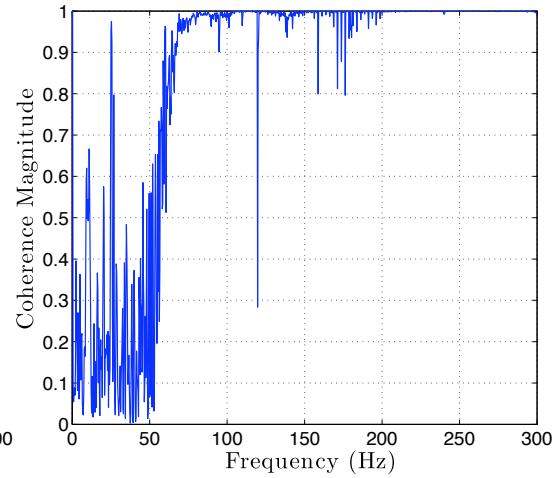

(f) Coherence – $V_2 = 150$ v.

Figure 2.28: FEM vs. experimental frequency response – nominal tension $\bar{\tau} = 10$ N.

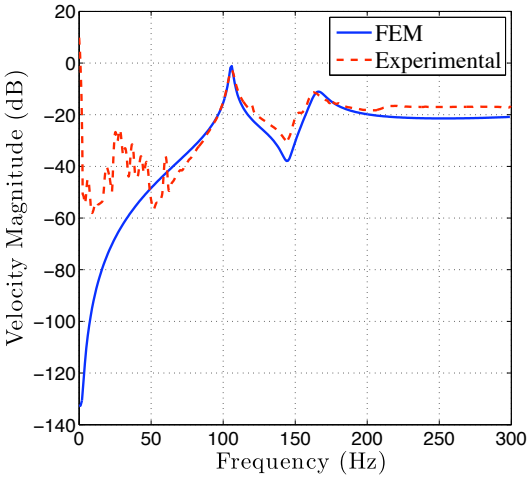

(a) Frequency Response – $V_2 = 0$ v

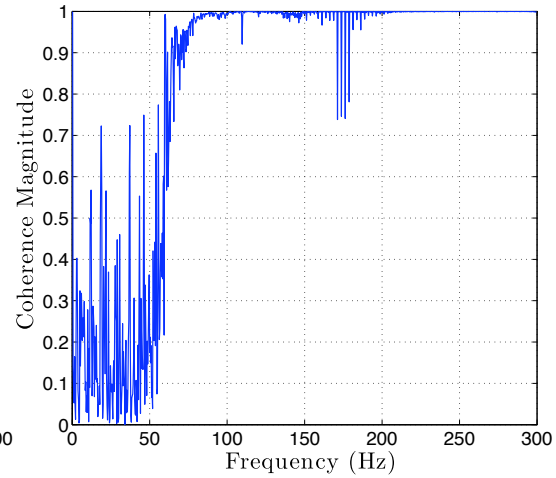

(b) Coherence – $V_2 = 0$ v

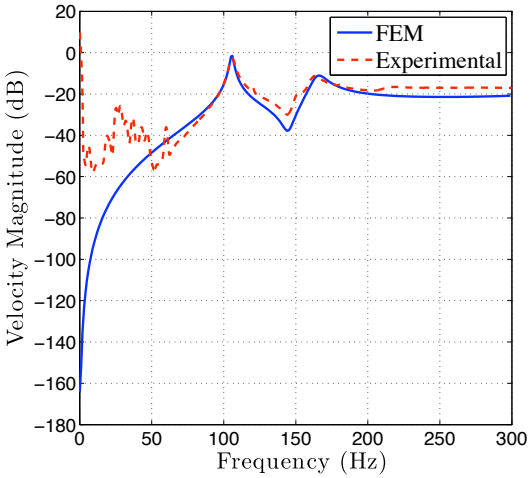

(c) Frequency response – $V_2 = 75$ v.

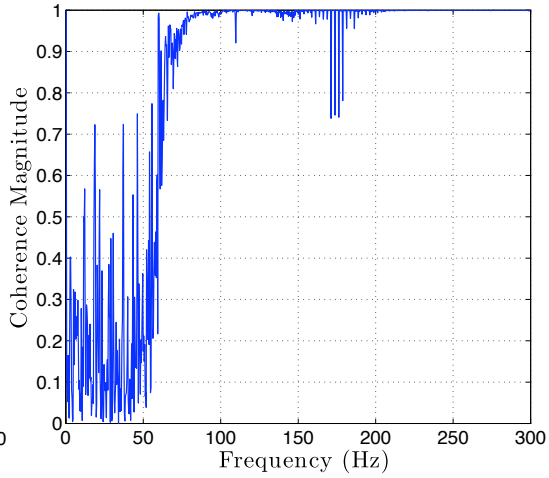

(d) Coherence – $V_2 = 75$ v.

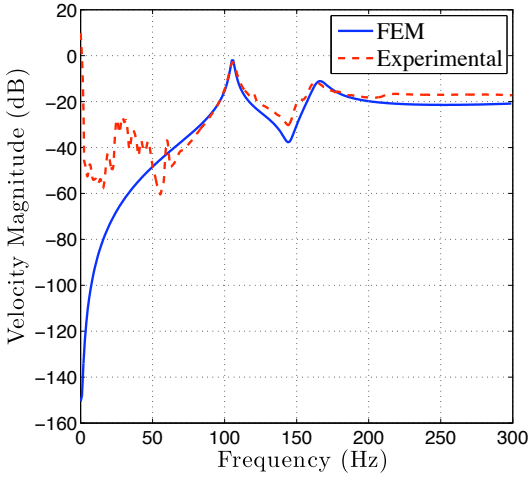

(e) Frequency response – $V_2 = 150$ v.

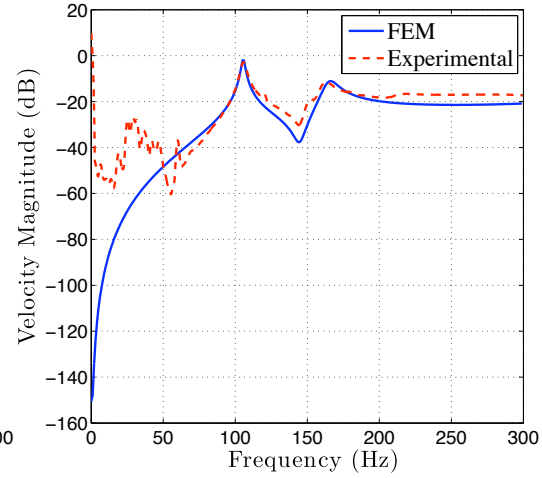

(f) Coherence – $V_2 = 150$ v.

Figure 2.29: FEM vs. experimental frequency response – nominal tension $\bar{\tau} = 12$ N.

Table 2.6: Frequency values – FEM vs. experimental results: nominal tension $\bar{\tau} = 10$ N.

TMFC Voltage[v]	Frequency[Hz]	FEM Result	Experimental Result	Error [%]
0	f_1	100.95	101.35	0.39
	f_2	159.55	157.55	1.26
75	f_1	100.30	100.80	0.49
	f_2	158.80	157.15	1.05
150	f_1	99.53	100.12	0.58
	f_2	158.10	156.62	0.94

Table 2.7: Frequency values – FEM vs. experimental results: nominal tension $\bar{\tau} = 12$ N.

TMFC Voltage[v]	Frequency[Hz]	FEM Result	Experimental Result	Error [%]
0	f_1	105.90	105.65	0.23
	f_2	165.80	163.05	1.68
75	f_1	104.82	104.80	0.09
	f_2	164.90	161.90	1.86
150	f_1	104.10	104.65	0.53
	f_2	163.98	161.55	1.51

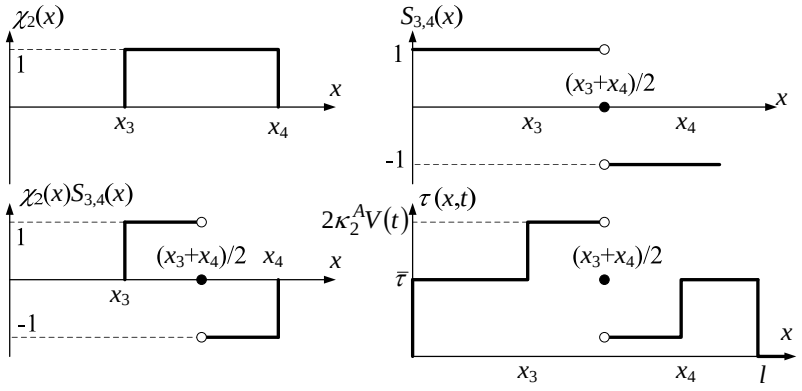

Figure 2.30: Tension characteristic function.

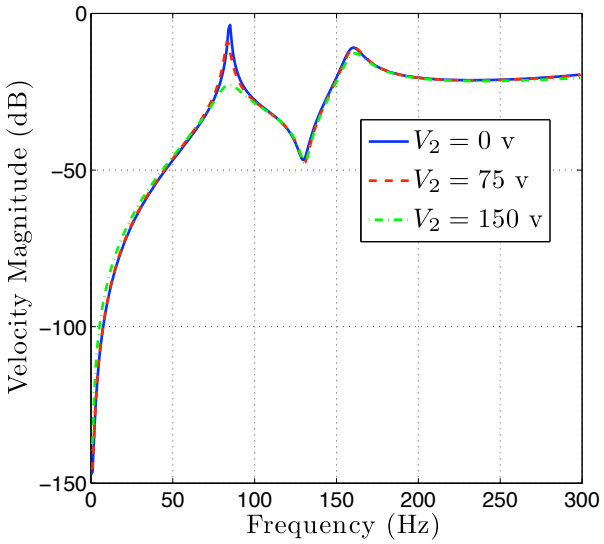

Figure 2.31: Frequency response with $\bar{\tau} = 8$ N and $x_3 = 12.2$ cm.

2.6 Chapter Summery

A thorough derivation of the linear model of a membrane strip augmented with multiple bimorph actuators is presented. Three cases were considered for further study and experimental validation. First, a membrane strip augmented with a single piezoelectric bimorph is treated. The model is validated experimentally in ambient and vacuum environments. Then, a membrane strip augmented with two MFC bimorphs is considered. Two configurations were further treated. The first configuration deployed two bimorphs that acted in bending only. The second configuration also deployed two MFC bimorphs, yet one of the bimorphs is actuated in bending and the other acted in tension. Both configurations were verified experimentally.

CHAPTER 3

MEMBRANE STRIP ACTUATED WITH BIMORPHS – CONTROL

As the models for various configurations of membrane strips has been developed in Chapter 2, it is appropriate now to treat the control problem. The control problem of membrane strips, and any structure for this sake, can be treated at two levels:

a) **Vibration Suppression** where the objective is to reject disturbances that might alter the configuration of the structure. In the case of membrane mirrors, there are a number of disturbances that can cause performance degradation of these instruments.

b) **Shape Control** refers to the reference tracking problem for continuous systems, *e.g.* structures. The shape control problem is of great relevance for membrane mirrors, since regulating the shape of the membrane mirror promises to improve the imagine quality and help remove optical aberrations. Section 1.6 presented a thorough literature review of the the shape control problem.

In the following, Section 3.1 presents the derivation of an optimal PI control law for the membrane strip augmented with a piezoceramic bimorph. The model of this structure and its experimental verification was presented in Section 2.2. Then, a control law for the model developed in Section 2.4 is presented in Section 3.2. Section 2.4 presented a model for a membrane strip augmented with two bimorphs. Since one of the bimorphs acts in bending and the other acts in tension, the model developed is nonlinear. For experimental verification, the system was treated in its quasilinear state. However, for control purposes, nonlinear control schemes are sought. Here, we choose the sliding mode

technique. The development and numerical simulations of the closed loop system are presented in Section 3.2 and the consequent subsections. Section 3.4 summarizes the chapter.

3.1 Control of Strip Actuated with Single Piezoceramic Bimorph

In this section, the a membrane strip augmented with a single piezoceramic bimorph near one of its boundaries, Fig. 2.4. To this end, consider the optimal LQR control problem in which the state space system presented in Eq. (2.16) on Page 40 is satisfied and the performance index of the form

$$J(\mathbf{x}(t), V_1(\cdot), t) = \int_0^\infty [\mathbf{x}(t)^T \mathbf{Q}\mathbf{x}(t) + V_1(t)^T R V_1(t)] \mathrm{d}t \ , \tag{3.1}$$

is to be minimized through finding an optimal control input V_1^*. Here, $\mathbf{Q} \in \mathbb{R}^{N\times N}$ is the state penalty positive definite matrix and $R \in \mathbb{R}$ is the positive input penalty. The control law derived by minimizing the cost function of Eq. (3.1) regulates the states, i.e. returns the membrane strip to its undeformed state when perturbed. However, the purpose here is to deform the structure to a desired static shape $\mathbf{x}_d = [\ \bar{\mathbf{w}}_d^T \quad 0_{1\times N}\ ]^T$. To perform this task, an alternative cost function is to be minimized

$$J(\mathbf{e}(t), V_1(\cdot), t) = \int_0^\infty [\mathbf{e}(t)^T \mathbf{Q}\mathbf{e}(t) + V_1(t)^T R V_1(t)] \mathrm{d}t \ ,$$

where

$$\mathbf{e}(t) = \mathbf{x}(t) - \mathbf{x}_d \ ,$$

is the error, which when substituted in Eq. (2.16) (on Page 40) yields the error dynamics of the system

$$\mathbf{e}(t) = \mathbf{A}\mathbf{e}(t) + \mathbf{B}V_1(t) + \mathbf{A}\mathbf{x}_d \ . \tag{3.2}$$

The vector $\{\mathbf{A}\mathbf{x}_d\}$ can be considered a constant disturbance, and the tracking problem transforms into a disturbance rejection problem as treated by Dorato et al. (2000). On

the presence of $\{\mathbf{A}\mathbf{x}_d\}$, some comments are in order. This vector quantity would vanish if

a) $\mathbf{x}_d$ is zero vector, which is not the case for the shape control problem. In other words, the problem treated here is the generalized case for the vibration suppression problem.

b) $\mathbf{x}_d$ lies in the null space of the matrix $\mathbf{A}$.

To comprehend the physics behind the second case, the examination of $\mathbf{A}$ and $\mathbf{x}_d$ is necessary. It turns out that $\mathbf{x}_d$ lies in the null space of $\mathbf{A}$ if the state matrix $\mathbf{A}$ does not have a stiffness block (see Eq. (2.17) on Page 40), which is impossible for structures.

Turning back to the control problem, the issue now is to reject the "disturbance" introduced by the presence of $\{\mathbf{A}\mathbf{x}_d\}$. From classical control theory, integration in the loop can be used to asymptotically reject constant disturbances. As Dorato et al. (2000) showed, the LQR theory can be used to deal with this problem. The purpose at this point is to drive $\dot{V}_1(t)$ and $\dot{\mathbf{e}}(t)$ to zero while driving $\{\mathbf{D}\mathbf{e}(t)\}$ ($\mathbf{Q}=\mathbf{D}^T\mathbf{D}$) to zero and $V_1(t)$ to a constant value that would asymptotically reject the disturbance posed by $\{\mathbf{A}\mathbf{x}_d\}$.

Hence, let us define an augmented state $\mathbf{z}(t)=[\ \dot{\mathbf{e}}^T(t)\quad \mathbf{e}^T(t)D^T\ ]^T$, and the following dynamics can be derived

$$\begin{aligned}\dot{\mathbf{z}}(t) &= \begin{bmatrix}\mathbf{A} & 0_{N\times N}\\ \mathbf{D} & 0_{N\times N}\end{bmatrix}\mathbf{z}(t)+\begin{bmatrix}\mathbf{B}\\ 0_{N\times 1}\end{bmatrix}v(t)\,,\\ &= \mathbf{A}_z\mathbf{z}(t)+\mathbf{B}_z v(t)\,,\end{aligned}$$

where the first row is determined by differentiating Eq. (3.2), $v(t)=\dot{V}_1(t)$ and the second row is an obvious identity. The augmented cost function becomes

$$J(\mathbf{z}(t),v(\cdot),t)=\int_0^\infty [\mathbf{z}(t)^T\mathbf{Q}_z\mathbf{z}(t)+v(t)^T R v(t)]\mathrm{d}t\ , \tag{3.3}$$

and $\mathbf{Q}_z$ is given by

$$\mathbf{Q}_z=\begin{bmatrix}0_{N\times N} & 0_{N\times N}\\ 0_{N\times N} & \mathbf{I}_{N\times N}\end{bmatrix}\ .$$

Following the treatment of Anderson and Moore (1990) one has to solve the steady state Riccati equation in order to minimize the cost function of Eq. (3.3),

$$-\dot{\mathbf{P}} = \mathbf{A}_z\mathbf{P} + \mathbf{P}^T\mathbf{A}_z - \mathbf{P}\mathbf{B}_z R^{-1}\mathbf{B}_z^T\mathbf{P} + \mathbf{Q}_z \ .$$

The resulting new control law will be

$$v^*(t) = -R^{-1}\mathbf{B}_z^T\mathbf{P}\mathbf{z}(t) = -\mathbf{K}\mathbf{z}(t) = -\mathbf{K}_1\dot{\mathbf{x}}(t) - \mathbf{K}_2\mathbf{D}\mathbf{x}(t) \ .$$

Integrating the above equation yields the optimal PI control law

$$u^*(t) = -\mathbf{K}_1\mathbf{x}(t) - \mathbf{K}_2\int_0^t \mathbf{D}\mathbf{x}(\eta)d\eta$$

For more details on the properties of the above approach, the interested reader should consult (Anderson and Moore, 1990) and (Dorato et al., 2000).

Following the approach of Ruggiero et al. (2004c), and for the particular problem under study, the penalty state matrix is chosen as

$$\mathbf{Q} = \begin{bmatrix} \mathbf{Q}_1 & 0_{N\times N} \\ 0_{N\times N} & \mathbf{Q}_2 \end{bmatrix} ,$$

$$\mathbf{Q}_1 = \left[\int_0^L q_2(x)\Big(EI(x)\phi_i''(x)\phi_j''(x) + \tau\phi_i'(x)\phi_j'(x)\Big)\mathrm{d}x\right]_{i,j=1,\cdots,N} ,$$

$$\mathbf{Q}_2 = \left[\int_0^L q_2(x)\Big(cI(x)\phi_i''(x)\phi_j''(x) + \gamma\phi_i(x)\phi_j(x)\Big)\mathrm{d}x\right]_{i,j=1,\cdots,N} ,$$

The cost functions $q_1(x)$ and $q_2(x)$ are chosen to be discontinuous, reflecting the physical properties of the structure

$$q_1(x) = \begin{cases} \alpha c_1 & \text{if} \quad x_1 \le x \le x_2 \\ c_1 & \text{otherwise} \end{cases} \quad \text{and} \quad q_2(x) = \begin{cases} \beta c_2 & \text{if} \quad x_1 \le x \le x_2 \\ c_2 & \text{otherwise} \end{cases} , \tag{3.4}$$

where α, β, c_1 and c_2 are positive real numbers. Basically, higher penalty is placed on the span of the structure where the actuator is placed.

3.1.1 Closed Loop Simulation

The controller presented in Section 3.1 is simulated for the structure presented in Table 2.1. Two tension values are considered to demonstrate the effectiveness of the controller. These, along with the corresponding controller's parameters are shown in Table 3.1.

Table 3.1: Controller Parameters

Parameter	**Case I** $\tau = 13.5$ N	**Case II** $\tau = 7.5$ N
α	10^2	10^2
β	10^2	10^2
c_1	10^4	10^2
c_2	10^4	10^2
R	0.5	1

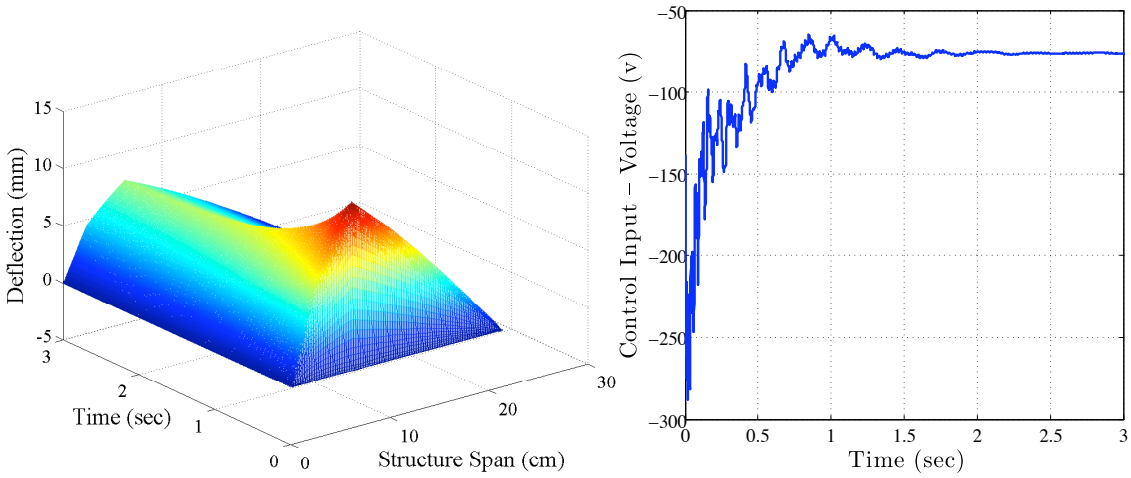

(a) Time history of strip's deformation.

(b) Time history of control effort.

Figure 3.1: Closed loop simulation of Case I – Single piezoceramic bimroph.

Figure 3.1a and Fig. 3.1b show the time history of the deformation and the control effort for Case I. The structure settles to the desired first mode shape in about 1.2 seconds. The steady state control voltage is -175 v in order to keep the structure at the desired reference.

For Case II, the structure was placed at a lower tension value, 7.5 N. Figure 3.2a and

Fig. 3.2b show the time history of the structure's deformation and the control effort. The steady state control voltage is -85 v. The difference between the steady state voltage of Case I and that of Case II can be explained by examining the model presented in Section 2.1. Case I has a higher tension than Case II. In Eq. (2.14), the tension increases the stiffness of the structure. The steady state voltage produced by the control law intends to balance the restoring force of the structure. As the restoring force increases, i.e., as the stiffness increases, the steady state voltage must increase.

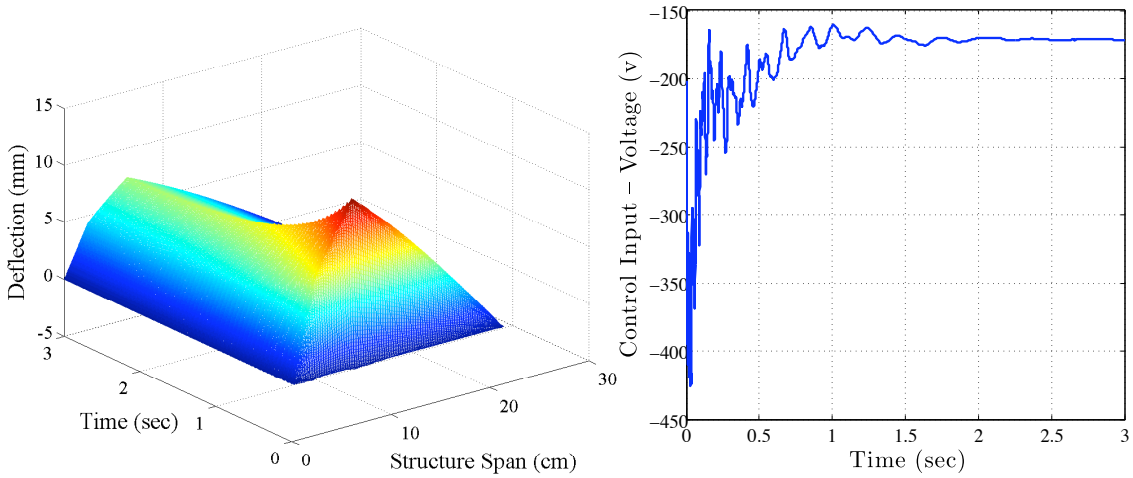

(a) Time history of strip's deformation.

(b) Time history of control effort.

Figure 3.2: Close loop simulation of Case II – Single piezoceramic bimroph

3.2 Control Law Development for Configuration II

Now, the control of the membrane strip augmented with two MFC bimorphs acting in Configuration II (one bimorph acts in bending and the other acts in tension) is considered. The model derived in Section 2.4 is nonlinear in nature, although it was experimentally validated in its quasilinear state. As the system is nonlinear, the sliding mode is the control technique of choice.

The sliding mode technique is a variable structure control technique where the dynamics of a nonlinear system is altered via application of a high-frequency switching control, (Utkin, 1992; Khalil, 2000). It is a popular approach that enables a robust con-

trol system in the presence of system uncertainties. In the following, two main control problems will be treated: (i) regulation and (ii) reference tracking. For the regulation problem, it is desired to maintain the membrane strip at its undeformed configuration after being disturbed. On the other hand, when dealing with structures, it is more appropriate to refer to reference tracking as shape control. The treatment of the shape control problem enables coupling the system at hand with an adaptive optics scheme.

3.2.1 System Uncertainties

The system expressed by Eq. (2.28) has been verified experimentally, albeit in its quasilinear form. Standard membrane mirror materials (*e.g.* Kapton and Maylar) are viscoelastic. Figure 3.3 shows the stress strain behavior of a Kapton strip. The strip has the same dimensions as the strip tested in Section 2.5. An Instron® machine (model no. 4204) was used to perform this test. The numerical bounds on the modulus of elasticity are obtained by calculating the maximum slope attained by the stress-strain curve of Fig. 3.3.

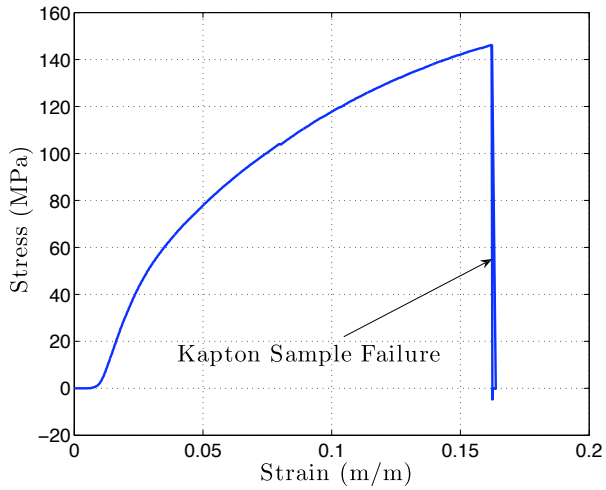

Figure 3.3: Stress-Strain curve of Kapton sample.

Moreover, it is always difficult to fully evaluate structural damping and air damping. In the following, the *over hat* indicates the maximum value that can be attained by the symbol underneath it. We assume that the membrane strip modulus of elasticity and

strain damping coefficient are such that,

$$E \leq \hat{E} \quad \text{and} \quad c_m \leq \hat{c}_m \,.$$

For the MFC patches, the bounds on the modulus of elasticity and the strain damping coefficient are

$$E_k \leq \hat{E}_k \quad \text{and} \quad c_k \leq \hat{c}_k \quad \text{where} \quad k = 1,2 \,.$$

Additionally, the air damping coefficient can be bounded,

$$\gamma \leq \hat{\gamma} \,.$$

3.2.2 Controller Development

In this section, we derive the sliding mode controller. We outline the procedure without details. For details about the control design, the reader is referred to Khalil (2000). The input voltage to the AMFC, $V_2(t)$, depends on time only, and hence can be pulled out of the integral. To this end, let

$$\mathbf{K}_1 = \left[\int_0^L (EI(x)\phi_i''(x)\phi_j''(x) + \bar{\tau}\phi_i'(x)\phi_j'(x))\mathrm{d}x \right]_{(i,j=1,\cdots,N)} ,$$

$$\mathbf{K}_2 = 2\kappa_A \left[\int_0^L S_{3,4}(x)\chi_2(x)\phi_i'(x)\phi_j'(x)\mathrm{d}x \right]_{(i,j=1,\cdots,N)} . \tag{3.5}$$

Hence, the equations of motion become

$$\begin{Bmatrix} \dot{\bar{\mathbf{w}}} \\ \dot{\bar{\mathbf{v}}} \end{Bmatrix} = \begin{bmatrix} \mathbf{0}_{N\times N} & \mathbf{I}_{N\times N} \\ -\mathbf{M}^{-1}\mathbf{K}_1 & -\mathbf{M}^{-1}\mathbf{C} \end{bmatrix} \begin{Bmatrix} \bar{\mathbf{w}} \\ \bar{\mathbf{v}} \end{Bmatrix} + \begin{Bmatrix} \mathbf{0}_{N\times 1} \\ -\mathbf{M}^{-1}\mathbf{K}_2\bar{\mathbf{w}} \end{Bmatrix} V_2(t) + \begin{Bmatrix} \mathbf{0}_{N\times 1} \\ \mathbf{M}^{-1}\mathbf{B}_1 \end{Bmatrix} V_1(t) \,, \tag{3.6}$$

which can be rearranged into a more standard form as

$$\begin{Bmatrix} \dot{\bar{\mathbf{w}}} \\ \dot{\bar{\mathbf{v}}} \end{Bmatrix} = \begin{bmatrix} \mathbf{0}_{N\times N} & \mathbf{I}_{N\times N} \\ -\mathbf{M}^{-1}\mathbf{K}_1 & -\mathbf{M}^{-1}\mathbf{C} \end{bmatrix} \begin{Bmatrix} \bar{\mathbf{w}} \\ \bar{\mathbf{v}} \end{Bmatrix} + \begin{bmatrix} \mathbf{0}_{N\times 1} & \mathbf{0}_{N\times 1} \\ \mathbf{M}^{-1}\mathbf{B}_1 & -\mathbf{M}^{-1}\mathbf{K}_2\bar{\mathbf{w}} \end{bmatrix} \begin{Bmatrix} V_1(t) \\ V_2(t) \end{Bmatrix} . \tag{3.7}$$

Equation (3.7) can be cast into the the standard form for applying the sliding mode control by defining new variables,

$$\eta = \bar{\mathbf{w}} \qquad \text{and} \qquad \xi = \bar{\mathbf{v}} \,.$$

Then, the equations can be written as

$$\begin{aligned} \dot{\eta} &= \xi \,, \\ \dot{\xi} &= f_a(\eta,\xi) + \mathbf{G}_a(\eta,\xi)u + \delta_\xi(\eta,\xi) \,, \end{aligned} \tag{3.8}$$

where

$$\begin{aligned} f_a(\eta,\xi) &= -\mathbf{M}^{-1}\bar{\mathbf{K}}_1\eta - \mathbf{M}^{-1}\bar{\mathbf{C}}\xi \,, \\ \mathbf{G}_a(\eta,\xi) &= \begin{bmatrix} \mathbf{M}^{-1}\mathbf{B}_1 & -\mathbf{M}^{-1}\mathbf{K}_2\eta \end{bmatrix} \,, \\ \delta_\xi(\eta,\xi,u) &= \mathbf{M}^{-1}[(\bar{\mathbf{K}}_1 - \mathbf{K}_1)\eta + (\bar{\mathbf{C}} - \mathbf{C})\xi] \,, \\ \mathbf{u} &= \begin{bmatrix} V_1(t) & V_2(t) \end{bmatrix}^T \,. \end{aligned} \tag{3.9}$$

Here, $\bar{\mathbf{K}}_1$ and $\bar{\mathbf{C}}$ are the nominal system matrices. The function $\delta_\xi(\eta,\xi,u)$ is a perturbation term that accounts for the difference between the nominal values and the actual values of the system matrices. Notice that $\mathbf{G}_a(\eta,\xi)$ is not square and that the η dynamics can be stabilized through an appropriate choice of ξ. Let $\xi = \phi(\eta) = -\alpha\eta$ with $\alpha > 0$; a choice that would cause η to decay exponentially. Note here that α is different from α of Eq. (3.4) in Section 3.1. Let $\mathbf{z} = \xi - \phi(\eta)$. Then, Eq. (2.28) can be written in terms of η and $\mathbf{z}$ as,

$$\begin{aligned} \dot{\eta} &= -\alpha\eta \,, \\ \dot{\mathbf{z}} &= f_a(\eta,\mathbf{z}) + \mathbf{G}_a(\eta,\mathbf{z})\mathbf{u} + \delta_\xi(\eta,\mathbf{z},\mathbf{u}) - \frac{\partial\phi}{\partial\eta}(\mathbf{z} + \phi(\eta)) \,. \end{aligned} \tag{3.10}$$

Define the control input to be,

$$\mathbf{u} = \mathbf{u}_{eq} + \mathbf{G}_a^+(\eta,\mathbf{z})\mathbf{v} \,, \tag{3.11}$$

where $\mathbf{v}$ is a new control input and $\mathbf{u}_{eq}$ is the control input necessary to cancel the nominal dynamics of the system,

$$\mathbf{u}_{eq} = \mathbf{G}_a^+(\eta,\mathbf{z})[-\mathbf{f}_a(\eta,\mathbf{z}) + \frac{\partial\phi}{\partial\eta}(\mathbf{z} + \phi(\eta))] \,.$$

Here, $\mathbf{G}_a^+(\eta,\mathbf{z})$ is the pseudo inverse of $\mathbf{G}_a(\eta,\mathbf{z})$, given as

$$\mathbf{G}_a^+(\eta,\mathbf{z}) = [\mathbf{G}_a^T(\eta,\mathbf{z})\mathbf{G}_a(\eta,\mathbf{z})]^{-1}\mathbf{G}_a(\eta,\mathbf{z})\,. \tag{3.12}$$

The dynamics are then described as,

$$\begin{aligned}\dot{\eta} &= -\alpha\eta\,,\\ \dot{\mathbf{z}} &= \mathbf{v} + \delta_\xi(\eta,\mathbf{z},\mathbf{u})\,.\end{aligned} \tag{3.13}$$

The perturbation term $\delta_\xi(\eta,\mathbf{z},\mathbf{u})$ can be bounded since $\mathbf{K}_1$ and $\mathbf{C}$ are bounded matrices. The nominal values of the stiffness and damping matrices are given by

$$\begin{aligned}\bar{\mathbf{K}}_1 &= \left[\int_0^L \left(\overline{EI}(x)\phi_i''(x)\phi_j''(x) + \bar{\tau}\phi_i'(x)\phi_j'(x)\right)\mathrm{d}x\right]_{(i,j=1,\cdots,N)}\,,\\ \bar{\mathbf{C}} &= \left[\int_0^L \left(\overline{cI}(x)\phi_i''(x)\phi_j''(x) + \bar{\gamma}\phi_i(x)\phi_j(x)\right)\mathrm{d}x\right]_{(i,j=1,\cdots,N)}\,,\end{aligned} \tag{3.14}$$

where $\overline{EI}$, $\overline{cI}$ and $\bar{\gamma}$ are the nominal values of the flexural rigidity, internal damping, and air damping respectively. Substituting the proposed value of the control input in the perturbed term and expanding yields,

$$\delta_\xi(\eta,\xi) = \mathbf{M}^{-1}[(\bar{\mathbf{K}}_1 - \mathbf{K}_1)\eta + (\bar{\mathbf{C}} - \mathbf{C})\xi]\,. \tag{3.15}$$

When evaluating the norm of $\delta_\xi(\eta,\mathbf{z})$, one can use the triangular inequality to obtain,

$$||\delta_\xi(\eta,\xi)|| \leq ||\mathbf{M}^{-1}\bar{\mathbf{K}}_1\eta|| + ||\mathbf{M}^{-1}\mathbf{K}_1\eta|| + ||\mathbf{M}^{-1}\bar{\mathbf{C}}\xi|| + ||\mathbf{M}^{-1}\mathbf{C}\xi||\,.$$

Recall that $||Ax|| \leq ||A||_i||x||$, where $||.||_i$ is the induced matrix norm on $\mathbb{R}^{N\times N}$ (*e.g.* Vidyasagar, 1993), hence

$$\begin{aligned}||\delta_\xi(\eta,\mathbf{z})|| &\leq ||\mathbf{M}^{-1}\bar{\mathbf{K}}_1||_i||\eta|| + ||\mathbf{M}^{-1}\mathbf{K}_1||_i||\eta|| + ||\mathbf{M}^{-1}\bar{\mathbf{C}}||_i||\mathbf{z}|| + ||\mathbf{M}^{-1}\mathbf{C}||_i||\mathbf{z}||\,,\\ &\leq \left(\frac{EI(x)+\max[EI(x)]}{\rho(x)}\right)||\eta|| + \left(\frac{cI(x)+\gamma+\max[cI(x)+\gamma]}{\rho(x)}\right)||\mathbf{z}||\,.\end{aligned} \tag{3.16}$$

To this end, define the function $\psi(\eta,\mathbf{z})$ as,

$$\psi(\eta,\xi) = \left(\frac{EI(x)+\max[EI(x)]}{\rho(x)}\right)||\eta|| + \left(\frac{cI(x)+\gamma+\max[cI(x)+\gamma]}{\rho(x)}\right)||\xi-\phi(\eta)||\,, \tag{3.17}$$

which bounds the perturbed term: $||\delta_\xi(\eta,\xi)|| \leq \psi(\eta,\xi)$. Moreover, recall that $\rho(x)$ is the linear density of the structure. As mentioned earlier, the linear density is not uniform throughout the structure. It attains a maximum value at the location of the actuators, and drops to that of the membrane strip elsewhere. Hence, define the function $\beta(\eta,\mathbf{z})$ to be

$$\beta(\eta,\xi) = \Big(\frac{\overline{EI}(x)+\max[EI(x)]}{\min[\rho(x)]}\Big)||\eta|| + \Big(\frac{\overline{cI}(x)+\bar{\gamma}+\max[cI(x)+\gamma]}{\min[\rho(x)]}\Big)||\xi-\phi(\eta)|| + p\ , \tag{3.18}$$

where $p \in \mathbb{R}^+$. Note that the function $\beta(\eta,\mathbf{z})$ is non-negative. Moreover, notice that

$$\max_{x\in[0,L]}(\beta(\eta,\xi)-\psi(\eta,\xi)) \geq p\ . \tag{3.19}$$

A proper choice of the new control input $\mathbf{v}$ would then be, (Khalil, 2000),

$$\mathbf{v} = -\beta(\eta,\mathbf{z})\text{sat}(\mathbf{z}) = -\beta(\eta,\mathbf{z})\begin{Bmatrix} \text{sat}(z_1) \\ \vdots \\ \text{sat}(z_N) \end{Bmatrix}\ , \tag{3.20}$$

where the saturation function is defined as,

$$\text{sat}(x) = \begin{cases} \dfrac{x}{\epsilon} & \text{if } \left|\dfrac{x}{\epsilon}\right| \leq 1 \\ \text{sign}\left(\dfrac{x}{\epsilon}\right) & \text{if } \left|\dfrac{x}{\epsilon}\right| > 1 \end{cases} \quad \text{where} \quad \epsilon > 0\ . \tag{3.21}$$

Note that as $\epsilon \to 0$ the *sat* function approaches the *sign* function. The use of the *sat* function enables the control effort to smoothly approach zero. Hence, the control input becomes,

$$\mathbf{u} = \mathbf{G}_a^+(\eta,\xi)[-\mathbf{f}_a(\eta,\xi) + \frac{\partial\phi}{\partial\eta}\xi - \beta(\eta,\xi)\text{sat}(\xi-\phi(\eta))]\ .$$

In terms of the original coordinates, this control law is given as

$$\mathbf{u} = \mathbf{G}_a^+(\bar{\mathbf{w}},\bar{\mathbf{v}})[-\mathbf{f}_a(\bar{\mathbf{w}},\bar{\mathbf{v}}) + \frac{\partial\phi}{\partial\bar{\mathbf{w}}}\bar{\mathbf{v}} - \beta(\bar{\mathbf{w}},\bar{\mathbf{v}})\text{sat}(\bar{\mathbf{v}}-\phi(\bar{\mathbf{w}}))]\ . \tag{3.22}$$

In the following section, the stability of the closed loop system is verified via Laypunov method.

3.2.3 Stability Proof

The following Lyapunov function candidate for the $\mathbf{z}$ subsystem is the standard quadratic function,

$$\mathscr{V}(\mathbf{z}) = \frac{1}{2}\mathbf{z}^T\mathbf{z} = \sum_{i=1}^{N} \mathscr{V}_i(z_i) \quad \text{where} \quad \mathscr{V}_i(z_i) = \frac{1}{2}z_i^2 \,. \tag{3.23}$$

The time derivative of the candidate Lyapunov function is

$$\dot{\mathscr{V}} = \sum_{i=1}^{N} \dot{\mathscr{V}}_i = \sum_{i=1}^{N} z_i \dot{z}_i = \sum_{i=1}^{N} z_i (v_i + (\delta_\xi)_i) \,. \tag{3.24}$$

However, for a single term of Eq. (3.24), we can state the following

$$\dot{\mathscr{V}}_i = \frac{\mathrm{d}}{\mathrm{d}t}\left(\frac{1}{2}z_i^2\right) \leq z_i\big(-\beta(\eta,\xi)\mathrm{sat}(z_i)\big) + |z_i|\psi(\eta,\xi) \,. \tag{3.25}$$

Here, two cases arise, depending on the value of $|z_i|$ relative to ϵ, Eq. (3.21),

a) If $|z_i| \leq \epsilon$, then

$$\begin{aligned} \dot{\mathscr{V}}_i &\leq z_i\big(-\beta(\eta,\xi)\mathrm{sat}(z_i)\big) + |z_i|\psi(\eta,\xi) \leq -\beta(\eta,\xi)\frac{|z_i|^2}{\epsilon} + |z_i|\psi(\eta,\xi) \,, \\ &\leq -\epsilon\beta(\eta,\xi) + \epsilon\psi(\eta,\xi) \leq -\epsilon p \,. \end{aligned} \tag{3.26}$$

Now, if $z_i = 0$, then the system does not leave the origin $\mathbf{z} = \mathbf{0}$ since $\mathscr{V}(\mathbf{z})$ is non-decreasing. Otherwise, one can divide both sides of Eq. (3.26) by $|z_i|$, resulting in

$$\frac{\mathrm{d}}{\mathrm{d}t}|z_i| \leq -\frac{\epsilon}{|z_i|}p \leq -p \,, \tag{3.27}$$

which means that $|z_i| \leq -pt + |z_i(0)|$.

b) Now, if $|z_i| \geq \epsilon$, then

$$\dot{\mathscr{V}}_i \leq z_i\big(-\beta(\eta,\xi)\mathrm{sign}(z_i)\big) + |z_i|\psi(\eta,\xi) \leq -|z_i|(\beta(\eta,\xi) - \psi(\eta,\xi)) \leq -p|z_i| \,. \tag{3.28}$$

The above inequality can be analyzed in a similar fashion. If $z_i = 0$, then the system will not leave the origin $\mathbf{z} = \mathbf{0}$. Otherwise, one has to solve for the following comparison differential equation,

$$\frac{\mathrm{d}}{\mathrm{d}t}|z_i| \leq -\frac{\epsilon}{|z_i|}p \leq -p \,. \tag{3.29}$$

which again yields that $|z_i| \leq -pt + |z_i(0)|$.

In both cases ($|z_i| \leq \epsilon$ or $|z_i| \geq \epsilon$), $z_i(t)$ converges to zero in a finite time $t = |z_i(0)|/p$. Consequently, the state $\mathbf{z}$ converges to zero in finite time, and remains at zero for future time. Once $\mathbf{z} = \mathbf{0}$, the dynamics of Eq. (3.8) reduce to

$$\dot{\eta} = \xi \quad \text{and} \quad \dot{\xi} = \phi(\eta)\,, \tag{3.30}$$

which is an asymptotically stable system at the equilibrium point (origin) by our previous choice of $\phi(\eta)$.

3.2.4 System Singularities

Examining Eq. (3.9) shows that the matrix $\mathbf{G}_a(\bar{\mathbf{w}}, \bar{\mathbf{v}})$ is a function of the deflection $\bar{\mathbf{w}}$. A singularity occurs when $\bar{\mathbf{w}} = 0$, since the second column of $\mathbf{G}_a(\bar{\mathbf{w}}, \bar{\mathbf{v}})$ will vanish, and hence $\mathbf{G}_a^{+}(\bar{\mathbf{w}}, \bar{\mathbf{v}})$ is not defined any more. Hence, this singularity is due to the TBM actuator. To alleviate this problem, a switching control algorithm is proposed. The idea is,

$$\mathbf{G}_a(\bar{\mathbf{w}}, \bar{\mathbf{v}}) = \begin{cases} \begin{bmatrix} \mathbf{M}^{-1}\mathbf{B}_1 & -\mathbf{M}^{-1}\mathbf{K}_2\bar{\mathbf{w}} \end{bmatrix} & \text{if } \mu[\mathbf{G}_a^T(\bar{\mathbf{w}}, \bar{\mathbf{v}})\mathbf{G}_a(\bar{\mathbf{w}}, \bar{\mathbf{v}})] < 10^{10}\epsilon_0 \\ \mathbf{M}^{-1}\mathbf{B}_1 & \text{otherwise} \end{cases}, \tag{3.31}$$

where $\mu(\mathbf{A})$ is the reciprocal condition estimator of $\mathbf{A} \in \mathbb{R}^{N \times N}$ and ϵ_0 is the distance from 1.0 to the next larger double precision number, (Anderson et al., 1999). In other words, as the membrane strip approaches the original configuration, the effect of the tension induced by the TBM diminishes. Fortunately, this switching command is not merely based on convenience. It is supported by the dynamics of the system that is observed intuitively. In fact, if the strip is undeformed, the TBM would not have any effect on the transverse motion of the membrane strip. Mathematically, this event coincides with the failure to calculate the pseudo inverse of $\mathbf{G}_a(\bar{\mathbf{w}}, \bar{\mathbf{v}})$.

As the switching between control algorithms is deployed, the system becomes a hybrid (continuous in time, discrete regarding the switching signal) switching system. Switching can destabilize the system even if the individual subsystems are stable, (Liberzon, 2003). However, in our case, the existence of a common Lyapunov function guarantees stability of the switched system, (Liberzon, 2003).

3.2.5 Shape Control

Recall that this work focuses on a membrane strip as a prelude to studying a circular membrane, Fig. 1.4. The ultimate goal of this research is to be able to correct for optical aberrations of a circular membrane mirror using mechanical actuation via smart materials. To be able to do this, a means to translate an optical aberration into a mechanical presentation must be established. Ruggiero (2005) showed that a mapping exists between the optical and mechanical realms. Optical aberrations are usually expressed in terms of Zernike polynomials. Ruggiero (2005) considered a circular lens. He expanded the Zernike polynomials into the mode shapes and concluded that optical aberrations up to the 5^{th} order can be canceled through deforming the membrane mirror into an appropriate combination of the mode shapes. Extended discussion of Zernike polynomials, image aberrations and correction approaches can be found in (Malacara, 1992) and (Tyson, 2000).

As this work treats a membrane strip augmented with smart actuators, the shape control problem of this structure will be treated herein. Shape control of structures has attracted many researchers. Varadarajan et al. (1998) presented an adaptive control law to perform shape control of laminated composite plates under quasi-statically varying unknown loads. Yang and Ngoi (2000) analytically addressed the control of beams augmented with PZTs. They presented several case studies for different boundary conditions. Chee et al. (2002) used slope as the fine tuning criterion on top of the common displacement-based shape control. They showed that their algorithm smoothes the resultant shape of the structure. Sun and Tong (2003) presented a design optimization of control voltage distribution for constrained static shape control of structures augmented with PZTs. Moreover, Sun and Tong (2005) treated the local shape control problem. Their target was to control the shape of a part of a structure rather than the entire structure while minimizing the energy used to achieve the desired shape. The shape control problem considered in this manuscript treats a structure actuated by two bimorphs, BMFC and TBM. Most of the previously published literature did not include an actuator affecting the tension.

Let the desired shape, *i.e.* the desired transverse deformation, be $\bar{\mathbf{w}}_d = \eta_d$ whereas the desired final velocity be zero. Define the following error variables,

$$\mathbf{e}_1 = \eta - \eta_d \quad \text{and} \quad \mathbf{e}_2 = \xi \,. \tag{3.32}$$

The initial conditions of the new variables are $\mathbf{e}_1(0) = -\eta_d$ and $\mathbf{e}_2(0) = \xi(0) = 0$ since the structure starts from the undeformed static configuration ($\eta(0) = 0$). The error dynamics are given as,

$$\begin{aligned} \dot{\mathbf{e}}_1 &= \mathbf{e}_2 \,, \\ \dot{\mathbf{e}}_2 &= f_a(\mathbf{e}_1, \mathbf{e}_2) + \mathbf{G}_a(\mathbf{e}_1, \mathbf{e}_2)\mathbf{u} + \delta_{e_2}(\mathbf{e}_1, \mathbf{e}_2) \,, \end{aligned} \tag{3.33}$$

where

$$\begin{aligned} f_a(\mathbf{e}_1, \mathbf{e}_2) &= -\mathbf{M}^{-1}\bar{\mathbf{K}}_1(\mathbf{e}_1 + \eta_d) - \mathbf{M}^{-1}\bar{\mathbf{C}}\mathbf{e}_2 \,, \\ \mathbf{G}_a(\mathbf{e}_1, \mathbf{e}_2) &= \begin{bmatrix} \mathbf{M}^{-1}\mathbf{B}_1 & -\mathbf{M}^{-1}\mathbf{K}_2(\mathbf{e}_1 + \eta_d) \end{bmatrix} \,, \\ \delta_{e_2}(\mathbf{e}_1, \mathbf{e}_2, \mathbf{u}) &= \mathbf{M}^{-1}[(\bar{\mathbf{K}}_1 - \mathbf{K}_1)(\mathbf{e}_1 + \eta_d) + (\bar{\mathbf{C}} - \mathbf{C})\mathbf{e}_2] \,. \end{aligned}$$

The input vector, $\mathbf{u}$, remains as defined in Eq. (3.9). The same procedure presented for the regulation problem is followed herein. Use the same function $\mathbf{e}_2 = \phi(\mathbf{e}_1) = -\alpha\mathbf{e}_1$ with $\alpha > 0$ to stabilize the $\mathbf{e}_1$ subsystem. Then, introduce $\mathbf{z} = \mathbf{e}_2 - \phi(\mathbf{e}_1)$ and develop the control law through bounding the perturbation term δ_{e_2}. For this case, the bounding function is given by,

$$\begin{aligned} \beta(\mathbf{e}_1, \mathbf{e}_2) = &\Big(\frac{\overline{EI}(x) + \max[EI(x)]}{\min[\rho(x)]}\Big)(\|\mathbf{e}_1\| + \|\eta_d\|) \\ &+ \Big(\frac{\overline{cI}(x) + \bar{\gamma} + \max[cI(x) + \gamma]}{\min[\rho(x)]}\Big)\|\mathbf{e}_2\| \,, \end{aligned} \tag{3.34}$$

and the resulting control input is,

$$\mathbf{u} = \mathbf{G}_a^{+}(\mathbf{e}_1, \mathbf{e}_2)[-f_a(\mathbf{e}_1, \mathbf{e}_2) + \frac{\partial \phi}{\partial \mathbf{e}_1}\mathbf{e}_2 - \beta(\mathbf{e}_1, \mathbf{e}_2)\text{sat}(\mathbf{e}_2 - \phi(\mathbf{e}_2))] \,. \tag{3.35}$$

The convergence of $\mathbf{e}_1$ and $\mathbf{e}_2$ to the origin yields the desired shape of the membrane strip. As in the regulation problem, a quadratic Lyapunov function can be used to prove

asymptotic stability of the closed-loop system. Additionally, the same switching command is implemented for the shape control problem, *i.e.*

$$\mathbf{G}_a(\mathbf{e}_1,\mathbf{e}_2)=\begin{cases}\begin{bmatrix}\mathbf{M}^{-1}\mathbf{B}_1 & -\mathbf{M}^{-1}\mathbf{K}_2(\mathbf{e}_1+\eta_d)\end{bmatrix} & \text{if } \mu[\mathbf{G}_a^T(\mathbf{e}_1,\mathbf{e}_2)\mathbf{G}_a(\mathbf{e}_1,\mathbf{e}_2)]<10^{10}\epsilon_0\\ \mathbf{M}^{-1}\mathbf{B}_1 & \text{otherwise}\end{cases}, \tag{3.36}$$

where $\mu(.)$ and ϵ_0 were defined previously on Page 80.

3.3 Case Study and Simulation

To demonstrate the efficacy of the controller, the structure presented in Section 2.5, is considered. The nominal properties of the specimen at hand are listed in Table 2.4. The bounds on the uncertain physical properties are,

$$\begin{aligned}&E\leq 6\text{GPa}\,,\quad c_m\leq 45\times 10^8\text{Kg/(m s)}\,,\\ &E_A\leq 39\text{GPa}\,,\quad c_m^A\leq 45\times 10^8\text{Kg/(m s)}\,,\\ &\gamma\leq 1\text{Kg/(m s)}\,.\end{aligned} \tag{3.37}$$

The bounding values of the uncertain parameters were obtained through comparison with the experimental results presented in Renno and Inman (2007b). The controller parameters used throughout were,

$$\alpha=30\quad\text{and}\quad\epsilon=10^{-4}\,. \tag{3.38}$$

As presented in Section 3.2, this work considers the regulation and shape control problems. The following subsections present simulation examples for both problems.

3.3.1 Regulation Examples

For the regulation problem, three cases are considered. In each case, the structure is disturbed using a forcing signal applied to the BMFC for an appropriate period of time. Then, the controller is activated to regulate the deformation of the structure.

- Case I: The uniform tension, $\bar{\tau}$, in the structure is set to 5 N. The quasilinear first natural frequency at this uniform tension value is 61 Hz. To excite the structure to the first mode shape, a sinusoidal voltage is applied to the BMFC. The amplitude of the signal is 200 v and the frequency is the first quasilinear natural frequency. This forcing signal is applied for 1.65 seconds. Then, the controller is turned on.

- Case II: For this case, the uniform tension, $\bar{\tau}$, is set to 3 N. The quasilinear second natural frequency at this value of uniform tension is 74 Hz. The structure is excited through the BMFC using a sinusoidal voltage. The amplitude of the forcing sinusoidal signal is 200 v and the frequency is 74 Hz. The forcing signal is applied for 1.35 seconds. Similar to Case I, the controller is activated after this period.

- Case III: This case is considered to further demonstrate the potency of the controller. The uniform tension, $\bar{\tau}$, in the structure is set to 3 N. The first three quasilinear natural frequencies of the structure are 47 Hz, 74 Hz and 174 Hz. Consequently, the forcing signal is the summation of three sinusoidal functions of the noted frequencies and amplitude 200 v. The forcing signal excites the structure for 1.5 seconds, after which the controller is activated. This case poses a challenge to the developed controller to suppress the complicated disturbance signal presented.

Figure 3.4 shows the open loop behavior of the membrane strip for Case I and Case II. The closed loop response is shown in Fig. 3.5. The membrane strip returns back to its original undeformed configuration in a smooth fashion for both Case I and Case II. The control input to the system is displayed in Fig. 3.6.

The results presented show an interesting behavior. It was demonstrated in Renno and Inman (2007b), experimentally as well as theoretically, that positive values of V_2 induce a softening effect in the structure. Positive voltage supplied to the AMFC caused the natural frequencies of the structure to drop to lower values. Conversely, negative voltage values would cause the stiffening of the structure. Notice that to bring back the membrane strip to its undeformed shape it is desired to stiffen the structure. This is exactly what is demonstrated in Fig. 3.6a and Fig. 3.6b. Moreover, as the maximum initial

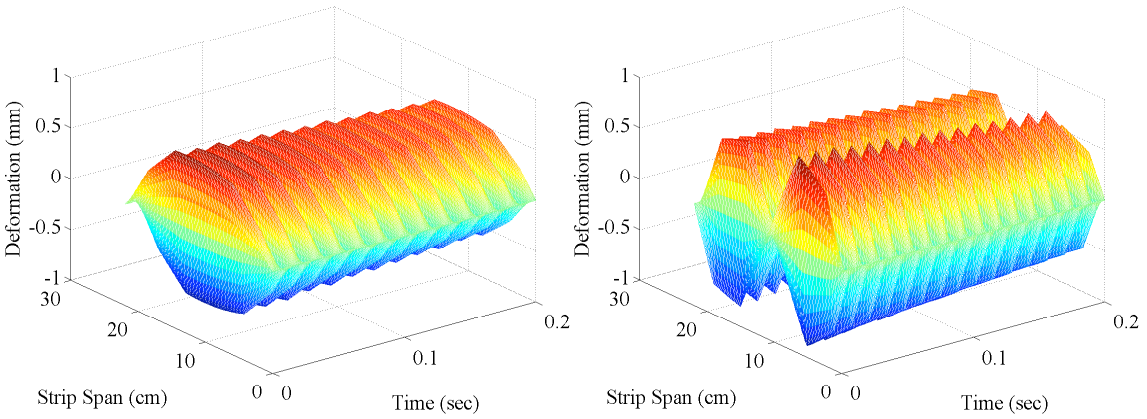

(a) Case I (b) Case II

Figure 3.4: Time History of Deformation – Open Loop Response

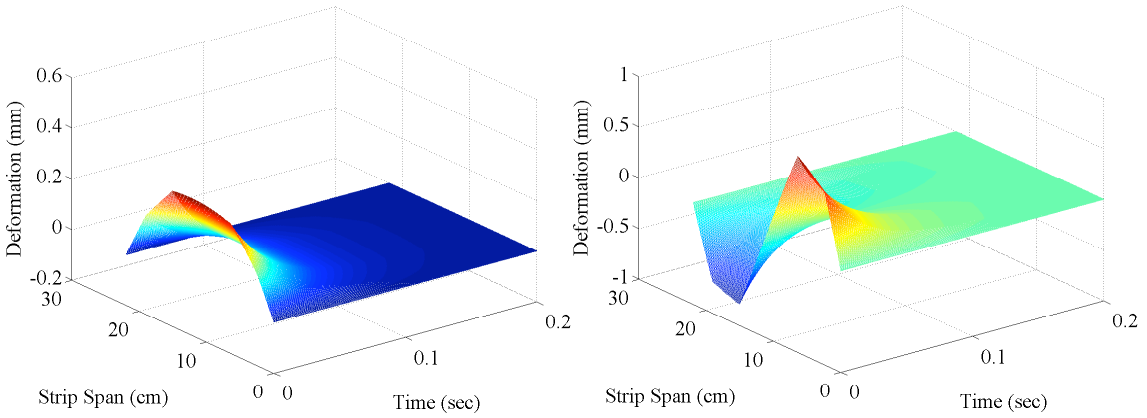

(a) Case I (b) Case II

Figure 3.5: Time History of Deformation – Closed Loop Response

displacement of the structure increased, the value of V_2 grew more negative. Figure 3.4a shows a maximum initial displacement of about 0.3 mm, whereas Fig. 3.4b shows a maximum initial displacement of about 0.5 mm. Recall that both Case I and Case II use the same amplitude for the open loop excitation. Case I targets the first mode shape whereas Case II targets the second mode shape. Moreover, Fig. 2.25a and Fig. 2.25b clearly indicate that the deformation amplitude is higher at the second natural frequency. However, the uniform tension in Case II is 3N which causes less stiffness in the structure and hence the higher amplitude observed in Fig. 3.4b.

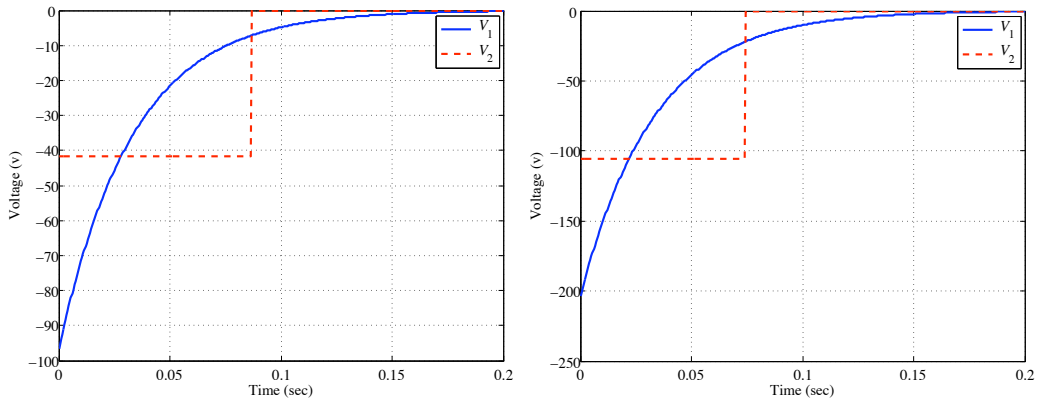

(a) Case I (b) Case II

Figure 3.6: Time History of Control Input – Case I and Case II

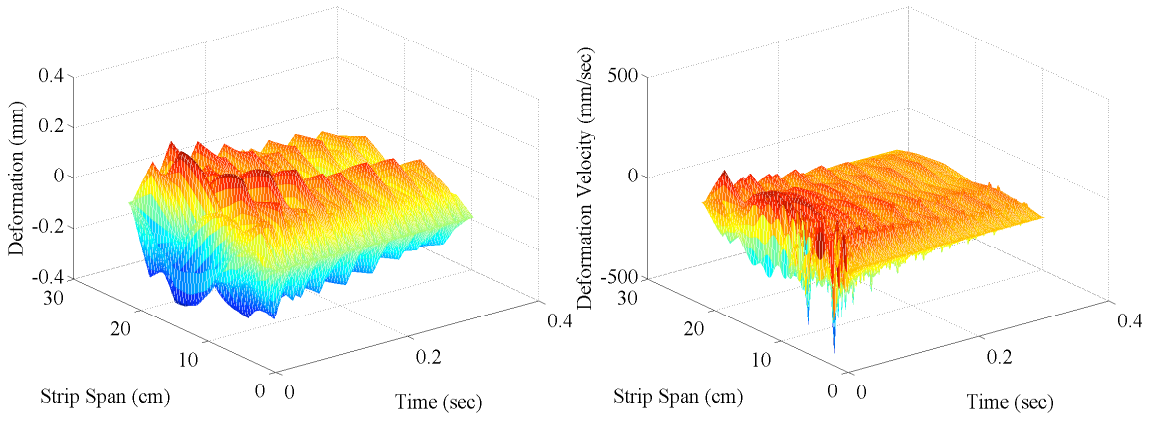

(a) Time History of Deformation (b) Time History of Deformation Velocity

Figure 3.7: Open Loop Behavior for Case III

Figure 3.7 shows the open loop behavior of the structure for Case III. Figure 3.7a displays the time history of the structure's deformation whereas Fig. 3.7b displays the time history of the structure's deformation velocity. Again, in this case, the controller is able to suppress the strip's vibration, as shown in Fig. 3.8a. The control effort is displayed in Fig. 3.8b.

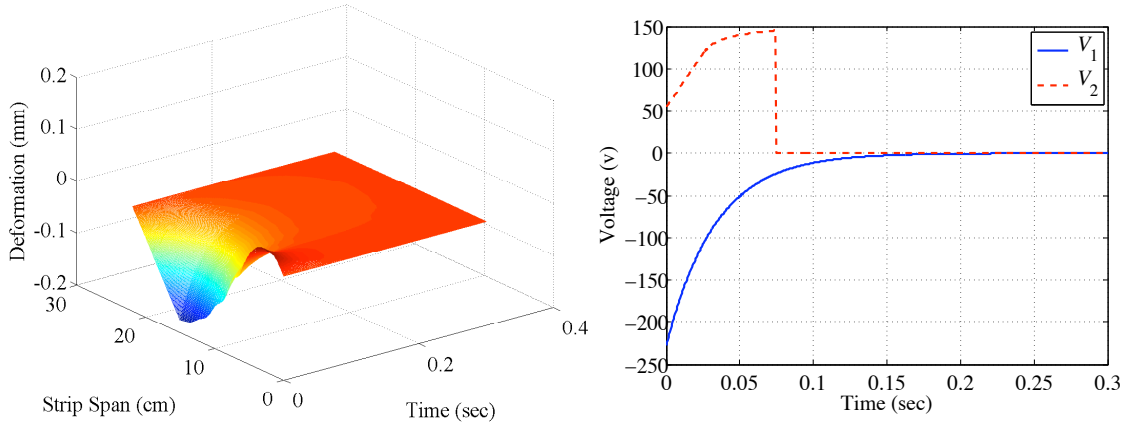

(a) Time History of Deformation

(b) Time History of Control Inputs

Figure 3.8: Closed Loop Behavior for Case III

3.3.2 Shape Control Examples

Now, instead of regulating the configuration of the membrane strip, it is desired to deform the membrane strip to a specified shape and hold it at this configuration. Two cases are presented here:

- Case IV: The uniform tension is set to 5 N. It is desired to deform the membrane strip to its first mode shape.

- Case V: Similar to Case IV, the reference command is the first mode shape, however, the uniform tension is 3 N.

For Case IV, the time history of deformation of the membrane strip and the voltage applied to the BMFC and AMFC are shown in Fig. 3.9a and Fig. 3.9b respectively.

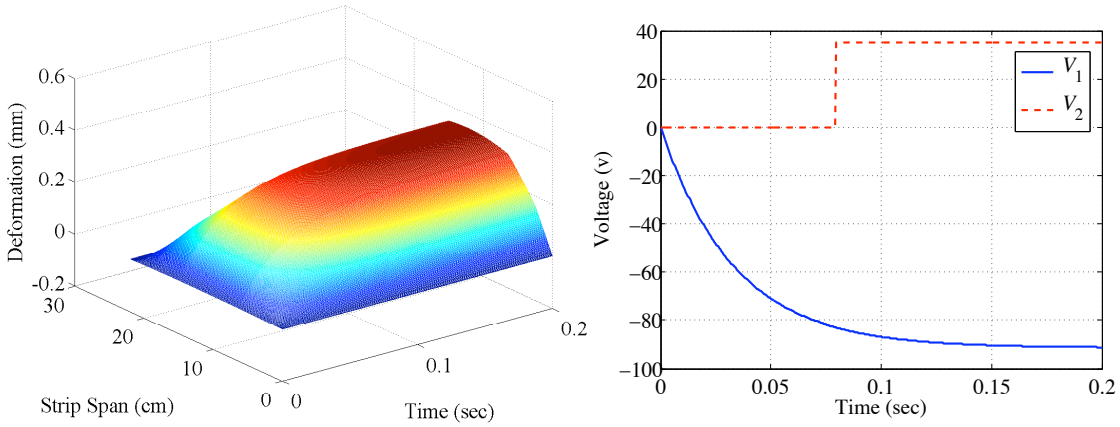

(a) Time History of Deformation

(b) Time History of Control Inputs

Figure 3.9: Closed Loop Behavior of Case IV

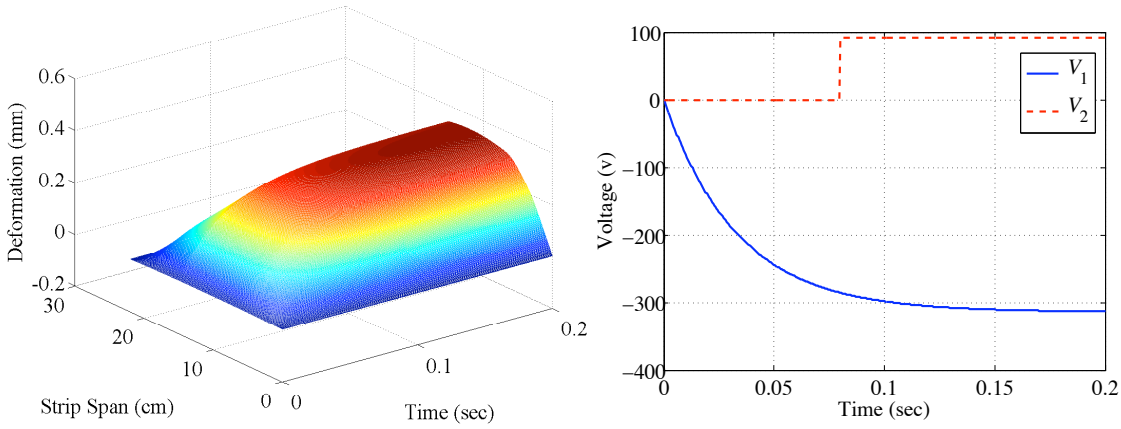

(a) Time History of Deformation

(b) Time History of Control Inputs

Figure 3.10: Closed Loop Behavior of Case V

Figure 3.10a and Fig. 3.10b display the time history of the deformation and the voltage applied to the BMFC and AMFC for Case V.

The results shown in Fig. 3.9 and Fig. 3.10 agree with the regulation examples presented previously. Recall that the purpose of Case IV and Case V is to deform the membrane strip. From elementary vibration, it is desirable to lower the stiffness of the structure in order to facilitate the deformation. This is particularly substantiated in Fig. 3.9b and Fig. 3.10b. The values of V_2, the voltage applied to the AMFC, are positive. According to the results presented in Section 2.5 and in Renno and Inman (2007a), positive values of V_2 induce a softening effect. It is also noticed that the value of V_2 for Case IV is less that the value of V_2 for Case V. This can be explained as follows. The maximum desired deformation in Case IV is 0.34 mm whereas the maximum desired deformation in Case V is 0.37 mm. In order to achieve a larger deformation, a larger steady state voltage value is required at the BMFC. Moreover, a larger softening effect is required, hence the larger value of V_2.

3.3.3 Effect of Tension Actuation

The literature surveyed in Subsection 3.2.5 used actuators acting in bending only. However, this work proposes using actuators in both bending and tension to perform regulation and shape control. To show the benefit of using both actuators, Case III and Case IV are considered again, with BMFC as the only actuator. Hence, in this case,

$$\mathbf{G}_a(\bar{\mathbf{w}}, \bar{\mathbf{v}}) = \mathbf{M}^{-1}\mathbf{B}_1 \ ,$$

and no switching is involved. So, the two cases considered here are,

- Case VI: Case III is simulated again with BMFC used for control only.
- Case VII: Case IV is simulated again with BMFC used for control only.

The control parameters used in the simulations are those of Eq. (3.38). Figure 3.11 displays the closed loop behavior of Case VI. The controller produces a higher voltage to suppress the vibration. Figure 3.11b shows an initial value of V_1 of 308.6 v whereas the

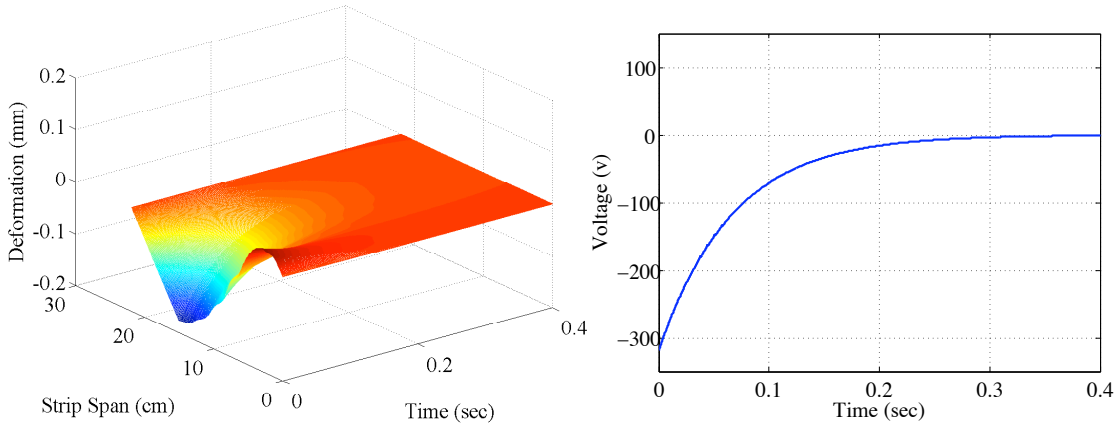

(a) Time History of Deformation

(b) Time History of Control Input – V_I

Figure 3.11: Closed Loop Behavior of Case VI

initial value of V_I is 223.4 v for Case III, see Fig. 3.8b. The closed loop performance is also affected. The structure's deformation decays in 0.32 seconds in Fig. 3.11a; clearly slower than the decay of Case III shown in Fig. 3.8a.

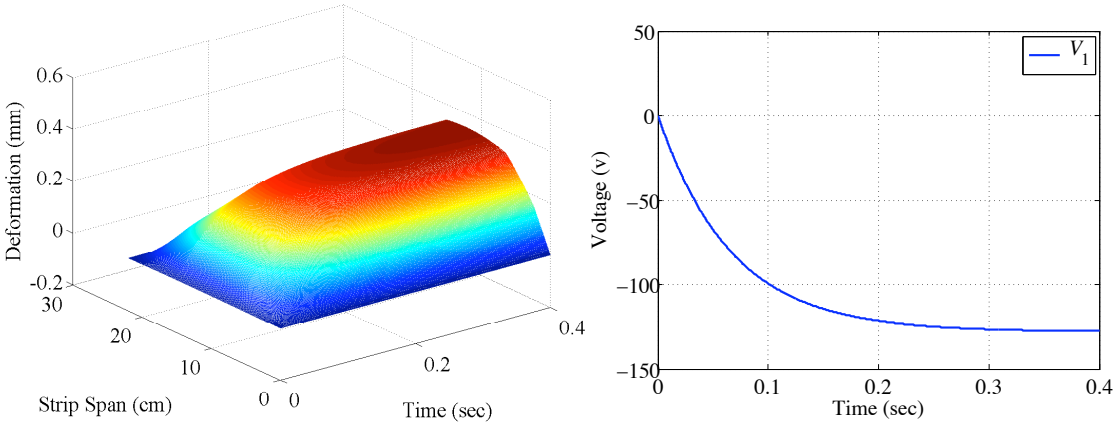

(a) Time History of Deformation

(b) Time History of Control Input – V_I

Figure 3.12: Closed Loop Behavior of Case VI

A similar trend appears in Case VII. The steady state value of V_I in Fig. 3.12b is larger than its counterpart of Case IV in Fig. 3.9b. Besides, it takes a longer time for the structure to reach the desired shape in Fig. 3.12a. It takes about 0.34 seconds for Case VII to reach the steady state, whereas it took 0.175 seconds for Case IV as shown in Fig. 3.9a, to reach steady state. In summary, including the tension actuation through the AMFC

improves the closed loop performance with less control effort at the BMFC. This is to be expected since for Case VI and Case VII, one actuator is used only. Moreover, the stiffness of the structure is independent of the BMFC, hence the higher values observed for V_1.

3.4 Chapter Summary

In this chapter, the static shape control problem is considered for two structures. For the membrane strip augmented with a single piezoelectric bimorph, the shape control problem is formulated as a constant disturbance rejection problem. A PI controller is used to deform the structure to its first mode shape. The PI control gains are obtained using the LQR theory. The closed loop system is simulated with two tension values to show the effectiveness of the control law. For the membrane strip augmented with two MFC bimorphs acting in bending and tension we develop a sliding mode controller for regulation and shape control. In regulation, the deformed equilibrium is stabilized whereas in shape control, a desired shape of the structure is achieved. If carefully designed, the sliding mode technique guarantees the stability of the system in the presence of system uncertainty. Traditionally, a bounding function is used to assure Lyapunov stability. Yet, the presence of the tension bimorph can cause a closed loop instability. Consequently, a switching controller is proposed to avoid instability which coincides with a structural singularity. The existence of a common Lyapunov function guarantees the stability of the switched system. Three regulation examples, and two shape control examples were presented. Examples are also presented to show the advantage of having a tension bimorph. The results clearly show that the controller has excellent stabilization and tracking properties.

CHAPTER 4

MODELING A CIRCULAR MEMBRANE ACTUATED BY SMART BIMORPHS

IN Chapter 2 and Chapter 3, a membrane strip augmented with piezoelectric bimorph actuators was investigated. In particular, Chapter 2 considered the modeling problem of such structure and presented experimental validations of the models developed. On the other hand, Chapter 3 treated the control problem of this structure. An optimal PI controller was derived for the membrane strip augmented with the piezoceramic bimorph. For the membrane strip augmented with two MFC bimorphs acting in bending and tension, a switching sliding mode controller was developed.

All the previous developments were to serve as a prelude for studying a circular membrane augmented with smart actuators located near its boundaries, Fig. 4.1. As the structure considered here is a circular membrane, a brief review of relevant literature is presented first. Smith (1994) used piecewise splines or Legendre polynomials to approximate the dynamics of circular structures in acoustic applications. The method was demonstrated with linear and weakly nonlinear systems. Banks et al. (1995) modeled a circular plate with imperfect boundaries. Approximate techniques relying on cubic B-splines were used to obtain the dynamics of the structure. Heyliger and Ramirez (2000) studied the free vibration of laminated circular piezoelectric plates and discs. Several different approximation functions were used in the radial and circumferential directions depending on the problem considered. Sekouri et al. (2004) presented an analytical approach for modeling a circular plate with distributed piezoelectric actuators under static and dynamic mechanical and electrical loading conditions. Prasad et al. (2006) modeled

a piezoelectric composite circular plate. The piezoelectric unimorphs were modeled as lumped elements of an equivalent electric circuit using conjugate power variables.

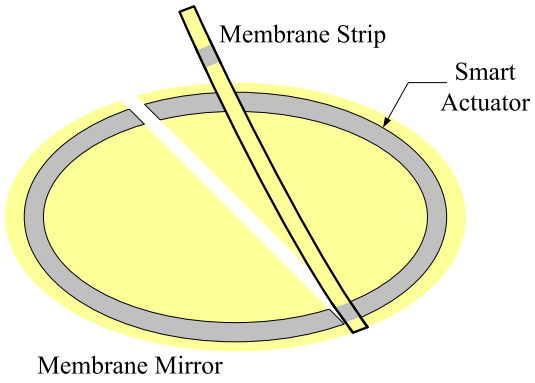

Figure 4.1: Circular membrane strip outfitted with a smart bimorph actuator around its outer rim.

All the above cited work considered plates augmented with smart actuators. However, the structure of interest here is a circular membrane that will be modeled as a plate under tension. The theory of plates is well developed and the interested reader is referred to the work of Alhazza and Alhazza (2004) which presents a comprehensive and thorough review of plate theory. Also, the volume by Ventsel and Krauthammer (2001) is a great resource for the treatment of plates and shells. Magrab (1979) presents detailed examples of plate vibration and dynamics as well.

The modeling of the structure of Fig. 4.1 will be presented in the following sections which are arranged as follows. Section 4.1 presents a derivation of the governing equation of a rectangular plate augmented with piezoelectric bimorphs. Then, the model is transformed into the polar coordinates, and the governing equation of the circular membrane augmented with bimorph actuators is obtained in Section 4.2. In Section 4.3, we develop the weak form of the governing equation, and we obtained the reduced order model of the system. The numerical implementation of the reduced order model is discussed in Section 4.4. Finally, Section 4.5 presents a summary of the chapter.

4.1 Structural Modeling

The structure will be modeled as a plate under tensile load. The *Kirchhoff* model (classical) is adopted here (Ventsel and Krauthammer, 2001). *Kirchhoff* made the following assumptions:

a) The plate is initially flat.

b) The transverse deflection of the mid-surface is small compared to the thickness of the plate. Hence, the slope of the deflected mid-surface is very small, and its square is negligible when compared to unity.

c) The normal straight lines to the mid-surface before deflection remain straight and normal to the mid-surface after the deflection. In other words, the vertical shear strains are negligible.

d) The incompressibility condition holds; i.e., the strain component normal to the mid-surface can be neglected.

e) The stress component normal to the mid-surface is small compared to the in-plane stresses, and hence can be neglected.

f) The displacement of the plate is assumed to be small, and hence the mid-surface remains unstrained after bending.

The dimensions of the membrane considered justify using the *Kirckhhoff* model. Indeed, Ruggiero and Inman (2006d) demonstrated experimentally that the *Kirchhoff* model yields satisfactory results for a rectangular membrane of comparable dimensions to the article used here. It is worth discussing the historic origin of the *Kirchhoff* theory we are using in this work. In 1850, *Gustav Robert Kirchhoff*, a Prussian physicist, resolved some issues that were not treated by *Sophie Germain*, *Simeon-Denis Poisson* and *Claude Louis-Marie Navier* who considered the flat plate problem as early as 1810. Hence, the thin, flat plate theory is referred to as *Kirchhoff* theory of plates. However, in the 1880's, a British mathematician, mechanician, and geophysicist *Augustus Edward Hough Love*,

generalized *Kirchhoff*'s developments to thin shells. Hence, when treating plates and shells, the theory relying on the assumptions presented above is referred to as *Love-Kirchhoff*'s theory. Since the treatment in this dissertation is of plates only, it is fair to refer to the theory used as *Kirchhoff* model. Nevertheless, the author felt that a historic note on the development is needed.

In the following subsections, the structural model will be derived. The idea behind developing the governing equation evolves as follows. To determine the governing equation, one needs to use Newton's second law. To achieve this, the forces and resultants need to be available. However, the internal forces are nothing but the integration of the stress over the volume. The stresses in turn are defined in terms of the strains which are related to the displacements. The following subsections lay out this thought process.

4.1.1 Strain-Displacement Relations

The following lays out the derivation of the equation governing the motion of the structure, heavily borrowed from (Ventsel and Krauthammer, 2001; Banks et al., 1996b; Qatu, 2004). The strain displacement relationship in orthogonal coordinates are given through the linear three dimensional theory of elasticity.
The normal strains are given by,

$$e_i = \frac{\partial}{\partial x_i}\left(\frac{U_i}{\sqrt{g_i}}\right) + \frac{1}{2g_i}\sum_{k=1}^{3}\frac{\partial g_i}{\partial x_k}\frac{U_k}{\sqrt{g_k}} \qquad i = 1,2,3\,, \tag{4.1a}$$

whereas the shear strains are given as,

$$\gamma_{ij} = \frac{1}{\sqrt{g_i g_j}}\left[g_i\frac{\partial}{\partial x_j}\left(\frac{U_i}{\sqrt{g_i}}\right) + g_j\frac{\partial}{\partial x_i}\left(\frac{U_j}{\sqrt{g_j}}\right)\right] \quad i,j = 1,2,3 \quad i \neq j\,. \tag{4.1b}$$

These equations present the strain-displacement equations. The coefficients g_i are a subset of metrics linking the length of a differential element to the differential displacements in the x-, y- and z-directions,

$$\begin{aligned} g_\alpha &= \left[A_\alpha\left(1+\frac{z}{R_\alpha}\right)\right] \quad \alpha = 1,2\,, \\ g_3 &= 1\,. \end{aligned} \tag{4.2}$$

For the theory of plates, the Lamé coefficients resolve to unity, $A_\alpha = 1$. On the other hand, the curvature tends to infinity, $\frac{1}{R_\alpha} = 0$. Hence, the strain displacement relationships become,

$$\begin{aligned} e_x &= \frac{\partial U}{\partial x}\,, & e_y &= \frac{\partial V}{\partial y}\,, & e_z &= \frac{\partial W}{\partial z}\,, \\ \gamma_{xy} &= \frac{\partial U}{\partial y} + \frac{\partial V}{\partial x}\,, & \gamma_{xz} &= \frac{\partial W}{\partial x} + \frac{\partial U}{\partial z}\,, & \gamma_{yz} &= \frac{\partial W}{\partial y} + \frac{\partial V}{\partial z}\,. \end{aligned} \tag{4.3}$$

Not that in the above equation, we replaced U_i for $i = 1,2,3$ by U, V and W respectively. To satisfy the third *Kirchhoff* assumption, the displacement is assumed linear through the thickness. The displacement of any point through the thickness of the structure is assumed to be of the following form,

$$\begin{aligned} U(x,y,z) &= u(x,y) + z\psi_x(x,y)\,, \\ V(x,y,z) &= v(x,y) + z\psi_y(x,y)\,, \\ W(x,y,z) &= w(x,y)\,, \end{aligned} \tag{4.4}$$

where u, v and w are the displacements of the mid-surface. It is worth noting that this assumptions is used within the *Riessner-Mindlin* theory as well. These theories are considered first order theories since the displacements are expressed up to the first order of the plate thickness. Higher order theories assume the in-plane displacements are of the following form,

$$\begin{aligned} U(x,y,z) &= u(x,y) + z\psi_x(x,y) + z^2\lambda_x(x,y) + z^3\mu_x(x,y) + \cdots\,, \\ V(x,y,z) &= v(x,y) + z\psi_y(x,y) + z^2\lambda_y(x,y) + z^3\mu_y(x,y) + \cdots\,, \end{aligned}$$

Additionally, ψ_x and ψ_y represent the rotation of the mid-surface during deformation. Within the *Kirchhoff* theory, the rotations are dependent upon the displacements. As the shear strains, γ_{xz} and γ_{yz}, are assumed to be zero, then

$$\psi_x(x,y) = -\frac{\partial w}{\partial x} \qquad \text{and} \qquad \psi_y(x,y) = -\frac{\partial w}{\partial y}\,. \tag{4.5}$$

Hence, the strain components at any point in the plate can be expressed in terms of the mid-surface strains,

$$e_x = \epsilon_x + z\kappa_x\,,$$

$$e_y = \epsilon_y + z\kappa_y \,,$$
$$\gamma_{xy} = \epsilon_{xy} + z\tau \,, \tag{4.6}$$

where ϵ_x and ϵ_y are the in-plane strain components of the mid-surface, in the $x-$ and $y-$directions respectively. Moreover, κ_x and κ_y correspond to the curvature change of the mid-surface in the $x-$ and $y-$ directions. The shear strain is ϵ_{xy} whereas τ corresponds to the twist of the mid-surface. These quantities are again given in terms of the displacement quantities as,

$$\epsilon_x = \frac{\partial u}{\partial x} \,, \qquad \epsilon_y = \frac{\partial v}{\partial y} \,, \qquad \epsilon_{xy} = \frac{\partial v}{\partial x} + \frac{\partial u}{\partial y} \,,$$
$$\kappa_x = -\frac{\partial^2 w}{\partial x^2} \,, \qquad \kappa_y = -\frac{\partial^2 w}{\partial y^2} \,, \qquad \tau = -2\frac{\partial^2 w}{\partial x \partial y} \,, \tag{4.7}$$

As the strain-displacement relationships are developed now, the next step is to treat the stress-strain relationships.

4.1.2 Constitutive Relations

It is assumed that the membrane and the patches experience the same strain. However, the stress will be different because the modulus of elasticity and Poisson's ratio of the actuator are different from those of the membrane. The in-plane normal stresses are given by,

$$\sigma_x = \begin{cases} \dfrac{E}{1-\nu^2}(e_x + \nu e_y) + \dfrac{c_m}{1-\nu^2}(\dot{e}_x + \nu \dot{e}_y) & \text{for membrane} \\ \dfrac{E_a}{1-\nu_a}(e_x + \nu_a e_y) + \dfrac{c_a}{1-\nu_a}(\dot{e}_x + \nu_a \dot{e}_y) & \text{for actuator} \end{cases} ,$$
$$\sigma_y = \begin{cases} \dfrac{E}{1-\nu^2}(e_y + \nu e_x) + \dfrac{c_m}{1-\nu^2}(\dot{e}_y + \nu \dot{e}_x) & \text{for membrane} \\ \dfrac{E_a}{1-\nu_a}(e_y + \nu_a e_x) + \dfrac{c_a}{1-\nu_a}(\dot{e}_y + \nu_a \dot{e}_x) & \text{for actuator} \end{cases} , \tag{4.8a}$$

and the in-plane shear stress is

$$\sigma_{xy} = \begin{cases} \dfrac{E}{2(1+\nu)}\gamma_{xy} + \dfrac{c_m}{2(1+\nu)}\dot{\gamma}_{xy} & \text{for membrane} \\ \dfrac{E_a}{2(1+\nu_a)}\gamma_{xy} + \dfrac{c_a}{2(1+\nu_a)}\dot{\gamma}_{xy} & \text{for actuator} \end{cases} , \tag{4.8b}$$

These equations are based upon the assumption that the actuator and membrane are perfectly bonded (infinite shear stiffness).

4.1.3 Force Resultants

The force and moment resultants will now be defined in terms of the stresses. In turn, the stresses are defined in terms of the strains, which are in turn defined in terms of the displacements. The force resultants are given as,

$$N_x = \int_h \sigma_x \mathrm{d}z \quad , \quad N_y = \int_h \sigma_y \mathrm{d}z \quad , \quad N_{xy} = \int_h \sigma_{xy} \mathrm{d}z \, . \tag{4.9}$$

The moment results are obtained similarly,

$$M_x = \int_h \sigma_x z \mathrm{d}z \quad , \quad M_y = \int_h \sigma_y z \mathrm{d}z \quad , \quad M_{xy} = \int_h \sigma_{xy} z \mathrm{d}z \, . \tag{4.10}$$

Note that the unit of the force and moment resultants here are force per unit length and moment per unit length. Substituting the stress-strain relations of Eq. (4.8) yields,

$$\begin{aligned} N_x &= \left[\frac{Eh}{1-\nu^2}(\epsilon_x + \nu\epsilon_y) + \frac{c_m h}{1-\nu^2}(\dot{\epsilon}_x + \nu\dot{\epsilon}_y) \right] \\ &+ \left[\frac{2E_a h_a}{1-\nu_a^2}(\epsilon_x + \nu\epsilon_y) + \frac{2c_a h_a}{1-\nu_a^2}(\dot{\epsilon}_x + \nu_a\dot{\epsilon}_y) \right] \chi_a(x,y) \, , \end{aligned} \tag{4.11a}$$

$$\begin{aligned} N_y &= \left[\frac{Eh}{1-\nu^2}(\epsilon_y + \nu\epsilon_x) + \frac{c_m h}{1-\nu^2}(\dot{\epsilon}_y + \nu\dot{\epsilon}_x) \right] \\ &+ \left[\frac{2E_a h_a}{1-\nu_a^2}(\epsilon_y + \nu\epsilon_x) + \frac{2c_a h_a}{1-\nu_a^2}(\dot{\epsilon}_y + \nu_a\dot{\epsilon}_x) \right] \chi_a(x,y) \, , \end{aligned} \tag{4.11b}$$

$$N_{xy} = \left[\frac{Eh}{2(1+\nu)}\epsilon_{xy} + \frac{c_m h}{2(1+\nu)}\dot{\epsilon}_{xy} \right] + \left[\frac{E_a h_a}{2(1+\nu_a)}\epsilon_{xy} + \frac{c_a h_a}{2(1+\nu_a)}\dot{\epsilon}_{xy} \right] \chi_a(x,y) \, , \tag{4.11c}$$

$$\begin{aligned} M_x &= \left[\frac{Eh^3}{12(1-\nu^2)}(\kappa_x + \nu\kappa_y) + \frac{c_m h^3}{12(1-\nu^2)}(\dot{\kappa}_x + \nu\dot{\kappa}_y) \right] \\ &+ \left[\frac{2E_a a_3}{3(1-\nu_a^2)}(\kappa_x + \nu_a\kappa_y) + \frac{2c_a a_3}{3(1-\nu_a^2)}(\dot{\kappa}_x + \nu\dot{\kappa}_y) \right] \chi_a(x,y) \, , \end{aligned} \tag{4.11d}$$

$$\begin{aligned} M_y &= \left[\frac{Eh^3}{12(1-\nu^2)}(\kappa_y + \nu\kappa_x) + \frac{c_m h^3}{12(1-\nu^2)}(\dot{\kappa}_y + \nu\dot{\kappa}_x) \right] \\ &+ \left[\frac{2E_a a_3}{3(1-\nu_a^2)}(\kappa_y + \nu_a\kappa_x) + \frac{2c_a a_3}{3(1-\nu_a^2)}(\dot{\kappa}_y + \nu\dot{\kappa}_x) \right] \chi_a(x,y) \, , \end{aligned} \tag{4.11e}$$

$$M_{xy} = \left[\frac{Eh^3}{24(1+\nu)}\tau + \frac{c_m h^3}{24(1+\nu)}\dot{\tau} \right] + \left[\frac{E_a a_3}{3(1+\nu_a)}\tau + \frac{c_a a_3}{3(1+\nu)}\dot{\tau} \right] \chi_a(x,y) \, . \tag{4.11f}$$

Equation (4.11) shows the force/moment resultants with one actuator attached to the membrane. It should be modified in the case of having multiple actuators.

4.1.4 Governing Equation

Now, if one carries the force balance on the level of a differential element. The force balance yields,

$$\rho(x,y)\frac{\partial^2 u}{\partial t^2} = \frac{\partial N_x}{\partial x} + \frac{\partial N_{yx}}{\partial y} + \hat{F}_x \,, \tag{4.12a}$$

$$\rho(x,y)\frac{\partial^2 v}{\partial t^2} = \frac{\partial N_y}{\partial y} + \frac{\partial N_{xy}}{\partial x} + \hat{F}_y \,, \tag{4.12b}$$

$$\rho(x,y)\frac{\partial^2 w}{\partial t^2} = \frac{\partial Q_x}{\partial x} + \frac{\partial Q_y}{\partial y} + \hat{F}_z \,, \tag{4.12c}$$

and the moments balance give,

$$\frac{\partial M_x}{\partial x} + \frac{\partial M_{yx}}{\partial y} - Q_x + \hat{M}_y = 0 \,, \tag{4.12d}$$

$$\frac{\partial M_y}{\partial y} + \frac{\partial M_{xy}}{\partial x} - Q_y + \hat{M}_x = 0 \,, \tag{4.12e}$$

The quantities $\hat{F}_x$, $\hat{F}_y$, $\hat{F}_z$, $\hat{M}_y$ and $\hat{M}_x$ are external forces/moments applied on the structure. In the *Kirchhoff* theory, Q_x and Q_y can be eliminated and the resulting equation that governs the transverse motion of the plate will be,

$$\begin{aligned}\rho_h(x,y)\frac{\partial^2 w}{\partial t^2} - \frac{\partial^2 M_x(x,y,t)}{\partial x^2} - 2\frac{\partial^2 M_{xy}(x,y,t)}{\partial x \partial y} - \frac{\partial^2 M_y(x,y,t)}{\partial y^2} \\ = -\frac{\partial^2 [M_x(x,y,t)]_a}{\partial x^2} - \frac{\partial^2 [M_y(x,y,t)]_a}{\partial y^2} \,.\end{aligned} \tag{4.13}$$

The quantity $[M_x(x,y,t)]_a$ and $[M_y(x,y,t)]_a$ are the moment resultants induced by the actuators in the x- and y- directions. Notice that Eq. (4.13) does not account for the tension within the membrane and the air damping. These can be added in a similar fashion for Eq. (2.3) on Page 32,

$$\begin{aligned}&\rho_h(x,y)\frac{\partial^2 w}{\partial t^2} - \frac{\partial^2 M_x(x,y,t)}{\partial x^2} - 2\frac{\partial^2 M_{xy}(x,y,t)}{\partial x \partial y} - \frac{\partial^2 M_y(x,y,t)}{\partial y^2} - \frac{\partial}{\partial x}\left(\alpha\frac{\partial w}{\partial x}\right) \\ &-\frac{\partial}{\partial y}\left(\beta\frac{\partial w}{\partial y}\right) + \gamma\frac{\partial w}{\partial t} = -\frac{\partial^2 [M_x(x,y,t)]_a}{\partial x^2} - \frac{\partial^2 [M_y(x,y,t)]_a}{\partial y^2} \,,\end{aligned} \tag{4.14}$$

where α and β are the axial loads in the x- and y- directions. As mentioned earlier, the above developments are heavily borrowed from the work of Ventsel and Krauthammer (2001) and the work of Qatu (2004).

4.2 Governing Equation in Polar Coordinate

The derivation presented in Subsection 4.1.4 was for a rectangular membrane augmented with one smart bimorph. However, membrane mirrors are usually circular. Moreover, the idea proposed in this dissertation is to model a structure like the one shown in Fig. 4.1. Notice that in Fig. 4.1 the smart actuator is monolithic. However, having one actuator is not practical. Hence, a more practical configuration is shown in Fig. 4.2. The circular membrane is augmented with m diametrically-symmetric bimorph actuators. With this configuration, every bimorph can be independently controlled. Moreover, and similar to the approach of Section 2.4, some of the actuators will act in bending and some will act in tension. Let p of the m actuators act in bending and the remaining q actuators act axially.

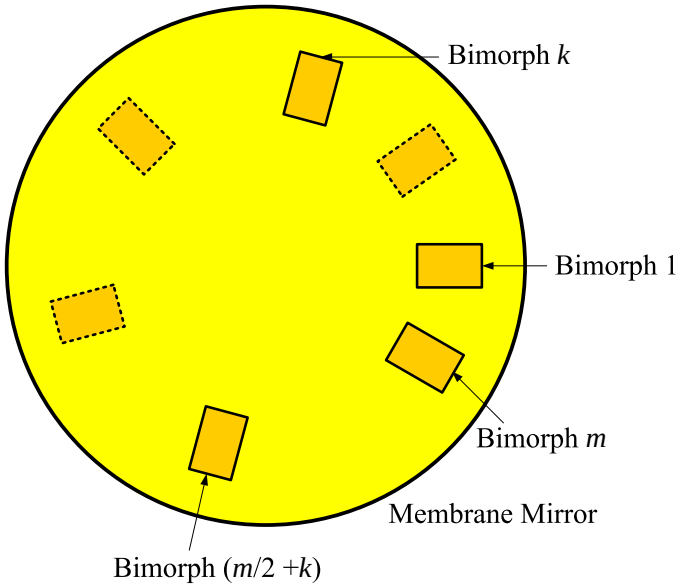

Figure 4.2: Schematic of membrane mirror augmented with m bimorph actuators.

The governing equations developed in the previous subsections are independent of the geometry, and hence a proper change of coordinates is sought to present the governing equation in terms of polar coordinates. This transformation is given by,

$$x = r\cos(\theta), \quad y = r\sin(\theta) \quad \text{and} \quad r^2 = x^2 + y^2, \quad \theta = \arctan\left(\frac{y}{x}\right).$$

Using the chain rule, one obtains that

$$\frac{\partial}{\partial x} = \frac{\partial}{\partial r}\frac{\partial r}{\partial x} + \frac{\partial}{\partial \theta}\frac{\partial \theta}{\partial x} = \frac{\partial}{\partial r}\cos(\theta) - \frac{1}{r}\frac{\partial}{\partial \theta}\sin(\theta)\,,$$
$$\frac{\partial}{\partial y} = \frac{\partial}{\partial r}\frac{\partial r}{\partial y} + \frac{\partial}{\partial \theta}\frac{\partial \theta}{\partial y} = \frac{\partial}{\partial r}\sin(\theta) + \frac{1}{r}\frac{\partial}{\partial \theta}\cos(\theta)\,.$$

Taking the x-axis in the direction of the radial line at $\theta = 0$ results in the radial bending moment M_r, the circumferential bending moment M_θ, and the twisting moment $M_{r\theta}$ to have the same values as M_x, M_y and M_{xy}. The tensile load terms require further treatment. These can be transformed as follows,

$$\begin{aligned}
&\frac{\partial}{\partial x}\left(\alpha\frac{\partial w}{\partial x}\right) = \cos(\theta)\frac{\partial}{\partial r}\left(\alpha\frac{\partial w}{\partial x}\right) - \sin(\theta)\frac{1}{r}\frac{\partial}{\partial \theta}\left(\alpha\frac{\partial w}{\partial x}\right)\\
&= \cos(\theta)\frac{\partial}{\partial r}\left[\alpha\left(\frac{\partial w}{\partial r}\cos(\theta) - \frac{1}{r}\frac{\partial w}{\partial \theta}\sin(\theta)\right)\right]\\
&-\sin(\theta)\frac{1}{r}\frac{\partial}{\partial \theta}\left[\alpha\left(\frac{\partial w}{\partial r}\cos(\theta) - \frac{1}{r}\frac{\partial w}{\partial \theta}\sin(\theta)\right)\right]\,.
\end{aligned} \tag{4.15}$$

Similarly, in the y-direction, the tensile load is presented as

$$\begin{aligned}
&\frac{\partial}{\partial y}\left(\beta\frac{\partial w}{\partial y}\right) = \sin(\theta)\frac{\partial w}{\partial r}\left(\beta\frac{\partial w}{\partial y}\right) + \cos(\theta)\frac{1}{r}\frac{\partial}{\partial \theta}\left(\beta\frac{\partial w}{\partial y}\right)\\
&= \sin(\theta)\frac{\partial}{\partial r}\left[\beta\left(\frac{\partial w}{\partial r}\sin(\theta) + \frac{1}{r}\frac{\partial w}{\partial \theta}\cos(\theta)\right)\right]\\
&+\cos(\theta)\frac{1}{r}\frac{\partial}{\partial \theta}\left[\beta\left(\frac{\partial w}{\partial r}\sin(\theta) + \frac{1}{r}\frac{\partial w}{\partial \theta}\cos(\theta)\right)\right]\,.
\end{aligned} \tag{4.16}$$

Note that for a circular membrane, the tension will be the same in all directions, hence $\alpha = \beta$. Finally, one arrives at the equation governing the transverse vibration of a circular plate under radial tensile load,

$$\begin{aligned}
&\rho_h\frac{\partial^2 w}{\partial t^2} - \frac{\partial^2 M_r}{\partial r^2} - \frac{2}{r}\frac{\partial M_r}{\partial r} + \frac{1}{r}\frac{\partial M_\theta}{\partial r} - \frac{2}{r}\frac{\partial^2 M_{r\theta}}{\partial r\partial \theta} - \frac{2}{r^2}\frac{\partial M_{r\theta}}{\partial \theta} - \frac{1}{r^2}\frac{\partial^2 M_\theta}{\partial \theta^2} + \gamma\frac{\partial w}{\partial t}\\
&-\cos(\theta)\frac{\partial}{\partial r}\left[\alpha\left(\frac{\partial w}{\partial r}\cos(\theta) - \frac{\sin(\theta)}{r}\frac{\partial w}{\partial \theta}\right)\right]\\
&+\frac{\sin(\theta)}{r}\frac{\partial}{\partial \theta}\left[\alpha\left(\frac{\partial w}{\partial r}\cos(\theta) - \frac{\sin(\theta)}{r}\frac{\partial w}{\partial \theta}\right)\right]\\
&-\sin(\theta)\frac{\partial}{\partial r}\left[\alpha\left(\sin(\theta)\frac{\partial w}{\partial r} + \frac{\cos(\theta)}{r}\frac{\partial w}{\partial \theta}\right)\right]\\
&-\frac{\cos(\theta)}{r}\frac{\partial}{\partial \theta}\left[\alpha\left(\sin(\theta)\frac{\partial w}{\partial r} + \frac{\cos(\theta)}{r}\frac{\partial w}{\partial \theta}\right)\right]\\
&= -\frac{\partial^2 (M_r)_a}{\partial r^2} - \frac{2}{r}\frac{\partial (M_r)_a}{\partial r} + \frac{1}{r}\frac{\partial (M_\theta)_a}{\partial r} - \frac{1}{r^2}\frac{\partial (M_\theta)_a}{\partial \theta^2}\,.
\end{aligned} \tag{4.17}$$

The terms corresponding to the tensile loading can be further simplified. The partial differentiation of the tensile loading terms will give rise to the more familiar term that usually appears in the governing equation of a membrane. This form is certainly more compact than the previous form, and is given as,

$$\rho_h \frac{\partial^2 w}{\partial t^2} - \frac{\partial^2 M_r}{\partial r^2} - \frac{2}{r}\frac{\partial M_r}{\partial r} + \frac{1}{r}\frac{\partial M_\theta}{\partial r} - \frac{2}{r}\frac{\partial^2 M_{r\theta}}{\partial r \partial \theta} - \frac{2}{r^2}\frac{\partial M_{r\theta}}{\partial \theta} - \frac{1}{r^2}\frac{\partial^2 M_\theta}{\partial \theta^2} - \alpha \nabla_r w$$
$$+\gamma \frac{\partial w}{\partial t} - \frac{1}{r^2}\frac{\partial w}{\partial \theta}\frac{\partial \alpha}{\partial \theta} - \frac{\partial w}{\partial r}\frac{\partial \alpha}{\partial r} = -\frac{\partial^2 (M_r)_a}{\partial r^2} - \frac{2}{r}\frac{\partial (M_r)_a}{\partial r} + \frac{1}{r}\frac{\partial (M_\theta)_a}{\partial r} - \frac{1}{r^2}\frac{\partial (M_\theta)_a}{\partial \theta^2} .$$

Here, the Laplacian operator, usually present in the membrane transverse motion equation, ∇_r, is present, albeit in its polar form,

$$\nabla_r = \frac{\partial^2}{\partial r^2} + \frac{1}{r}\frac{\partial}{\partial r} + \frac{1}{r^2}\frac{\partial^2}{\partial \theta^2} .$$

In the above derivation, the assumption is that α is not uniform throughout the domain of the structure. This is actually the case of the structure under study. In fact, the tension is given as,

$$\alpha(r,\theta,t) = \bar{\alpha}(r,\theta) + 2\sum_{k=1}^{q} \mathscr{K}_S^k S_k(r) S_k(\theta) \chi_k(r,\theta) V_k(t) , \tag{4.18}$$

where $\bar{\alpha}(r,\theta)$ is the nominal tension placed on the structure through its boundary and $\mathscr{K}_S^k$ is the stretching constant of the k-th bimorph, given as

$$\mathscr{K}_S^k = \frac{-E_k d_{31}^k}{1-\nu_k} .$$

Hence, the second term in Eq. (4.18) corresponds to the axial loading caused by the bimorphs that are acting in tension or compression. The indicator function, $S_k(.)$, reflects the fact that the piezoelectric bimorph experiences equal but opposite strains about it midpoint. This stretching behavior occurs in both directions, r and θ. Mathematically, this function is defined as,

$$S_k(x) = \begin{cases} 1 & \text{if} \quad x < (x_k + x_{k+1})/2 \\ 0 & \text{if} \quad x = (x_k + x_{k+1})/2 \\ -1 & \text{if} \quad x > (x_k + x_{k+1})/2 \end{cases} . \tag{4.19}$$

Moreover, notice that in Eq. (4.18), the local tension induced by the tension bimorphs acts in both coordinate directions, the radial r and circumferential θ. The characteristic function $\chi_k(r,\theta)$ is also present to assert the location of the bimorph actuator. The summation in Eq. (4.18) goes up to q for there are only q actuators that act in tension.

The moment resultants for the circular plate are also transformed into polar coordinates,

$$\begin{aligned} M_r &= DK_r + \tilde{D}K_\theta + C\dot{K}_r + \tilde{C}\dot{K}_\theta \,, \\ M_\theta &= DK_\theta + \tilde{D}K_r + C\dot{K}_\theta + \tilde{C}\dot{K}_r \,, \\ M_{r\theta} &= M_{\theta r} = \frac{D}{2}\tau - \frac{\tilde{D}}{2}\tau + \frac{C}{2}\dot{\tau} - \frac{\tilde{C}}{2}\dot{\tau} \,, \end{aligned} \tag{4.20}$$

where

$$K_r = -\frac{\partial^2 w}{\partial r^2} \quad , \quad K_\theta = -\frac{1}{r}\frac{\partial w}{\partial r} - \frac{1}{r^2}\frac{\partial^2 w}{\partial \theta^2} \quad , \quad \tau = -\frac{2}{r}\frac{\partial^2 w}{\partial r \partial \theta} + \frac{2}{r^2}\frac{\partial w}{\partial \theta} \,. \tag{4.21}$$

The mass per unit area, flexural rigidity and the Kelvin-Voigt damping are now defined in the polar domain,

$$\begin{aligned} \rho_h(r,\theta) &= \rho h + 2\sum_{k=1}^{m} \rho_k h_k \,, \\ D(r,\theta) &= \frac{Eh^3}{12(1-\nu^2)} + \frac{2}{3}\sum_{k=1}^{m} \frac{E_k a_3^k}{1-\nu_k^2}\chi_k(r,\theta) \,, \\ \tilde{D}(r,\theta) &= \frac{Eh^3\nu}{12(1-\nu^2)} + \frac{2}{3}\sum_{k=1}^{m} \frac{E_k a_3^k \nu_k}{1-\nu_k^2}\chi_k(r,\theta) \,, \\ C(r,\theta) &= \frac{c_m h^3}{12(1-\nu^2)} + \frac{2}{3}\sum_{k=1}^{m} \frac{c_k a_3^k}{1-\nu_k^2}\chi_k(r,\theta) \,, \\ \tilde{C}(r,\theta) &= \frac{c_m h^3\nu}{12(1-\nu^2)} + \frac{2}{3}\sum_{k=1}^{m} \frac{c_k a_3^k \nu_k}{1-\nu_k^2}\chi_k(r,\theta) \,. \end{aligned} \tag{4.22}$$

The coefficient a_3^k is the constant of the k-th bimorph, and is given as (Banks et al., 1995),

$$a_3^k = \left(\frac{h}{2} + h_k\right)^3 - \left(\frac{h}{2}\right)^3 .$$

The actuation moment resultants in the polar domain are given as,

$$(M_r)_a = (M_\theta)_a = -\sum_{k=1}^{p} \mathscr{K}_k^B V_k(t)\chi_k(r,\theta) \,, \tag{4.23}$$

with $\mathscr{K}_k^B$ being the bending constant of the k-th bimorph (Banks et al., 1995),

$$\mathscr{K}_k^B = \frac{E_k}{1-\nu_k} d_{31}^k (h + h_k) .$$

Notice that the summation in Eq. (4.23) goes up to p which is the number of bimorphs acting in bending.

Finding a closed form solution for Eq. (4.18) is a daunting task. In fact, a closed form solution for a circular plate without augmented actuators does not exist. The presence of the actuator amplifies the complexity of the problem. For this, we resort to variational methods to the find an approximate solution of Eq. (4.18).

4.3 Weak Formulation of Circular Membrane

To bypass the discontinuity of the structure, a weak form of the governing equation will be sought. As a first step, the following approximation is assumed

$$w(t,r,\theta) = \sum_{i=1}^{N} q_i(t)\varphi_i(r,\theta) . \tag{4.24}$$

This approximation is merely separating the solution into a temporal and a spatial function. Notice that the product of a spatial function depends on both polar coordinates, r and θ as the membrane is not axisymmetric. In the following, the time and spatial arguments of q_i and φ_i will be dropped. Substituting this approximation into the governing equation, one obtains

$$\begin{aligned}
&\sum_{i=1}^{N} \Bigg\{ \rho_h \ddot{q}_i \varphi_i \\
&+ \frac{\partial^2}{\partial r^2}\left[q_i \left\{ D\frac{\partial^2 \varphi_i}{\partial r^2} + \tilde{D}\left(\frac{1}{r}\frac{\partial \varphi_i}{\partial r} + \frac{1}{r^2}\frac{\partial^2 \varphi_i}{\partial \theta^2} \right) \right\} + \dot{q}_i \left\{ C\frac{\partial^2 \varphi_i}{\partial r^2} + \tilde{C}\left(\frac{1}{r}\frac{\partial \varphi_i}{\partial r} + \frac{1}{r^2}\frac{\partial^2 \varphi_i}{\partial \theta^2} \right) \right\} \right] \\
&+ \frac{2}{r}\frac{\partial}{\partial r}\left[q_i \left\{ D\frac{\partial^2 \varphi_i}{\partial r^2} + \tilde{D}\left(\frac{1}{r}\frac{\partial \varphi_i}{\partial r} + \frac{1}{r^2}\frac{\partial^2 \varphi_i}{\partial \theta^2} \right) \right\} + \dot{q}_i \left\{ C\frac{\partial^2 \varphi_i}{\partial r^2} + \tilde{C}\left(\frac{1}{r}\frac{\partial \varphi_i}{\partial r} + \frac{1}{r^2}\frac{\partial^2 \varphi_i}{\partial \theta^2} \right) \right\} \right] \\
&- \frac{1}{r}\frac{\partial}{\partial r}\left[q_i \left\{ D\left(\frac{1}{r}\frac{\partial \varphi_i}{\partial r} + \frac{1}{r^2}\frac{\partial^2 \varphi_i}{\partial \theta^2} \right) + \tilde{D}\frac{\partial^2 \varphi_i}{\partial r^2} \right\} + \dot{q}_i \left\{ C\left(\frac{1}{r}\frac{\partial \varphi_i}{\partial r} + \frac{1}{r^2}\frac{\partial^2 \varphi_i}{\partial \theta^2} \right) + \tilde{C}\frac{\partial^2 \varphi_i}{\partial r^2} \right\} \right] \\
&+ \frac{2}{r}\frac{\partial^2}{\partial r \partial \theta}\left[q_i \left\{ \frac{D-\tilde{D}}{2}\left(\frac{2}{r}\frac{\partial^2 \varphi_i}{\partial r \partial \theta} - \frac{2}{r^2}\frac{\partial \varphi_i}{\partial \theta} \right) \right\} + \dot{q}_i \left\{ \frac{C-\tilde{C}}{2}\left(\frac{2}{r}\frac{\partial^2 \varphi_i}{\partial r \partial \theta} - \frac{2}{r^2}\frac{\partial \varphi_i}{\partial \theta} \right) \right\} \right] \\
&+ \frac{2}{r^2}\frac{\partial}{\partial \theta}\left[q_i \left\{ \frac{D-\tilde{D}}{2}\left(\frac{2}{r}\frac{\partial^2 \varphi_i}{\partial r \partial \theta} - \frac{2}{r^2}\frac{\partial \varphi_i}{\partial \theta} \right) \right\} + \dot{q}_i \left\{ \frac{C-\tilde{C}}{2}\left(\frac{2}{r}\frac{\partial^2 \varphi_i}{\partial r \partial \theta} - \frac{2}{r^2}\frac{\partial \varphi_i}{\partial \theta} \right) \right\} \right]
\end{aligned}$$

$$
\begin{aligned}
&+\frac{1}{r^2}\frac{\partial^2}{\partial\theta^2}\Big[q_i\Big\{D\Big(\frac{1}{r}\frac{\partial\varphi_i}{\partial r}+\frac{1}{r^2}\frac{\partial^2\varphi_i}{\partial\theta^2}\Big)+\tilde{D}\frac{\partial^2\varphi_i}{\partial r^2}\Big\}+\dot{q}_i\Big\{C\Big(\frac{1}{r}\frac{\partial\varphi_i}{\partial r}+\frac{1}{r^2}\frac{\partial^2\varphi_i}{\partial\theta^2}\Big)+\tilde{C}\frac{\partial^2\varphi_i}{\partial r^2}\Big\}\Big]\\
&-q_i\Big[\alpha\Big(\frac{\partial^2\varphi_i}{\partial r^2}+\frac{1}{r}\frac{\partial\varphi_i}{\partial r}+\frac{1}{r^2}\frac{\partial^2\varphi_i}{\partial\theta^2}\Big)+\frac{1}{r^2}\frac{\partial\alpha}{\partial\theta}\frac{\partial\varphi_i}{\partial\theta}+\frac{\partial\alpha}{\partial r}\frac{\partial\varphi_i}{\partial r}\Big]+\gamma\dot{q}_i\varphi_i\Big\}\\
&=-\frac{\partial^2(M_r)_a}{\partial r^2}-\frac{2}{r}\frac{\partial(M_r)_a}{\partial r}+\frac{1}{r}\frac{\partial(M_\theta)_a}{\partial r}-\frac{1}{r^2}\frac{\partial(M_\theta)_a}{\partial\theta^2}\,.
\end{aligned}
\tag{4.25}
$$

Now, multiply the governing equation by φ_j and integrate over the domain of the membrane. Regrouping terms about q_i and its derivatives,

$$
\begin{aligned}
&\sum_{i=1}^{N}\Bigg\{\ddot{q}_i\int_\Omega\rho_h\varphi_i\varphi_j\mathrm{d}\Omega\\
&+\dot{q}_i\int_\Omega\Big[\frac{\partial^2\mathscr{A}}{\partial r^2}+\frac{2}{r}\frac{\partial\mathscr{A}}{\partial r}-\frac{1}{r}\frac{\partial\tilde{\mathscr{A}}}{\partial r}+\frac{2}{r}\frac{\partial^2\mathscr{B}}{\partial r\partial\theta}+\frac{2}{r^2}\frac{\partial\mathscr{B}}{\partial\theta}+\frac{1}{r^2}\frac{\partial^2\tilde{\mathscr{A}}}{\partial\theta^2}+\gamma\varphi_i\Big]\varphi_j\mathrm{d}\Omega\\
&+q_i\int_\Omega\Big[\frac{\partial^2\mathscr{C}}{\partial r^2}+\frac{2}{r}\frac{\partial\mathscr{C}}{\partial r}-\frac{1}{r}\frac{\partial\tilde{\mathscr{C}}}{\partial r}+\frac{2}{r}\frac{\partial^2\mathscr{E}}{\partial r\partial\theta}+\frac{2}{r^2}\frac{\partial\mathscr{E}}{\partial\theta}+\frac{1}{r^2}\frac{\partial^2\tilde{\mathscr{C}}}{\partial\theta^2}\\
&-\alpha\Big(\frac{\partial^2\varphi_i}{\partial r^2}+\frac{1}{r}\frac{\partial\varphi_i}{\partial r}+\frac{1}{r^2}\frac{\partial^2\varphi_i}{\partial\theta^2}\Big)-\frac{1}{r^2}\frac{\partial\alpha}{\partial\theta}\frac{\partial\varphi_i}{\partial\theta}-\frac{\partial\alpha}{\partial r}\frac{\partial\varphi_i}{\partial r}\Big]\Bigg\}\varphi_j\mathrm{d}\Omega\\
&=\int_\Omega\Big[-\frac{\partial^2(M_r)_a}{\partial r^2}-\frac{2}{r}\frac{\partial(M_r)_a}{\partial r}+\frac{1}{r}\frac{\partial(M_\theta)_a}{\partial r}-\frac{1}{r^2}\frac{\partial(M_\theta)_a}{\partial\theta^2}\Big]\varphi_j\mathrm{d}\Omega\,,
\end{aligned}
\tag{4.26}
$$

where

$$
\mathscr{A}=C\frac{\partial^2\varphi_i}{\partial r^2}+\tilde{C}\Big(\frac{1}{r}\frac{\partial\varphi_i}{\partial r}+\frac{1}{r^2}\frac{\partial^2\varphi_i}{\partial\theta^2}\Big)\,, \tag{4.27a}
$$

$$
\tilde{\mathscr{A}}=C\Big(\frac{1}{r}\frac{\partial\varphi_i}{\partial r}+\frac{1}{r^2}\frac{\partial^2\varphi_i}{\partial\theta^2}\Big)+\tilde{C}\frac{\partial^2\varphi_i}{\partial r^2}\,, \tag{4.27b}
$$

$$
\mathscr{B}=(C-\tilde{C})\Big(\frac{1}{r}\frac{\partial^2\varphi_i}{\partial r\partial\theta}-\frac{1}{r^2}\frac{\partial\varphi_i}{\partial\theta}\Big)\,, \tag{4.27c}
$$

$$
\mathscr{C}=D\frac{\partial^2\varphi_i}{\partial r^2}+\tilde{D}\Big(\frac{1}{r}\frac{\partial\varphi_i}{\partial r}+\frac{1}{r^2}\frac{\partial^2\varphi_i}{\partial\theta^2}\Big)\,, \tag{4.27d}
$$

$$
\tilde{\mathscr{C}}=D\Big(\frac{1}{r}\frac{\partial\varphi_i}{\partial r}+\frac{1}{r^2}\frac{\partial^2\varphi_i}{\partial\theta^2}\Big)+\tilde{D}\frac{\partial^2\varphi_i}{\partial r^2}\,, \tag{4.27e}
$$

$$
\mathscr{E}=(D-\tilde{D})\Big(\frac{1}{r}\frac{\partial^2\varphi_i}{\partial r\partial\theta}-\frac{1}{r^2}\frac{\partial\varphi_i}{\partial\theta}\Big)\,. \tag{4.27f}
$$

Notice the analogy of the structure of the above expressions, where $\mathscr{A}$ and $\tilde{\mathscr{A}}$ are analogous to $\mathscr{C}$ and $\tilde{\mathscr{C}}$ respectively. Moreover, $\mathscr{B}$ is analogous to $\mathscr{E}$.

The multiplication of Eq. (4.25) by φ_j was not arbitrary. In this work, the functions φ_i and φ_j are chosen to be the mode shapes of the structure considered for modeling.

These mode shapes can be obtained numerically through ANSYS®. Consequently, these mode shapes are orthogonal; a property that will be utilized to obtain the reduced order model. In the polar domain, the orthogonality condition is given as

$$\int_{\Omega} \varphi_i \varphi_j \mathrm{d}\Omega = \int_0^R \int_0^{2\pi} r \varphi_i \varphi_j \mathrm{d}r\mathrm{d}\theta \ ,$$

since the differential area in a polar domain is $\mathrm{d}\Omega = r\mathrm{d}r\mathrm{d}\theta$.

The term multiplying $\ddot{q}_i$ is usually termed the mass matrix. This is given as,

$$\mathbf{M} = \left[\int_{\Omega} r \rho_h \varphi_i \varphi_j \mathrm{d}r\mathrm{d}\theta \right]_{i,j=1,\cdots,N} . \tag{4.28}$$

As a series of *integration by parts* operations will be carried on next, a brief note regarding this operation is provided in Appendix A. The integration by parts will be carried out on a term by term basis. First, the expression multiplying $\dot{q}_i$ in Eq. (4.26) will be treated,

$$\int_{\Omega} \frac{\partial^2 \mathscr{A}}{\partial r^2} \varphi_j r \mathrm{d}r\mathrm{d}\theta = \int_{\partial\Omega} \frac{\partial \mathscr{A}}{\partial r} n_r r \varphi_j \mathrm{d}\theta$$

$$- \int_{\partial\Omega} \mathscr{A} \left(\varphi_j + r \frac{\partial \varphi_j}{\partial r} \right) n_r \mathrm{d}\theta + \int_{\Omega} \mathscr{A} \left(2 \frac{\partial \varphi_j}{\partial r} + r \frac{\partial^2 \varphi_j}{\partial r^2} \right) \mathrm{d}r\mathrm{d}\theta \ , \tag{4.29a}$$

$$\int_{\Omega} 2 \frac{\partial \mathscr{A}}{\partial r} \varphi_j \mathrm{d}r\mathrm{d}\theta = \int_{\partial\Omega} 2 \mathscr{A} \varphi_j n_r \mathrm{d}\theta - \int_{\Omega} 2 \mathscr{A} \frac{\partial \varphi_j}{\partial r} \mathrm{d}r\mathrm{d}\theta \ , \tag{4.29b}$$

$$- \int_{\Omega} \frac{\partial \tilde{\mathscr{A}}}{\partial r} \varphi_j \mathrm{d}r\mathrm{d}\theta = - \int_{\partial\Omega} \tilde{\mathscr{A}} \varphi_j n_r \mathrm{d}\theta + \int_{\Omega} \tilde{\mathscr{A}} \frac{\partial \varphi_j}{\partial r} \mathrm{d}r\mathrm{d}\theta \ , \tag{4.29c}$$

$$\int_{\Omega} 2 \frac{\partial^2 \mathscr{B}}{\partial r \partial \theta} \varphi_j \mathrm{d}r\mathrm{d}\theta = 2 \int_{\partial\Omega} \frac{\partial \mathscr{B}}{\partial \theta} \varphi_j n_r \mathrm{d}\theta - 2 \int_{\partial\Omega} \mathscr{B} \frac{\partial \varphi_j}{\partial r} n_\theta \mathrm{d}r + 2 \int_{\Omega} \mathscr{B} \frac{\partial^2 \varphi_j}{\partial r \partial \theta} \mathrm{d}r\mathrm{d}\theta \ , \tag{4.29d}$$

$$\int_{\Omega} \frac{2}{r} \frac{\partial \mathscr{B}}{\partial \theta} \varphi_j \mathrm{d}r\mathrm{d}\theta = \int_{\partial\Omega} \frac{2}{r} \mathscr{B} \varphi_j \mathrm{d}r - \int_{\Omega} \mathscr{B} \frac{2}{r} \frac{\partial \varphi_j}{\partial \theta} \mathrm{d}r\mathrm{d}\theta \ , \tag{4.29e}$$

$$\int_{\Omega} \frac{1}{r} \frac{\partial^2 \tilde{\mathscr{A}}}{\partial \theta^2} \varphi_j \mathrm{d}r\mathrm{d}\theta = \int_{\partial\Omega} \frac{\partial \tilde{\mathscr{A}}}{\partial \theta} \frac{1}{r} \varphi_j n_\theta \mathrm{d}r - \int_{\partial\Omega} \tilde{\mathscr{A}} \frac{1}{r} \frac{\partial \varphi_j}{\partial \theta} n_\theta \mathrm{d}r + \int_{\Omega} \tilde{\mathscr{A}} \frac{1}{r} \frac{\partial^2 \varphi_j}{\partial \theta^2} \mathrm{d}r\mathrm{d}\theta \ . \tag{4.29f}$$

When added, these terms lead to the damping matrix, given as

$$\mathbf{C} = \left[\int_{\Omega} \left(\mathscr{A} r \frac{\partial^2 \varphi_j}{\partial r^2} + \tilde{\mathscr{A}} \frac{\partial \varphi_j}{\partial r} + 2 \mathscr{B} \frac{\partial^2 \varphi_j}{\partial r \partial \theta} - \frac{2\mathscr{B}}{r} \frac{\partial \varphi_j}{\partial \theta} + \frac{\tilde{\mathscr{A}}}{r} \frac{\partial^2 \varphi_j}{\partial \theta^2} + \gamma r \varphi_i \varphi_j \right) \mathrm{d}r\mathrm{d}\theta \right]_{i,j=1,\cdots,N} . \tag{4.29g}$$

To obtain the stiffness matrix, a similar process is carried out,

$$\int_\Omega \frac{\partial^2 \mathscr{C}}{\partial r^2}\varphi_j r\mathrm{d}r\mathrm{d}\theta = \int_{\partial\Omega} \frac{\partial \mathscr{C}}{\partial r} n_r r\varphi_j \mathrm{d}\theta$$
$$-\int_{\partial\Omega} \mathscr{C}\Big(\varphi_j + r\frac{\partial \varphi_j}{\partial r}\Big)n_r\mathrm{d}\theta + \int_\Omega \mathscr{C}\Big(2\frac{\partial \varphi_j}{\partial r} + r\frac{\partial^2\varphi_j}{\partial r^2}\Big)\mathrm{d}r\mathrm{d}\theta\,, \tag{4.30a}$$

$$\int_\Omega 2\frac{\partial \mathscr{C}}{\partial r}\varphi_j \mathrm{d}r\mathrm{d}\theta = \int_{\partial\Omega} 2\mathscr{C}\varphi_j n_r \mathrm{d}\theta - \int_\Omega 2\mathscr{C}\frac{\partial \varphi_j}{\partial r}\mathrm{d}r\mathrm{d}\theta\,, \tag{4.30b}$$

$$-\int_\Omega \frac{\partial \tilde{\mathscr{C}}}{\partial r}\varphi_j \mathrm{d}r\mathrm{d}\theta = -\int_{\partial\Omega} \tilde{\mathscr{C}}\varphi_j n_r \mathrm{d}\theta + \int_\Omega \tilde{\mathscr{C}}\frac{\partial \varphi_j}{\partial r}\mathrm{d}r\mathrm{d}\theta\,, \tag{4.30c}$$

$$\int_\Omega 2\frac{\partial^2 \mathscr{E}}{\partial r\partial\theta}\varphi_j \mathrm{d}r\mathrm{d}\theta = 2\int_{\partial\Omega} \frac{\partial \mathscr{E}}{\partial\theta}\varphi_j n_r \mathrm{d}\theta - 2\int_{\partial\Omega} \mathscr{E}\frac{\partial \varphi_j}{\partial r} n_\theta \mathrm{d}r + 2\int_\Omega \mathscr{E}\frac{\partial^2\varphi_j}{\partial r\partial\theta}\mathrm{d}r\mathrm{d}\theta\,, \tag{4.30d}$$

$$\int_\Omega \frac{2}{r}\frac{\partial \mathscr{E}}{\partial\theta}\varphi_j \mathrm{d}r\mathrm{d}\theta = \int_{\partial\Omega} \frac{2}{r}\mathscr{E}\varphi_j \mathrm{d}r - \int_\Omega \mathscr{E}\frac{2}{r}\frac{\partial \varphi_j}{\partial\theta}\mathrm{d}r\mathrm{d}\theta\,, \tag{4.30e}$$

$$\int_\Omega \frac{1}{r}\frac{\partial^2 \tilde{\mathscr{C}}}{\partial\theta^2}\varphi_j \mathrm{d}r\mathrm{d}\theta = \int_{\partial\Omega} \frac{\partial \tilde{\mathscr{C}}}{\partial\theta}\frac{1}{r}\varphi_j n_\theta \mathrm{d}r - \int_{\partial\Omega} \tilde{\mathscr{C}}\frac{1}{r}\frac{\partial \varphi_j}{\partial\theta} n_\theta \mathrm{d}r + \int_\Omega \tilde{\mathscr{C}}\frac{1}{r}\frac{\partial^2\varphi_j}{\partial\theta^2}\mathrm{d}r\mathrm{d}\theta\,, \tag{4.30f}$$

$$-\int_\Omega \frac{1}{r}\frac{\partial \alpha}{\partial\theta}\frac{\partial \varphi_i}{\partial\theta}\varphi_j \mathrm{d}r\mathrm{d}\theta = -\int_{\partial\Omega} \frac{\alpha}{r}\frac{\partial \varphi_i}{\partial\theta}\varphi_j n_\theta \mathrm{d}r + \int_\Omega \frac{\alpha}{r}\Big(\frac{\partial^2\varphi_i}{\partial\theta^2}\varphi_j + \frac{\partial \varphi_i}{\partial\theta}\frac{\partial \varphi_j}{\partial\theta}\Big)\mathrm{d}r\mathrm{d}\theta\,, \tag{4.30g}$$

$$-\int_\Omega r\frac{\partial \alpha}{\partial r}\frac{\partial \varphi_i}{\partial r}\varphi_j \mathrm{d}r\mathrm{d}\theta = -\int_{\partial\Omega} \alpha r\frac{\partial \varphi_i}{\partial r}\varphi_j n_r \mathrm{d}\theta + \int_\Omega \alpha\Big(\frac{\partial \varphi_i}{\partial r}\varphi_j + r\frac{\partial^2\varphi_i}{\partial r^2}\varphi_j + r\frac{\partial \varphi_i}{\partial r}\frac{\partial \varphi_j}{\partial r}\Big)\mathrm{d}r\mathrm{d}\theta\,. \tag{4.30h}$$

When adding the above components, one obtains the stiffness matrix,

$$\mathbf{K} = \Bigg[\int_\Omega \Big\{\mathscr{C} r\frac{\partial^2\varphi_j}{\partial r^2} + \tilde{\mathscr{C}}\frac{\partial \varphi_j}{\partial r} + 2\mathscr{E}\frac{\partial^2\varphi_j}{\partial r\partial\theta} - \frac{2\mathscr{E}}{r}\frac{\partial \varphi_j}{\partial\theta} + \frac{\tilde{\mathscr{C}}}{r}\frac{\partial^2\varphi_j}{\partial\theta^2} + \alpha\Big(\frac{1}{r}\frac{\partial \varphi_i}{\partial\theta}\frac{\partial \varphi_j}{\partial\theta} + r\frac{\partial \varphi_i}{\partial r}\frac{\partial \varphi_j}{\partial r}\Big)\Big\}\mathrm{d}r\mathrm{d}\theta\Bigg]_{i,j=1,\cdots,N}\,. \tag{4.30i}$$

Notice now that all the irregular terms do not undergo any spatial differentiation; only integration. Furthermore, the right hand side of Eq. (4.26) needs similar treatment to yield an input matrix,

$$-\int_\Omega \frac{\partial^2 (M_r)_a}{\partial r^2}\varphi_j r\mathrm{d}r\mathrm{d}\theta = -\int_{\partial\Omega} \frac{\partial (M_r)_a}{\partial r} n_r r\varphi_j \mathrm{d}\theta + \int_{\partial\Omega} (M_r)_a\Big(\varphi_j + r\frac{\partial \varphi_j}{\partial r}\Big)n_r\mathrm{d}\theta$$

$$- \int_{\Omega} (M_r)_a \left(2\frac{\partial \varphi_j}{\partial r} + r\frac{\partial^2 \varphi_j}{\partial r^2}\right) \mathrm{d}r\mathrm{d}\theta \,, \tag{4.31a}$$

$$-\int_{\Omega} 2\frac{\partial (M_r)_a}{\partial r}\varphi_j \mathrm{d}r\mathrm{d}\theta = -\int_{\partial\Omega} 2(M_r)_a \varphi_j n_r \mathrm{d}\theta + \int_{\Omega} 2(M_r)_a \frac{\partial \varphi_j}{\partial r}\mathrm{d}r\mathrm{d}\theta \,, \tag{4.31b}$$

$$\int_{\Omega} \frac{\partial (M_\theta)_a}{\partial r}\varphi_j \mathrm{d}r\mathrm{d}\theta = \int_{\partial\Omega} (M_\theta)_a \varphi_j n_r \mathrm{d}\theta - \int_{\Omega} (M_\theta)_a \frac{\partial \varphi_j}{\partial r}\mathrm{d}r\mathrm{d}\theta \,, \tag{4.31c}$$

$$\begin{aligned} -\int_{\Omega} \frac{1}{r}\frac{\partial^2 (M_\theta)_a}{\partial \theta^2}\varphi_j \mathrm{d}r\mathrm{d}\theta \;&=\; -\int_{\partial\Omega} \frac{\partial (M_\theta)_a}{\partial \theta}\frac{1}{r}\varphi_j n_\theta \mathrm{d}r + \int_{\partial\Omega} (M_\theta)_a \frac{1}{r}\frac{\partial \varphi_j}{\partial \theta} n_\theta \mathrm{d}r \\ &\quad - \int_{\Omega} (M_\theta)_a \frac{1}{r}\frac{\partial^2 \varphi_j}{\partial \theta^2}\mathrm{d}r\mathrm{d}\theta \,. \end{aligned} \tag{4.31d}$$

The above components can be added, and using Eq. (4.23), yields the individual input vectors,

$$B_k = \left[\int_{\Omega} \mathscr{K}_k^B \left(r\frac{\partial^2 \varphi_j}{\partial r^2} + \frac{\partial \varphi_j}{\partial r} + \frac{1}{r}\frac{\partial^2 \varphi_j}{\partial \theta^2}\right)\chi_k(r,\theta)\mathrm{d}r\mathrm{d}\theta\right]_{j=1,\cdots,N} \qquad k = 1,\cdots,p \,. \tag{4.31e}$$

Hence, the input matrix is

$$\bar{\mathbf{B}} = \begin{bmatrix} B_1 & \cdots & B_p \end{bmatrix} . \tag{4.31f}$$

The input vector for the bending bimorphs is,

$$\mathbf{V}(t) = \begin{bmatrix} V_1(t) & \cdots & V_p(t) \end{bmatrix}^T . \tag{4.32}$$

Hence, the behavior of the system is described through,

$$\mathbf{M}\ddot{q}(t) + \mathbf{C}\dot{q}(t) + \mathbf{K}q(t) = \bar{\mathbf{B}}\mathbf{V}(t) \,. \tag{4.33}$$

With the governing equation at hand, the model developed is illustrated through a case study. The case study demonstrates the approach discussed above, and provides a numerical model to be used for control illustration in Chapter 5.

4.4 Model Implementation

The model developed in Section 4.3 requires some steps to be obtained. In summary, the mode shapes are obtained through an FEA conducted in ANSYS®. These mode shapes are used in the Galerkin expansion in MATLAB®. Fig. 4.3 shows a circular Kapton membrane augmented with four MFC bimorph actuators. The actuators are placed at 90° angular intervals. Table 4.1 displays the physical properties of the membrane used.

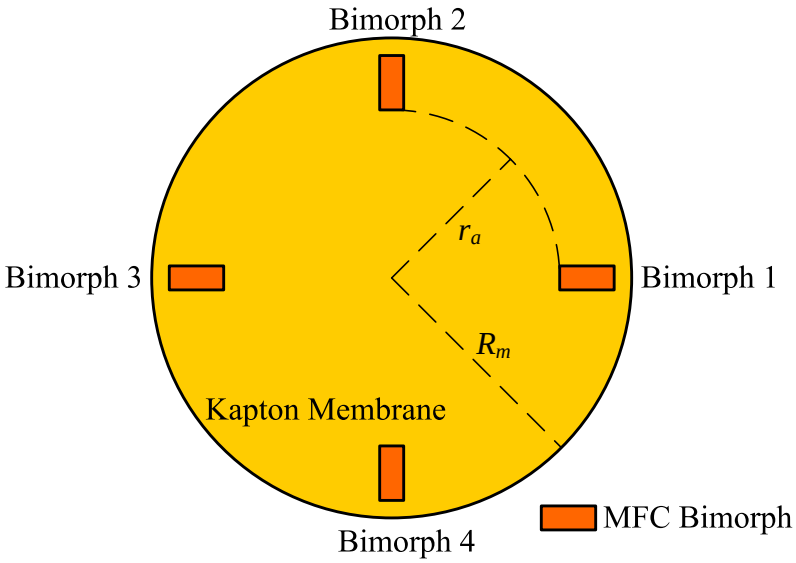

Figure 4.3: Membrane mirror with four MFC bimorph actuators used to illustrate the modeling approach of Section 4.3. Here $R_m = 15$ cm and $r_a = 8.8$ cm.

Table 4.1: Physical properties of the circular Kapton membrane augmented with four actuators.

Property	Kapton	MFC Patch
Density [kg/m^3]	1420	994
Young's Modulus [GPa]	3	34.5
Thickness [mm]	51×10^{-3}	0.3

The radius of the membrane is $R_m = 15$ cm and the radius at which the MFC patches are placed is $r_a = 8.8$ cm (for $a = 1, \cdots, 4$). All the bimorphs act in bending, hence $p = 4$ in Eq. (4.23) on Page 103. A tension of 100 N/m was applied to the edge of the membrane

mirror ($\bar{\alpha} = 100$ N/m in Eq. (4.18) on Page 102). This tension value is comparable to the value Shepherd et al. (2006b) measured for their test article.

4.4.1 FEM Modeling in ANSYS®

We propose to use the mode shapes of the structure as obtained through a FEA performed using ANSYS®. ANSYS® is a multi-purpose finite element software that is commercially available and is widely used in industry and academia as an analysis and design tool.

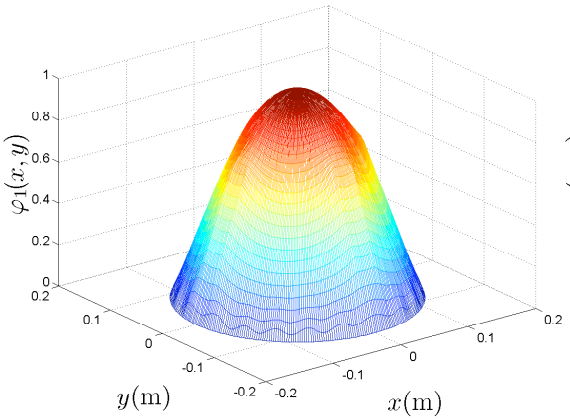

(a) Mode 1.

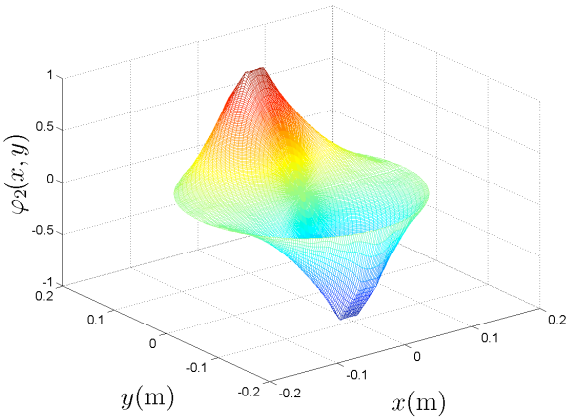

(b) Mode 2.

Figure 4.4: The first and second mode shapes obtained from ANSYS®.

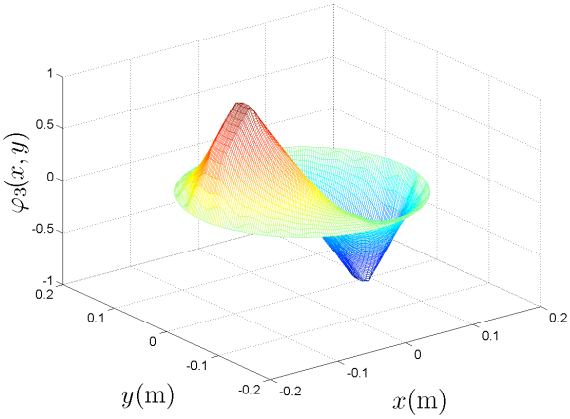

(a) Mode 3.

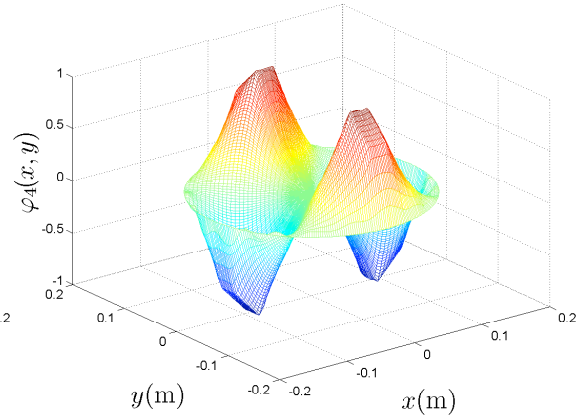

(b) Mode 4.

Figure 4.5: The third and fourth mode shapes obtained from ANSYS®.

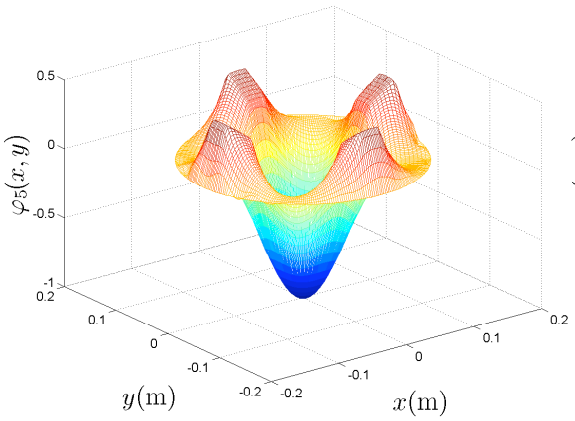

(a) Mode 5.

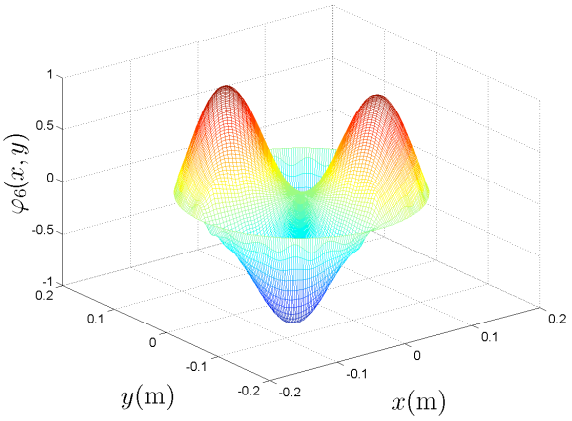

(b) Mode 6.

Figure 4.6: The fifth and sixth mode shapes obtained from ANSYS®.

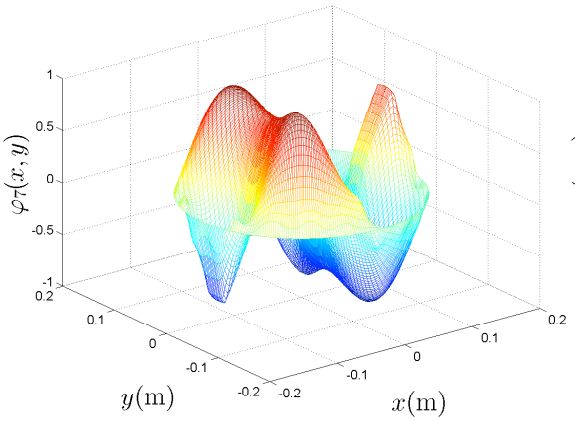

(a) Mode 7.

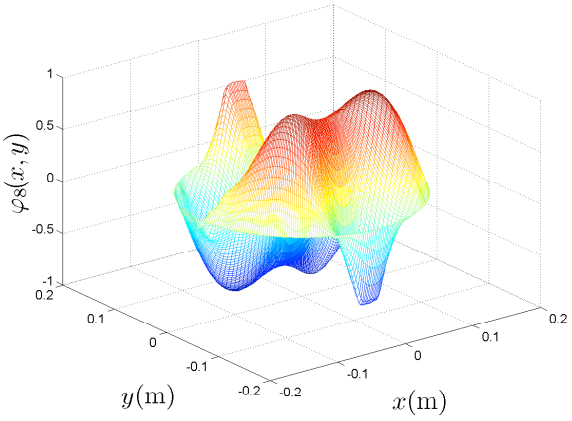

(b) Mode 8.

Figure 4.7: The seventh and eighth mode shapes obtained from ANSYS®.

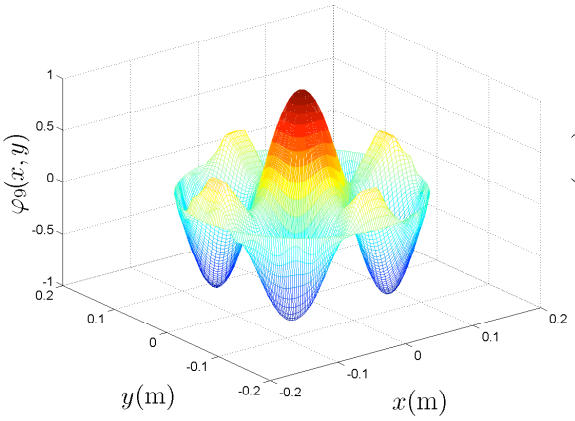

(a) Mode 9.

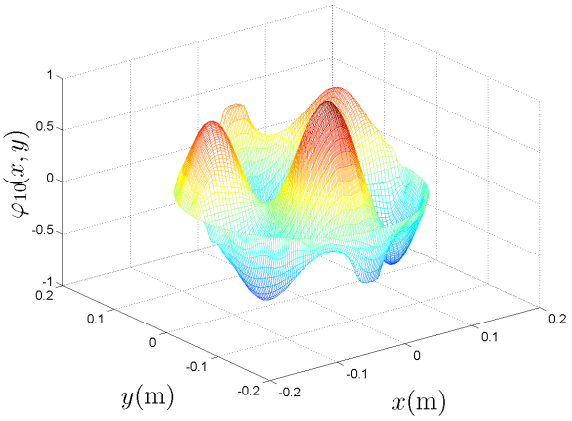

(b) Mode 10.

Figure 4.8: The ninth and tenth ten mode shapes obtained from ANSYS®.

We create a model of a the circular membrane and four MFC bimorphs augmented at $\pi/2$ angular intervals. The code used to generate the model, creating the mesh, and carrying out the proper analyses is provided in Listing B.1 of Appendix B. Figure 4.4 through Fig. 4.8 display the first ten mode shapes of the membrane. The mode shapes are normalized to unity as dictated by,

$$\int_{\Omega} \varphi_i \varphi_j \mathrm{d}\Omega = \int_0^R \int_0^{2\pi} r \varphi_i \varphi_j \mathrm{d}r \mathrm{d}\theta = \delta_{ij} \ ,$$

where δ_{ij} is the Kronecker delta, defined as

$$\delta_{ij} = \begin{cases} 1, & \text{if} \quad i = j \\ 0, & \text{if} \quad i \neq j \end{cases} \ .$$

4.4.2 Numerical Differentiation

The mode shapes in Fig. 4.4 through Fig. 4.8 exhibit localized effects at the location of the bimorphs. The developments of Section 4.3 require the differentiation of the mode shapes with respect to the radial, r, and circumferential, θ, variables. However, to avoid obtaining erroneous results of the first, second and mixed derivatives, we will avoid differentiating the across the boundaries of the bimorphs. Figure 4.9 shows the two points, $P_{i,j}$ and $P_{i+1,j}$. The derivative between these two points is avoided, and hence the point P_b is used to evaluate the derivative from both sides of the boundary of the bimorph. The numerical differentiation schemes used are all given in Appendix C. The illustration shown in Fig. 4.9 is for the differentiation in the radial direction. With this approach, the partial derivatives of the mode shapes will also be discontinuous, hence retaining the discontinuity of the mode shapes.

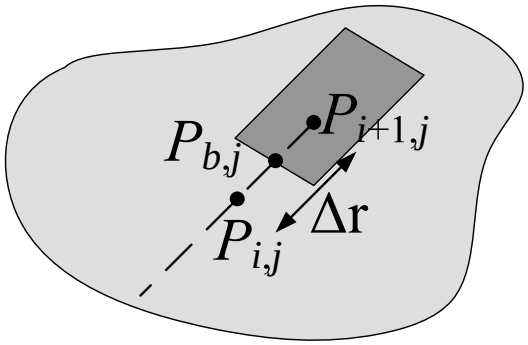

Figure 4.9: Piecewise differentiation in the radial direction.

4.4.3 Numerical Integration

Another issue that comes up when implementing the model of Section 4.3 is the numerical integration of terms such as

$$\int_{\Omega} \frac{1}{r}\frac{\partial^2 \varphi_j}{\partial \theta^2} \mathrm{d}r\mathrm{d}\theta = \int_0^R \int_0^{2\pi} \frac{1}{r}\frac{\partial^2 \varphi_j}{\partial \theta^2} \mathrm{d}r\mathrm{d}\theta \ ,$$

$$\text{or} \quad \int_{\Omega} \frac{1}{r}\frac{\partial \varphi_j}{\partial r} \mathrm{d}r\mathrm{d}\theta \ .$$

The challenge here is that the integrand above is not defined at $r = 0$. Terms similar to this term appear in the calculation of the stiffness matrix, **C**, the damping matrix, **K**, and when calculating the terms $\mathscr{A}$, $\tilde{\mathscr{A}}$, $\mathscr{B}$, $\mathscr{C}$, $\tilde{\mathscr{C}}$, and $\mathscr{E}$ of Eq. (4.27). To avoid this numerical problem, there are two approaches:

a) Instead of starting the integration from zero, one can start the integration from ϵ, which is a small number. Hence, the integration does not start from the center of the membrane, rather from the perimeter of a concentric circle with radius ϵ.

b) Another approach would be to approximate the behavior of the shape function $\varphi(r,\theta)$ near $r = 0$. If the shape function can be approximated as a quadratic function of r, or higher order (cubic, quartic, quintic, etc ...), then

$$\varphi(r,\theta) = a_2 r^2 + a_0 \ ,$$

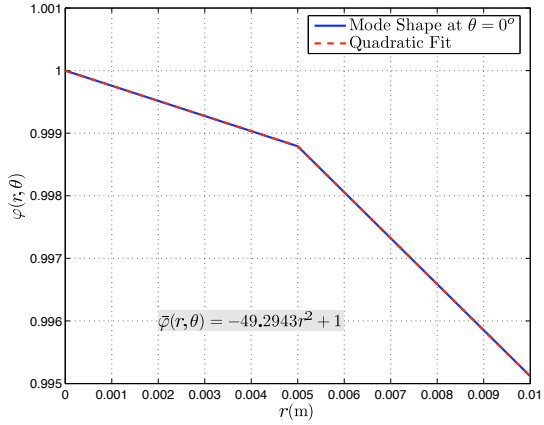

(a) Approximation of mode 1 at $\theta = 0^o$.

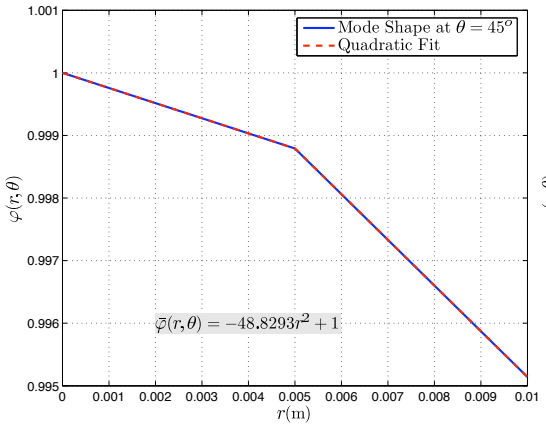

(b) Approximation of mode 1 at $\theta = 45^o$.

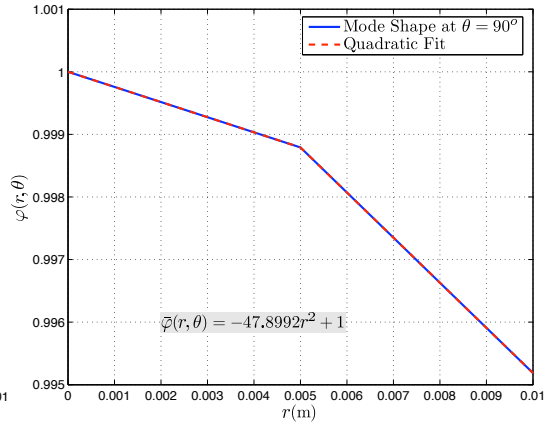

(c) Approximation of mode 1 at $\theta = 90^o$.

Figure 4.10: Quadratic approximation of mode 1 at various circumferential values.

$$\frac{1}{r}\frac{\partial \varphi(r,\theta)}{\partial r} = 2a_2 \quad \text{and} \quad \frac{1}{r}\frac{\partial \varphi(r,\theta)}{\partial \theta} = 0\,. \tag{4.34}$$

This is particularly true for the first, fifth and ninth modes. The remaining modes have the point $r = 0$ as a node (Fig. 4.4 through Fig. 4.8), and hence these terms do not pose a numerical difficulty.

Figure 4.10, Fig. 4.11 and Fig. 4.12 display the behavior of the first, fifth and ninth mode in the neighborhood of $r = 0$ at various angles. There, the mode shape behave as a quadratic function, and hence the assumption of Eq. (4.34) is valid. Both approaches of Item a and Item b on Page 113 were compared, and there was no practical difference in the resulting system matrices. Hence, the approach of Item a was adopted for the simplicity of implementation.

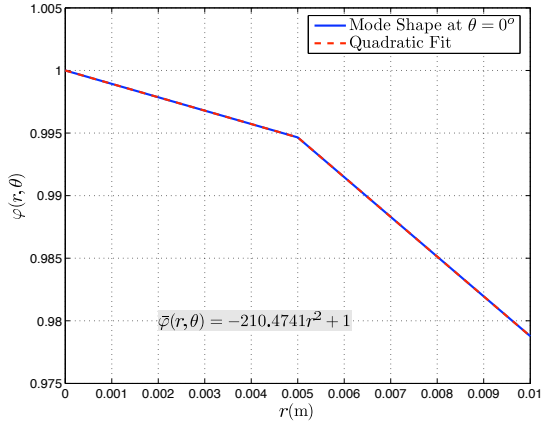

(a) Approximation of mode 5 at $\theta = 0^o$.

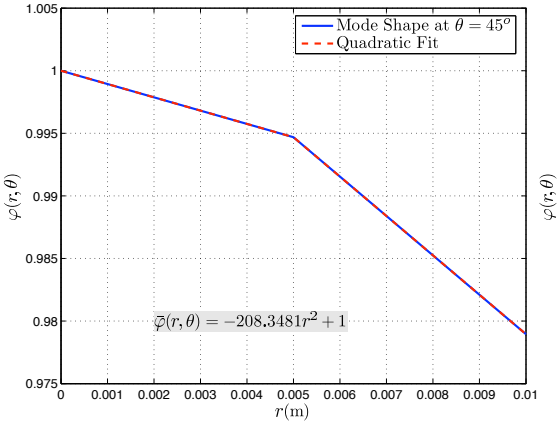

(b) Approximation of mode 5 at $\theta = 45^o$.

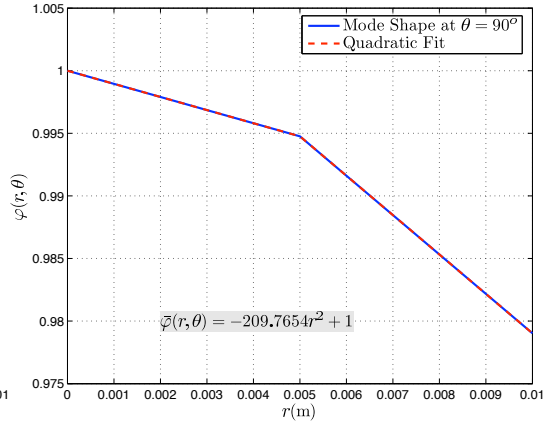

(c) Approximation of mode 5 at $\theta = 90^o$.

Figure 4.11: Quadratic approximation of mode 5 at various circumferential values.

4.4.4 Model Comparison with ANSYS®

Here, we verify the results obtained via ANSYS® and the results obtained through the Galerkin expansion. We first present the first ten natural frequencies. The error is calculated according to,

$$\text{Error } \% = \frac{|f_{ANSYS} - f_{Galerkin}|}{f_{ANSYS}} \times 100 \tag{4.35}$$

Table 4.2 displays the first ten frequencies of the membrane mirror. None of the errors displayed in Table 4.2 exceed 0.9 %. The low error values gives confidence in the numerical model developed and obtained in this section.

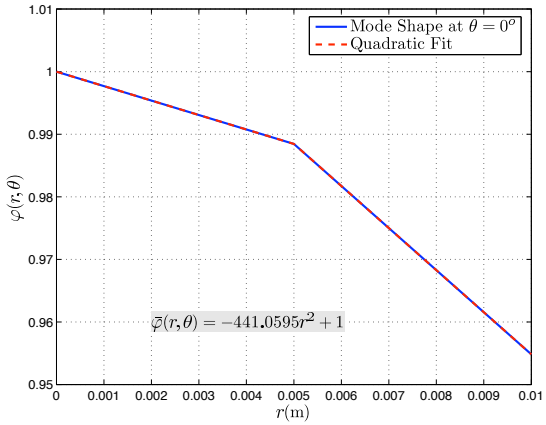

(a) Approximation of mode 9 at $\theta = 0^o$.

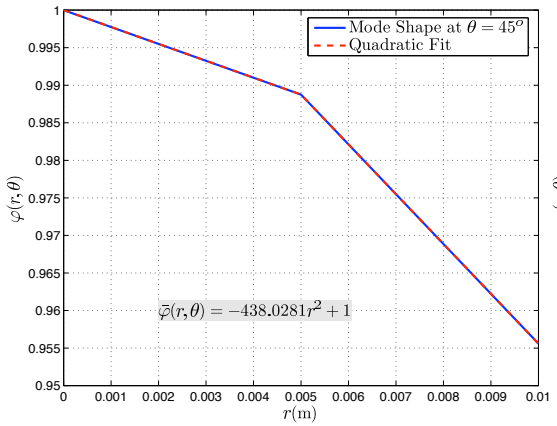

(b) Approximation of mode 9 at $\theta = 45^o$.

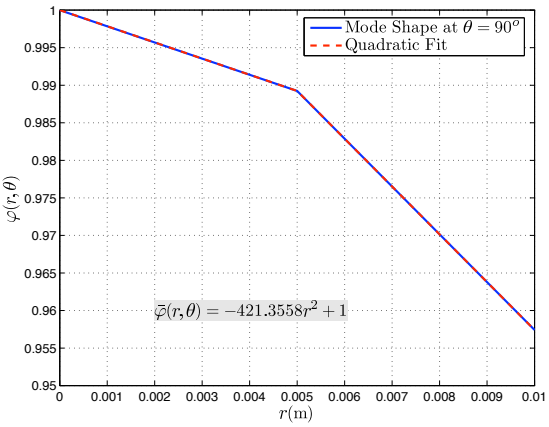

(c) Approximation of mode 9 at $\theta = 90^o$.

Figure 4.12: Quadratic approximation of mode 9 at various circumferential values.

Table 4.2: The first ten natural frequencies of the membrane mirror augmented with four MFC bimorphs.

Mode Number	f_{ANSYS} (Hz)	$f_{Galerkin}$ (Hz)	**Error %**
1	79.176	79.198	0.02
2	110.10	110.35	0.22
3	123.74	124.20	0.37
4	162.28	163.30	0.62
5	193.59	194.10	0.26
6	236.64	237.00	0.15
7	249.17	249.96	0.31
8	258.97	259.12	0.05
9	267.70	268.25	0.20
10	285.23	287.8	0.90

4.5 Chapter Summary

In this chapter, we develop a reduced order model of a circular membrane augmented with four MFC bimorphs. The reduced order model was obtained through a Galerkin expansion and mode shapes obtained through a commercial FEA software package (ANSYS®).

The membrane mirror is modeled as a thin plate under the Kirchhoff theory of plates and shells. Hence, the transverse vibrations of the membrane are considered only. The governing equations are derived from the constitutive and equilibrium equations of a thin plate augmented with a four bimorphs. The mass per unit area and the flexural stiffness of the bimorphs is included in the derived model. Air damping and Kelvin-Voigt damping are included in the model as well.

To perform the Galerkin expansion, the test functions are obtained from ANSYS®. The structure is modeled in ANSYS®and the mode shapes are obtained. Then, these mode shapes (obtained via an FEA) are used as the test functions of the Galerkin expansion. This chapter presented the details of implementing the Galerkin expansion for the structure under study. Numerical issues relevant to obtaining the reduced order model were also discussed and relevant addendum are provided in Appendix A and Appendix C.

The natural frequencies obtained through ANSYS®and through the numerical model obtained from the Galerkin expansion are compared and found to be very close, with the error being less than one percent for the first ten transverse frequency of vibration.

CHAPTER 5

CONTROL OF A CIRCULAR MEMBRANE FOR ADAPTIVE OPTICS

The objective of this dissertation is to correct for optical aberrations in an incoming wavefront through suitable correction of the surface deflection of a circular membrane mirror augmented with smart bimorph actuators. In Chapter 2 we presented a model of a membrane strip augmented with smart bimorph actuators. We modeled various configurations and validated the models experimentally. In Chapter 3, we treated the control problem of membrane strips augmented with smart bimorph actuators and developed linear and nonlinear controllers for these structures. Then, we moved to the structure of main interest: a circular membrane mirror augmented with smart bimorph actuators in Chapter 4 where we developed a reduced order model of the structure using the Galerkin expansion and ANSYS® software. Now, we will treat the control problem for this structure with the correction for optical aberrations as our control objective. We will use adaptive control techniques to correct for optical aberrations and will present a mapping between the mechanical and optical domains to achieve the control objective.

This chapter is organized as follows. In Section 5.1, a brief introduction of Zernike polynomials and their use to describe optical aberrations is presented. In Section 5.2, we present a brief introduction of adaptive control and the motivation for using it. A simple motivating example is used to demonstrate the impetus behind using adaptive control. Section 5.3 lays the mapping we will use to converse between the optical and mechanical domain. The smart actuators have direct control authority over the mechanical deflection of the membrane. However, the objective is to correct for optical aberrations,

and consequently, a clear mapping has to be established between these two domains. In Section 5.4, we present the controller design. We present stability proofs along with all the derivations. A numerical case study is presented in Section 5.5. The chapter is summarized in Section 5.6.

5.1 Zernike Polynomials and Optical Aberrations

Aberrations in an incoming wavefront are usually described using a linear combination of Zernike polynomials over a circular pupil. Zernike polynomials were first introduced by Zernike (1934, 1954) and later popularized by Noll (1976). An optical aberration of the k-th order can be expressed as a linear combination of Zernike circular polynomials as

$$\begin{aligned} W(t,r,\theta) &= \sum_{n=0}^{k}\sum_{m=0}^{n} A_{nm}(t)U_{nm}(r,\theta) \\ &= \sum_{n=0}^{k}\sum_{m=0}^{n} A_{nm}(t)R_n^{n-2m}(r)\begin{cases}\sin[(n-2m)\theta] & n-2m>0\\ \cos[(n-2m)\theta] & n-2m\leq 0\end{cases}, \end{aligned} \tag{5.1}$$

where $A_{nm}(t)$ is the time-varying amplitude, in general, of each Zernike function $U_{nm}(r,\theta)$, and the radial polynomial $R_n^{n-2m}(r)$ is defined as

$$R_n^{n-2m}(r)=\sum_{s=0}^{m}\frac{(-1)^s(n-s)!}{s!(m-s)!(n-m-s)!}r^{n-2s}. \tag{5.2}$$

Table 5.1 displays the radial Zernike polynomials up to the 5$^{\text{th}}$ order. Figure 5.1 displays the first six Zernike functions and the corresponding optical aberration. Equation (5.1) can be simplified further by introducing a positive number l, such that

$$m=\frac{n-l}{2}. \tag{5.3}$$

One can take advantage of m being always an even number, and that $n\geq l$, and write Eq. (5.1) as

$$W(t,r,\theta)=\sum_{n=0}^{k}\sum_{l=0}^{n} R_n^l(a_{nl}(t)\cos(l\theta)+b_{nl}(t)\sin(l\theta)), \tag{5.4}$$

where l takes only values with the same parity as n, and use was made of the fact that $R_n^l = R_n^{-l}$. The coefficients a_{nl} and b_{nl} are related to the coefficients $A_{nl}(t)$ through

$$a_{nl}(t) = A_{n\frac{(n+l)}{2}}(t) \quad \text{and} \quad b_{nl}(t) = A_{n\frac{(n-l)}{2}}(t)\,. \tag{5.5}$$

Consequently, the double summation in Eq. (5.1) is replaced by a single summation, thus simplifying the notation

$$W(t,r,\theta) = \sum_{n=0}^{k}\sum_{m=0}^{n} A_{nm}(t)U_{nm}(r,\theta) = \sum_{r=1}^{L} A_r(t)U_r(r,\theta)\,, \tag{5.6}$$

where, instead of the coefficients n and m, a single index r is defined by its appearance order in the double sum,

$$r = \frac{n(n+1)}{2} + m + 1\,, \tag{5.7}$$

and L is the total number of Zernike polynomials used

$$L = \frac{(k+1)(k+2)}{2}\,, \tag{5.8}$$

and k remains to be the degree of the wavefront aberration.

The most important property of Zernike polynomials is that they constitute an orthogonal basis which is utilized to describe a wavefront aberration within a circular pupil. This condition is expressed as,

$$\int_0^1\int_0^{2\pi} U_{nm}U_{n'm'}\rho\,\mathrm{d}\rho\,\mathrm{d}\theta = \frac{\pi}{2(n+1)}\delta_{nn'}\delta_{mm'}\,. \tag{5.9}$$

Moreover, the mean value of all Zernike polynomials is zero, except for the piston mode, Fig. 5.1a. In the following, an optical aberration in an incoming wavefront will be considered. The optical aberration will be in the form of Eq. (5.6). This optical aberration will map into a desired deformation of the circular membrane to correct for the optical aberration.

Table 5.1: Zernike polynomials $U_{nm}(r,\theta)$ up to the 5$^{\text{th}}$ order.

n	**m**	**n − 2m**	**Zernike Polynomial**	**Optical Interpretation**
0	0	0	1	Piston (constant)
1	0	1	$r\sin(\theta)$	Tilt about y-axis
	1	−1	$r\cos(\theta)$	Tilt about x-axis
2	0	2	$r^2\sin(2\theta)$	Astigmatism with axis at $\pm 45^o$
	1	0	$2r^2-1$	Focus shift
	2	−2	$r^2\cos(2\theta)$	Astigmatism with axis at 0^o or 90^o
3	0	3	$r^3\sin(3\theta)$	Triangular astigmatism with base on the x-axis
	1	1	$(3r^3-2r)\sin(\theta)$	Third-order coma along x-axis
	2	−1	$(3r^3-2r)\cos(\theta)$	Third-order coma along x-axis
	3	−3	$r^3\cos(3\theta)$	Triangular astigmatism with base on the y-axis
4	0	4	$r^4\sin(4\theta)$	
	1	2	$(4r^4-3r^2)\sin(2\theta)$	
	2	0	$5r^4-6r^2+1$	Third-order spherical aberration
	3	−2	$(4r^4-3r^2)\cos(2\theta)$	
	4	−4	$r^4\cos(4\theta)$	
5	0	5	$r^5\sin(5\theta)$	
	1	3	$(5r^5-4r^3)\sin(3\theta)$	
	2	1	$(10r^5-12r^3+3r)\sin(\theta)$	
	3	−1	$(10r^5-12r^3+3r)\cos(\theta)$	
	4	−3	$(5r^5-4r^3)\cos(3\theta)$	
	5	−5	$r^5\cos(5\theta)$	

5.2 Brief Introduction to Adaptive Control

When modeling systems (mechanical, electrical, hydraulic or of any other type), engineers usually seek simple mathematical models often overlooking some parametric and dynamic properties. Consequently, the presence of parametric and dynamic uncertainties in mathematical models is extremely hard to avoid. For instance, robotic manipulators pick payloads that might be of unknown inertial parameters. Power systems, are sometimes subjected to large variations in loading scenarios. A fire-fighting aircraft experiences a huge change of mass as water is loaded from an open water source and unloaded onto burning areas. The examples mentioned are samples of real-life systems, which one might say that all exhibit parametric and modeling uncertainties. Controlling such systems is a formidable task, and this is where adaptive control comes into play. In other words, adaptive control is an approach for controlling real-life systems.

However, someone might question the use of adaptive control since many systems are already operating using classical control techniques. A recent approach is to augment existing controllers that have proved performance for a range of parameters with adaptive control techniques. With this approach, adaptation is used to improve the closed loop performance beyond the limits of the standard controller.

The fundamental concept of adaptive control is to estimate the unknown parameters of the system in real-time based on the measured response of the signals of the system. The control input will be a function of the estimated parameters and the measured response of the system. In other words, an adaptive controller is a feedback controller with a real-time parameter estimator. Adaptive control is inherently nonlinear (even if the controlled system is linear), and its design and analysis (proof of stability) is strongly based on the Lyapunov stability theory.

The underlying philosophy of adaptive control is mimicking the behavior of biological systems. For example, creatures, animals, birds, insects are continuously adapting to changes in the environment. Human beings are continuously adjusting to the surrounding circumstances. Thus, the development of adaptive control techniques initiates an “intelligent behavior” for an engineering system. The controller changes with

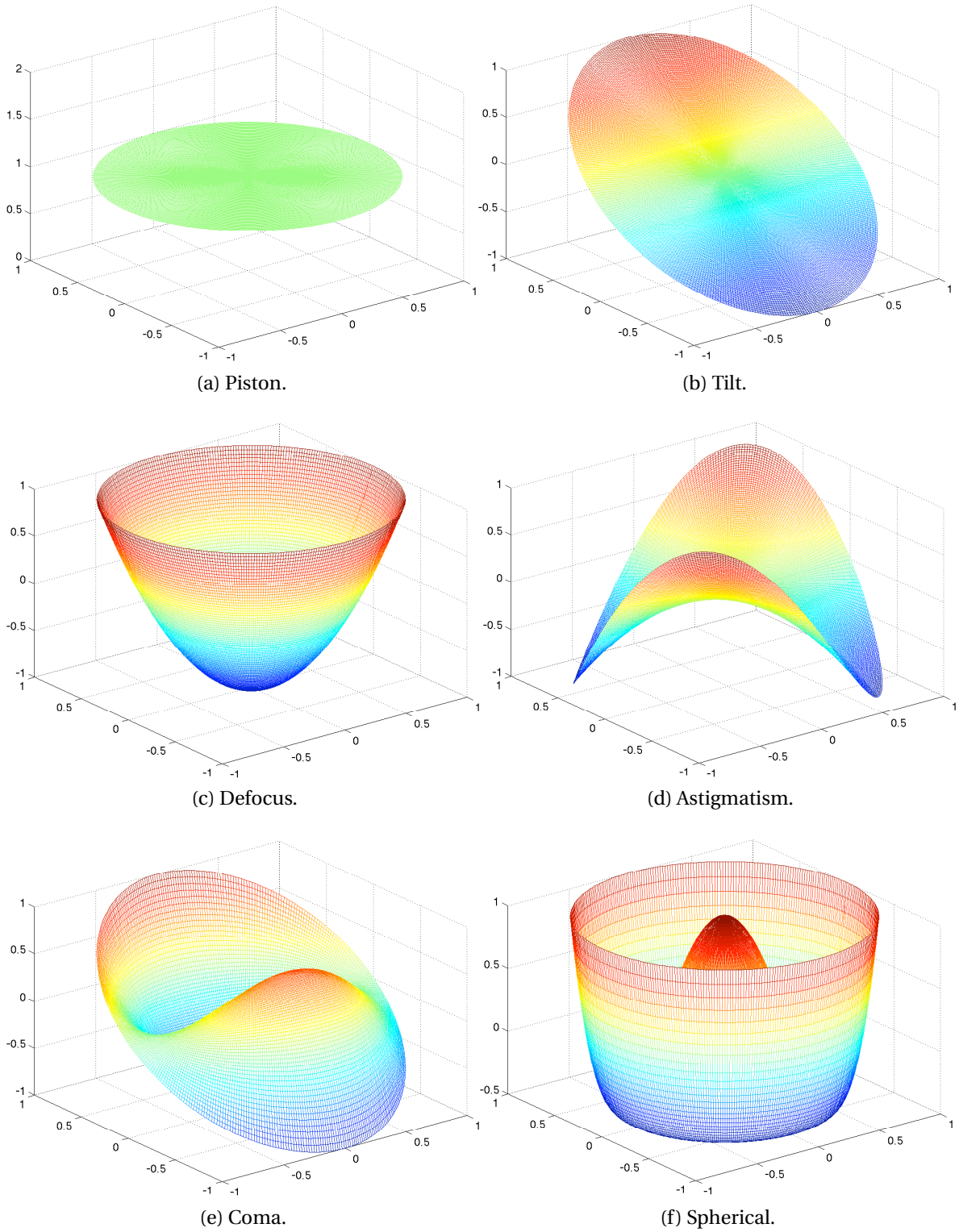

(a) Piston.

(b) Tilt.

(c) Defocus.

(d) Astigmatism.

(e) Coma.

(f) Spherical.

Figure 5.1: First six Zernike functions and the corresponding optical aberration.

time to adapt to the needs of the system in order to achieve the control objectives. Now, we present a motivating example highlighting some features of adaptive control. For additional references on adaptive control, the reader is advised to consult (Sastry and Bodson, 1989), (Marino and P., 1995) and (Khalil, 2000).

5.2.1 Motivating Example

To gain some practical insights into the adaptive control area, we present a simple first order example. Consider the following model of a first order system

$$\dot{x}(t) = a x(t) + u(t) \quad , \quad x(0) = x_0 \, . \tag{5.10}$$

Here, we assume that a itself is unknown with hard bounds, i.e., $a_{min} \leq a \leq a_{max}$ with a_{min} and a_{max} known. Then, a natural straightforward control choice would be,

$$u_{lin}(t) = -k_{lin} x(t) \quad , \quad k_{lin} > a_{max} \, ,$$

leading to

$$\dot{x}(t) = -(k_{lin} - a) x(t) \, .$$

Since $k_{lin} > a_{max}$, it is guaranteed that the system is stable. One can directly solve the above differential equation and observe that the response decays exponentially. However, this design suffers from two deficiencies:

1. The design is overly conservative. The stability of the closed loop system relies on knowing a conservative a_{max} to make sure that the selected gain is large enough, i.e., $k_{lin} > a_{max}$ to achieve a negative pole in the system $\dot{x}(t) = -(k_{lin} - a) x(t)$. If the estimation of a_{max} is not good for the entire range of operations of the system, and at some point in time, the selected feedback gain fails to satisfy $k_{lin} > a_{max}$, the system becomes unstable. Such a case could happen in aircraft control where during the flight envelope, the conservative enough linear gain might lose its dominance over the unknown parameter and the results might be catastrophic.

2. Being conservative is not only in estimating a_{max}, and as a result selecting k_{lin} to be large enough. There is another pitfall of this approach. The controller will be

producing maximum control effort for the entire control duration, which might lead to exhausting the hardware. One might question this strategy: why use the maximum control effort if everything is going smooth, i.e., the unknown parameter a is well within the range estimated.

The above two points present a motivation for developing a controller that adapts to the parameters of the system while keeping the closed loop stable. Adaptive control provides an alternative design for the system in Eq. (5.10). In the spirit of adaptation, we let the control input be

$$u_{ad}(t) = k(t)x(t)\,,$$

where the feedback gain is time varying now. The feedback gain evolves according to a first order differential equation, given by

$$\dot{k}(t) = -\gamma x^2(t)\,,$$

where γ is called the adaptation gain and can be selected to be any positive number. Substituting the proposed control law in the system dynamics leads to the following closed-loop system,

$$\dot{x}(t) = a_m x(t) + (k(t) + a - a_m)x(t) \quad , \quad a_m < 0\,, \tag{5.11}$$

where a_m is introduced (added and subtracted from the original system) to model the desired transient behavior (overshoot, settling time, etc.). In such case, one don't even need to know the bounds of a, and stabilization is achieved independent of it. The idea behind what we are doing comes from Lyapunov stability theory, where we propose the following as a candidate Lyapunov function,

$$V(x(t), k(t)) = \frac{1}{2}x^2(t) + \frac{1}{2\gamma}(k(t) + a - a_m)^2\,.$$

The derivative of the above Lyapunov function is,

$$\dot{V}(x(t), k(t)) = x(t)\dot{x}(t) + \frac{1}{\gamma}\dot{k}(t)(k(t) + a - a_m)\,. \tag{5.12}$$

which simplifies to

$$\dot{V}(x(t), k(t)) = a_m x^2(t) \leq 0\,, \tag{5.13}$$

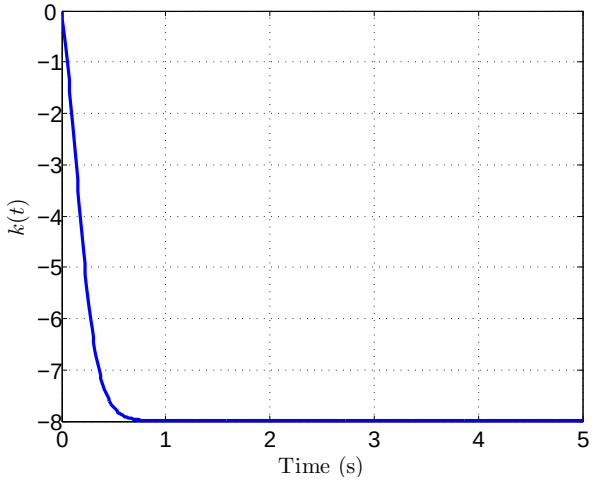

(a) Adaptive feedback gain $k(t)$.

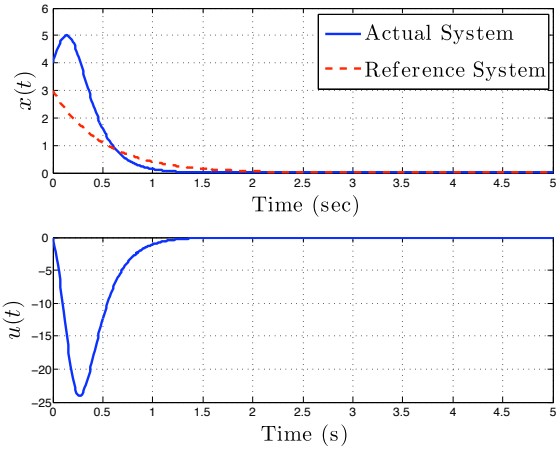

(b) Performance of an adaptive controller.

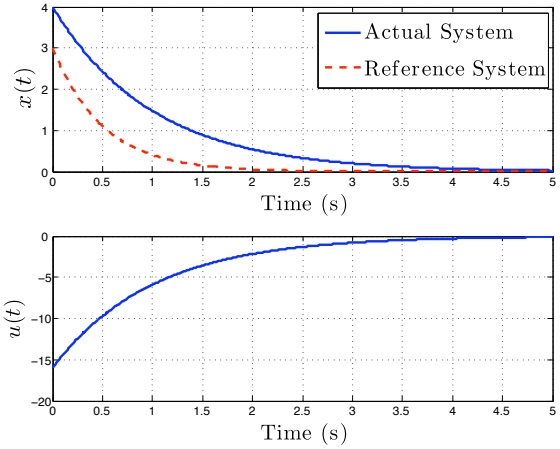

(c) Performance of a linear controller.

Figure 5.2: Control input and output time histories for $a = 3$, $a_m = -2$, , $\gamma = 1, k_{lin} = 4$, $x(0) = 4$, $x_m(0) = 3$, $a_{max} = 3.75$.

since a_m is negative by design of the system. Thus, a time-varying $k(t)$, Fig. 5.2a, with a correctly selected adaptation law can achieve stabilization at less expense than that of a fixed-gain controller designed for conservative bounds for the unknown parameter a, Fig. 5.2.

The simple adaptive controller provided herein is an inverse Lyapunov design, i.e., it is derived from Lyapunov analysis. Notice that the adaptive controller is nonlinear, although the system under study is linear.

We now turn our attention to defining the relationship between the optical modes and mechanical modes of the circular membrane.

5.3 Mapping Between Optical and Mechanical Domains

After introducing the Zernike polynomials and a brief overview of the concept and motivation for adaptive control, we focus now on relating the mechanical domain to the optical domain, as proposed by Ruggiero (2005). The optical aberration described in Section 5.1 can be expressed as a linear combination of Zernike functions. It is described in terms of the deformation of the surface given as,

$$W(t,r,\theta)=\sum_{r=1}^{L}A_r(t)U_r(r,\theta)\,. \tag{5.14}$$

Fig. 5.3 shows a sample wavefront aberration over a circular domain of unit radius. But,

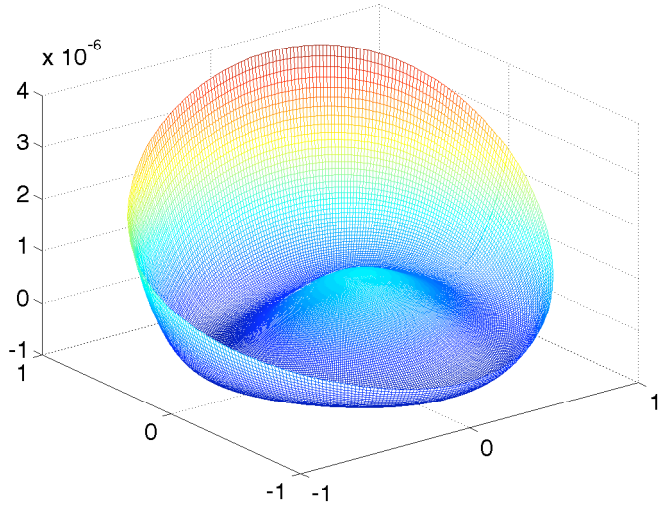

Figure 5.3: Sample optical aberration over a circular mirror of unit radius. The instantaneous amplitudes of the Zernike modes are: $A_1 = 0.72, A_2 = 0.30, A_3 = 0.83, A_4 = 0.56, A_5 = 0.37, A_6 = 0.70, A_7 = 0.54, A_8 = 0.44, A_9 = 0.69$ and $A_{10} = 0.62$ (all units are in nm.)

we know that the surface deformation of the circular membrane is described as

$$w(t,r,\theta)=\sum_{i=1}^{N}q_i(t)\varphi_i(r,\theta)\,, \tag{5.15}$$

from Section 4.3. A fundamental difference appears after one states the above equations. The Zernike functions $U_{mn}(r,\theta)$ do not satisfy the mechanical boundary conditions of the circular membrane mirror. This can be seen if one examines the radial Zernike polynomials of Table 5.1 or the three dimensional plots of Fig. 5.1 and Fig. 5.3. However, the test functions (mode shapes), $\varphi_i(r,\theta)$ do satisfy the mechanical boundary conditions of the structure as seen in Fig. 4.4 through Fig. 4.8, and as necessitated by the derivation of Section 4.3.

In adaptive optics, to be able to correct for the wavefront aberration $W(r,\theta,t)$, the reflective surface (membrane mirror in this work) should deform to to the shape produced by the wavefront aberration,

$$W(t,r,\theta) = w(t,r,\theta) \quad \Rightarrow \quad \sum_{r=1}^{L} A_r(t)U_r(r,\theta) = \sum_{i=1}^{N} q_i(t)\varphi_i(r,\theta)\,. \tag{5.16}$$

The Zernike functions and the modes shapes of a circular membrane are known. The mode shapes of a circular membrane are usually represented through Bessel functions (Meirovitch, 1997). Shepherd et al. (2006b) presented a transformation between the Zernike functions and the Bessel functions for the clear aperture region of circular membrane. In this work, the clear aperture region would be for $r < r_a$ in Fig. 4.3 on Page 109. Moreover, in this work, the mode shapes are not determined in terms of the Bessel function because the circular membrane exhibits varying physical properties (such as thickness, flexural stiffness and structural damping). Consequently, we resort to a numerical transformation in this dissertation. Moreover, our objective is to match the optical aberration with the mechanical deformation within the clear aperture we are defining. It is physically impossible to match the mechanical deformation of the membrane mirror to the wavefront aberration since the two have a fundamental difference: the Zernike functions used as a basis to describe the wavefront aberration do not match the physical boundary condition of the circular membrane. Hence,

$$\sum_{r=1}^{L} A_r(t)U_r(r,\theta) = \sum_{i=1}^{N} q_i(t)\varphi_i(r,\theta) \quad \forall\, 0 \le \theta \le 2\pi \quad \text{and} \quad \forall\, r \le r_a\,. \tag{5.17}$$

In order to simplify the notation, we will refer to the Zernike function and mode shapes

within the clear aperture by $\bar{U}_r(r,\theta)$ and $\bar{\varphi}_i(r,\theta)$, or

$$\bar{U}_r(r,\theta) = U_r(r,\theta) \quad \text{and} \quad \bar{\varphi}_i(r,\theta) = \varphi_i(r,\theta) \quad \forall\ r \le r_a\ . \tag{5.18}$$

To this end, our goal is to relate the amplitudes of the optical aberration, $A_r(t)$ to the modal amplitudes, $q_i(t)$. The assumption here is that the amplitudes of the optical aberration are readily available. This is a common practice in the field of adaptive optics where a Shack-Hartmann wavefront sensor could be used to measure the amplitude of each Zernike function. Hence, Eq. (5.17) can be modified to

$$A_1(t)\bar{U}_r(r,\theta) + \ldots + A_L(t)\bar{U}_r(r,\theta) = q_1(t)\bar{\varphi}_1(r,\theta) + \ldots + q_N(t)\bar{\varphi}_N(r,\theta)\,, \tag{5.19a}$$

which can be cast into matrix form,

$$\begin{bmatrix} \bar{U}_1(r,\theta) & \ldots & \bar{U}_L(r,\theta) \end{bmatrix} \begin{Bmatrix} A_1(t) \\ \vdots \\ A_L(t) \end{Bmatrix} = \begin{bmatrix} \bar{\varphi}_1(r,\theta) & \ldots & \bar{\varphi}_N(r,\theta) \end{bmatrix} \begin{Bmatrix} q_1(t) \\ \vdots \\ q_N(t) \end{Bmatrix}. \tag{5.19b}$$

Then, one can solve for the mechanical modal amplitudes as,

$$\begin{Bmatrix} q_1(t) \\ \vdots \\ q_N(t) \end{Bmatrix} = \begin{bmatrix} \bar{\varphi}_1(r,\theta) & \ldots & \bar{\varphi}_N(r,\theta) \end{bmatrix}^{+} \begin{bmatrix} \bar{U}_1(r,\theta) & \ldots & \bar{U}_L(r,\theta) \end{bmatrix} \begin{Bmatrix} A_1(t) \\ \vdots \\ A_L(t) \end{Bmatrix}, \tag{5.20}$$

where the superscript "+" indicates the psuedo-inverse of the matrix. Additional information regarding the implementation of the transformation of Eq. (5.20) is provided in Appendix D.

5.4 Controller Design

The model derived in Chapter 4 can be used to develop a control algorithm for the structure under study, Fig. 4.3 on Page 109. We cast the governing equation, Eq. (4.33) of Page 108, in the state space form

$$\dot{x} = Ax + \bar{B}u(t)\,, \tag{5.21}$$

where

$$A = \begin{bmatrix} 0 & I \\ M^{-1}K & M^{-1}C \end{bmatrix} \quad , \quad B = \begin{bmatrix} 0 \\ M^{-1}\bar{B} \end{bmatrix} \quad , \quad x = \begin{Bmatrix} q \\ \dot{q} \end{Bmatrix} \quad \text{and} \quad u(t) = V(t)\,. \tag{5.22}$$

The derivation conducted in Chapter 4 sought a linear model of the structure. However, real structures are plagued with dynamic and parametric uncertainties. Here we assume that the magnitude of uncertainty is relatively small, and hence the uncertainties can be approximated through a linear combination of known nonlinear functions. This will be expanded further in the following.

In this section, we seek an adaptive control law that will enable the membrane to correct for time varying optical aberrations. However, since we have obtained a linear model of the system, we will take advantage of this derivation, and construct a linear controller for the system. We will then augment the linear controller with an adaptive law that is activated whenever the performance of the linear controller ceases to satisfy the performance criteria.

At this point, a word regarding controller augmentation is in order. Augmenting an existing controller with an additional adaptive controller to enhance the performance of the closed loop system is called Lyapunov redesign. Typically in engineering applications, a nominal controller is usually designed and in most of the time achieves acceptable performance. However, as we discussed in Section 5.2, this strategy has its limitations. It would be extremely desirable, for example, to augment an existing LQR controller that has good stability margins, good tracking, and acceptable transient characteristics, with an adaptive controller. The augmented controller deploys the adaptive controller only when the performance of the LQR controller is not good enough. The design has to have conservative guidelines such that in the absence of uncertainties, the adaptation laws will not be activated. However, in the presence of uncertainties, the contribution of the adaptive controller will increase as the adaptation gains increase. It is easier to visualize adaptive augmentation in a scalar differential system, hence an illustrative example is presented in Appendix E.

5.4.1 Control Problem Formulation

To implement the control scheme described above, one needs to define a reference model that the system has to track. A common choice of a reference model is the optimal control law for the nominal linearized system. In other words, the LQR controller is used to define a reference system which is linearized and has no uncertainties. This closed loop reference system will be the target for the closed loop of the actual system. To this end, assume the model of the structure of Fig. 4.3 is written as,

$$\dot{x}(t) = Ax(t) + B\Lambda(u(t) + f(x)) \tag{5.23}$$

where A is the known $(N \times N)$ state matrix given in Eq. (5.22), B is the known $(N \times m)$ input matrix (also given in Eq. (5.22)), $\Lambda = \text{diag}(\lambda_1, \cdots, \lambda_m)$ represents the uncertainties in the control effectiveness and the sign(Λ) is known. The function $f(x)$ is a vector of uncertain matched nonlinear functions, i.e.,

$$f(x) = W^T \Phi(x(t)) \text{ , where } W \in \mathbb{R}^{s \times m} \text{ and } \Phi(x(t)) \in \mathbb{R}^{s \times m} . \tag{5.24}$$

In the above, W is a matrix of unknown constants and $\Phi(x(t))$ is a matrix of known nonlinear functions. For the known nonlinear functions, we select a set of radial basis functions. A radial basis function (RBF) is a real valued function, whose value depends only on the distance from a center, i.e., $\Phi(x(t)) = \Phi(\|x(t) - c\|)$. Any function that satisfies this property is radial, and the norm is Euclidean. In Eq. (5.24), RBFs are used to build up an approximation of $f(x)$. We further select the Gaussian type of RBFs, and these are given by

$$\Phi(x(t)) = e^{-\frac{(x-c)^2}{r^2}} , \tag{5.25}$$

where c represents the mean value of the variable and r represents the standard deviation of the Gaussian function. For Eq. (5.24), we would have a matrix of mean values and standard deviations, since every element of the vector function $f(x)$ is a function in itself, and it needs a vector of mean values and standard deviations to be approximated. Hence, c and r are $s \times m$ matrices. Figure 5.4 shows the normalized RBFs if $s = 1$.

As mentioned previously, Eq. (5.24) presents a linear combination to approximate the uncertainties in the system. This is based on the assumption that the uncertainties

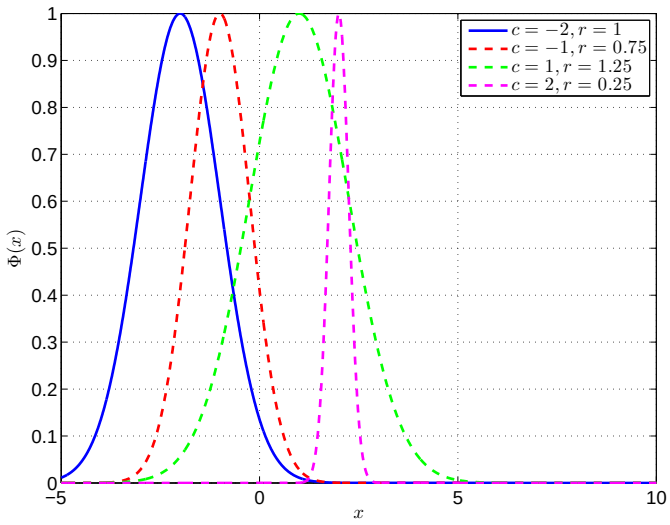

Figure 5.4: Normalized radial bounded functions of the form of Eq. (5.25), with $c = (-2,-1,1,2)$ and $r = (1, 0.75, 1.25, 0.25)$ (m has to be 4 since we have four actuators).

have a small magnitude. In other system, even though the number of parametric uncertainties might be relatively small (compared to the complexity of the system), the magnitude of the uncertainty might be large. Consequently, the linear approximation of uncertainties we are using here would not be efficient enough, and other techniques shall be used. One of these techniques is the generalized polynomial chaos theory (among others). The interested reader is referred to the article of Xiu and Karniadakis (2002) which is a classical in this area. Sandu et al. (2006a,b) used the generalize polynomial chaos theory to model complex nonlinear multibody systems.

Now, we turn our attention again to the model presented in Eq. (5.21), we can design an LQR controller (Dorato et al., 2000). This LQR controller can be expressed as

$$u_{lin}(t) = -K_{LQR}^{T} x(t) + K_g r(t)\,, \tag{5.26}$$

where the feed-forward gain K_g is usually selected to achieve asymptotic tracking for a step input dependent upon the particular regulated output of interest, while K_{LQR} is computed using the positive semi-definite symmetric solution of the corresponding Riccati equation. The above control law leads to the following nominal linear system that has the desired specifications

$$\dot{x}_m(t) = A_m x(t) + B_m r(t)\,, \tag{5.27}$$

where $A_m = A - BK_{LQR}$, and $B_m = BK_g$. The above derivation provides us with a reference model that the actual system has to track. Following the direct adaptive model reference control technique, and in the spirit of LQR controller augmentation, the control law can be expressed as,

$$u(t) = u_{lin}(t) + u_{ada}(t)\,, \tag{5.28}$$

where the adaptive control input is

$$u_{ada}(t) = K_x^T(t)x(t) + K_r(t)r(t) - \hat{W}^T(t)\Phi(x(t))\,, \tag{5.29}$$

and the linear control input was defined in Eq. (5.26). The control input can then be presented as,

$$u(t) = \left(K_x^T(t) - K_{LQR}^T\right)x(t) + \left(K_r(t) + K_g\right)r(t) - \hat{W}^T(t)\Phi(x(t))\,. \tag{5.30}$$

If one substitutes the above control input in Eq. (5.23), the closed loop dynamics would be described as

$$\dot{x}(t) = \left[A + B\Lambda(K_x^T(t) - K_{LQR}^T)\right]x(t) + B\Lambda(K_r + K_g)r(t) + B\Lambda\Delta W^T(t)\Phi(x(t))\,, \tag{5.31}$$

where $\Delta W = \hat{W}(t) - W$ is the parameter estimation error.

Comparing the dynamics of Eq. (5.31) to Eq. (5.27), we can formulate two assumptions to guarantee the existence of the adaptive feedback signal. First, we assume that

$$\exists K_x^* \text{ such that } A + B\Lambda\left((K_x^*)^T - K_{LQR}^T\right) = A_m\,, \tag{5.32a}$$

and

$$\exists K_r^* \text{ such that } B\Lambda(K_r^* + K_g) = B_m\,. \tag{5.32b}$$

It is not required to calculate the ideal gains K_x^* and K_r^*, however their existence is a necessary condition for the existence of the adaptive feedback signal.

We now formulate the tracking error signal as $e(t) = x(t) - x_m(t)$. Using the reference system dynamics, Eq. (5.27), the closed loop system dynamics, Eq. (5.31), and the matching conditions Eq. (5.32), we can obtain the error dynamics,

$$\dot{e}(t) \;=\; \dot{x}(t) - \dot{x}_m(t)$$

$$= A_m e(t) + B\Lambda\left(\Delta K_x^T(t)x(t) + \Delta K_r(t)r(t) - \Delta W^T(t)\Phi(x(t))\right), \quad (5.33)$$

where $\Delta K_x(t) = K_x(t) - K_x^*(t)$ and $\Delta K_r = K_r(t) - K_r^*$ denote the state gain and reference input gain errors respectively. The following adaptation laws are considered,

$$\begin{aligned}
\dot{K}_x(t) &= -\Gamma_x x(t) e^T(t) PB\,\text{sign}(\Lambda), \\
\dot{K}_r(t) &= -\Gamma_r r(t) e^T(t) PB\,\text{sign}(\Lambda), \\
\dot{\hat{W}}(t) &= \Gamma_W \Phi(x(t))\, e^T(t) PB\,\text{sign}(\Lambda), \qquad (5.34)
\end{aligned}$$

where Γ_x, Γ_r and Γ_W are positive definite symmetric gain matrices of the state, the reference input and the unknown parameters W, respectively. Moreover, P is a positive definite symmetric matrix which satisfies the algebraic Lyapunov equation,

$$A_m^T P + P A_m = -Q,$$

for any arbitrary positive definite Q. To this end, we need to show the stability of the closed loop system. The following candidate Lyapunov function is proposed to analyze the stability of the system,

$$\begin{aligned}
V(e(t), \Delta K_x(t), \Delta K_r(t), \Delta W(t)) = e^T(t)Pe(t) + \text{trace}\left(\Delta K_x^T(t)\Gamma_x^{-1}\Delta K_x(t)|\Lambda|\right) \\
+\text{trace}\left(\Delta K_r^T(t)\Gamma_r^{-1}\Delta K_r(t)|\Lambda|\right) + \text{trace}\left(\Delta W^T(t)\Gamma_W^{-1}\Delta W(t)|\Lambda|\right), \quad (5.35)
\end{aligned}$$

where $\text{trace}(\Lambda) \equiv \sum_{i=1}^m \lambda_{ii}$. The time derivative of the candidate Lyapunov function is along the system trajectories Eq. (5.33) and Eq. (5.34) is:

$$\begin{aligned}
\dot{V} &= \dot{e}^T(t)Pe(t) + e^T(t)P\dot{e}(t) + \frac{\mathrm{d}}{\mathrm{d}t}\text{trace}\left(\Delta K_x^T(t)\Gamma_x^{-1}\Delta K_x(t)|\Lambda|\right) \\
&+ \frac{\mathrm{d}}{\mathrm{d}t}\text{trace}\left(\Delta K_r^T(t)\Gamma_r^{-1}\Delta K_r(t)|\Lambda|\right) + \frac{\mathrm{d}}{\mathrm{d}t}\text{trace}\left(\Delta W^T(t)\Gamma_W^{-1}\Delta W(t)|\Lambda|\right). \quad (5.36)
\end{aligned}$$

Notice that,

$$\begin{aligned}
&\dot{e}^T(t)Pe(t) + e^T(t)P\dot{e}(t) = e^T(t)A_m^T Pe(t) \\
&+\left(\Delta K_x^T(t)x(t) + \Delta K_r(t)r(t) - \Delta W^T(t)\Phi(x(t))\right)^T \Lambda^T B^T Pe(t) \\
&e^T(t)PA_m e(t) + e^T(t)PB\Lambda\left(\Delta K_x^T(t)x(t) + \Delta K_r(t)r(t) - \Delta W^T(t)\Phi(x(t))\right) \\
&= -e^T(t)Qe(t)
\end{aligned}$$

$$+2e^T(t)PB\Lambda\left(\Delta K_x^T(t)x(t)+\Delta K_r(t)r(t)-\Delta W^T(t)\Phi(x(t))\right) \tag{5.37}$$

Moreover,

$$\begin{aligned}&\frac{\mathrm{d}}{\mathrm{d}t}\mathrm{trace}\left(\Delta K_x^T(t)\Gamma_x\Delta K_x(t)|\Lambda|\right)=\mathrm{trace}\left(\frac{\mathrm{d}}{\mathrm{d}t}\left(\Delta K_x^T(t)\Gamma_x^{-1}\Delta K_x(t)\right)|\Lambda|\right)\\&=\mathrm{trace}\left(\Delta\dot{K}_x^T(t)\Gamma_x\Delta K_x(t)|\Lambda|\right)+\mathrm{trace}\left(\Delta K_x^T(t)\Gamma_x^{-1}\Delta\dot{K}_x(t)|\Lambda|\right)\ .\end{aligned}$$

However the trace of a matrix equals the trace of its transpose, hence

$$\mathrm{trace}\left(\Delta\dot{K}_x^T(t)\Gamma_x\Delta K_x(t)|\Lambda|\right)=\mathrm{trace}\left(|\Lambda^T|\Delta K_x^T(t)\Gamma_x^{-1}\Delta\dot{K}_x(t)\right)\ ,$$

and since Λ is diagonal, and since the $\mathrm{trace}(ab)=\mathrm{trace}(ba)$ for any square matrices a and b, then

$$\mathrm{trace}\left(\Delta K_x^T(t)\Gamma_x\Delta\dot{K}_x(t)|\Lambda|\right)=\mathrm{trace}\left(\Delta\dot{K}_x^T(t)\Gamma_x^{-1}\Delta K_x(t)|\Lambda|\right)\ .$$

So, one arrives at

$$\frac{\mathrm{d}}{\mathrm{d}t}\mathrm{trace}\left(\Delta K_x^T(t)\Gamma_x\Delta K_x(t)|\Lambda|\right)=2\mathrm{trace}\left(\Delta K_x^T(t)\Gamma_x^{-1}\Delta\dot{K}_x(t)|\Lambda|\right)\ . \tag{5.38}$$

Similarly, the remaining terms in Eq. (5.36) yield,

$$\begin{aligned}&\dot{V}=-e^T(t)Qe(t)+2e^T(t)PB\Lambda\left(\Delta K_x^T(t)x(t)+\Delta K_r(t)r(t)-\Delta W(t)\Phi(x(t))\right)\\&+2\mathrm{trace}\left(\Delta K_x^T(t)\Gamma_x^{-1}\Delta\dot{K}_x(t)|\Lambda|\right)+2\mathrm{trace}\left(\Delta K_r^T(t)\Gamma_r^{-1}\Delta\dot{K}_r(t)|\Lambda|\right)\\&+2\mathrm{trace}\left(\Delta W^T(t)\Gamma_W^{-1}\Delta\dot{W}(t)|\Lambda|\right)\ .\end{aligned} \tag{5.39}$$

Using the trace identity that

$$a^Tb=\mathrm{trace}(ba^T)\,,$$

one can change the way the second term of the Lyapunov derivative to,

$$\begin{aligned}&e^T(t)PB\Lambda\left(\Delta K_x^T(t)x(t)+\Delta K_r(t)r(t)-\Delta W^T(t)\Phi(x(t))\right)\\&=\mathrm{trace}\left(\Delta K_x^T(t)x(t)e^T(t)PB\Lambda\right)+\mathrm{trace}\left(\Delta K_r(t)r(t)e^T(t)PB\Lambda\right)\\&-\mathrm{trace}\left(\Delta W^T(t)\Phi(x(t))\,e^T(t)PB\Lambda\right)\ .\end{aligned} \tag{5.40}$$

Then, Eq. (5.39) is rearranged to

$$\dot{V}=-e^T(t)Qe(t)+2\mathrm{trace}\left(\Delta K_x^T(t)\left[\Gamma_x^{-1}\Delta\dot{K}_x(t)+x(t)e^T(t)PB\mathrm{sign}(\Lambda)\right]|\Lambda|\right)$$

$$+2\text{trace}\left(\Delta K_r^T(t)\left[\Gamma_r^{-1}\Delta\dot{K}_r(t)+r(t)e^T(t)PB\text{sign}(\Lambda)\right]|\Lambda|\right)$$
$$+2\text{trace}\left(\Delta W^T(t)\left[\Gamma_W^{-1}\Delta\dot{W}(t)-\Phi(x(t))\,e^T(t)PB\text{sign}(\Lambda)\right]|\Lambda|\right)\,. \tag{5.41}$$

Since $\Delta\dot{K}_x(t)=\dot{K}_x(t)$, $\Delta\dot{K}_r(t)=\dot{K}_r(t)$, $\Delta\dot{W}(t)=\dot{\hat{W}}(t)$, and invoking the adaptation laws stated in Eq. (5.34), the derivative of the Lyapunov function becomes,

$$\dot{V}=-e^T(t)Qe(t)\leq 0\,, \tag{5.42}$$

which is negative semi-definite. So far we have shown that the proposed adaptation laws result in a negative semi-definite time derivative of the candidate Lyapunov function (which is positive semi-definite by construction). As per Lyapunov's theory, the equilibrium of Eq. (5.33) and Eq. (5.34) is stable. Consequently, $e(t)$, ΔK_x, ΔK_r and ΔW are bounded. Since $x(t)=e(t)+x_m(t)$, and since $x_m(t)$ is the state of the reference model which is bounded, then $x(t)$ is also bounded. The above developments guarantee for us that the error is bounded, but does not prove that $x(t)\rightarrow x_m(t)$. To establish such result, we first compute the second time derivative of the Lyapunov function,

$$\ddot{V}=-\dot{e}^T(t)Q+e^T(t)Q\dot{e}(t)=-2e^T(t)Q\dot{e}(t)$$
$$=-2e^T(t)Q\left[A_m e(t)+B\Lambda\left(\Delta K_x^T(t)x(t)+\Delta K_r(t)r(t)-\Delta W^T(t)\Phi(x(t))\right)\right]\,, \tag{5.43}$$

which is bounded since all the signals are bounded (the reference $r(t)$ is usually a bounded signal). Before invoking Barbalat's lemma, we state it below for completeness:

Lemma 5.4.1 ***Barbalat's Lemma*** *If $f(t)$ has a finite limit as $t\rightarrow\infty$ and if $\dot{f}(t)$ is uniformly continuous (or $\ddot{f}(t)$ is bounded), then $\dot{f}(t)\rightarrow 0$ as $t\rightarrow\infty$.*

Barbalat's Lemma can be applied to the problem we are considering. In Eq. (5.43), we show that the $\ddot{V}$ is bounded, which means that $\dot{V}$ is uniformly continuous, and V has a finite limit by construction. As a result, $\dot{V}\rightarrow 0$ or $e(t)\rightarrow 0$ asymptotically. Hence, $x(t)$ converges to $x_m(t)$ asymptotically.

5.5 Case Study

The controller developed in Section 5.4 is simulated for the structure of Chapter 4. The numerical simulation was conducted using MATLAB® where the sampling time

was set to 0.01 s and the simulation time was 10 s.

In the following we demonstrate the efficacy of the controller with three simulations. In all the simulations presented, the adaptation gains of the controller were the same, Table 5.2. For obtaining the LQR controller, the state penalty matrix was $10^3\mathbf{I}_{N\times N}$ and the input penalty matrix was set to $\mathbf{I}_{m\times m}$ ($m=4$ since we use 4 actuators). Moreover, for

Table 5.2: Adaptation gains of the controller used for both case studies ($s=5$).

Adaptation Gain Matrix	Value
Γ_x	$10^4\mathbf{I}_{N\times N}$
Γ_r	$10\mathbf{I}_{m\times m}$
Γ_W	$10^5\mathbf{I}_{s\times s}$

obtaining the nominal LQR gain, the properties in Table 4.1 are used. Recall that the LQR gain matrix is obtained based on a nominal value of the state matrix. The nominal value of the state matrix is a reflection of nominal properties of the structure, Table 4.1. For the simulation results displayed in this section, we used different physical properties, so we can demonstrate the efficacy of the adaptive controller. We assume the real physical properties of the circular membrane are listed in Table 5.3. These values are unknown to us; the nominal values are used for the LQR design and the real values are used for the simulation of the closed loop system. The values of Table 5.3 indicate that the nominal

Table 5.3: Real and nominal physical properties of the circular membrane.

Property	Kapton		MFC Patch	
	Real	Nominal	Real	Nominal
Density [kg/m^3]	1200	1420	1500	994
Young's Modulus [GPa]	7	3	50	34.5
Thickness [mm]	45×10^{-3}	51×10^{-3}	0.35	0.3

area density (at the actuator location) is 43.2% less than the real area density, and that the nominal flexural stiffness (at the actuator location) is 56.5% less than the real flexural stiffness. The area density and flexural stiffness can be calculated using Eq. (4.22).

For the first simulation, we assume that the coefficients of the defocus and astigmatism modes are the only coefficients retained. In a practical setting, the piston, tip and tilt modes can be corrected by moving the rigid frame holding the mirror (Shepherd

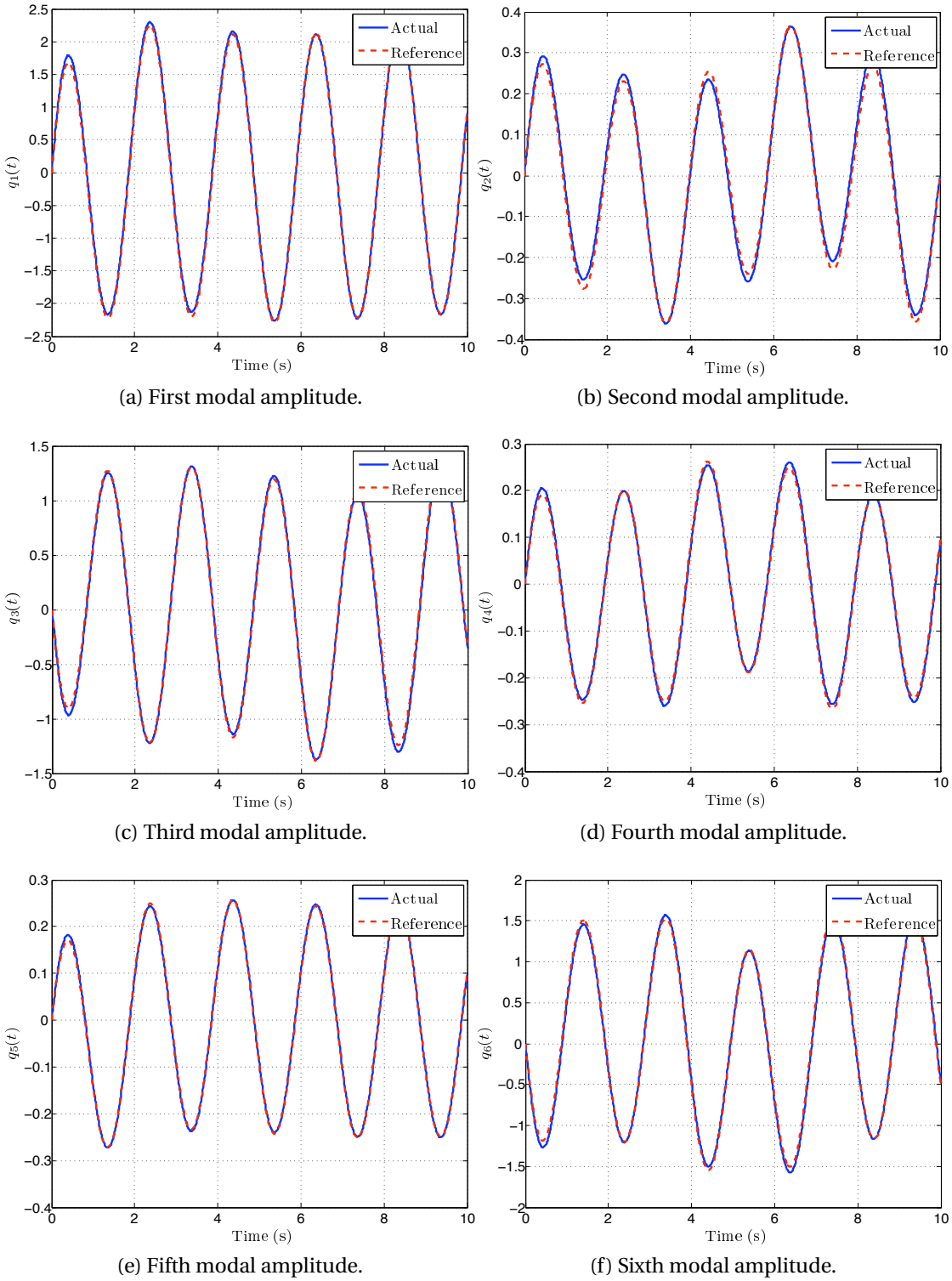

(a) First modal amplitude.

(b) Second modal amplitude.

(c) Third modal amplitude.

(d) Fourth modal amplitude.

(e) Fifth modal amplitude.

(f) Sixth modal amplitude.

Figure 5.5: Time history of modal amplitudes, in nm, to correct for defocus and astigmatism for the first case.

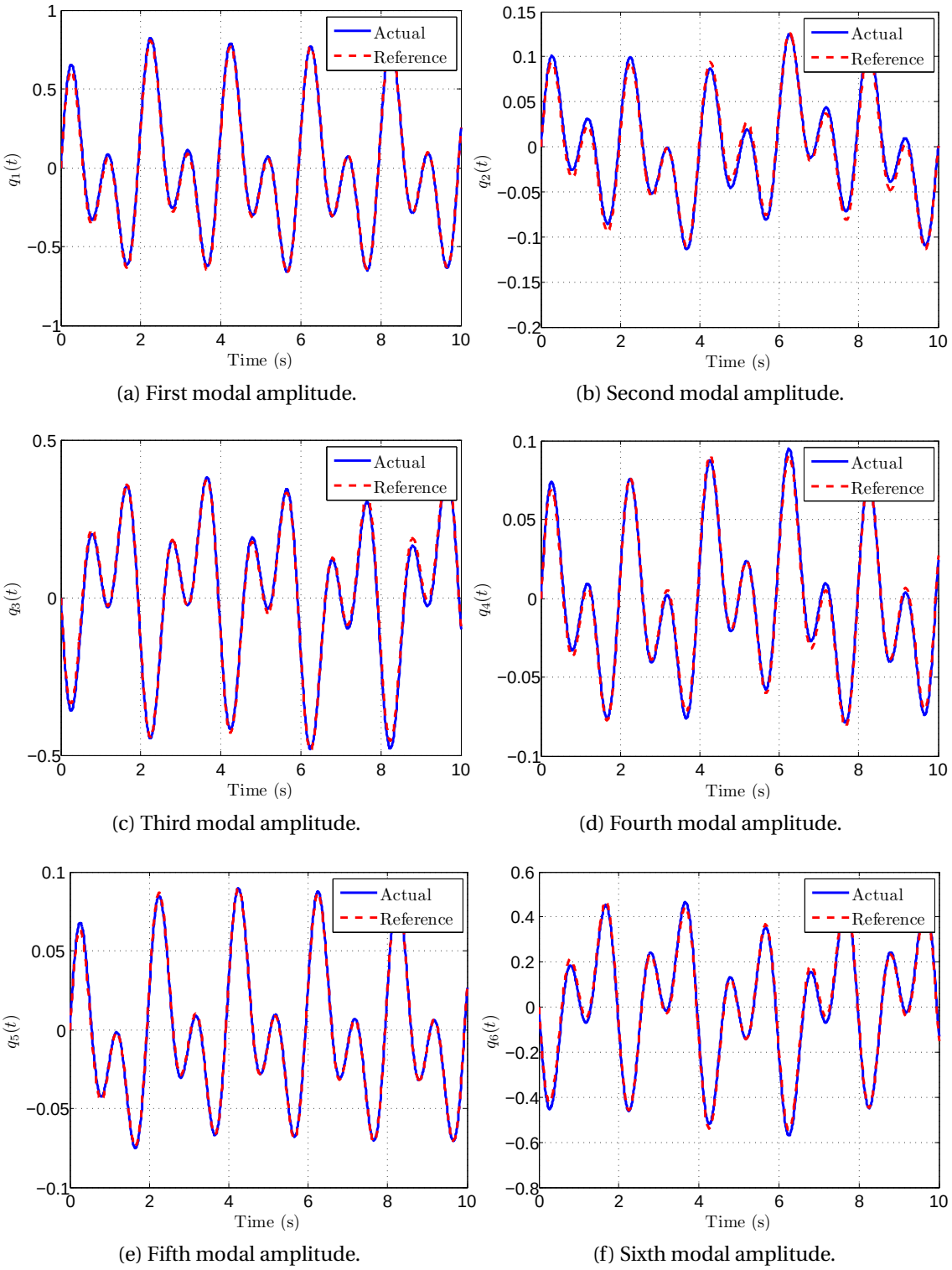

(a) First modal amplitude.

(b) Second modal amplitude.

(c) Third modal amplitude.

(d) Fourth modal amplitude.

(e) Fifth modal amplitude.

(f) Sixth modal amplitude.

Figure 5.6: Time history of modal amplitudes, in nm, to correct for defocus and astigmatism for the second case.

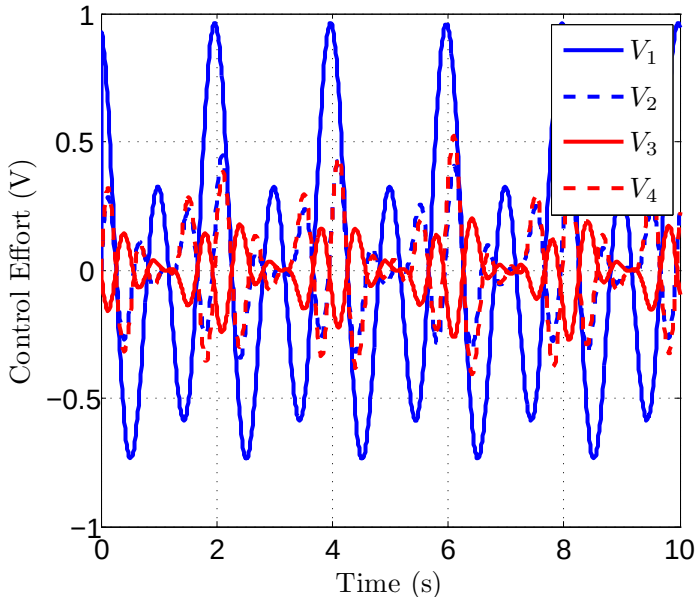

Figure 5.7: Control effort of the four MFC bimorph actuators for the second case.

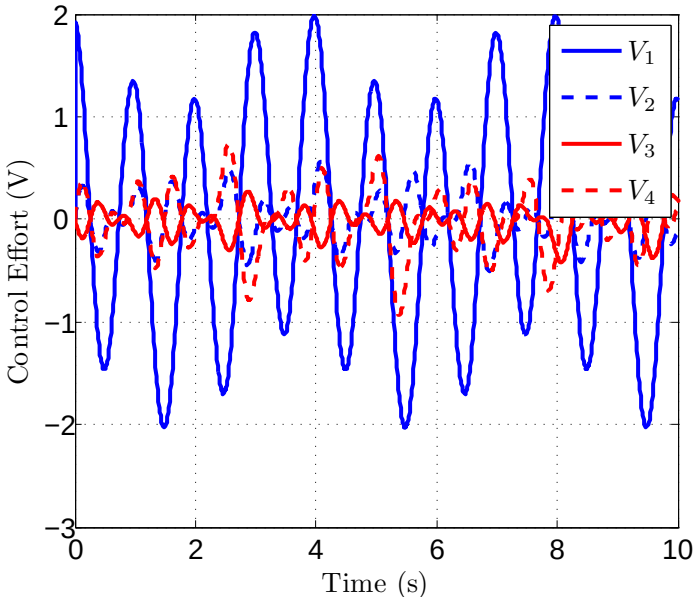

Figure 5.8: Control effort of the four MFC bimorph actuators for the first case.

et al., 2006b). The errors due to the defocus mode are often due to the beam length, and they are usually corrected for through changing the position of the mirror. We recognize that the defocus mode is a low order mode and usually is ignored when characterizing the surface of a mirror. However, we choose to use it along with the astigmatism modes to demonstrate the efficacy of the controller developed. The initial conditions, i.e., the initial deformation of the mirror is considered zero for the first two simulation cases.

The time amplitudes of the defocus and astigmatism modes are $\sin(2\pi t)$ nm and $\sin(\pi t)$ nm, respectively. Six modal amplitudes are used to represent the deformation of the circular membrane. The reference trajectory of the modal amplitudes is obtained through the transformation detailed in Appendix D and good tracking is achieved through the adaptive controller, Fig. 5.5. Although the actuators are symmetrically located on the structure, Fig. 4.3, their contributions are not since the optical aberration is a combination of two modes with varying frequencies, Fig. 5.8.

For the second case, the optical aberration is a combination of defocus and astigmatism. The amplitudes of the corresponding Zernike functions are $0.5\sin(\pi t)$ nm and $\sin(2\pi t)$ nm respectively. Here also, we assume zero initial conditions, i.e., the membrane mirror is initial flat. By transforming the optical amplitudes into mechanical amplitudes, the reference trajectories of the mechanical amplitudes are obtained and their tracking is achieved satisfactorily, Fig. 5.6. Again, although the actuators are symmetric in the geometric sense, Fig. 4.3, their contribution lacks this symmetry, Fig. 5.7.

Since we are interested in forcing the membrane to match the shape of the optical aberration in the clear aperture area, we observe that the adaptive controller can achieve this goal. The errors between the deflection of the membrane in the clear aperture area and the desired Zernike shape decrease with time, Fig. 5.9 and Fig. 5.10. The absolute value of the error is highest at the center of the circular membrane, since this point is the physically the least controlled point by the bimorph actuators.

In the third simulation, the optical aberration consists of the defocus and astigmatism modes too, with amplitudes of $0.5\sin(\pi t)$ nm and $0.5\sin(\pi t)$ nm, respectively. Here, random non-zero initial conditions are used in the numerical simulation. The purpose of this example is to further demonstrate the efficacy of the controller where we show

that the controller still can achieve stabilization of the closed loop system. Although the tracking of the desired second modal amplitude undergoes some difficulties, Fig. 5.11, the deformation error decreases as time progresses, Fig. 5.12. In this simulation case, the transient effect of the closed loop system is strongly felt in exciting the second mode, Fig. 5.11, which is something that cannot be really guaranteed when using adaptive controller algorithms. The design of adaptive controllers that meet transient design criteria is a topic that attracted the attention of many researchers, and the interested reader is referred to the work of Cao and Hovakimyan (2007, 2008) for more information.

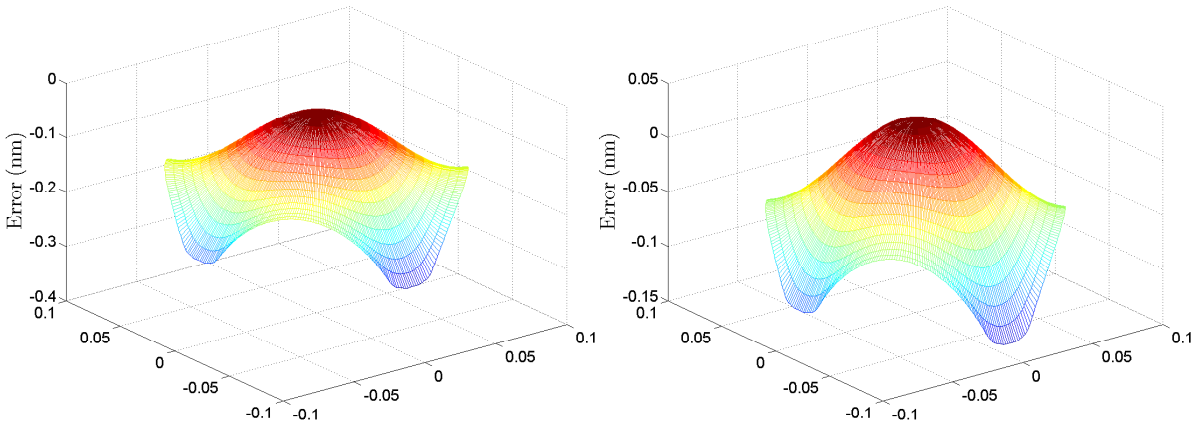

(a) Error at $t = 2$s.

(b) Error at $t = 4$s.

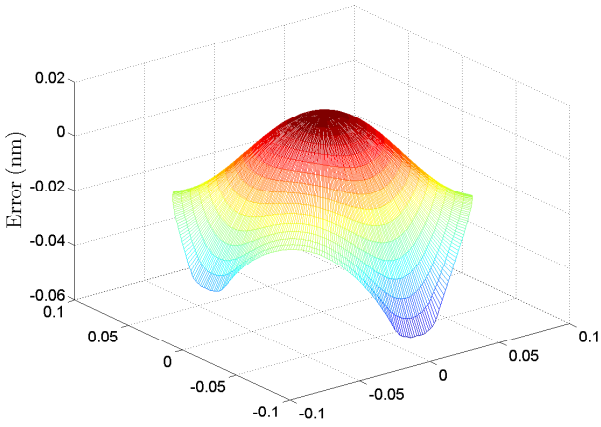

(c) Error at $t = 6$s.

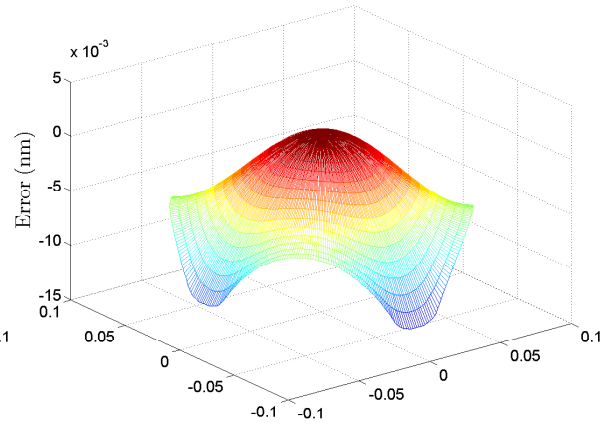

(d) Error at $t = 8$s.

Figure 5.9: Error between desired deformation and actual aberration shape for the first simulation case (within the clear aperture area $r \leq r_a$).

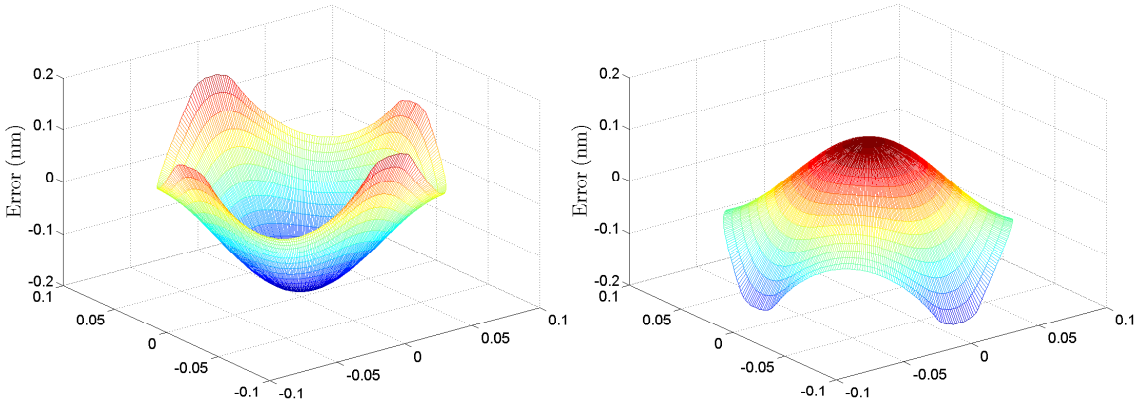

(a) Error at $t = 2$s.

(b) Error at $t = 4$s.

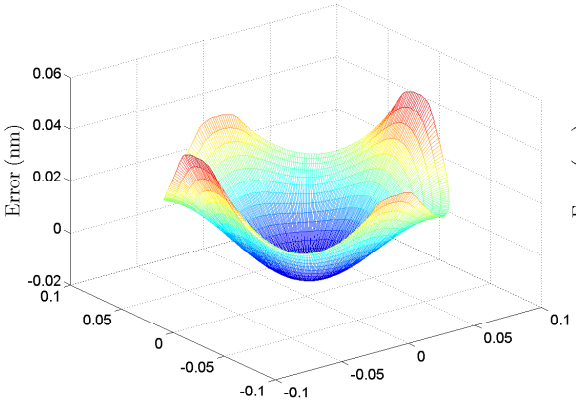

(c) Error at $t = 6$s.

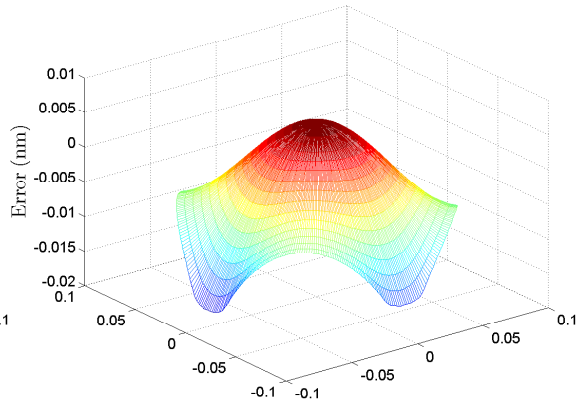

(d) Error at $t = 8$s.

Figure 5.10: Error between desired deformation and actual aberration for the second simulation case (within the clear aperture area $r \leq r_a$).

5.6 Chapter Summary

In this chapter, we bridge the gap between the mechanics and optics of a circular membrane. We first briefly present how an optical aberration of an incoming wavefront over a circular membrane is described mathematically. For this purpose we introduce Zernike functions, and we discuss some of their properties. Since Zernike functions are used to describe optical aberrations, they do not adhere to the mechanical boundary conditions of the circular membrane. Second, we develop a numerical transformation of on optical aberration into a desired mechanical deformation by matching the optical aberration to the mechanical deformation inside a clear aperture region of the circular membrane. We assume that the optical aberration can be determined using a Shack-

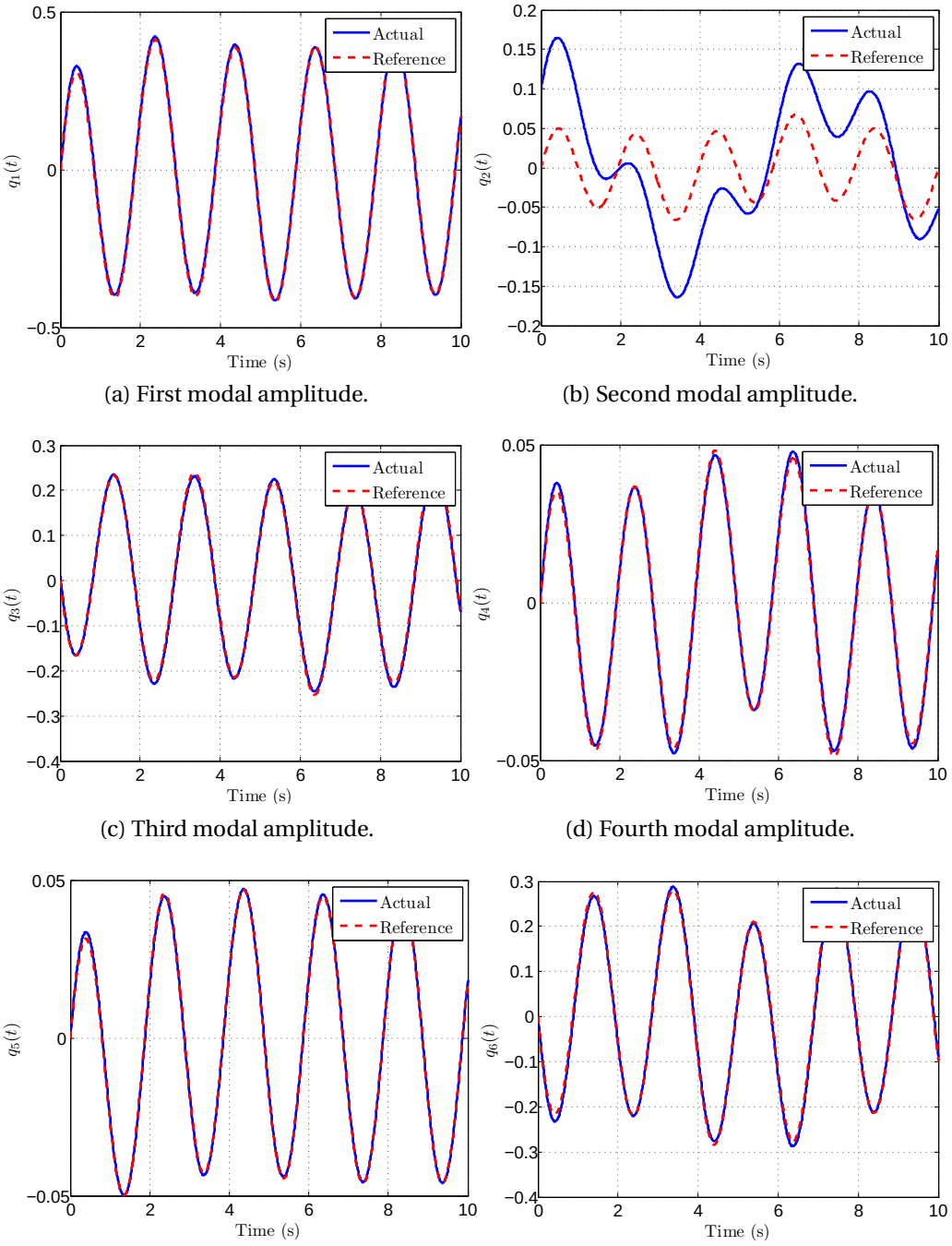

(a) First modal amplitude.

(b) Second modal amplitude.

(c) Third modal amplitude.

(d) Fourth modal amplitude.

(e) Fifth modal amplitude.

(f) Sixth modal amplitude.

Figure 5.11: Time history of modal amplitudes, in nm, to correct for defocus and astigmatism in the third case.

Hartmann wavefront sensor. Since most system cannot be modeled exactly, and are usually plagued by modeling and parametric uncertainties, we choose to use adaptive

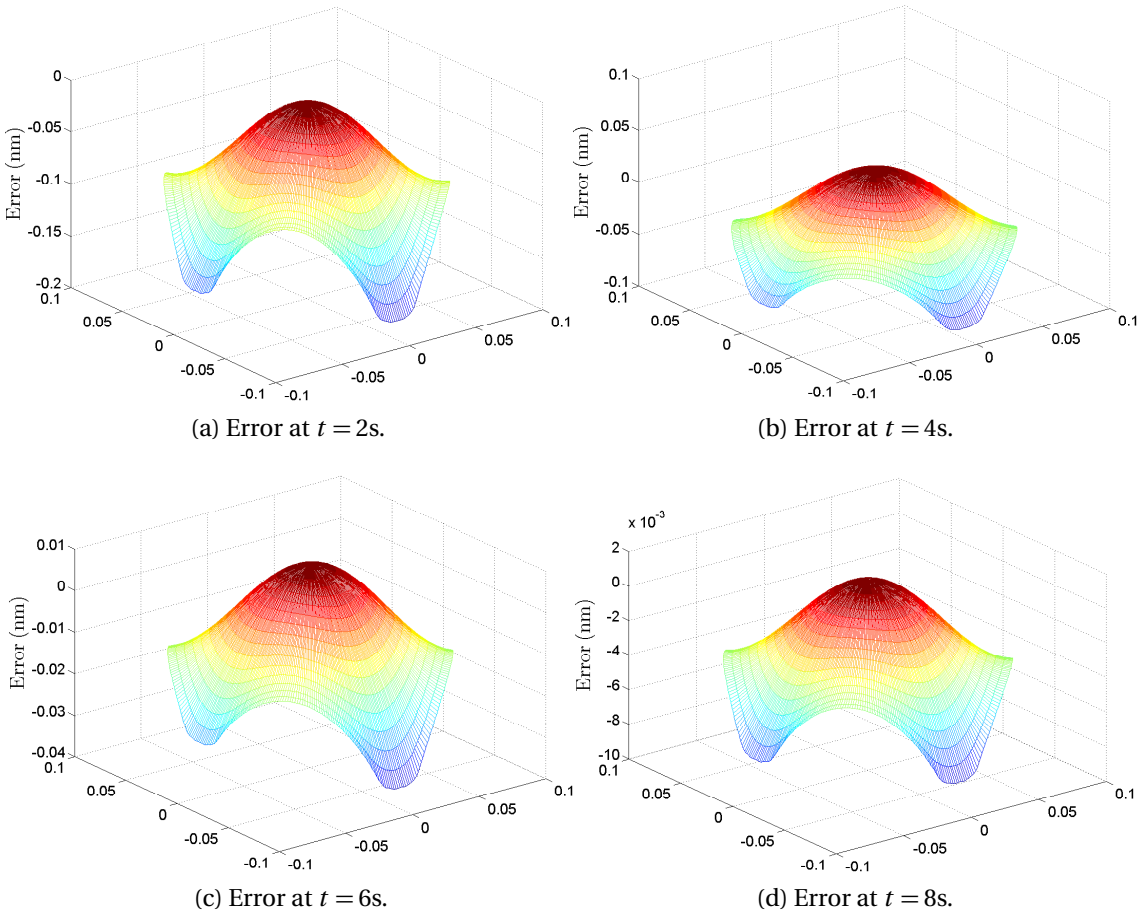

(a) Error at $t = 2$s.

(b) Error at $t = 4$s.

(c) Error at $t = 6$s.

(d) Error at $t = 8$s.

Figure 5.12: Error between desired deformation and actual aberration for the third simulation case (within the clear aperture area $r \leq r_a$).

control. We briefly introduce adaptive control as a concept, and then discuss using augmented adaptive control. In this scheme, we use an linear quadratic regulator (LQR) augmented with an adaptive controller to achieve tracking of a desired shape inside the clear aperture. The adaptive controller interferes in the presence of uncertainties or nonlinearities. Finally, we present a case study with three simulation demonstrations. We show that the desired shape is achieved and the optical aberration are canceled.

CHAPTER 6

SUMMARY AND CONCLUSIONS

PLACING large telescopes in space for space exploration and reconnaissance missions is a priority for the US Air Force. The US Air Force is striving to equip these telescopes with ultra-large membrane mirrors. The impetus behind this is the low-weight of membranes which will directly translate into cheap launching costs. Moreover, membrane mirrors promise to provide high quality optical imaging. Hence, they present themselves as an alternative for rigid mirrors currently used. To see such technology in application, a thorough understanding of membrane mirrors, a way of controlling their shape and any undesirable dynamics is a must. In the current work, we focus on the modeling and control of a piezoelectric bimorph augmented to a thin membrane material. Two configurations are considered. At first, we focus on membrane strips as a prelude for studying a circular membrane. We develops models and controllers for a membrane strip augmented with piezoelectric bimorphs acting axially and in bending. We then modeled a circular membrane and developed a controller to cancel optical aberrations over its interior "clear aperture" region. Below, we summarize the key contributions of this work.

6.1 Key Contributions

The objective of the dissertation is to cancel the optical aberrations in an incoming wavefront over the aperture of a circular membrane. The approach used in this work is to augment these membranes with piezoelectric bimorphs near their boundaries.

We approached the problem as follows: we first studied a membrane strip augmented

with a piezoceramic bimorphs near its boundary. The membrane strip was axially loaded, so we modeled the structure as a beam under tension. Furthermore, we used a weak formulation of the dynamic equation to avoid the noncontinuity that arises in the system due to the presence of the discrete actuator. This was a necessity since the flexural stiffness and the linear density of the piezoelectric bimorph is significantly higher that the flexural stiffness of the membrane strip. An experimental article was created in the lab and laser vibrometry was used to measure the deformation at a specific point of the structure. We first validated the model developed for a general case. Then, we observed the stiffening effect due to axially loading the membrane. We also tested the article in a vacuum chamber and documented the outgassing phenomenon. Then, we considered the control problem of this structure. We focused mainly on the shape control problem. A proportional integral (PI) controller was developed and the gains of the controller were obtained via the linear quadratic regulator theory. A PI controller was a necessity for this configuration to achieve zero steady state error along the span of the structure.

Then, we extended the previous modeling work to a membrane strip augmented with multiple bimorph actuators. We considered the case of having two bimorph actuators near the ends of the membrane strip. The bimorphs were made of macro fiber composite patches. These patches use iterdigitated electrodes for poling and subsequent actuation of an internal layer of machined piezoceramic fibers. They are expected to have less linear density and flexural stiffness that piezoceramics, and hence will not change the combined structure as much as a monolithic piezoceramic will. Here, we treated two cases. In the first case, both bimorph actuators would be acting in bending. This configuration was tested experimentally, and the model was validated. In the second case, one of the bimorphs acted axially, whereas the other acted in bending. This case received more attention for the effect of axial actuation was complex to comprehend. The membrane strip is placed under tension, however the axial bimorph exerts equal but opposite forces about its midpoint, hence changing the tension locally in the structure. This change often led to softening effect, even though the structure was stiffening in a global sense. In other words, when the strip was subjected to increased tension, the natural frequencies of the structure would increase, but as the voltage applied to the

bimorph acting axially increased, the natural frequencies would decrease. The explanation to this behavior is as follows: since the axial bimorph exerted equal but opposite forces about its midpoint, for the test article we considered, the compressive side of the axial bimorph was closer to the boundary of the structure, and hence its effect was dominant leading to the softening effect we observed.

Moreover, the presence of the axial bimorph leads to a nonlinear system. Hence, the sliding mode technique is used to design the controller of the membrane strip. However, a singularity arises near the equilibrium configuration. In other words, when the membrane strip is not deflected, the axial bimorph loses its control authority. This can by physically explained as follows: when the membrane strip is not deflected, the only way to deflect it from its equilibrium configuration is through transverse excitation. The axial force (applied through the bimorph or through any other means), no matter how arbitrarily large, won't move the membrane strip in the transverse direction. To resolve this issue, we derive a switching sliding mode controller. At large deflections, both controllers are activated: the axial and bending bimorphs. However, when the membrane strip is close to the equilibrium configuration, the axial bimorph is deactivated and the bending bimorph is the only actuator driving the system. In general, a switching controller can lead to instabilities. However, the switching sliding mode controller we presented is considered within the Lyapunov stability theory. Since the same Lyapunov function is used to prove the stability of both closed loop systems (before and after switching), the combined (switching) closed loop system is stable according to Lyapunov stability theory.

After presenting a thorough study of membrane strips augmented with piezoelectric actuators that act axially and/or in bending, we turned our attention to studying a circular membrane augmented with piezoelectric actuators. The finite element approach used when studying the membrane strips often yielded large numerical models which would make it hard to implement the controllers experimentally. Therefore, for the circular membrane case, we follow a different approach. We model the mechanics of the circular membrane augmented with piezoelectric bimorphs using ANSYS®, a commercial finite element software package. Using ANSYS®, we can obtain the modes shapes

of the structure. These mode shapes were then used in a Galerkin expansion of the fundamental equation governing the transverse vibration of the membrane.

Then, we implemented a controller to correct for optical aberrations. We first present a brief overview of the Zernike functions which are used as a basis to describe an optical aberration in an incoming wavefront. Then, we introduce a transformation between Zernike functions and the mechanical mode shapes. This transformation allows us to determine the desired transverse deflection of the circular membrane in order to cancel the optical aberration in the incoming wavefront. After obtaining the desired transverse deflection, we choose to apply an augmented adaptive controller. We first design a linear controller based on the linear quadratic regulator theory. Then, we augment this controller with an adaptive controller. The result is an adaptive controller with a linear quadratic regulator as its base performance. Case studies are present that demonstrate the effectiveness of the controller, and its ability to cancel optical aberrations that consist of astigmatism and defocus modes.

6.2 Remarks and Future Work

Real implementation of the controller by the end of this work is the only check of the theory presented here. The ability to correct for optical aberrations in a real adaptive optic system is the challenge to be faced. Experimental verification of the circular membrane modeling and closed loop performance is a formidable task that could not be achieved at the facilities available in Virginia Tech. A Shack-Hartmann wavefront sensor costs about $60,000 and the project did not have funding to support such purchase.

Tensioning the membrane material was another obstacle that was faced throughout the experiments conducted in this work. When dealing with the governing equation of a beam under axial loading, it is simplistic to assume that the tension is uniform through the area of the beam. However, in an experimental setting, and specially for the membrane strips we worked with in the lab: it is extremely difficult to achieve such uniformity. Often the membrane strip would warp and one could visually see that the tension is not uniform through the width of the membrane strip. This caused torsion modes to

appear when exciting the structure using the bimorphs in the transverse direction. In some cases, some of the torsional and bending modes are very close together so that the model could not differentiate between them. We used a laser scanning vibrometer to distinguish between them.

Achieving uniform radial tension for a circular membrane remains a challenge even to government agencies (for example the Air Force Research Laboratory) conducting research in the area of adaptive optics and membrane technologies (Marker, 2007). It was extremely difficult to achieve near uniform tension in our university lab setting, at least for model validation purposes.

The concept of membrane mirrors replacing traditional solid mirrors is a realizable idea. Despite the strides made in the area, additional research remains to be conducted in the area of modeling membrane mirrors. In the age of digital control, and with the ever increasing demands on engineering systems in general, less complex models are in high demand. Moreover, a more efficient transformation is required between the optical and mechanical realms to produced the desired deformation to be achieved by the controller.

APPENDIX **A**

INTEGRATION BY PARTS IN 2-DIMENSIONS

The integration by parts (in its general form) is given as

$$\int_{\Omega} \frac{\partial u}{\partial x_k} v \, \mathrm{d}x = \int_{\partial\Omega} u v n_k \, \mathrm{d}\sigma - \int_{\Omega} u \frac{\partial u}{\partial x_k} \mathrm{d}x \,, \tag{A.1}$$
$$u = u(x_1, \cdots, x_n) \quad \text{and} \quad v = v(x_1, \cdots, x_n) \,,$$

where x_k is the k-th variable and $\partial\Omega$ is the boundary of integration Ω. Moreover, n_k is the k-th component of $\mathbf{n}$, which is the outward unit surface-normal to the integration domain. In polar terms,

$$\int_{\Omega} u_r v \, \mathrm{d}r\mathrm{d}\theta = \int_{\partial\Omega} u v n_r \, \mathrm{d}\theta - \int_{\Omega} u v_r \, \mathrm{d}r\mathrm{d}\theta \,, \tag{A.2a}$$

$$\int_{\Omega} u_\theta v \, \mathrm{d}r\mathrm{d}\theta = \int_{\partial\Omega} u v n_\theta \, \mathrm{d}r - \int_{\Omega} u v_\theta \, \mathrm{d}r\mathrm{d}\theta \,. \tag{A.2b}$$

The integration domain noted above is displayed in Fig. A.1 to clear any confusion that might arise due to the form of Eq. (A.1). The misconception might spring from the fact that the physical domain at hand is a circle. Hence, one might think to obtain the outward normal to the circular domain which is simply given by,

$$\mathbf{n} = [\ 1 \quad 0\ ]^T \,. \tag{A.3}$$

which is correct for the physical domain as the outward normal will always be in the radial direction only. Notice that Eq. (A.2)b would suggest that

$$\int_{\Omega} u_\theta v \, \mathrm{d}r\mathrm{d}\theta = -\int_{\Omega} u v_\theta \, \mathrm{d}r\mathrm{d}\theta \,; \tag{A.4}$$

a statement that cannot be general to any two functions $u(r,\theta)$ and $v(r,\theta)$. However, in Eq. (A.1), the outward normal is meant to be that of the integration domain. Using the physical outward normal would lead to erroneous results. Consequently, we display the integration domain is displayed in Fig. A.1. This integration domain is no different than that used when dealing with integration by parts over a rectangular coordinates system (or any other coordinate system).

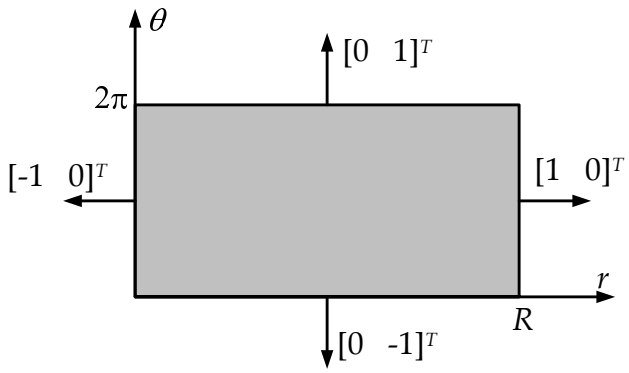

Figure A.1: Integration domain with r and θ as variables.

A.1 Illustrative Example

To illustrate the concept presented above, a simple example is used for demonstration. Define two function $u(r,\theta)$ and $v(r,\theta)$,

$$u(r,\theta) = r^2\cos(\theta) + re^{\theta}\cos(\theta)\,,$$
$$v(r,\theta) = (r^2+\sin(\theta)) + \sin(\theta) + R^2\cos\left(\theta - \frac{\pi}{2}\right) \qquad R=1\,.$$

First, the integration by parts with respect to r will be considered. Compute the following integral numerically,

$$I = \int_0^R \int_0^{2\pi} u_r(r,\theta)v(r,\theta)\mathrm{d}\theta\,\mathrm{d}r = -185.815\,. \tag{A.5}$$

However, through the integration by parts, one can obtain the same result.

$$I = \int_0^{2\pi} u(R,\theta)v(R,\theta)\mathrm{d}\theta - \int_0^{2\pi} u(0,\theta)v(0,\theta)\mathrm{d}\theta - \int_0^R \int_0^{2\pi} u(r,\theta)v_r(r,\theta)\mathrm{d}\theta\,\mathrm{d}r$$

$$
\begin{aligned}
&= \pi - 0 - \frac{1}{20}(-7 + 7e^{2\pi} + 12\pi) \\
&= -185.815\,. \qquad \text{(A.6)}
\end{aligned}
$$

In Eq. (A.6), the first two terms correspond to the boundary integral. There are an additional two terms that vanished due to the structure of the integration boundary presented in Fig. A.1. Along $\theta = 0$ and $\theta = 2\pi$, the r component of the normal is zero, and hence these terms vanish.

Now, consider the integration by parts with respect to θ. We will numerically compute the following integral,

$$
J = \int_0^R \int_0^{2\pi} u_\theta(r,\theta) v(r,\theta) \mathrm{d}\theta \, \mathrm{d}r = -290.72\,. \qquad \text{(A.7)}
$$

Implementing the integration by parts scheme, one obtains,

$$
\begin{aligned}
I &= \int_0^R u(r,2\pi)v(r,2\pi)\mathrm{d}r - \int_0^R u(r,0)v(r,0)\mathrm{d}r - \int_0^R \int_0^{2\pi} u(r,\theta) v_\theta(r,\theta)\mathrm{d}\theta\,\mathrm{d}r \\
&= \left(\frac{1}{6} + \frac{e^{2\pi}}{5}\right) - \frac{11}{30} - \left(\frac{37(1+e^{2\pi})}{50} + \frac{2\pi}{3}\right) \\
&= -290.72\,. \qquad \text{(A.8)}
\end{aligned}
$$

Again, the boundaries sections where $r = 0$ and $r = R$ vanish for the θ component of the outward normal is zero at those sections.

APPENDIX B

ANSYS® CODE

Listing B.1 below displays the ANSYS® batch file used to generate the model described in Subsection 4.4.1 on Page 110. The code generates the model, meshes the structure, and carries out the analysis necessary to obtain the mode shapes of the structure. Then, the results are written to data files for further analysis.

Below are some keys to understanding the coding of Listing B.1.

a) **Keywords** are usually preceded by "/". These commands provide general control to the ANSYS® sessions such as controlling the overall behavior of the session and entering/exiting various sessions (solution, data post processing, etc...).

b) **Keywords** are commands that operate in the preprocessing mode such as assigning material properties and element type.

c) **Keywords** are usually preceded by "*". These commands make up *ANSYS® Parametric Design Language*, abbreviated as APDL. APDL is a collection of commands and macro files that constitute ANSYS® programming language. The commands of APDL are (somewhat) similar to those of *Fortran77*.

d) **Keywords** are options required by the commands.

e) `Comments are preceded with the exclamation mark "!".`

The element type chosen for this analysis is **SHELL63** which has both bending and membrane capabilities with six degrees of freedom at each node. The tension load is applied to the structure, and a static analysis is carried out. Then, a modal analysis is

conducted. The option **PSTRES** is selected to allow incorporating the effect of tension in the modal analysis.

In total, 10,581 nodes are used to mesh the structure. Out of this total number, 10,432 are generated by the author to constitute a (29×359) polar grid in r and θ respectively. This grid excludes the center of the membrane and its boundary. A center node is added separately, and the equally space grid at the circumference of the membrane is added in MATLAB®and its displacement is set to zero to satisfy the boundary conditions. Taking these additions into account, the matrices present the mode shapes are indeed (31×359) arrays, which constitute 11,129 data points.

Listing B.1: ANSYS®Batch File

```
/BATCH ,list
! ================================================
/PREP7 ,Membrane
! ================================================
/TITLE,Membrane Mirror -- Four Bimorphs
/REPLOT
! Physical properties of the membrane
! ================================================
Rm = 0.15 ! Raduis of the membrane
Hm = 51E-6 ! Membrane thickness
Em = 3E9 ! Modulus of elasticity
NUmm = 0.3 ! Poisson's ratio
Rhom = 1420 ! Mass density
EPS = 0.005 ! Inner radius to avoid dealing with the
                  ! exact center of the circle
! Define PI
! ================================================
PI = 3.141592653589793E+000
! Define the tension per unit length
! ================================================
TAU = 100
```

```
! Physical properties of the actuator
! ================================================
! Position of first bimorph
B1X1 = 0.088
B1X2 = 0.126
B1Y1 = -0.0125
B1Y2 = 0.0125
! ================================================
Ha = 0.3E-3 ! Thickness
Wa = B1Y2-B1Y1 ! Width
La = B1X2-B1X1 ! Length
Ea = 34.5E9 ! Modulus of elasticity
NUa = 0.3 ! Poisson's ratio
Rhoa = 994 ! Mass density
! Mesh steps
! ================================================
RNUMBER = 29
TNUMBER = 359
NMODES = 10
! Properties of non-composite and composite regions
! ================================================
! Thickness
H1 = Hm
H2 = Hm + 2*Ha
! Density
Rho1 = Rhom
Rho2 = (Rhom*(Ha*Wa*La)+2*Rhoa*(Ha*Wa*La))/((Ha*Wa*La)+2*(Ha*Wa*La))
! Poisson's ratio
NU1 = NUmm
NU2 = (Numm+NUa)/2
! Modulus of elasticity
E1 = Em
```

```
aa3 = (Hm/2+Ha)**3-(Hm/2)**3
E2 = (Em*Hm**3+8*Ea*aa3)/(H2**3)
! CREATE MATERIAL MODELS
! Establish material model for non-composite region
! ================================================
MP,EX,1,E1 ! Young's modulus
MP,PRXY,1,NU1 ! Poisson's ratio
MP,DENS,1,Rho1 ! Density
! Establish material model for composite region
! ================================================
MP,EX,2,E2 ! Young's modulus
MP,PRXY,2,NU2 ! Poisson's ratio
MP,DENS,2,Rho2 ! Density
! Create an element type to be used
! ================================================
ET,1,SHELL63
R,1,H1,H1,H1,H1, , ,
R,2,H2,H2,H2,H2, , ,
! Create the area for the membrane strip
! ================================================
CYL4,0,0,Rm
! Create the area for the first bimorph
! ================================================
RECTNG,B1X1,B1X2,B1Y1,B1Y2
! Create the second bimorph
RECTNG,B1Y1,B1Y2,B1X1,B1X2
! Mirror the first bimorph
ARSYM,X,2, , , ,0,0
! Mirror the second bimorph
ARSYM,Y,3, , , ,0,0
! Partition the membrane area
! ================================================
```

```
APTN, ALL
ALIST, ALL
! Assign regions attributes
! ================================================
ASEL, , , ,2,5
AATT,2,2,
ASEL, , , ,6
AATT,1,1,
ASEL, , , ,ALL
! Create the hardpoints
! ================================================
*DIM,rr,ARRAY,RNUMBER,1
*DIM,th,ARRAY,TNUMBER,1
*DIM,XX,ARRAY,RNUMBER,TNUMBER
*DIM,YY,ARRAY,RNUMBER,TNUMBER
*DO,I,1,RNUMBER,1
        rr(I,1) = EPS + (I-1)*(Rm-2*EPS)/(RNUMBER-1)
*ENDDO
*DO,I,1,TNUMBER,1
        th(I,1) = (I-1)*2*PI/TNUMBER
*ENDDO
! Creat a hard point at the center
! ================================================
HPTCREATE,AREA,6,,COORD,0,0,0
! Create a hard point on the areas
! ================================================
*DO,I,1,RNUMBER,1
        *DO,J,1,TNUMBER,1
                XX(I,J) = rr(I)*cos(th(J))
                YY(I,J) = rr(I)*sin(th(J))
                *IF , YY(I,J) , GT , B1Y1 , AND , YY(I,J) , LT , B1Y2 , THEN
                        *IF , XX(I,J) , GT , B1X1 , AND , XX(I,J) , LT , B1X2 , THEN
```

```
                    HPTCREATE,AREA,2,,COORD,XX(I,J),YY(I,J),0
                *ELSEIF , XX(I,J), LT , -B1X1 , AND , XX(I,J) , GT , -B1X2 , THEN
                    HPTCREATE,AREA,4,,COORD,XX(I,J),YY(I,J),0
                *ELSE
                    HPTCREATE,AREA,6,,COORD,XX(I,J),YY(I,J),0
                *ENDIF
            *ELSEIF , YY(I,J) , GT , B1X1 , AND , YY(I,J) , LT , B1X2 , THEN
                *IF , XX(I,J) , GT , B1Y1 , AND , XX(I,J) , LT , B1Y2 , THEN
                    HPTCREATE,AREA,3,,COORD,XX(I,J),YY(I,J),0
                *ELSE
                    HPTCREATE,AREA,6,,COORD,XX(I,J),YY(I,J),0
                *ENDIF
            *ELSEIF , YY(I,J) , LT, -B1X1 , AND , YY(I,J) , GT , -B1X2 , THEN
                *IF , XX(I,J) , GT , B1Y1 , AND , XX(I,J) , LT , B1Y2 , THEN
                    HPTCREATE,AREA,5,,COORD,XX(I,J),YY(I,J),0
                *ELSE
                    HPTCREATE,AREA,6,,COORD,XX(I,J),YY(I,J),0
                *ENDIF
            *ELSE
                HPTCREATE,AREA,6,,COORD,XX(I,J),YY(I,J),0
            *ENDIF
        *ENDDO
*ENDDO
! Mesh the structure
! ================================================
MSHKEY,0
MSHAPE,1,2D
CHKMSH,'AREA'
ASEL, , , ,ALL
AMESH,ALL
! Refine the mesh
! ================================================
```

```
! EREF,ALL, , ,1,0,1,1
! Boundary conditions for lines 1,2,3 and 4 on area 3
! ================================================
DL,1,6,UZ,0
DL,1,6,ROTY,0
DL,1,6,ROTZ,0
DL,2,6,UZ,0
DL,2,6,ROTY,0
DL,2,6,ROTZ,0
DL,3,6,UZ,0
DL,3,6,ROTY,0
DL,3,6,ROTZ,0
DL,4,6,UZ,0
DL,4,6,ROTY,0
DL,4,6,ROTZ,0
! Tensile force on the membrane perimiter
! ================================================
LSEL, , , ,1,4,
SFL,ALL,PRES,-TAU*2*PI*Rm
! Static solution
! ================================================
ANTYPE,STATIC ! Static analysis
PSTRES,ON ! Include prestress effects
FINISH
/SOLU
SOLVE
FINISH
! Modal solution
! ================================================
/SOLU
ANTYPE,MODAL ! Perform modal analysis
MODOPT,SUBSP,NMODES,,,,ON ! Specify the number of modes to be extracted
```

```
MXPAND,NMODES ! Specify the number of modes for the expansion
PSTRES,ON ! Prestress effects are included
! Fix the boundaries
! ================================================
NSEL,ALL
D,ALL,UX,0
D,ALL,UY,0
! Delete tension force
! ================================================
LSEL, , , ,1,4,
SFLDELE, ALL, PRES
! Perform the modal analysis
! ================================================
/SOLU
/STATUS,SOLU
SOLVE
! Generate the hard points file
! ================================================
KSEL,S,HPT,,ALL
KNUM = 1 + RNUMBER*TNUMBER
*DIM,KMASK,ARRAY,KNUM+21
*DIM,KARRAY,ARRAY,KNUM+21,4
*VGET,KMASK(1),KP,1,KSEL
*VMASK,KMASK(1)
*VGET,KARRAY(1,1),KP,-21,LOC,X
*VMASK,KMASK(1)
*VGET,KARRAY(1,2),KP,-21,LOC,Y
*VMASK,KMASK(1)
*VGET,KARRAY(1,3),KP,-21,ATTR,NODE
*VMASK,KMASK(1)
*VFIL,KARRAY(1,4),RAMP,1,1
*CFOPEN,HARDLIST,TXT
```

```
!*VWRITE
!('HARDPOINT',10x,'X',10x,'Y')
*VMASK,KMASK(1)
*VWRITE,KARRAY(1,4),KARRAY(1,1),KARRAY(1,2),KARRAY(1,3)
(F10.0,tl1,' ',F10.6,' ',F10.6,' ',F10.0,t11)
*CFCLOS
*UILIST,HARDLIST.txt
! Generate the nodal solutions file
! ================================================
!*DIM,FNAME,STRING,RNUMBER,1
*DO,I,1,NMODES,1
        /POST1
        SET,,, ,,, ,I
        /PREP7
        NSEL,ALL
        ! Get maximum node number
        ! (in effect, this is the total number of nodes)
        *GET,NNUMMAX,NODE,,NUM,MAX
        ! Delete NMASK array (works after the first loop)
        *DEL,NMASK
        ! Delete NARRAY array (also works after the first loop)
        *DEL,NARRAY
        ! Define NMASK array: this will hold the node numbers
        *DIM,NMASK,ARRAY,NNUMMAX
        ! Define NARRAY array to hold results
        ! Result will have four columns
        ! (node number, then three displacements)
        *DIM,NARRAY,ARRAY,NNUMMAX,4
        ! Get the number of nodes for the first column
        *VGET,NMASK(1),NODE,1,NSEL
        *VMASK,NMASK(1)
        ! Get UX for the nodes
```

```
        *VGET,NARRAY(1,1),NODE,1,U,X
        ! Reactivate masking for next operation
        *VMASK,NMASK(1)
        ! GET UY for the nodes
        *VGET,NARRAY(1,2),NODE,1,U,Y
        *VMASK,NMASK(1)
        ! GET UZ for nodes only if selected
        *VGET,NARRAY(1,3),NODE,1,U,Z
        ! Fill vector from 1 to NNUMMAX (node no.)
        *VFIL,NARRAY(1,4),RAMP,1,1
        ! Open file that will be used to store the nodal solution
        *CFOPEN,STRCAT('DATAMODE',CHRVAL(I)),TXT
        ! Write header information
        !*VWRITE
        !('NODE',10x,'UX',10x,'UY',10x,'UZ')
        ! Use mask, then write only selected nodes
        *VMASK,NMASK(1)
        *VWRITE,NARRAY(1,4),NARRAY(1,1),NARRAY(1,2),NARRAY(1,3)
        (F10.0,tl1,' ',F10.6,' ',F10.6,' ',F10.6)
        ! Close the file
        *CFCLOS
*ENDDO
FINISH
```

On line 220 of the code of Listing B.1, a command saves the node information in the form of: node number, x-position and y-position. The code starting on line 221 saves the data of every mode shape to a separate text file. This file is composed of node number, and node transverse deflection. The first file can be used as a guide for creating a matrix corresponding to every mode shape.

APPENDIX C

NUMERICAL DIFFERENTIATION

The equations of Chapter 4 involves many numerical differentiation operations of the shape functions $\varphi_i(x,y)$. These functions are organized into matrices, with the indices of the radial and circumferential coordinates as the indices of the entries of a rectangular matrix. Figure C.1 represents the data points of these shape functions. We are interested in obtaining the first partial, second partial and mixed partial derivatives of these 2-dimensional functions. The grid is uniform in both directions.

For the first and second partial derivatives, we use a three point difference scheme, as given in (e.g. Tannehill et al., 1997, Chapter 2). The subsequent approximations are based on the grid given in Fig. C.1.

The approximation of the first derivative is,

$$\begin{aligned}
\left.\frac{\partial u}{\partial x}\right)_{i,j} &= \frac{u_{i+1,j}-u_{i-1,j}}{2\Delta x}+O(\Delta x^2)\,,\\
\left.\frac{\partial u}{\partial x}\right)_{1,j} &= \frac{-3u_{1,j}+4u_{2,j}-u_{3,j}}{2\Delta x}+O(\Delta x^2)\,,\\
\left.\frac{\partial u}{\partial x}\right)_{n_i,j} &= \frac{3u_{n_i,j}-4u_{n_i-1,j}+u_{n_i-2,j}}{2\Delta x}+O(\Delta x^2)\,,
\end{aligned} \tag{C.1}$$

and that of the second derivative is,

$$\begin{aligned}
\left.\frac{\partial^2 u}{\partial x^2}\right)_{i,j} &= \frac{-u_{i+2,j}+16u_{i+1,j}-30u_{i,j}+16u_{i-1,j}-u_{i-2,j}}{12\Delta x^2}+O(\Delta x^4)\,,\\
\left.\frac{\partial^2 u}{\partial x^2}\right)_{1,j} &= \frac{-u_{4,j}+4u_{3,j}-5u_{2,j}+2u_{1,j}}{\Delta x^2}+O(\Delta x^2)\,,\\
\left.\frac{\partial^2 u}{\partial x^2}\right)_{n_i,j} &= \frac{2u_{n_i,j}-5u_{n_i-1,j}+4u_{n_i-2,j}-u_{n_i-3,j}}{\Delta x^2}+O(\Delta x^2)\,,
\end{aligned} \tag{C.2}$$

where the least accuracy in this approximation is of the second order.

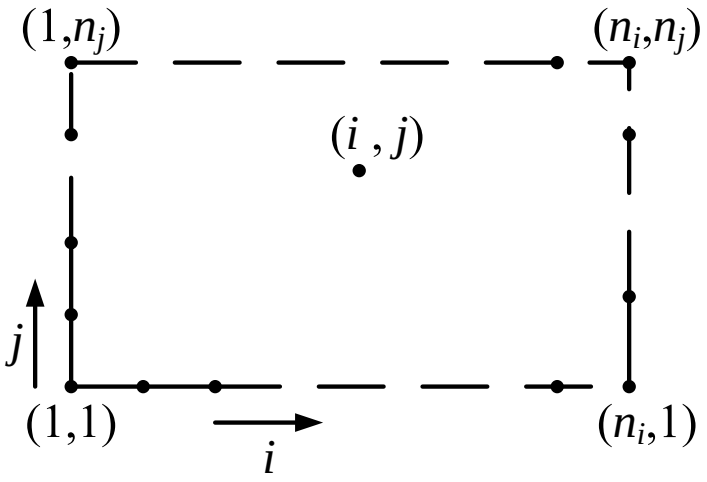

Figure C.1: Grid used in numerical differentiation.

The mixed partial derivative is a more involved than the second partial derivative. First, for any point with location (i,j) on the grid, the mixed partial derivative is given as,

$$\left.\frac{\partial^2 u}{\partial x \partial y}\right)_{i,j} = \frac{1}{2\Delta x}\left(\frac{u_{i+1,j+1}-u_{i+1,j-1}}{2\Delta y} - \frac{u_{i-1,j+1}-u_{i-1,j-1}}{2\Delta y}\right) + O[(\Delta x)^2,(\Delta y)^2]\,. \quad \text{(C.3)a}$$

This formulation provides a second order accuracy in both directions. The approximations below are for the boundaries of the grid. According to Fig. C.1, the approximations below represent the lower, upper, left and right boundaries of the grid respectively.

$$\begin{aligned}
&\left.\frac{\partial^2 u}{\partial x \partial y}\right)_{i,1} = \frac{1}{2\Delta x}\left(\frac{u_{i+1,2}-u_{i+1,1}}{\Delta y} - \frac{u_{i-1,2}-u_{i-1,1}}{\Delta y}\right) + O[(\Delta x)^2,\Delta y] \quad i \neq 1,n_i\,,\\
&\left.\frac{\partial^2 u}{\partial x \partial y}\right)_{i,n_j} = \frac{1}{2\Delta x}\left(\frac{u_{i+1,n_j}-u_{i+1,n_j-1}}{\Delta y} - \frac{u_{i-1,n_j}-u_{i-1,n_j-1}}{\Delta y}\right) + O[(\Delta x)^2,\Delta y] \quad i \neq 1,n_i\,,\\
&\left.\frac{\partial^2 u}{\partial x \partial y}\right)_{1,j} = \frac{1}{2\Delta x}\left(\frac{u_{2,j+1}-u_{2,j-1}}{\Delta y} - \frac{u_{1,j+1}-u_{1,j-1}}{\Delta y}\right) + O[\Delta x,(\Delta y)^2] \quad j \neq 1,n_j\,,\\
&\left.\frac{\partial^2 u}{\partial x \partial y}\right)_{n_i,j} = \frac{1}{2\Delta x}\left(\frac{u_{n_i,j+1}-u_{n_i,j-1}}{\Delta y} - \frac{u_{n_i-1,j+1}-u_{n_i-1,j-1}}{\Delta y}\right)\\
&+O[\Delta x,(\Delta y)^2] \quad j \neq 1,n_j\,. \qquad \text{(C.3)b}
\end{aligned}$$

Equation (C.3)b excluded the corner points of the grid. The approximation of these points is given below. Note that at the corner points, the accuracy of the approxima-

tion drops to the first order.

$$\left.\frac{\partial^2 u}{\partial x \partial y}\right)_{1,n_j} = \frac{1}{\Delta x}\left(\frac{u_{2,j}-u_{2,n_j-1}}{\Delta y} - \frac{u_{1,n_j}-u_{1,n_j-1}}{\Delta y}\right) + O(\Delta x, \Delta y)\,,$$

$$\left.\frac{\partial^2 u}{\partial x \partial y}\right)_{n_i,1} = \frac{1}{\Delta x}\left(\frac{u_{n_i,2}-u_{n_i,1}}{\Delta y} - \frac{u_{n_i-1,2}-u_{n_i-1,1}}{\Delta y}\right) + O(\Delta x, \Delta y)\,,$$

$$\left.\frac{\partial^2 u}{\partial x \partial y}\right)_{n_i,n_j} = \frac{1}{\Delta x}\left(\frac{u_{n_i,n_j}-u_{n_i,n_j-1}}{\Delta y} - \frac{u_{n_i-1,n_j}-u_{n_i-1,n_j-1}}{\Delta y}\right) + O(\Delta x, \Delta y)\,,$$

$$\left.\frac{\partial^2 u}{\partial x \partial y}\right)_{1,1} = \frac{1}{\Delta x}\left(\frac{u_{2,2}-u_{2,1}}{\Delta y} - \frac{u_{1,2}-u_{1,1}}{\Delta y}\right) + O(\Delta x, \Delta y)\,. \qquad \text{(C.3)c}$$

APPENDIX D

NUMERICAL TRANSFORMATION BETWEEN OPTICAL AMPLITUDES AND MECHANICAL MODAL AMPLITUDES

The transformation in Eq. (5.20) is possible if the functions $\bar{U}_r(r,\theta)$ and $\bar{\varphi}_i(r,\theta)$ of the structure are readily available analytical functions. Although the Zernike functions $\bar{U}_r(r,\theta)$ are analytical function provided in Eq. (5.1) and Table 5.1, the mode shapes of this structure are not. Since the membrane mirror is augmented with smart bimorph actuators, such analytical functions for the mode shapes are hard to find. Moreover, since the mode shapes of the structure were obtained from ANSYS®, Chapter 4, they are available only as numerical values. To this end, assume that the circular grid of the clear aperture is divided into n circumferential and m radial elements (i.e., $r_m = r_a$ of Fig. 4.3 on Page 109). Equation (5.19)b should be satisfied at every point of the circular grid. Hence, from Eq. (5.19)b, we can deduce the following equations,

$$\begin{array}{lll} \bar{U}(r_1,\theta_1)A(t)=\bar{\varphi}(r_1,\theta_1)q(t) & \dots & \bar{U}(r_1,\theta_n)A(t)=\bar{\varphi}(r_1,\theta_n)q(t) \\ \bar{U}(r_2,\theta_1)A(t)=\bar{\varphi}(r_2,\theta_1)q(t) & \dots & \bar{U}(r_2,\theta_n)A(t)=\bar{\varphi}(r_2,\theta_n)q(t) \\ \vdots & & \vdots \\ \bar{U}(r_m,\theta_1)A(t)=\bar{\varphi}(r_m,\theta_1)q(t) & \dots & \bar{U}(r_m,\theta_n)A(t)=\bar{\varphi}(r_m,\theta_n)q(t) \end{array} , \tag{D.1}$$

where

$$\bar{U}(r_i,\theta_j)=\begin{bmatrix} \bar{U}_1(r_i,\theta_j) & \dots & \bar{U}_L(r_i,\theta_j) \end{bmatrix} \quad , \quad \bar{\varphi}(r_i,\theta_j)=\begin{bmatrix} \bar{\varphi}_1(r_i,\theta_j) & \dots & \bar{\varphi}_N(r_i,\theta_j) \end{bmatrix} , \tag{D.2}$$

and

$$A(t) = \begin{bmatrix} A_1(t) & \dots & A_L(t) \end{bmatrix}^T \quad \text{and} \quad \begin{bmatrix} q_1(t) & \dots & q_N(t) \end{bmatrix}^T . \tag{D.3}$$

Every equation of Eq. (D.1) could be used to obtain $q(t)$ as per Eq. (5.20) evaluated at any point (r_i, θ_j). Consequently, the linear system of equations at hand is over determined, since we have $n \times m$ equations with only N unknowns. Then, the equations displayed above can be regrouped as,

$$\underbrace{\begin{bmatrix} \begin{bmatrix} \bar{U}(r_1,\theta_1) \\ \vdots \\ \bar{U}(r_1,\theta_n) \end{bmatrix} \\ \begin{bmatrix} \bar{U}(r_2,\theta_1) \\ \vdots \\ \bar{U}(r_2,\theta_n) \end{bmatrix} \\ \vdots \\ \begin{bmatrix} \bar{U}(r_m,\theta_1) \\ \vdots \\ \bar{U}(r_m,\theta_n) \end{bmatrix} \end{bmatrix}}_{O} A(t) = \underbrace{\begin{bmatrix} \begin{bmatrix} \bar{\varphi}(r_1,\theta_1) \\ \vdots \\ \bar{\varphi}(r_1,\theta_n) \end{bmatrix} \\ \begin{bmatrix} \bar{\varphi}(r_2,\theta_1) \\ \vdots \\ \bar{\varphi}(r_2,\theta_n) \end{bmatrix} \\ \vdots \\ \begin{bmatrix} \bar{\varphi}(r_m,\theta_1) \\ \vdots \\ \bar{\varphi}(r_m,\theta_n) \end{bmatrix} \end{bmatrix}}_{M} q(t) , \tag{D.4}$$

where O is $(n \times m) \times L$ and M is $(n \times m) \times N$. Then, the transformation can be stated as

$$q(t) = M^+ O A(t) , \tag{D.5}$$

which minimizes the sum of the squares of the estimation errors in every element of $q(t)$, otherwise known as a least square estimation. The "+" superscript indicated the pseudo-inverse of M, which is expressed as,

$$M^+ = M^T (M M^T)^{-1} .$$

Figure D.1 shows the estimates of the defocus and astigmatism modes shown previously in Fig. 5.1. In this case, the optical amplitudes for the defocus and astigmatism mode was the same, 1 μm. The estimation is carried inside the clear aperture only, i.e., between $r = 0$ and $r = 8.8$ which is the radial location of the MFC bimorph actuators

(Fig. 4.3 on Page 109). The last radial point in the plot is $r = 8.5$ since no grid point could be placed on the boundaries of the MFC actuator (see Section 4.4 and Subsection 4.4.2).

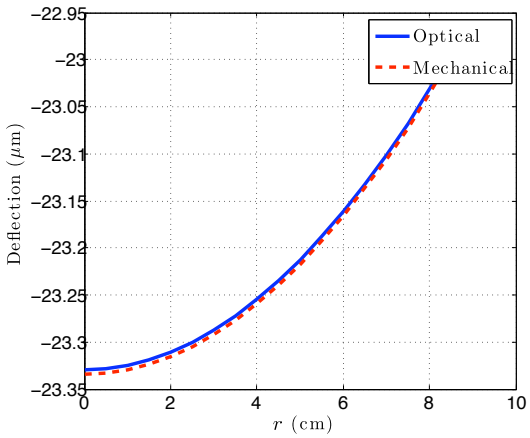

(a) Estimation of the defocus mode. The section shown is taken at $\theta = 0^o$.

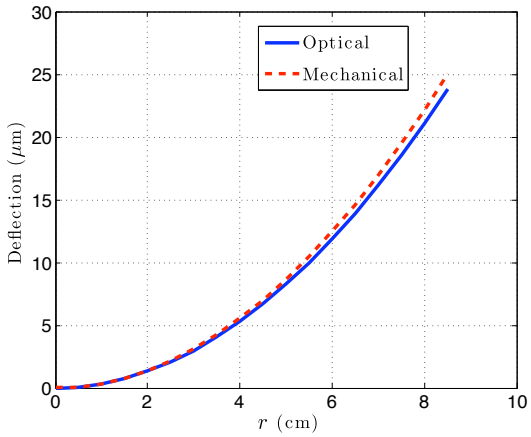

(b) Estimation of the astigmatism mode. The section shown is take at $\theta = 90^o$.

Figure D.1: Estimation of the defocus and astigmatism modes inside the clear aperture. The last radial point is at $r = 8.5$ cm.

APPENDIX **E**

ADAPTIVE AUGMENTATION EXAMPLE – SCALAR SYSTEM

A general scalar system can be described through $\dot{x}(t) = F(x(t), u(t))$ where $x(t)$ is the state of the system, $u(t)$ is the control input of the system and $F(\cdot,\cdot)$ is generally nonlinear. If the system is affine, free of parametric excitations, then

$$\dot{x}(t) = ax(t) + b\lambda u(t) + f(x) \quad , \quad x(0) = x_0 \,, \tag{E.1}$$

where a is unknown, b is known and λ is the uncertainty in the control effectives whose sign is only known, and the system nonlinearity can be isolated into the function $f(x)$. Usually, engineers designing control systems would have an estimate (or nominal value) for a, say a_0 and would know little about the function $f(x)$. The uncertainty in a could be added to the system nonlinearity without loss of generality, and we assume that the nonlinearities of the system are in the span of b, hence the system of Eq. (E.1) can be described as

$$\dot{x}(t) = a_0 x(t) + b\lambda(u(t) + W^T \Phi(x)) \quad , \quad x(0) = x_0 \,. \tag{E.2}$$

Here, we assumed that the nonlinear function $f(x)$ can be represented by $\lambda b W \Phi(x)$ where W is a $(N \times 1)$ vector of unknown parameters and $\Phi(x)$ is a vector of known continuous functions. Moreover, we assume the following output equation $y(t) = cx(t)$. A linear quadratic regulator can be designed for the nominal system $\dot{x}(t) = a_0 x(t) + b\,u(t)$. The resulting control law would be in the form of

$$u_{lin} = -k_{LQR} x(t) \,,$$

and if we are interested in tracking a given bounded signal, then the control input should be

$$u_{lin} = -k_{LQR}x(t) + k_g r(t)\,,$$

where k_g is the feed-forward gain given as,

$$k_g = [c(a_0 - b\,k_{LQR})^{-1}b]^+\,,$$

and the "+" superscript indicates the pseudo-inverse of the superscripted matrix. Note that in this example, the pseudo-inverse is the reciprocal of the superscripted scalar quantity. Obtaining the optimal feedback and feed-forward gains naturally defines a reference model,

$$\dot{x}_m(t) = \underbrace{(a_0 - k_{LQR}b)}_{a_m} x_m(t) + \underbrace{b\,k_g}_{b_m} r(t) \quad , \quad x_m(0) = x_{m0}\,, \tag{E.3}$$

whose evolving state is used to define an error signal $e(t) = x(t) - x_m(t)$. The adaptive control law is

$$u_{ada} = k_x(t)x(t) + k_r(t)r(t) - \hat{W}^T(t)\Phi(x)\,, \tag{E.4}$$

where $k_x(t)$ is a time varying state gain, $k_r(t)$ is a time varying reference gain, and $\hat{W}(t)$ is the estimate of the unknown vector W. The total control input is the sum of the linear quadratic regulator input and the adaptive control input, given as

$$u(t) = \left(k_x(t) - k_{LQR}\right)x(t) + \left(k_r(t) + k_g\right)r(t) - \hat{W}^T(t)\Phi(x)\,. \tag{E.5}$$

The above control input can be substituted in Eq. (E.2) to yield

$$\dot{x}(t) = \left(a_0 + b\lambda(k_x(t) - k_{LQR})\right)x(t) + b\lambda(k_r(t) + k_g)r(t) - b\lambda\Delta W^T(t)\Phi(x)\,, \tag{E.6}$$

where $\Delta W(t) = \hat{W}(t) - W(t)$ is the parameter estimation error. Next, we formulate assumptions to guarantee the existence of the adaptive feedback signals by comparing Eq. (E.3) and Eq. (E.6). We assume that

$$\exists\; k_x^*,\; b\lambda(k_x^* - k_{LQR}) = a_m - a \quad \text{and} \quad \exists\; k_r^*,\; b\lambda(k_r^* + k_g) = b_m\,. \tag{E.7}$$

Note that the true knowledge of the gains k_x^* and k_r^* is not required; we only assume

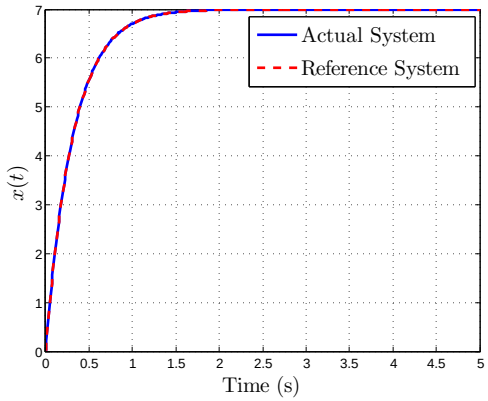

(a) Time history of the state $x(t)$.

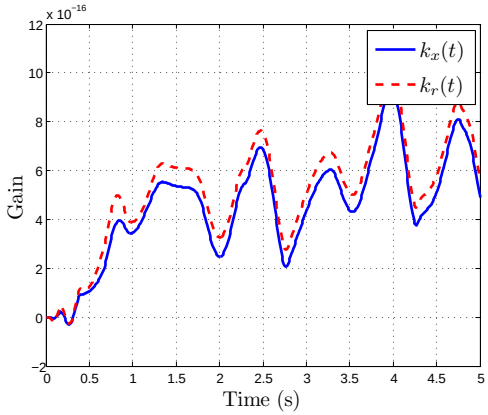

(b) Time histories of the state and reference gains.

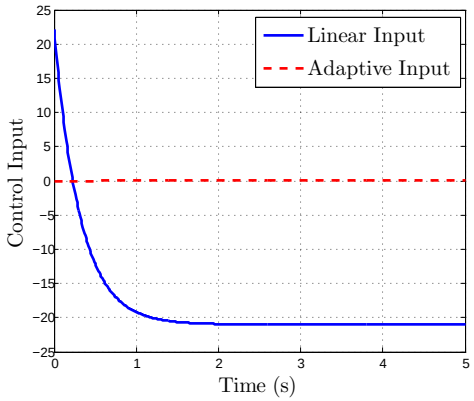

(c) Time history of the control inputs u_{lin} and u_{ada}.

Figure E.1: Overall controller performance in the absence of system uncertainties ($a = a_0$).

they exist. Through these assumptions, and employing the definition of the error signal, the tracking error dynamics are written:

$$\dot{e}(t) = a_m e(t) + b\lambda \left(\Delta k_x(t) x(t) + \Delta k_r(t) r(t) - \Delta W^T(t) \Phi(x) \right) , e(0) = e_0 , \tag{E.8}$$

where $\Delta k_x(t) = k_x(t) - (k_x^* - k_{LQR})$, $\Delta k_r(t) = k_r(t) - (k_r^* + k_g)$ denote the gain errors. We propose the following adaptation laws:

$$\begin{aligned}
\dot{k}_x(t) &= -\gamma_x x(t) e(t) P b \text{sign}(\lambda) \quad , \quad k_x(0) = k_{x0} , \\
\dot{k}_r(t) &= -\gamma_r r(t) e(t) P b \text{sign}(\lambda) \quad , \quad k_r(0) = k_{r0} , \\
\dot{\hat{W}}(t) &= \Gamma_W \Phi(x(t)) e(t) P b \text{sign}(\lambda) \quad , \quad \hat{W}(0) = \hat{W}_0 \quad \Gamma \in \mathbb{R}^{N \times N} ,
\end{aligned} \tag{E.9}$$

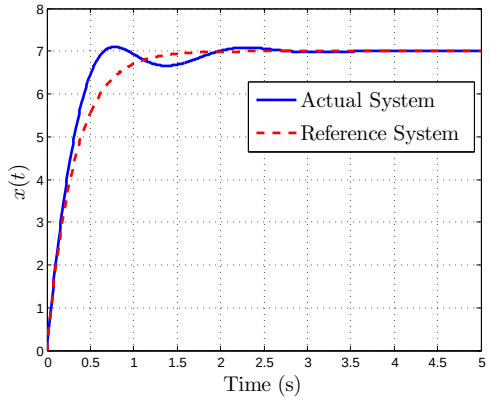

(a) Time history of the state $x(t)$.

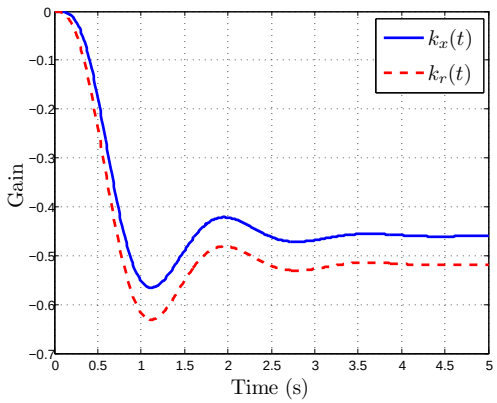

(b) Time histories of the state and reference gains.

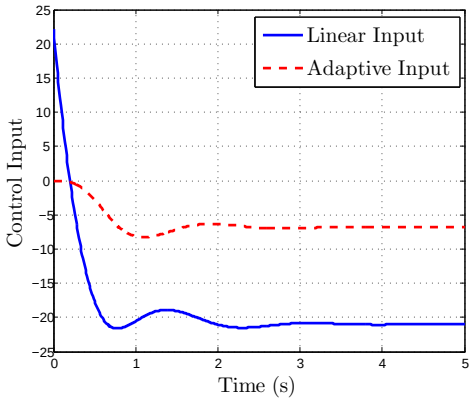

(c) Time history of the control inputs u_{lin} and u_{ada}.

Figure E.2: Overall controller performance in the presence of system uncertainties ($a \neq a_0$).

where $\gamma_x > 0$, $\gamma_r > 0$ and $\Gamma_W = \Gamma^T > 0$ are the adaptation gains. We define the Lyapunov candidate function:

$$V(e(t), \Delta k_x(t), \Delta k_r(t), \Delta W(t)) = \\ e(t)Pe + |\lambda| \left(\frac{1}{\gamma_x} (\Delta k_x(t))^2 + \frac{1}{\gamma_r} (\Delta k_r(t))^2 + \Delta W^T(t) \Gamma_W^{-1} \Delta W(t) \right) , \qquad \text{(E.10)}$$

with p being the solution of the algebraic Lyapunov equation. Since the system is scalar, p is given as

$$p = -\frac{q}{2a_m} ,$$

and since a_m is negative, then $p > 0$ for arbitrary $q > 0$. The time derivative of the candidate Lyapunov function along the system trajectories is

$$\dot{V} = -qe^2(t) + 2e(t)pb\lambda \left(\Delta k_x(t)x(t) + \Delta k_r(t)r(t) - \Delta W^T(t)\Phi(x) \right)$$

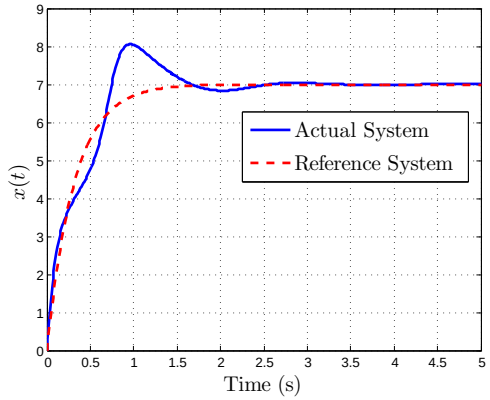

(a) Time history of the state $x(t)$.

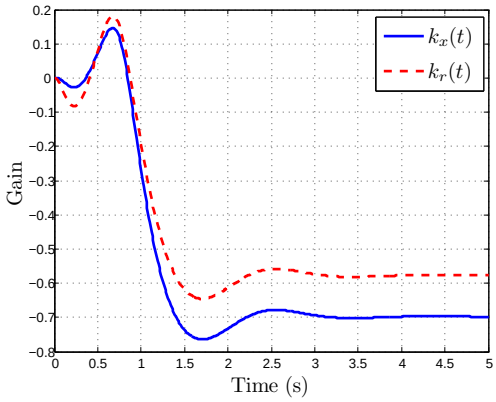

(b) Time histories of the state and reference gains.

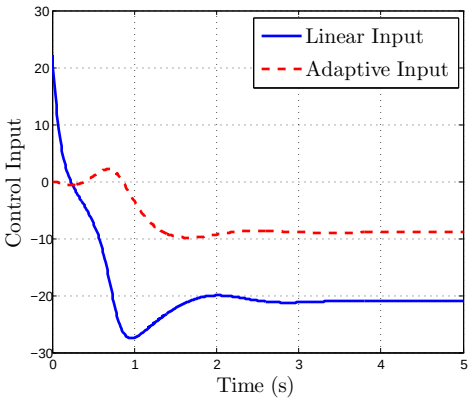

(c) Time history of the control inputs u_{lin} and u_{ada}.

Figure E.3: Overall controller performance in the presence of system nonlinearities ($f(x) = 5\sin(x) + 5\cos(x) + 2$) and absence of uncertainties ($a = a_0$).

$$
\begin{aligned}
&+2\frac{|\lambda|}{\gamma_x}\Delta k_x(t)\Delta\dot{k}_x(t) + 2\frac{|\lambda|}{\gamma_r}\Delta k_r(t)\Delta\dot{k}_r(t) + 2|\lambda|\Delta W^T(t)\Gamma_W^{-1}\Delta\dot{W}(t) \\
&= -qe^2(t) + 2|\lambda|\Delta k_x(t)\left(e(t)pbx(t)\text{sign}(\lambda) + \frac{\dot{k}_x(t)}{\gamma_x}\right) \\
&+2|\lambda|\Delta k_r(t)\left(e(t)pbr(t)\text{sign}(\lambda) + \frac{\dot{k}_r(t)}{\gamma_r}\right) \\
&+2|\lambda|\Delta W^T(t)\left(-e(t)pb\Phi(x)\text{sign}(\lambda) + \Gamma_W\dot{\hat{W}}(t)\right),
\end{aligned}
$$

which after invoking the adaptation laws becomes

$$\dot{V} = -qe^2(t) < 0\,.$$

Since the first derivative of the candidate Lyapunov function is negative semidefinite, then all signals are bounded, and through applying Barbalat's lemma (see Subsection 5.4.1,

Page 136), we conclude that $e(t) \to 0$, i.e., $x(t) \to x_m(t)$ as time increases.

So, the above controller is a model reference adaptive controller that uses an LQR controller as its baseline controller. For the simulation conducted here, the following values were used

$$a_0 = 3,\ a = 4,\ b = 1,\ c = 1,\ x_0 = 0,\ x_{m0} = 0,\ \lambda = 1,\ r(t) = 7,\ N = 5$$
$$\gamma_x = 1,\ \gamma_r = 1,\ \Gamma_W = I_{N\times N},\ k_x(0) = 0,\ k_r(0) = 0,\ \hat{W}(0) = 0_{N\times 1}$$

In the absence of nonlinearities in the system, the uncertainty in the system remains only in a. If the nominal value of a, a_0 is close to its real value, the adaptive controller does not produce any input, Fig. E.1. However, if our estimate deviates from the real value of a (which we do not know), then the adaptive control interferes correction the dynamics of the system, Fig. E.2. With this approach, already existing controllers are augmented with an adaptive controller that interferes only when the system deviates from its baseline performance. If the system exhibits nonlinearities (for this case $f(x) = 5\sin(x)+5\cos(x)+2$), the adaptive controller will interfere, even in the absence of system uncertainties, Fig. E.3.

Bibliography

Accorsi, M., Lu, K., Leonard, J., Benney, R., and Stein, K. (1999). Issues in Parachute Structural Modeling - Damping and Wrinkling. In *Proceedings of CEAS/AIAA Aerodynamic Decelator Systems Technology Conference*, Toulouse, France.

Adetona, O., Horta, L., Taleghani, B., Blandino, J., and Woods, K. (2003). Vibration Studies of an Inflatable/Rigidizable Hexapod Structure with a Tensioned Membrane. In *Proceedings of AIAA/ASME/ASCE/AHS/ASC Structures, Structural Dynamics and Material Conference*, Norfolk, VA.

Adler, A. (2000). *Finite Element Approaches for Static and Dynamic Analysis of Partially Wrinkled Membrane Structures*. Phd dissertation, University of Colorado, Boulder, CO.

Adler, A. and Mikulas, M. (2001). Application of a Wrinkled Membrane Finite Element Approach to Advanced Membrane Structures. In *AIAA Space Conference and Exposition*, Albuquerque, NM.

Alhazza, K. A. and Alhazza, A. A. (2004). A Review of the Vibrations of Plates and Shells. *The Shock and Vibration Digest*, 36(5):377–395.

Anderson, B. and Moore, J. (1990). *Optimal Control: Linear Quadratic Methods*. Prentice Hall, Englewood Cliffs, NJ.

Anderson, E., Bai, Z., Bishof, C., Blackford, S., Demmel, J., Dongarra, J., Du Croz, J., Greenbaum, A., Hammarling, S., McKenny, A., and Sorensen, D. (1999). *LAPACK Users' Guide*. Philadelphia, PA, 3rd edition.

Andoh, F., Washington, G., Yoon, H.-S., and Utkin, V. (2004). Efficient Shape Control of Distributed Reflectors with Discrete Piezoelectric Actuators. *Journal of Intelligent Material Systems and Structures*, 15:3–15.

Ash, J., Jenkins, C., Marker, D., and Wilkes, J. (2004). Shape Achievement of Optical Membrane Mirrors Using Coating/Substrate Intrinsic Stresses. *AIAA Journal of Spacecraft and Rockets*, 41(4):551–557.

Balas, M. (1982). Trends in Large Space Structure Control Theory: Fondest Hopes, Wildest Dreams. *IEEE Transactions on Automatic Control*, 27(3):522–535.

Bales, G., Hall, J., Flint, E., and Glaese, R. (2003). Experimental Issues that Impact in-Vaccum Dynamic Characterization of Thin Film Membranes. In *Proceedings of AIAA/ASME/ASCE/AHS/ASC Structures, Structural Dynamics and Material Conference*, Norfolk, VA.

Banks, H., Inman, D., Leo, D., and Wang, Y. (1996a). An Experimentally Validated Damage Detection Theory in Smart Structures. *Journal of Sound and Vibration*, 191(5):859–880.

Banks, H., Smith, R., and Wang, Y. (1996b). *Smart Material Structures: Modeling, Estimation and Control*. John Wiley and Sons, Hoboken, NJ.

Banks, H., Smith, R. C., and Wang, Y. (1995). Modeling and Parameter Estimation for an Imprefectly Clamped Plate. Technical Report CRSC-TR95-2, CRSC, Boston, MA.

Banks, H., Wang, Y., Inman, D., and Slater, J. (1994). Approximation and Parameter Identification for Damped Second Order Systems with Unbounded Input Operators. *Control: Theory and Advanced Technology*, 10:873–892.

Baruh, H. (2001). Control of The Elastic Motion of Lightweight Structures. In *Proceedings of AIAA/ASME/ASCE/AHS/ASC Structures, Structural Dynamics and Material Conference*, Seattle, WA.

Bekey, I. (1999). A 25 m Diameter Space Telescope Weighing Less Than 150 kg. In *Proceedings of AIAA Space Technology Conference & Exposition*, Albuquerque, NM. AIAA.

Belvin, K. (2004). Advances in Structures for Large Space Systems. In *AIAA Space Conference and Exhibit*, San Diego, CA.

Bhoir, N. and Singh, S. (2005). Control of Unsteady Aeroelastic System via State-Dependent Riccati Equation Method. *AIAA Journal of Guidance, Control and Dynamics*, 28(1):78–84.

Blandino, J., Dharamsi, U., Johnston, J., and Miles, J. (2002). The Effect of Asymmetric Mechanical and Thermal Loading on Membrane Wrinkling. In *Proceedings of AIAA/ASME/ASCE/AHS/ASC Structures, Structural Dynamics and Material Conference*, Denver, CO.

Blandino, J., Johnston, J., Miles, J., and Soplop, J. (2001). Thin Film Membrane Wrinkling due to Mechanical and Thermal Loads. In *Proceedings of AIAA/ASME/ASCE/AHS/ASC Structures, Structural Dynamics and Material Conference*, Seattle, WA.

Cadogan, D., Scarborough, S., Lin, J., and Sapna III, G. (2002). Shape Memory Composite Development for Use in Gossamer Space Inflatable Structures. In *Proceedings of AIAA/ASME/ASCE/AHS/ASC Structures, Structural Dynamics and Material Conference*, Denver, CO.

Cao, C. and Hovakimyan, N. (2007). Novel $\mathscr{L}_1$ neural network adaptive control architecture with guaranteed transient performance. *IEEE Transactions on Neural Networks*, 18(4):1160 – 1171.

Cao, C. and Hovakimyan, N. (2008). Design and analysis of a novel $\mathscr{L}_1$ adaptive control architecture with guaranteed transient performance. *IEEE Transactions on Automatic Control*, 53(2):586 – 591.

Carreras, R. and Marker, D. (2004). Control Model for a Large Optical Membrane Mirror with Inner Ring Control. In *Intelligent Automation and Control Trends, Principles, and*

Applications - Proceedings of the Sixth Biannual World Automation Congress, WAC, pages 359–364, Seville, Spain.

Cassapakis, C. and Thomas, M. (1995). Inflatable Structures Technology Development Overview. In *AIAA 1995 Space Programs and Technologies Conference*, Huntsvill, AL.

Celina, M., Dargaville, T., Assink, R., and Martin, J. (2005). Selection and Optimization of Piezoelectric Polyvinylidene Fluoride Polymers for Adaptive Optics in Space Environments. *High Performance Polymers*, 17:575–592.

Chee, C., Tong, L., and Steven, G. (2002). Static Shape Control of Composite Plates Using a Slope-Displacement-Based Algorithm. *AIAA Journal of Spacecraft and Rockets*, 40(8):1611–1618.

Cheung, D., Barnes, T., and Haskel, T. (2003). Feedback Interferometry with Membrane Mirror for Adaptive Optics. *Optics Communications*, 218:33–41.

Chmielewski, A., Moore, C., and Howard, R. (2000). The Gossamer Initiative. In *Poceedings of IEEE Aerospace Conference*, volume 7, pages 429–438.

Chodimella, S., Moore, J., and Patrick, B. (2005). Design, Fabrication and Validation of an Ultra-Lightweight Membrane Mirror. In *Proceedings of SPIE*, Bellingham, WA.

Choi, S., Chu, S.-H., Song, K., and King, G. (2002). Microwave-Driver Multifunctional Capability of Membrane Structures. In *Proceedings of NanoTech - "At the Edge of Revolution"*, Houston, TX.

da Costa Rodrigues, G. N. M. (2006). Piezoelectric Actuation of Deformable Membrane Mirror. MS Thesis, Université Libre de Bruxelles, Brussels, Belgium.

Darooka, D. and Jensen, D. (2001). Advanced Space Structure Concepts and their Development. In *Proceedings of AIAA/ASME/ASCE/AHS/ASC Structures, Structural Dynamics and Material Conference*, Seattle, WA.

Davis, D. and Agnes, G. (2002). Environmental Disturbance Modeling for Inflatable Space Structures. In *43rd AIAA/ASME/ASCE/AHS Structures, Structural Dynamics, and Materials Conference*, Denver, CO.

Dayton, D., Restaino, S., Gonglewski, J., Gallegos, J., McDermott, S., Browne, S., Rogers, S., Vaidyanathan, M., and Shilko, M. (2000). Laboratory and Field Demonstration of a Low Cost Membrane Mirror Adaptive Optics System. *Optics Communications*, 176:339–345.

deBlonk, B. (2003). Selecting Models to Predict the Optical-Level Behavior of Membrane Primary Mirrors. In *Proceedings of AIAA/ASME/ASCE/AHS/ASC Structures, Structural Dynamics and Material Conference*, Norfolk, VA.

deBoor, C., Hollig, K., and Riemenschneider, S. (1992). *Box Splines*, volume 98 of *Applied Mathematical Sciences*. Springer-Verlag.

Dimakov, S., Bogdanov, M., Gorlanov, A., Kislitsyn, B., Klimentév, S., and Zhuk, D. (2003). Electrically Controlled Pre-Shaped Membrane Mirror for Systems with Wavefront Correction. In Gonglewski, J., Vorontsov, M., and Gruneisen, M., editors, *Proceedings of Advanced Wavefront Control: Methods, Devices, and Applications III*, volume 5162, pages 147–156, Bellingham, WA.

Ding, H., Yang, B., Lou, M., and Fang, H. (2002). A Two-Viable Parameter Membrane Model for Wrinkling Analysis of Membrane Structures. In *Proceedings of AIAA/ASME/ASCE/AHS/ASC Structures, Structural Dynamics and Material Conference*, Denver, CO.

Dixit, S., Hyde, R., Weisberg, A., Early, J., Rushford, M., and Britten, J. (2002). Development of Large Aperture, Light-Weight Fresnel Lenses for Gossamer Space Telescopes. In *Proceedings of AIAA/ASME/ASCE/AHS/ASC Structures, Structural Dynamics and Material Conference*, Denver, CO.

Dorato, P., Abdallah, C., and Cerone, V. (2000). *Linear Quadratic Control, An Introduction*. Krieger Publishing Company, Malabar, FL.

DuPont (2002). *DuPont Technical Bulletin, H-78317*. DuPont, Wilmington, DE.

Early, J. (2002). Solar Sail - Fresnel Zone Plate Lens for a Large Space Based Telescope. In *Proceedings of AIAA/ASME/ASCE/AHS/ASC Structures, Structural Dynamics and Material Conference*, Denver, CO.

Endelman, L. (1990). The Hubble Telescope: Mission, History, and Systems. In *SPIE International Congress on High-Speed Photography and Photonics*, volume 1358, pages 422–441.

Fernández, E. and Artal, P. (2003). Membrane Deformable Mirror for Adaptive Optics: Performance Limits in Visual Optics. *Optics Express*, 11(9):1056–1069.

Ficocelli, M. and Ben Amara, F. (2005). Control System Design for Retinal Imaging Adaptive Optics Systems. In *Proceedings of IMECE2005, ASME International Mechanical Engineering Congress and Exposition*, Orlando, FL.

Flint, E., Bales, G., Glaese, R., and Bradford, R. (2003). Experimentally Characterizing the Dynamics of 0.5m+Diameter Doubly Curved Shells made from Thin Films. In *Proceedings of AIAA/ASME/ASCE/AHS/ASC Structures, Structural Dynamics and Material Conference*, Norfolk, VA.

Forster, E. and Livne, E. (2000). Integrated Structure/Actuation Synthesis of Strain Actuated Devices for Shape Control. In *Proceedings of AIAA/ASME/ASCE/AHS/ASC Structures, Structural Dynamics and Material Conference*, Reston, VA.

Garner, C. and Leipold, M. (2000). Developments and Activities in Solar Sail Propulsion. In *Proceedings of AIAA/ASME/SAE/ASEE Joint Propulsion Conference and Exhibit*, Huntsvill, AL.

Gaspar, J., Mann, T., Behun, V., Wilkie, W., and Pappa, R. (2004). Development of Modal Test Techniques for Validation of a Solar Sail Design. In *Proceedings of AIAA/ASME/ASCE/AHS/ASC Structures, Structural Dynamics and Material Conference*, Palm Springs, CA.

Gavrin, A., Blizard, K., Leo, D., and Bennett, M. (2004). Electroactive Smart Polymers for Space Optics. *Proceedings of SPIE - The International Society for Optical Engineering*, 5390:217–224. Actuation;Thin membranes;Ionic polymers;Mirror shape control;.

Glaese, R. and Bales, G. (2004). Demonstration of Dynamic Tailoring for Gossamer Structures. In *Proceedings of AIAA/ASME/ASCE/AHS/ASC Structures, Structural Dynamics and Material Conference*, Palm Springs, CA.

Gooding, J. C., Babuška, V., Griffith, D. T., Ingram, B. R., and Robertson, L. M. (2007). Study of Free-Free Beam Structural Dynamics Perturbation Due to Mounted Cable Harnesses. In *Proceedings of AIAA/ASME/ASCE/AHS/ASC Structures, Structural Dynamics and Material Conference*, Las Vegas, NV.

Gorinevsky, D. and Hyde, T. (2002). Adaptive Membrane for Large Lightweight Space Telescopes. In *Proceedings of SPIE, Highly Innovative Space Telescope Concepts*, volume 4849.

Gorinevsky, D., Hyde, T., and Cabuz, C. (2001). Distributed Localized Shape Control of Gossamer Space Structures. In *Proceedings of AIAA/ASME/ASCE/AHS/ASC Structures, Structural Dynamics and Material Conference*, Seattle, WA.

Greeschik, G., Palisoc, A., Cassapakis, C., Veal, G., and Mikulas, M. (1998). Approximating Paraboloids with Axisymmetric Pressurized Membranes. In *Proceedings of AIAA/ASME/ASCE/AHS/ASC Structures, Structural Dynamics and Material Conference*, volume 4, pages 2772–2782.

Greschik, G. (2006). Solar Sail Scalability and the Concept of a "Truly Scalable" Architechture. In *Proceedings of AIAA/ASME/ASCE/AHS/ASC Structures, Structural Dynamics and Material Conference*, New Port, RI.

Grosso, R. and Yellin, M. (1977). The Membrane Mirror as an Adaptive Optical Element. *Optical Society of America*, 67(3):399–406.

Gullapalli, S., Flood, R., Yang, E.-H., and Lih, S.-S. (2003). New Technologies for the

Actuation and Control of Large Aperture Lightweight Optical Quality Mirrors. In *Proceedings of IEEE Aerospace Conference*, volume 4, Big Sky, MT.

Gunderson, L., Jenkins, C., Wilkes, J., and Marker, D. (2004). Pressuer-Augmented Near Net-Shape Membrane Mirror. In *Proceedings of AIAA/ASME/ASCE/AHS/ASC Structures, Structural Dynamics and Material Conference*, Palm Springs, CA.

Hamelinck, R., Rosielle, N., Steinbuch, M., and Doelman, N. (2005). Large Adaptive Deformable Membrane Mirror with High Actuator Density: Design and First Prototype. In Jiang, W., editor, *Proceedings of 5th International Workshop of Adaptive Optics for Industry and Medicine*, volume 6018.

Hedgepeth, J. (1981). Critical Requirements for the Design of Large Space Structures. NASA Contractor Report (prepared for Langley Research Center under Contact NAS1-15347), No. 3484, Astro Research Corporation, Carpinteria, CA.

Heyliger, P. and Ramirez, G. (2000). Free Vibration of Laminated Circular Piezoelectric Plates and Discs. *Journal of Sound and Vibration*, 229(4):935–956.

Hishinuma, Y. and Yang, E.-H. (2005). Large Aperture Deformable Mirror with a Transferred Single-Crystal Silico Membrane Actuated Using Large-Stroke PZT Uniform Actuators. In *Proceedings of IEEE International Conference on Solid-State Sensors, Actuators and Microsystems*, pages 1167–1170, Seoul, Korea.

Hoagg, J., Bernstein, D., Lacy, S., and Venugopal, R. (2003). Adaptive Control of a Flexible Membrane Using Acoustic Excitation and Optical Sensing. In *Proceedings of AIAA Guidance, Navigation, and Control Conference and Exhibit*, Austin, TX.

Holland, D., Virgin, L., and Belvin, W. (2003). Investigation of Structural Dynamics in a 2-Meter Square Solar Sail Model Including Axial Load Effects. In *Proceedings of AIAA/ASME/ASCE/AHS/ASC Structures, Structural Dynamics and Material Conference*, Norfolk, VA.

Hollig, K. (2001). *Finite Element Methods with B-Splines*. Frontiers in Applied Mathematics. Society of Industrial and Applied Mathematics, Philadelphia, PA.

Hu, Y.-R. and Vukovich, G. (2003). Active Robust Shape Control of Flexible Structure. In *Proceedings of AIAA/ASME/ASCE/AHS/ASC Structures, Structural Dynamics and Material Conference*, Norfolk, VA.

Inman, D. (2007). *Engineering Vibrations*. Prentice Hall, Upper Saddle River, NJ 07458.

Iroshnikov, N., Ivanov, V., and Lachinova, S. (1999). Controlling of Spatial Patterns in Nonlinear Optical System with Feedback. In *Proceedings of SPIE Conference on High-Resolution Wavefront Control: Methods, Devices and Applications*, volume 3760, pages 129–140, Denver, CO.

Jenkins, C., editor (2001). *Gossamer Spacecraft: Membrane and Inflatable Structures Technology for Space Applications*, volume 191 of *Progress in Astonautics and Aeronautics*. AIAA, Reston, VA.

Jenkins, C., editor (2006). *Recent Advances in Gossamer Spacecraft*, volume 212 of *Progress in Astonautics and Aeronautics*. AIAA, Reston, VA.

Jenkins, C. and Faisal, S. (2001). Thermal Load Effects on Precision Membranes. *AIAA Journal of Spacecraft and Rockets*, 38(2):207–211.

Jenkins, C., Kalanovic, V., Padmanabhan, K., and Faisal, S. (1999). Intelligent Shape Control for Precision Membrane Antennae and Reflectors in Space. *Smart Materials and Structures*, 8:857–867.

Jha, A. and Inman, D. (2004). Sliding mode Control of a Gossamer Structure Using Smart Materials. *Journal of Vibration & Control*, 10(8):1199–1220.

Johnston, J. (2002). Finite Element Analysis of Wrinkled Membrane Structures for Sunshield Applications. In *Proceedings of AIAA/ASME/ASCE/AHS/ASC Structures, Structural Dynamics and Material Conference*, Denver, CO.

Johnston, J., Blandino, J., and McEvoy, K. (2004). Analytical and Experimental Characterization of Gravity Induced Deformations in Subscale Gossamer Structures. In *Proceedings of AIAA/ASME/ASCE/AHS/ASC Structures, Structural Dynamics and Material Conference*, Palm Springs, CA.

Kalanovic, V., Padmanabhan, K., and Jenkins, C. (1999). Discrete cell model for shape control of precision membrane antennae and reflectors. *American Society of Mechanical Engineers, Aerospace Division (Publication) AD*, 59:227 – 237. Discrete cell model;Shape control;Inflatable membrane structures;Precision membrane antennae;Precision reflectors;Feedback error learning;Surface precision;.

Khalil, H. (2000). *Nonlinear Systems*. Prentice Hall, Upper Saddle River, NJ 07458, 3^{rd} edition.

Korde, U., Jenkins, C., Farke, J., and Hofacker, M. (2006). Adaptive Rectangular Membranes Actuated Near Boundaries. In *Proceedings of SPIE Smart Structures and Materials: Smart Structures and Integrated Systems*, volume 6173.

Kukathasan, K. and Pelligrino, S. (2002). Vibration of Prestressed Membrane Structures in air. In *Proceedings of AIAA/ASME/ASCE/AHS/ASC Structures, Structural Dynamics and Material Conference*, Denver, CO.

Kukathasan, K. and Pelligrino, S. (2003). Nonlinear Vibration of Wrinkled Membranes. In *Proceedings of AIAA/ASME/ASCE/AHS/ASC Structures, Structural Dynamics and Material Conference*, Norfolk, VA.

Lee, K. and Lee, S. (2006). Analysis of Gossamer Structures Using Assumed-Strain Solid-Shell Finite Elements. *AIAA Journal of Spacecraft and Rockets*, 43(6):1301–1307.

Leifer, J., Belvin, W., Black, J., and Behun, V. (2003). Evaluation of Shear Compliant Borders for Wrinkle Reduction in Thin Film Membrane Structures. In *Proceedings of AIAA/ASME/ASCE/AHS/ASC Structures, Structural Dynamics and Material Conference*, Norfolk, VA.

Li, E., Yun, D., Wang, H., and Zhang, Y. (2006). Application of Eigenmode in the Adaptive Optics System Based on a Micromachined Membrane Deformable Mirror. *Applied Optics*, 45(22):5651–5656.

Liberzon, D. (2003). *Switching in Systems and Control*. Systems & Control: Foundation & Applications. Birkhäuser, Boston, MA.

Lin, C.-H. and Hsu, W. (2003). The Enhancement on Optical Attenuation by a Tunable Non-Smooth Mirror. *Proceedings of SPIE - The International Society for Optical Engineering*, 5116 II:480 – 487. Enhancement attenuation;Variable optical attenuator;Transmission matrix;Gaussian beam theory;.

Lindler, J. E. and Flint, E. M. (2004). Boundary Actuation Shape Control Strategies for Thin Film Single Surface Shells. In *Collection of Technical Papers - AIAA/ASME/ASCE/AHS/ASC Structures, Structural Dynamics and Materials Conference*, volume 5, pages 3360–3370, Palm Springs, CA, United States.

Lopez, B., Lih, S.-S., Leifer, J., and Guzman, G. (2004). Study of Ripple Formation in Unidirectionally-Tensioned Membranes. In *Proceedings of AIAA/ASME/ASCE/AHS/ASC Structures, Structural Dynamics and Material Conference*, Palm Springs, CA.

Lyshevski, S. E. (2003). Mems Smart Variable-Geometry Flexible Flight Control Surfaces: Distributed Control and High-Fidelity Modeling. *Proceedings of the IEEE Conference on Decision and Control*, 5:5426–5431. Distributed embedded control;High-performance systems;.

Magrab, E. B. (1979). *Vibration of Elastic Structural Members*. Mechanics of Structural Systems. Sijthoff & Noordhoff, Alphen aan den Rijn, The Netherlands.

Main, J., Martin, J., and Nelson, G. (1999). Noncontact Shape Control of Membrane Mirrors. In *Proceedings of the Ultra Lightweight Space Optics Challenge Workshop*, Napa, CA.

Maji, A. and Starnes, M. (2000). Shape Measurement and Control of Deployable Membrane Structures. *Experimental Mechanics*, 40(2):154–159.

Malacara, D. (1992). *Optical Shop Testing*. Pure and Applied Optics. John Wiley and Sons, New York, NY, 2^{nd} edition.

Malin, M., Macy, W., and Ferguson, G. (1983). Edge Actuation for Figure Control. In *Proceedings of SPIE - The International Society for Optical Engineering*, volume 365, pages 114 – 122, San Diego, CA, USA.

Marino, R. and P., T. (1995). *Nonlinear Control Design: Geometric, Adaptive & Robust*. Prentice Hall.

Marker, D. (February 14, 2007). Personal communication: progress meeting at Virginia Tech.

Marker, D. and Jenkins, C. (1997). Surface Precision of Optical Membrane with Curvature. *Otpics Express*, 1(11):324–331.

Marker, D., Rotge, J., Carreras, R., Duneman, D., and Wilkes, J. (1999). Minimum Strain Requirements for Optical Membranes. In *Proceedings of SPIE Conference on High-Resolution Wavefront Control: Methods, Devices and Applications*, Denver, CO.

Marker, D., Wilkes, J., Ruggiero, E., and Inman, D. (2005). Membrane adaptive optics. In Gruneisen, M., Gonglewski, J., and Giles, M., editors, *Proceedings of Advanced Wavefrong Control: Methods, Devices, and Applications III*, volume 5894, pages 1–8, Bellingham, WA. SPIE.

Meirovitch, L. (1997). *Principles and Techniques of Vibrations*. Prentice Hall.

Meyer, C., Leifer, J., Lopez, B., Jones, D., and Caddell, B. (2004). Zero- and One-g Comparison of Ripple Amplitude in Single-Curved Parabolic Membranes Using Photogrammetry. In *Proceedings of AIAA/ASME/ASCE/AHS/ASC Structures, Structural Dynamics and Material Conference*, Palm Springs, CA.

Miyazaki-Kawasaki, Y. and Furuya, H. (2001). Static Shape Control of Membrane Structures by Piezoelectric Films Bonded around Creases. In *Proceedings of AIAA/ASME/ASCE/AHS/ASC Structures, Structural Dynamics and Material Conference*, Seattle, WA.

Moore, J., Patrick, B., Chodimella, S., Marker, D., and deBlonk, B. (2005). Design and Testing of a One-Meter Membrane Mirror with Active Boundary Control. In *Proceedings of SPIE*, Bellingham, WA.

Mracek, C. and Cloutier, J. (1998). Control Designs for the Nonlinear Benchmark Problem via the State-Dependent Riccati Equation Method. *International Journal of Robust and Nonlinear Control*, 8:401–433.

Murphey, T. (2001). The Constitutive Modeling of Thin Films with Random Material Wrinkles. In *Proceedings of AIAA/ASME/ASCE/AHS/ASC Structures, Structural Dynamics and Material Conference*, Seattle, WA.

Murphey, T. and Mikulas, M. (1999). Nonlinear Effects of Material Wrinkles on the Stiffness of Thin Polymer Films. In *Proceedings of AIAA Guidance, Navigation, and Control Conference and Exhibit*, volume 2, St. Louis, MO.

Nader, M., Gattringer, H., Krommer, M., and Irschik, H. (2003). Shape Control of Flexural Vibrations of Circular Plates by Shaped Piezoelectric Actuation. *Journal of Vibration and Acoustics, Transactions of the ASME*, 125:88–84.

Nakaya, K., Nishimaki, S., Mori, O., and Kawaguchi, J. (2007). Dynamics of Large Membrane for Solar Sail-Craft. In *Proceedings of the ASME International Design Engineering Technical Conferences and Computers and Information in Engineering Conference*, Las Vegas, NV.

Nichols, J., Duneman, D., and Jasso, J. (1993). Performance Evaluation of an Edge-Actuated, Modal, Deformable Mirror. *Optical Engineering*, 22:366–370.

Noll, R. (1976). Zernike Polynomials and Atmospheric Turbulence. *Journal of the Optical Society of America*, 66(3):207–211.

Ozlu, E., Zhe, J., Chandra, S., Cheng, J., and Wu, X. (2006). Feasibility Study of a Smart Motion Generator Utilizing Electromagnetic Microactuator Arrays. *Smart Materials and Structures*, 15(3):859–868. Electromagnetic microactuator arrays;Smart motion generator;Optical manufacturing;.

Papa, R., Black, J., Blandino, J., Jones, T., Danehy, P., and Dorrington, A. (2003a). Dot-Projection Photogrammetry and Videogrammetry of Gossamer Space Structures. *AIAA Journal of Spacecraft and Rockets*, 40(6):858–867.

Papa, R., Lassiter, J., and Ross, B. (2003b). Structural Dynamics Experimental Activities in Ultralightweight and Inflatable Space Structures. *AIAA Journal of Spacecraft and Rockets*, 40(1):15–23.

Park, G., Ruggiero, E., and Inman, D. (2002). Dynamic Testing of Inflatable Structures Using Smart Materials. *Smart Materials and Structures*, 11:147–155.

Paterson, C., Munro, I., and Dainty, J. (2000). A Low Cost Adaptive Optics System Using a Membrane Mirror. *Optics Express*, 6(9):175–185.

Patrick, B., Moore, J., Chodimella, S., Maji, A., Marker, D., and Wilkes, J. (2005). Meter-Class Membrane Mirror with Active Boundary Control. In *Proceedings of AIAA/ASME/ASCE/AHS/ASC Structures, Structural Dynamics and Material Conference*, Austin, TX.

Patrick, B., Moore, J., Chodimella, S., Marker, D., and deBlonk, B. (2006). Final Testing and Evaluation of a Meter-Class Actively Controlled Membrane Mirror. In *Proceedings of AIAA/ASME/ASCE/AHS/ASC Structures, Structural Dynamics and Material Conference*, New Port, RI.

Peng, F., Hu, Y.-R., and Ng, A. (2004). Active Control of Inflatable Structure Membrane Wrinkles Using Genetic Algorithm and Neural Networks. In *Proceedings of AIAA/ASME/ASCE/AHS/ASC Structures, Structural Dynamics and Material Conference*, Palm Springs, CA.

Peng, F., Hu, Y.-R., and Ng, A. (2006). Testing of Membrane Space Structure Shape Control Using Genetic Algorithm. *AIAA Journal of Spacecraft and Rockets*, 43(4):788–793.

Peng, F., Jiang, X.-X., Hu, Y.-R., and Ng, A. (2005). Application of Shape Memory Alloy Actuators in Active Shape Control of Inflatable Space Structures. In *IEEE Aerospace Conference*, pages 1–10.

Perreault, J., Bifano, T., and Levine, B. (1999). Adaptive Optic Correction Using Silicon Based Deformable Mirrors. In *Proceedings of SPIE Conference on High-Resolution*

Wavefront Control: Methods, Devices and Applications, volume 3760, pages 12–22, Denver, CO.

Perreault, J., Bifano, T., Levine, B., and Horenstein, M. (2002). Adaptive Optic Correction Using Microelectromechanical Deformable Mirrors. *Optical Engineering*, 41(3):561–566.

Polejaev, V., Barbier, P., Carhart, G., Plett, M., Rush, D., and Vorontsov, M. (1999). Adaptive Compenstation of Dynamic Wavefront Aberrations Based on Blind Optimization Technique. In *Proceedings of SPIE Conference on High-Resolution Wavefront Control: Methods, Devices and Applications*, volume 3760, pages 88–95, Denver, CO.

Pollard, E., deBlonk, B., Erwin, R., and Jenkins, C. (2004). Characterizing the Non-Linear Behavior of Membrane Optics. In *Proceedings of SPIE*, Bellingham, WA.

Prasad, S., Gallas, Q., Horowitz, S., Homeijer, B., Sankar, B., Cattafesta, L., and Sheplak, M. (2006). Analytical Electrostatic Model of a Piezoelectric Composite Circular Plate. *AIAA Journal*, 44(10):2311–2318.

Prenter, P. (1975). *Splines and Variational Methods*. John Wiley and Sons, New York.

Qatu, M. (2004). *Vibration of Laminated Shells and Plates*. Elsevier Academic Press.

Quadrelli, M. and Sirlin, S. (2001). Modeling and Control of Membranes for Gossamer Spacecraft Part 1: Theory. In *Proceedings of AIAA/ASME/ASCE/AHS/ASC Structures, Structural Dynamics and Material Conference*, Seattle, WA.

Redding, D., Shi, F., Basinger, S., Cohen, D., Green, J., Lowman, A., and Ohara, C. (2003). Wavefront Sensing and Control for Large Space Optics. In *Proceedings of IEEE Aerospace Conference*, volume 4.

Renno, J. and Inman, D. (2007a). An Experimentally Validated Model of a Membrane Mirror Strip Actuated Using Multiple Active Fiber Composites for Adaptive Optics. *AIAA Journal of Spacecraft and Rockets*, 4(55):1140–1152.

Renno, J. and Inman, D. (2007b). Modeing of a Membrane Mirror Strip Actuated Using Multiple Active Fiber Composites. In *Proceedings of IMAC XXV, Conference and Exposition on Structural Dynamics*, Orlando, FL.

Renno, J., Tarazaga, P., Seigler, M., and Inman, D. (2006). Modeling of a Membrane Mirror Actuated Using Piezoelectric Bimorph. In *Proceedings of IMECE2006, ASME International Mechanical Engineering Congress and Exposition*, Chicago, IL.

Reynolds, R., Ferguson, T., and Funkhouser, J. (2001). Measurement of residual wrinkles in polymer membranes. In *Proceedings of AIAA/ASME/ASCE/AHS/ASC Structures, Structural Dynamics and Material Conference*, Seattle, WA.

Rogers, J. and Agnes, G. (2002). Active Axisymmetric Optical Membranes. In *43rd AIAA/ASME/ASCE/AHS Structures, Structural Dynamics, and Materials Conference*, Denver, CO.

Rogers, J. and Agnes, G. (2003). Modeling Discontinous Axisymmetric Active Optical Membranes. In *AIAA Journal of Spacecraft and Rockets*, volume 40.

Ruggiero, E. (2005). *Modeling and Control of SPIDER Satellite Components*. Phd dissertation, Department of Mechanical Engineering, Virginia Polytechnic Institute and State University, Blacksubrg, VA.

Ruggiero, E., Bonnema, G., and Inman, D. (2003a). Application of SISO and MIMO Modal Analysis Techniques on a Membrane Mirror Satellite. In *Proceedings of IMECE2003, ASME International Mechanical Engineering Congress and Exposition*, Washington, D.C.

Ruggiero, E. and Inman, D. (2006a). Enhancing the Effective Bandwidth of a Membrane Optic Using a Shallow, Fluid-Filled Cavity. In *Proceedings of AIAA/ASME/ASCE/AHS/ASC Structures, Structural Dynamics and Material Conference*, New Port, RI.

Ruggiero, E. and Inman, D. (2006b). Gossamer Spacecraft: Recent Trends in Design, Analysis, Experimentation and Control. *AIAA Journal of Spacecraft and Rockets*, 43(1):10–24.

Ruggiero, E. and Inman, D. (2006c). Modeling and Control of a 2-D Membrane Mirror with a PZT Bimorph. In *Proceedings of IMECE2006, ASME International Mechanical Engineering Congress and Exposition*, Chicago, IL.

Ruggiero, E., Jacobs, J., and Babb, B. (2004a). A SPIDER Technology Overview. In *Proceedings of AIAA/ASME/ASCE/AHS/ASC Structures, Structural Dynamics and Material Conference*.

Ruggiero, E., Jha, A., Park, G., and Inman, D. (2003b). A Literature Review of Ultra-Light and Inflated Toroidal Satellite Components. *The Shock and Vibration Digest*, 35(3):171–181.

Ruggiero, E., Park, G., and Inman, D. (2004b). Multi-input Multi-output Vibration Testing of an Inflatable Torus. *Mechanical Systems and Signal Processing*, 18(5):1187–1201.

Ruggiero, E., Singler, J., Burns, J., and Inman, D. (2004c). Finite Element Formulation for Static Shape Control of a Thin Euler-Bernoulli Beam Using Piezoelectric Actuators. In *Proceedings of IMECE2004, ASME International Mechanical Engineering Congress and Exposition*, Anaheim, CA.

Ruggiero, E. J. and Inman, D. J. (2006d). Modeling and Control of a 2-D Membrane Mirror with a PZT Bimorph. In *Proceedings of American Society of Mechanical Engineers, Aerospace Division*, Chicago, IL, United States.

Sakamoto, H. and Park, K. (2006). Active Vibration Suppression Strategy for a Membrane Reflector/Mirror Undergoing Slewing Maneuvers. In *Proceedings of AIAA/ASME/ASCE/AHS/ASC Structures, Structural Dynamics and Material Conference*, New Port, RI.

Salama, M. and Jenkins, C. (2001). Intelligent Gossamer Structures: A Review of Recent Developments and Future Trends. In *Proceedings of AIAA/ASME/ASCE/AHS/ASC Structures, Structural Dynamics and Material Conference*, Seattle, WA.

Sandu, A., Sandu, C., and Ahmadian, M. (2006a). Modeling Multibody Systems with

Uncertainties. Part I: Theoretical and Computational Aspects. *Multibody System Dynamics*, 15(4):369 – 391.

Sandu, C., Sandu, A., and Ahmadian, M. (2006b). Modeling Multibody Systems with Uncertainties. Part II: Numerical Applications. *Multibody System Dynamics*, 15(3):241 – 262.

Sastry, S. and Bodson, M. (1989). *Adaptive Control: Stability, Convergence & Robustness*. Prentice Hall.

Scott, R., Brown, M., and Levesley, M. (2003). Robust Multivariable Control of a Double Beam Cantilever Smart Structure. *Smart Materials and Structures*, 12:731–743.

Sekouri, E. M., Hu, Y.-R., and Ngo, A. D. (2004). Modeling of a Circular Plate with Piezoelectric Actuators. *Mechatronics*, 14:1007–1020.

Shepherd, M., Cobb, R., and Baker, W. (2006a). Clear Aperture Design Criterion for Deformable Membrane Mirror Control. In *IEEE Aerospace Conference*, volume 2006, Big Sky, MT.

Shepherd, M., Peterson, G., Cobb, R., and Palazotto, A. (2006b). Quasi-Static Optical Control of In-Plane Actuated, Deformable Mirror: Experimental Comparison with Finite Element Analysis. In *Proceedings of AIAA/ASME/ASCE/AHS/ASC Structures, Structural Dynamics and Material Conference*, New Port, RI.

Slade, K. and Tinker, M. (1999). Analytical and Experimental Investigation of the Dynamics of Polyimide Inflatable Cylinders. In *Proceedings of AIAA/ASME/ASCE/AHS/ASC Structures, Structural Dynamics and Material Conference*, volume 4, St. Louis, MO.

Smith, R. C. (1994). A Galerkin Method for Linear PDE Systems in Circular Geometries with Structural Acoustic Applications. Technical Report NASA-CR-194925, NASA.

Sobers, D., Agnes, G., and Mollenhauer, D. (2003). Smart Structures for Control of Optical Surfaces. In *Proceedings of AIAA/ASME/ASCE/AHS/ASC Structures, Structural Dynamics and Material Conference*.

Solter, M., Horta, L., and Panetta, A. (2003). A Study of a Prototype Actuator Concept for Membrane Boundary Control. In *Proceedings of AIAA/ASME/ASCE/AHS/ASC Structures, Structural Dynamics and Material Conference*, Norfolk, VA.

Spitzer, L., J. (1946). The Astronomical Advantages of an Extra-Terrestrial Observatory. *Astronomy Quarterly*, 7:131.

Strang, G. and Fix, G. (1973). *An Analysis of The Finite Element Method*. Prentice Hall, Upper Saddle River, NJ 07458.

Su, X., Abdi, F., Taleghani, B., and Blandino, J. R. (2003). Wrinkling Analysis of a Kapton Square Membrane under Tensile Loading. *Collection of Technical Papers - AIAA/ASME/ASCE/AHS/ASC Structures, Structural Dynamics and Materials Conference*, 7:5332–5338.

Sun, D. and Tong, L. (2003). Optimum Control Voltage Design for Constrained Static Shape Control of Piezoelectric Structures. *AIAA Journal*, 41(12):2444–2450.

Sun, D. and Tong, L. (2005). Energy Optimization in Local Shape Control of Structures with Nonlinear Piezoelectric Actuators. *AIAA Journal*, 43(10):2210–2217.

Sung, Y.-G. (2002). An Estimator-Based Sliding-Mode Control for Maneuvering a Flexible Spacecraft. *Journal of Sound and Vibration*, 256(1):155–171.

Sutjahjo, E., Su, X., Abdi, F., and Taleghani, B. (2004). Dynamic Wrinkling Analysis of Kapton Membrane under Tensile Loading. *Collection of Technical Papers - AIAA/ASME/ASCE/AHS/ASC Structures, Structural Dynamics and Materials Conference*, 4:2477–2483.

Takami, H. and Iye, M. (1994). Membrane Deformable Mirror for SUBARU Adaptive Optics. In *Proceedings of SPIE - The International Society for Optical Engineering*, volume 2201, pages 762–767.

Tannehill, J. C., Anderson, D. A., and Pletcher, R. H. (1997). *Computational Fluid Mechanics and Heat Transfer*. Computational and Physical Processes in Mechanics and Thermal Sciences. Taylor and Francis, second edition.

Tessler, A., Sleight, D., and Wang, J. (2003). Nonlinear Shell Modeling of Thin Membranes with Emphasis on Structural Wrinkling. In *Proceedings of AIAA/ASME/ASCE/AHS/ASC Structures, Structural Dynamics and Material Conference*, Norfolk, VA.

Tyson, R. K. (2000). *Introduction to Adaptive Optics*, volume TT41 of *SPIE Tutorial Texts in Optical Engineering*. SPIE Press.

Tzou, H., Chai, W., and Wang, D. (2002). Micro-Actuations and Location Sensitivity of Actuator Patches Laminated on Toroidal Shells. In *Proceedings of the ASME Design Engineering Division*, volume 115, pages 247–256.

Tzou, H., Chai, W., and Wang, D. (2004). Micro-Control Actions and Location Sensitivity of Actuator Patches Laminated on Toroidal Shells. *Journal of Vibration and Acoustics, Transactions of the ASME*, 126(2):284–297.

Utkin, V. (1992). *Sliding Modes in Control and Optimization*. Springer-Verlag, New York.

Varadarajan, S., Chandrashkhara, K., and Agarwal, S. (1998). Adaptive Shape Control of Laminated Composite Plates Using Piezoelectric Materials. *AIAA Journal*, 36(9):1694–1698.

Vdovin, G., Sarro, P., Gonté, F., Collings, N., and Dandliker, R. (1999). Recent Progress in Technology and Applications of Membrane Micromachined Deformable Mirrors. In *Proceedings of SPIE Conference on High-Resolution Wavefront Control: Methods, Devices and Applications*, Denver, CO.

Ventsel, E. and Krauthammer, T. (2001). *Thin Plates and Shells: Theory, Analysis and Applications*. Marcel Dekker, Inc., New York, NY.

Vidyasagar, M. (1993). *Nonlinear Systems Analysis*. Classics in Applied Mathematics. SIAM, 2^{nd} edition.

Vorontsov, M. (1999). High-Resolution Wavefront Control: Adaptive Optics and Image Processing Applications. In *Proceedings of SPIE Conference on High-Resolution Wavefront Control: Methods, Devices and Applications*, volume 3760, pages 54–60, Denver, CO.

Wang, H., Xiangang, L., Hanmin, Y., and Chunlei, D. (2006). Principle of a New Deformable Mirror Actuated by Liquid Drops. In *Proceedings 2nd International Symposium on Advanced Optical Manufacturing and Testing Technologies: Advanced Optical Manufacturing Technologies*, volume 6149.

Wang, X., Zheng, W., and Hu, Y.-R. (2007). Active Flatness Control of Membrane Structures Using Adaptive Genetic Algorithm. In Davis, L. P., Henderson, B., and McMickell, M. B., editors, *Proceedings of SPIE Industrial and Commercial Applications of Smart Structures and Technologies*, volume 6527.

Whites, K. and Knowles, T. (2001). Electromagnetic Force and Torque Calculations for Fibrous Ultra-Lightweight Sails. In *Proceedings of AIAA/ASME/ASCE/AHS/ASC Structures, Structural Dynamics and Material Conference*, Seattle, WA.

Wilkes, J., Jenkins, C., Marker, D., Carreras, R., Duneman, D., and Rotge, J. (1999). Concave Membrane Mirrors from Aspheric to near Parabolic. In *Proceedings of SPIE Conference on High-Resolution Wavefront Control: Methods, Devices and Applications*, Denver, CO.

Williams, R., Inman, D., and Austin, E. (2001). Local Effects of PVDF Patches on Inflatable Space-Based Structures. In *Proceedings of AIAA/ASME/ASCE/AHS/ASC Structures, Structural Dynamics and Material Conference*, Seattle, WA.

Witherspoon, S. and Tung, S. (2002). Design and Fabrication of an EAP Actuator System for Space Inflatable Structures. In *Proceedings of AIAA/ASME/ASCE/AHS/ASC Structures, Structural Dynamics and Material Conference*, Denver, CO.

Wong, Y. and Pelligrino, S. (2002). Computation of Wrinkle Amplitude in Thin Membrane. In *Proceedings of AIAA/ASME/ASCE/AHS/ASC Structures, Structural Dynamics and Material Conference*, Denver, CO.

Wong, Y. and Pelligrino, S. (2003). Prediction of Wrinkle Amplitudes in Square Solar Sails. In *Proceedings of AIAA/ASME/ASCE/AHS/ASC Structures, Structural Dynamics and Material Conference*, Norfolk, VA.

Xiu, D. and Karniadakis, G. E. (2002). The Wiener-Askey Polynomial Chaos for Stochastic Differential Equations. *SIAM Journal of Scientific Computing*, 24(2):619 – 644.

Yang, B., Ding, H., Lou, M., and Fang, H. (2001). A New Approach to Wrinkling Prediction for Space Membrane Structures. In *Proceedings of AIAA/ASME/ASCE/AHS/ASC Structures, Structural Dynamics and Material Conference*, Seattle, WA.

Yang, S. and Ngoi, B. (2000). Shape Control of Beams by Piezoelectric Actuators. *AIAA Journal*, 38(12):2292–2298.

Young, L. and Pai, P. (2004). Numerical and Experimental Dynamic Characteristics of Thin-Film Membranes. In *Proceedings of AIAA/ASME/ASCE/AHS/ASC Structures, Structural Dynamics and Material Conference*, Palm Springs, CA.

Zernike, F. (1934). Begunstheorie des Schneidenver-Fahrens und Seiner Verbesserten Form der Phasenkontrastmethode. *Physica*, 1(689).

Zernike, F. (1954). *The Diffraction Theory of Aberrations*. Natural Bureau of Standards, Washington, D.C.